Exciton and Charge Transfer Interactions in Molecular Aggregates

A thesis submitted for the degree of

Doctor of Philosophy

in

Chemistry

by

Devika S.

School of Chemistry
Indian Institute of Science Education and Research
Thiruvananthapuram (IISER TVM)
Thiruvananthapuram-695551
Vithura, Kerala, India

June 2022

Declaration

I hereby declare that the Ph.D. thesis entitled *"Exciton and Charge Transfer Interactions in Molecular Aggregates"* is an original work carried out by me under the supervision of Prof. Mahesh Hariharan at the School of Chemistry, Indian Institute of Science Education and Research Thiruvananthapuram (IISER TVM) and it has not been submitted elsewhere for the award of any other degree, diploma or title. In keeping with the general practice of reporting the scientific observations, due acknowledgements have been made wherever the work described is based on the findings of other investigators.

Place : IISER Thiruvananthapuram   **Devika S.**

Date : 1st June 2022   IPHD15010

Certificate

This is to certify that the work embodied in the thesis entitled "*Exciton and Charge Transfer Interactions in Molecular Aggregates*" has been carried out by Ms. Devika S. (IPHD15010) under my supervision and guidance at the School of Chemistry, Indian Institute of Science Education and Research Thiruvananthapuram (IISER TVM) and the same has not been submitted elsewhere for a degree.

Place : IISER Thiruvananthapuram

Date : 1st June 2022

Prof. Mahesh Hariharan

(Thesis supervisor)

Dedicated to my

Family

"The most beautiful thing we can experience is the mysterious. It is the source of all true art and science. He to whom the emotion is a stranger, who can no longer pause to wonder and stand wrapped in awe, is as good as dead; his eyes are closed. The insight into the mystery of life, coupled though it be with fear, has also given rise to religion. To know what is impenetrable to us really exists, manifesting itself as the highest wisdom and the most radiant beauty, which our dull faculties can comprehend only in their most primitive forms-this knowledge, this feeling is at the center of true religiousness"

- Albert Einstein

Acknowledgements

Every beautiful journey comes to an end and while looking back at the seven long years as an integrated Ph.D. student at IISER TVM, it seems essential to appreciate that it is the journey that really matters in the end. This thesis dissertation marks the end of my exciting journey as a graduate student at IISER TVM, the development of which would not have been possible without the constant guidance and support offered to me by many people. And, at this juncture, I would like to acknowledge all those prominent figures who have played a significant role in shaping my budding research career.

First and foremost, I would like to express my sincere gratitude for the invaluable assistance offered by my mentor and supervisor, Prof. Mahesh Hariharan (school of chemistry, IISER TVM). During my doctoral study, along with the excellent research facilities, he was generous in providing relentless support and constructive feedback, without which, this journey would have been inconceivable. He truly inspired me with his model of guidance which included endless enthusiasm towards solving each research problem, irrespective of them being trivial or non-trivial, and also for extending unbiased leadership and round-the-clock availability to his students. He always motivated his students to develop independent thinking and problem-solving capabilities by providing the freedom to explore and channelise one's own interests, which has assisted me to take up self-responsibility towards overcoming the various challenges associated with a particular research work and to push my limits farther. It has been a great privilege for me to have the opportunity to work under the guidance of Prof. Mahesh Hariharan.

I would like to extend my sincere thanks to Prof. J. N. Moorthy and Prof. V. Ramakrishnan, the present and former Directors of IISER TVM for providing adequate research facilities of international standards to carry out my research work. I am also grateful to my Doctoral Committee members, Prof. K. George Thomas and Dr. Reji Varghese for their timely suggestions and guidance. I would also like to thank the faculty members of School of chemistry, for being excellent teachers during my course works and also for extending their support and motivation in times of need. I extend my wholehearted thanks to Prof. Bern Kohler,

Preface

Self-assembly of molecules driven by weak intermolecular interactions in the ground electronic state have profound impact in the resultant electronic excited states generated upon photoexcitation. The collective excited states of the molecular assembly, also called molecular exciton states, can have properties remarkably different from those of the chromophores in isolation or retain the individual characteristics under special conditions. Exploring such light-matter interactions between the organic chromophores and the consequent excitonic energy transport following photon absorption has garnered significant attention among the scientific community. The electronic coupling between the neighboring molecules enables excitation energy transfer giving way to delocalization of the excitation energy over different chromophores. These phenomena are abundantly observed in natural systems, wherein the excitation energy transfer is imminent for the photosynthetic function of light harvesting units and possibly for the photoprotection of DNA against harmful UV rays. Seeking inspiration from natural systems, investigations leading to the development of bioelectronics originated in the direction of modulating the spatial extent of an exciton and the average electron-hole separation and to understand the processes of charge separation and recombination.

Chapter 1 gives a brief discussion about molecular aggregates and the type of intermolecular interactions driving the supramolecular architecture of these aggregates. The efficiency of excitonic and charge transfer interactions between the closely-spaced molecules in organic aggregates have a huge dependence on the packing structure. Understanding the origin and fundamentals of the different types of excitonic interactions in molecular aggregates and the structure-property relationship forms the later part of the first chapter. Finally, the chapter will conclude with a bird's-eye view of the importance of excitonic and charge transfer interactions in natural systems and organic electronic materials.

Moving from this, in **chapter 2**, the role of excitonic interactions in determining the remarkable yet enigmatic photoprotective function of a chromophoric system that is abundantly found in the animal kingdom, called eumelanin, will be discussed. Eumelanin is a ubiquitous biological pigment demonstrating several salient biofunctions including photoprotection. Origin of the photoprotective broadband absorption spectrum of eumelanin has long been a topic of scientific debate. Despite

several decades of study, the chemical structure along with the nature and assembly motifs of the constituent chromophores of eumelanin remain elusive. In the natural world, the supramolecular architecture of eumelanin symbolizes an organized and efficient organic system for photoprotection that nature developed through evolution. Recent theoretical and experimental investigations on melanin have widened this depiction by including the role of noncovalent interactions between the fundamental oligomers in the hierarchical assembly structure, such as π–π stacking, hydrogen bonding and charge transfer interactions. However, detailed reports on understanding the structure-property relationship of eumelanin have been restricted owing to the difficulties in achieving precise control of eumelanin assembly structure arising from the high reactivity of the intermediate species during the oxidative polymerization of eumelanin. Herein, we report an atypical chiral packing arrangement of 5,6-dihydroxyindole (DHI) arranged in herringbone fashion, incorporating diastereomeric zig-zag helical stacks. Unlike any of the previously understood π–π stacked structural motifs of eumelanin precursors, the DHI chromophores in the present work are arranged in a herringbone fashion with respect to each other. Each of the zig-zag helical stacks originate from a bifurcated hydrogen bonding interaction between the phenolic substituents in adjacent DHI chromophores. The excitation energy delocalization pathways evaluated for the crystalline arrangement of DHI using fragment-based excited state analysis shows effective exciton delocalization along the chromophores connecting each of the diastereomeric stacks. Along with the single crystals of DHI monomer, formation of covalently connected DHI trimer aggregates is also observed in the chloroform solution which form double-helical crystals in the mesoscopic scale. Thus, the crystalline evidence followed by the ensuing photophysics presented here of DHI, a eumelanin precursor, adds to the library of melanin packing structures identified so far and provides a bottom-up strategy to solve the melanin mystery.

The influence of charge-transfer interactions, both in the ground and excited states, in trapping and twisting small electron-rich aromatic chromophores such as azobenzene, using an electron deficient perylenediimide host unit will be discussed in **chapter 3**. Chirality of self-assembled architectures hold substantial implications in the ensemble properties of organic chromophores such as the intermolecular interactions, excited state photophysics and crystallinity. Integrating the principles of chirality and host-guest chemistry has always ignited the scientific curiosity to develop bioinspired materials and in drug research. Herein, we report a novel self-assembly strategy wherein racemic octabrominated perylenediimide (OBPDI) host facilitated complete transfer of racemic information to incoming achiral aromatic

guests. Electron deficient OBPDI with the interplay of non-covalent interactions such as π-hole•••π and Br•••Br halogen bonding interactions generated size-tunable voids in the crystal system. The synergistically generated voids facilitated trapping of electron rich benzenoids with the guest molecules imbibing the same chiral sense of OBPDI scaffold due to induction of the geometrical twist in OBPDI. The crystalline hierarchy of OBPDI cocrystals embraced a novel pattern of organization involving homochiral segregation of the mixed chromophores in the same crystal system to yield twisted double racemic cocrystals. The robust effect of OBPDI in modulating the structure of small aromatic moieties promoted the encapsulation and tuning of planar trans-azobenzene in OBPDI crystal system to a twisted architecture without involving complex synthetic designs. The twist induced in azobenzene raised the potential energy of the molecule to a conformation signifying the azobenzene photoisomerization route via inversion pathway. The twisted azobenzene thus trapped in the OBPDI cocrystal represents the first crystalline evidence for the various theoretical and spectroscopic evaluation of the structural changes involved during azobenzene trans-cis isomerization.

The sensitive and unpredictable dependence of charge transfer coupling on the molecular morphology which is applied to tune the charge transport characteristics of triphenylamine and tetrabenzoacene derivatives forms the premise of **chapter 4**. π-conjugated aromatic molecules with well-ordered π-π stacked solid state arrangements have globally attracted attention in recent years for their utility as charge conductors. The Marcus-Hush formalism highlights the role of internal reorganization energy and intermolecular electronic coupling in determining the charge transport efficiency through the crystalline lattices of organic chromophores. This theoretical approach calls for a complete evaluation of both the parameters to understand the full spectrum of charge transport in organic crystals. In this regard, herein, we present a comprehensive computational evaluation of the structure-property correlation between charge transport characteristics and crystalline packing arrangement of a series of tetrabenzoacene (TBA) chromophores having different substituent groups attached to the core. The tetrabenzoacenes with flat π-aromatic core find wide applications as precursors for the generation of 2D polymers equivalent to the supramolecular graphene sheets. Thus, analyzing the dependency of charge mobility on the structural parameters of the TBA derivatives provides a molecular level information which can greatly assist in the development of better organic semiconductors. Hirshfeld surface analysis revealed that the TBA derivatives aligned in cofacial packing arrangements in the crystalline state, but, the TBA crystals exhibited sub-maximal charge transporting efficiencies. This prompted the probing of

different molecular stacking positions of TBA that can possibly provide high charge transfer rates when compared to the charge mobility in the existent crystalline lattices of TBA. Highly slip-stacked interchromophoric arrangements of TBA have been observed herein to showcase high charge transfer rates which could be attributed to the different distribution of nodes in the frontier molecular orbitals of the respective TBA derivatives. The thermodynamic preference of the TBA chromophores to adopt the arrangements that facilitated lower charge mobility was explored using symmetry adapted perturbation theory which quantitatively estimated the different energetic contributions to the total interaction energy. The present results can provide significant insights into the importance of achieving suitable energetically feasible interchromophoric arrangements facilitating high rates of charge transfer through chemical or physical modifications to develop better charge conducting materials.

Further, the second part of **chapter 4** covers a first comprehensive computational evaluation of the correlation between charge transport characteristics and crystalline packing arrangement of triphenylamine (TPA) chromophore by tuning the substituent groups attached to the core. Interestingly, the substituent groups attached to the propeller-shaped TPA moiety have influenced the crystalline packing of the derivatives in such a way that overlap of the phenyl rings of the TPA core could be achieved in varying degrees which, otherwise, is expected to showcase weak intermolecular coupling owing to the restriction imposed by the non-planar geometry of the TPA core. The diverse packing arrangements have rendered multifarious charge transport efficiencies to the TPA derivatives that, on an overall note, behaved as hole transporters. The crystal structure and their stability characterizations were performed by employing computational techniques such as quantum theory of atoms in molecules, Hirschfeld analysis, Penda's interacting quantum atoms technique and symmetry adapted perturbation theory analysis while the charge transport characteristics were evaluated using the semi-classical Marcus theory of charge transfer rates. The present results can provide significant insights in choosing the best substituent groups to develop better TPA hole transporting materials for optoelectronic applications.

Contents

Ch. 4. Modulating Charge Transport through Chromophoric Modifications

PART A: In Silico Exploration for Maximal Charge Transport in Organized Tetrabenzoacenes through Pitch and Roll Displacements

PART B: Deciphering the Multifarious Charge-Transport Behaviour of Crystalline Propeller-Shaped Triphenylamine Analogues

List of Figures

List of Tables

List of Schemes

Chapter 1

Introduction: When Chromophores Communicate With Each Other

1.1 Molecular aggregates

π-conjugated organic chromophores play important roles in driving the photo-induced functionalities of various biological and artificial machineries.[1]–[3] In most cases, the organic chromophoric units form molecular aggregates that can lead to the onset of unique optical and electronic properties which depends on the molecular stacking mode.[4]–[12] In the year 1963, the pioneering work of Kasha and coworkers attributed the origin of the aggregate photophysics to molecular exciton theory, wherein the interactions between molecular transition dipoles in the aggregates lead to the observed photoprocesses. In optoelectronic devices, the organic materials are often employed in the condensed phase as films or crystals.[3],[5],[6],[13],[14] While, in the nature, the supramolecular architectures prudently formed by specific π-conjugated molecules define the corresponding photofunction of photosynthetic light harvesting systems, DNA etc.[5],[15]–[17] The diversity in the photoexcited state phenomena observed in multi-chromophoric assemblies is determined by the migration pattern of the photogenerated collective excitations or molecular excitonic states.[6],[8],[18]–[25] Realizing the numerous weak interactions that cause the formation of exquisite molecular architectures is essential to decode the working principle of the different naturally occurring photoactive machineries and later, for the development of bioinspired optoelectronic materials.[13]

The wide recognition of X-ray crystallography and crystal engineering techniques have promoted organic molecular crystals to act as model systems for elucidating the correlation between packing structure and electronic/optical properties displayed by the photoactive materials.[26] The molecular units in the crystalline motifs are held-together and stabilised through the interplay of various noncovalent interactions such as hydrogen bonds, π-π interaction, halogen bonds etc.[27]–[30] These driving forces can be categorised based on the varied extent of energetic stabilisation provided by the contributions from electrostatic (multipole), dispersion, induction and short-range exchange–repulsion terms.[13]

1.2. Intermolecular noncovalent interactions

The strength of the noncovalent intermolecular interactions (Table 1.1) ranges from 0.25~40 kcal/mol, unlike the comparatively stronger covalent/chemical bonds (50~160 kcal/mol).[13] Attaining control over the noncovalent interactions is essential for engineering chromophoric assemblies that provide desirable optical properties, as is employed while directing the covalent bonds during the chemical synthesis process. The packing modes of multicomponent systems are highly important for controlling the charge transport abilities of organoelectronics. This is exemplified in light emitting diodes wherein the emissive wavelengths can be tuned with respect to the multicomponent architecture. The packing structures majorly directed by π-π stacking interactions are well known to create efficient π-ways for channelling the charges through the organic framework.[17],[31] Nature has mastered the art of arranging large number of chromophores to form functional systems. One such example is the symmetric aggregation of chlorophyll molecules which serve as the functional units in the light harvesting systems of photosynthetic bacteria and plants using π-π stacking interactions.[15],[16],[32] Differently sized cyclic configurations of chlorophyll molecular aggregates are identified in purple bacteria while, in the green bacteria the chromophoric aggregates form rod shaped geometries. The appropriate

Table 1.1: *Strength scale for some frequently observed noncovalent interactions*

Type of noncovalent interaction	Energy (kcal mol^{-1})
Hydrogen bonds	~1-40
π-π	~2-10
Halogen bonds	~1-42
Van der Waals interactions	~0.25-2

spatial arrangements ensure efficient transfer of the energy absorbed from sunlight between the constituting chromophore units which is an essential step for photosynthesis. Likewise, hydrogen bonds form yet another class of intermolecular interactions ubiquitous in a wide variety of systems ranging from water molecules to DNA and in protein structures. The 3-dimensional double-helical structure of DNA (Figure 1.1) formed by the interplay of stacking and hydrogen bonding interactions between the nucleobases is strongly linked to the storage and transfer of genetic information function of DNA.[25],[30] The concept of halogen bonds was first introduced by Metrangelo and coworkers wherein, halogen atoms (Cl, Br or I) experience depletion of electron density, also called σ hole, which facilitates an
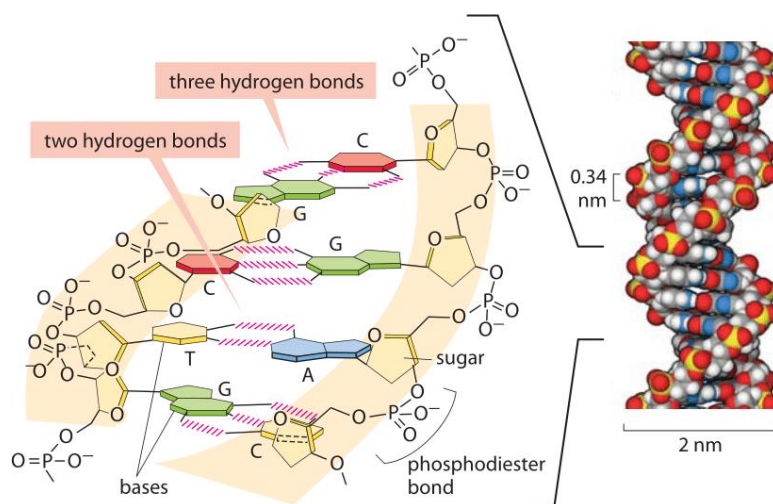
Figure 1.1: *Nitrogen base pairing in the 3-dimensional double-helical structure of DNA. The four nitrogen bases form stable hydrogen bonds with one partner. Adenine (A) pairs only with Thymine (T) through two hydrogen bonds while Guanine (G) pairs with Cytosine (C) via three hydrogen bonds. Adapted from ref* [33].

interaction with adjacent electron-donor atoms.[28],[34]–[36] There can exist multiple noncovalent interactions simultaneously directing the packing structure based on the C/H ratios, substituent groups present and steric constraints. Subtle variations in the chemical composition of the organic molecule can significantly alter the packing structure and hence create great discrepancies in the optoelectronic properties. Detailed description of some of the commonly observed non-covalent interactions are provided in the next sections.

1.2.1. π-π stacking interactions

In π-π stacking interactions, π-orbitals of the organic chromophore interact with each other. Three major stacking interactions are commonly defined to occur between two aromatic surfaces, namely, the cofacial, parallel-displaced and edge-to-face stacking interactions leading to different packing orientations. The commonly understood packing modes in small organic crystals include the herringbone and sandwich herringbone, slip-stacked, brick-layer, γ, and β structures (Figure 1.2).[1],[37]–[40] As proposed in a model developed by Hunter and Sanders,[40] electrostatic interactions between the aromatic π-surfaces are believed to have a major control over the packing geometries arising from π-π stacking interactions. Later on, energetic contributions from dispersion and van der Waals forces have also been realized. Photophysical properties such as charge transport in organic crystals show varying efficiencies based on how effective are the face-to-face or edge-to-face interactions in the packing structure. More π-π orbital overlap between the adjacent molecules in an aggregate structure can boost the electronic coupling leading to efficient charge transport phenomena.[41] In this regard, cofacial packing modes can be considered as the most efficient conduits for charge transport, though, attaining such ideal configurations have been found to be quite challenging owing to the strong electronic repulsion between the chromophoric units. The herringbone and slip-stacked packing motifs offer multidimensional channels for charge transport and
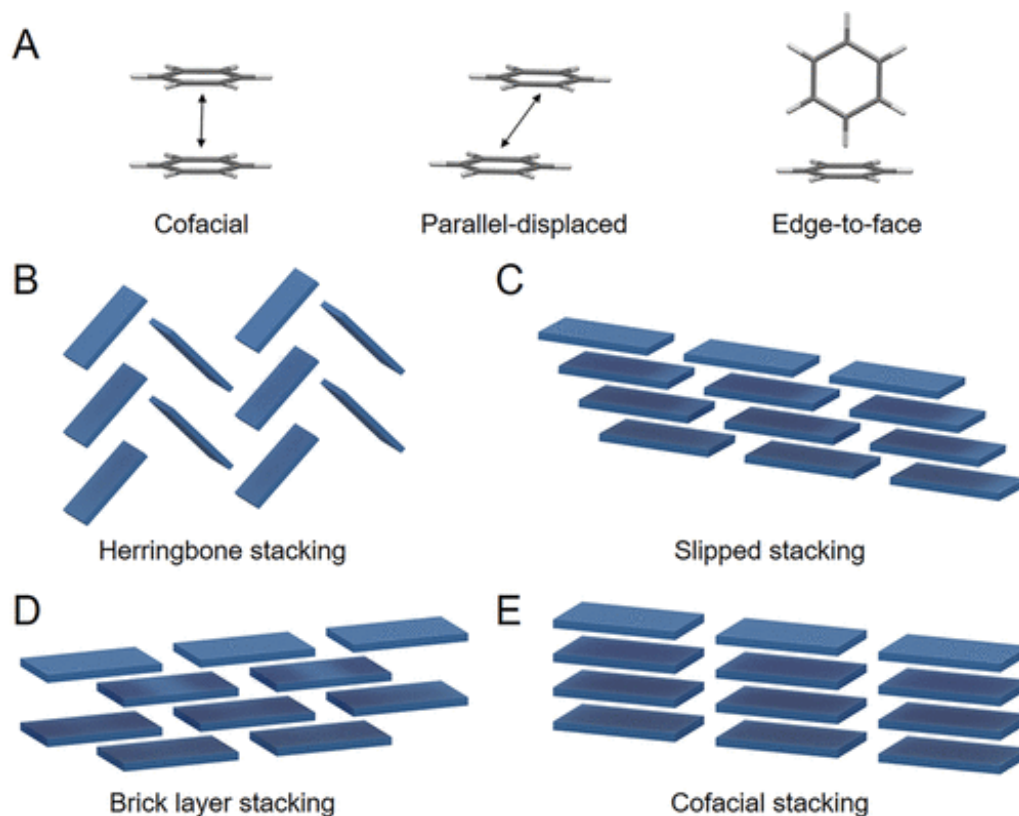
Figure 1.2: *(A) The three stacking geometries represented by the benzene dimer: cofacial, parallel-displaced, and edge-to face. (B-E) shows the four crystalline packing modes exhibited by small conjugated molecules, which includes: (B) herringbone stacking (C) slip-stacking (D) brick layer stacking and (E) cofacial stacking. Adapted from ref* [37]. *Copyright © 2018, American Chemical Society.*

these packing orientations are comparatively more feasible to attain than the perfectly eclipsed architectures.

1.2.2. Hydrogen bonds

The type of interaction wherein a hydrogen atom which is covalently connected to an electronegative atom (X) is attracted to another electronegative atom (A) in its vicinity is called hydrogen bonding interaction (X-H···A). Hydrogen bonds possess high directionality. The strength of hydrogen bonds is majorly determined by the electronegativity of the X and A moieties. The hydrogen bonds are commonly understood to be electrostatic in nature. However, recent research works have identified hydrogen bonds to show covalent behaviour as described by the charge

transfer interaction between the bonding atoms.[27],[42],[43] Very strong hydrogen bonds have been recognized to have pronounced covalent character with the interaction energy ranging from 20-40 kcal/mol. Additionally, assistance from charge, resonance or cooperative effects between the interacting atoms have been shown to strengthen the covalent character of the hydrogen bond.[44] The recognition of hydrogen bonds as an electrostatic interaction originates from the electrostatic attraction between the H and A atoms in the X-H⋯A interaction driven by the electronegativity differences between the linked moieties. Some examples of hydrogen bonds predominantly having electrostatic character include the N−H⋯O, O−H⋯O, and O−H⋯N bonds. Recently, more open definitions for hydrogen bonds have been brought up complimented by spectroscopic evidences by recognizing the interaction between weak electron donors such as C-H group and π-ring acceptor moieties to fall within the category of hydrogen bonds.[45],[46]

1.2.3. Halogen bonds

The interaction between an electrophilic region localised on a halogen atom (X) associated with a molecular entity (R) and a nucleophilic centre (Y) on the same/another (R/Z) entity is termed as a halogen bonding interaction (R-X⋯Y-Z). Similar to the hydrogen bonds, the halogen bonds are also associated with high directionality and strength making them a preferred tool for the design of self-assembled systems. Halogen bonds are classified into two types encompassing clear geometric and chemical distinctions: type I ($\theta_1 = \theta_2$) and type II (where $\theta_1 \approx 90°$ and $\theta_2 \approx 180°$) where θ corresponds to the interacting angle (Figure 1.3).[28],[34],[47] The type I interactions are majorly dispersive forces and operates mostly at shorter distances while, the type II interactions possessing electrostatic character are frequently found closer to the van der Waals limit.
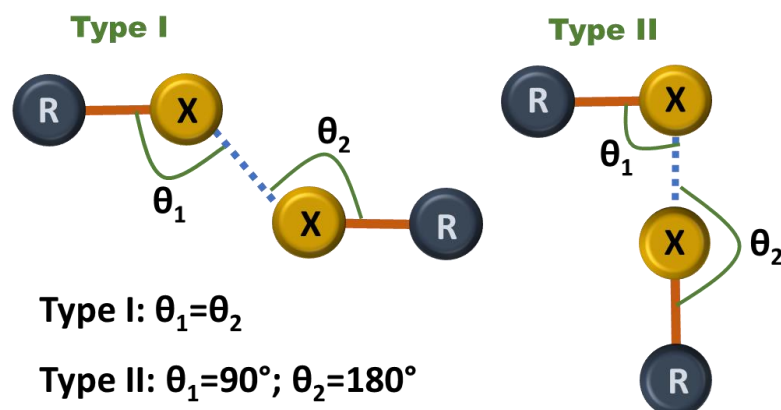
Figure 1.3: *Types of halogen bonding interaction.*

1.2.4. Donor-acceptor interactions

In certain crystalline aggregate systems composed of electron donor and acceptor chemical species, the stabilising interactions exhibit pronounced charge transfer characteristics leading to different types of packing arrangements. Such organic donor-acceptor (D-A) cocrystals find importance in the development of organic ferroelectrics and organic semiconductors due to the long-range arrangement of the charge transfer dipoles in the aggregate motif.[48] The D-A cocrystals are associated with densely packed structures which assists in minimizing the trapping of impurities within the aggregates and generating suitable energetics for efficient charge transport. Control and feasibility of the formation of D-A aggregate superstructures depends on the energy level ordering of the donor (ionisation potential) and acceptor (electron affinity) moieties and also utilizing chromophores with extended π-conjugated backbones.

With this brief understanding about the noncovalent forces that facilitate the formation of aggregates in organic molecules, the later sections of this chapter unify the fundamentals behind the light-matter interactions and the different mechanisms through which the absorbed light energy is channelised in organic aggregates. The diverse photoprocesses exhibited by organic aggregates originate from the

interactions between chromophores in the photoexcited states. The section 1.4 will detail the structure-property relationship in various natural and artificial model systems.

1.3. Electron transfer and excitation energy transfer

The phenomenon of charge transport via the diffusion of electrons and, transport of excitation energy via the delocalisation of excitons in organic molecular aggregates are two crucial processes in diverse areas of research. For the efficient functioning of many opto-electronic devices wherein, interconversion between electric and light energy is involved, the rates of electron transfer (ET) and excitation energy transfer (EET) processes (Figure 1.4) carry fundamental importance.[49] Likewise, the creation and diffusion of excitons as well as the charge transfer process find importance in various biochemical machineries such as those in photosynthesis and respiration. In photosynthesis, light harvesting and photoprotection is facilitated by the efficient excitation energy transfer between the singlet excited states (SEET) and the triplet excited states (TEET) of the assembled chromophoric moieties. The effects of excitonic interactions and EET in multichromophoric systems is evidenced by the difference in photophysics of the aggregate structure with respect to the isolated chromophores. A fundamental level understanding of the ET, EET and excitonic interactions in the excited states of multichromophores which decides the photophysics of molecular aggregates is provided below.

1.3.1. Excitonic coupling

When a molecule absorbs a photon having a particular wavelength, it gets excited from the ground state to an excited state with an energy gap that matches the wavelength of the absorbed photon. In a classical picture, this electronic transition can be viewed as the oscillating displacement of an electron that can lead to a change in the spatial distribution of electron density in the excited state when compared to the

ground state. The instantaneous dipole so created is called the electric transition dipole moment (μ).[24] The transition dipole moment is a vector that has a magnitude corresponding to the intensity of the electronic transition, while, the vector direction is determined by the orientation of electron displacement during the process of light absorption. The transition dipole moments associated with the $S_0 \rightarrow S_1$ and $S_0 \rightarrow S_2$ transitions in naphthalene and anthracene molecules are represented in figure 1.5.
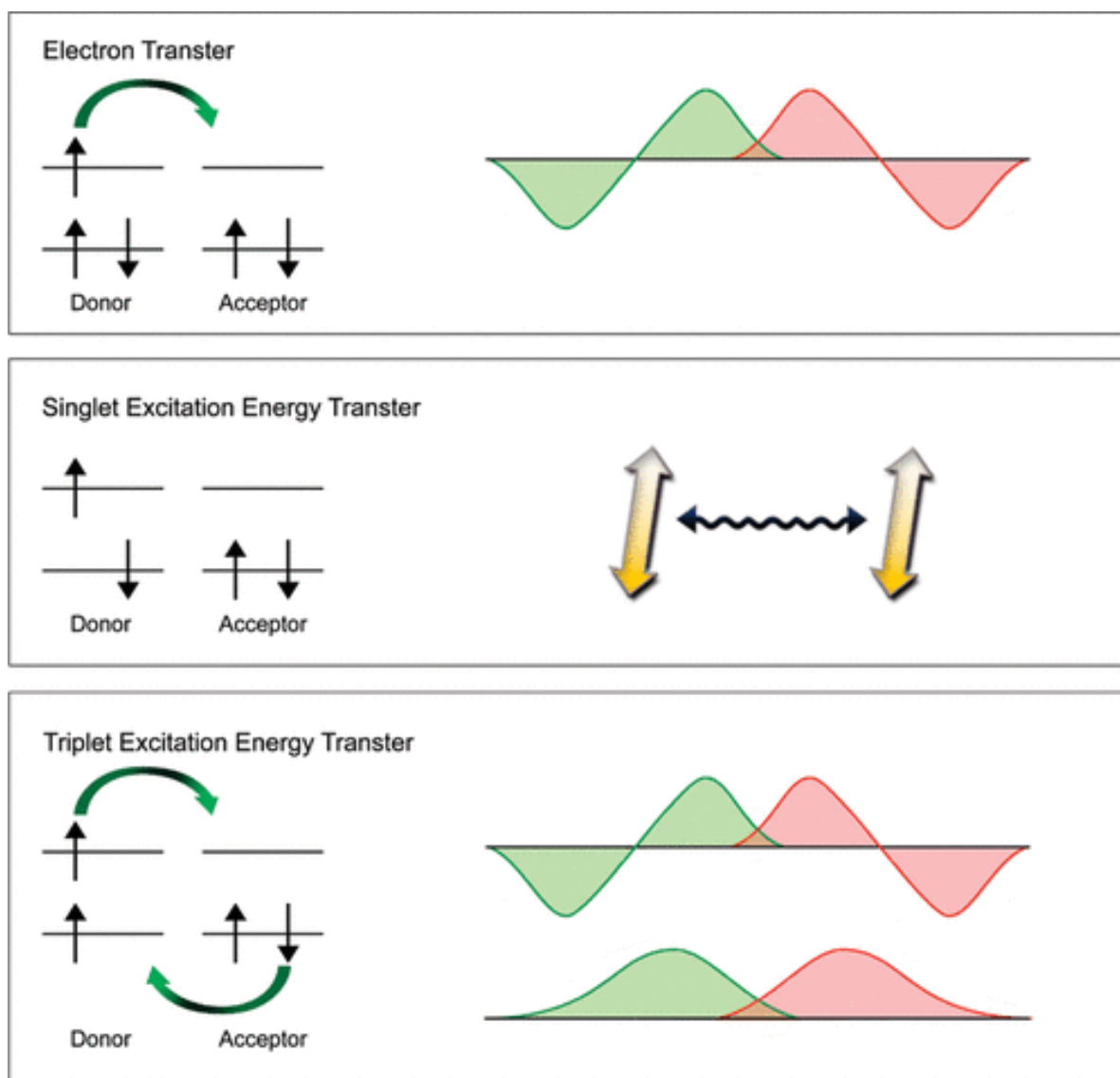
Figure 1.4: *Electron transfer (ET) and different excitation energy transfer (EET) processes visualised in various artificial and natural machineries. Adapted with permission from ref* [49]. *Copyright © 2009, American Chemical Society.*
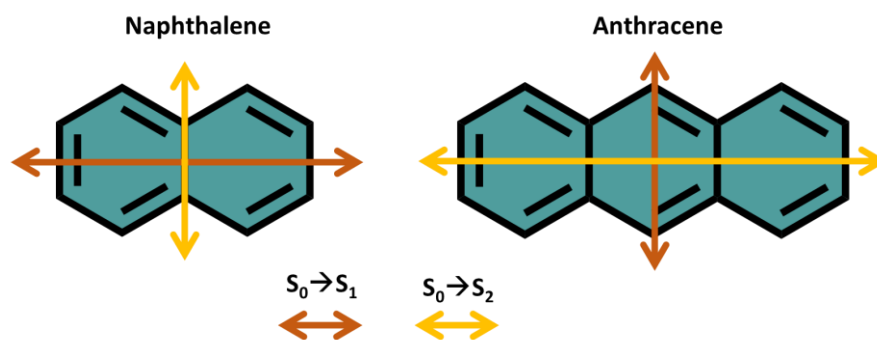
Figure 1.5*: Shows the transition dipole moment for the $S_0 \rightarrow S_1$ and $S_0 \rightarrow S_2$ transitions in naphthalene and anthracene molecules.*

In organic molecular aggregates where, multiple chromophores are located in close proximity, the electronic excitation no longer stays confined to a particular chromophore, but instead, becomes delocalised over the adjacent molecular units. Such electronic states that are generated in molecular aggregates, owing to a phenomenon called exciton coupling between the interacting molecules are termed as molecular exciton states. The excitonic states are formed when original excited states of the individual chromophores are coupled to one another as a consequence of sharing of excitation energy between the molecules. Based on the packing structure of organic aggregates driven by the various noncovalent interactions, the photogenerated excitons or collective neutral excitations can be transported over the aggregate structure or may remain localised on one of the interacting units. The optical excitations in the molecular aggregates are comprised of both electronic and vibrational degrees of freedom due to the significant nuclear rearrangements that can occur within the constituent chromophores.

Six decades ago, Michael Kasha proposed one of the first models to describe the photoexcited state properties of molecular aggregates. The initial attempts by Davydov, McRae and Kasha, which were directed towards understanding the enhanced phosphorescence with a simultaneous loss of fluorescence emission in certain molecular aggregates, led to the development of the renowned molecular

exciton theory. According to the exciton theory, the observed photophysical phenomena in linearly packed aggregates depend on the coulombic coupling between the neighbouring chromophores.

The excitonic coupling can be understood based on a simple dimer model wherein, a dye aggregate consisting of two interacting molecular units (A and B) and having degenerate energy levels, give rise to a set of two non-degenerate energy levels. The newly formed excitonic states in the dimer system are linear combinations of the initial unperturbed excited energy levels of the individual chromophore units. One of the excitonic state in the aggregate lies higher in energy with respect to the original monomer excited state while, its twin counterpart, lies lower in energy to the monomer excited state (EQs 1.1 and 1.2).[7],[15]

$$\psi_{symm} = \frac{1}{\sqrt{2}}(A'B + AB') \qquad \text{(EQ 1.1)}$$

$$\psi_{antisymm} = \frac{1}{\sqrt{2}}(A'B - AB') \qquad \text{(EQ 1.2)}$$

Eqs 1.1 & 1.2 represent the two linear combinations of the initial excited states of molecules A and B (prime indicates electronic excitation). The packing structure of the dye aggregate, which, determines the slip-angle or the angle between the transition dipoles and the line joining the centres of the two molecules, decides which of the two excitonic states would get populated upon photoexcitation of the dye aggregates. The feasibility of photoexcitation to a particular excitonic state in the dimer model depends on the phase relationship or the relative phases of motion between the transition dipoles of the two chromophores. The transition dipoles can be "in-phase" or "out-of-phase" with respect to each other based on the geometry of molecular packing.

In case of parallel transition dipoles, i.e. when the chromophores are arranged in face-to-face orientation (at a slip angle > 54.4°), allowed electronic excitation occurs to the higher excitonic state. Hence, as a result of the excitonic coupling, the electronic

absorption spectrum of such cofacial aggregates is blue-shifted compared to the absorption band of the monomer chromophore. These aggregates are also called H-aggregates, where "H" stands for "hypsochromic". The H-aggregates are usually associated with low radiative decay rates since the fluorescence emission is understood to proceed from the lowest excited state and the population of higher energy excitonic state can favour other non-radiative decay pathways such as intersystem crossing. The cofacial or parallel packing in H-aggregates, however, is ideal for efficient charge transport through the aggregate system due to the enhanced π-π orbital overlap.

In contrast, for the dye aggregates having colinear or head-to-tail arrangements of the transition dipoles, the bulk of the oscillator strength is carried by the lowest excitonic state, leading to red-shifted absorption spectrum when compared to the monomer absorption bands. Such slip-stacked aggregates (at a slip angle $< 54.4°$) are called J- ("J" after "Jelley") or Schiebe aggregates. They are generally associated with strong fluorescent character or "superradiance" phenomenon. Apart from the mutual orientation of the transition dipoles in the chromophoric units, the magnitude of excitonic coupling depend on other factors such as: magnitude of the transition dipole moment, degeneracy of the unperturbed energy states and distance between the chromophoric units. The transition dipoles having greater spatial length can interact significantly with the nearby dipoles leading to stronger excitonic coupling, while for weak electronic transitions, the excitonic coupling is almost negligible.

In addition to the through-space coulombic coupling facilitated formation of excitonic states in molecular aggregates, the close spaced chromophoric units can also undergo wavefunction overlap and intermolecular charge transfer (CT). Such charge transfer interactions can also affect the formation and energetics of the excitonic states and thereby, can have profound impact on the photophysical and transport properties exhibited by the organic aggregates. Unlike the coulombic excitonic coupling which

generally acts at long ranges, the intermolecular CT-mediated interactions can be classified as short-range excitonic coupling that can independently affect the overall photophysics of the aggregates. The CT coupling also depends on the mutual orientation of the chromophore units along with the nature of wavefunction distribution in the highest occupied molecular orbitals (HOMO) and lowest unoccupied molecular orbitals (LUMO) of the individual chromophores. Thus, the total excitonic coupling in molecular aggregates can be considered as the sum of the long-range coulombic and short-range charge transfer interactions between the neighbouring molecular units. Sometimes, based on the type of chromophore and the packing motif, one type of excitonic coupling can outweigh the other leading to a rich array of photophysical behaviours. For eg., helical π-stacks of certain biomolecules such as carotenoid lutein behave as coulomb-coupled H-aggregates, despite the presence of closely spaced chromophores. The increasing twist angle in helical stacks weakens the intermolecular orbital overlap thereby leading to low charge-transfer coupling contribution towards the total excitonic coupling.

1.3.2. Interchromophoric interactions facilitating excitation energy transfer in molecular aggregates

According to the generalized theory for excitonic coupling, a rich array of photophysical behaviours are exhibited by the different aggregate/crystal architectures due to the varying degrees of short- and long-range intermolecular interactions between the chromophores. For eg., just within the subset of herringbone-packed organic crystals, the coupling between the excited states is observed to range from Kasha-like to Frenkel-CT mixed states. This is exemplified by the oligophenylenevinylenes wherein, the molecules with large $S_0 \rightarrow S_1$ transition dipole moments induce dominant Coulombic coupling, while, the oligoacenes such as tetracene and pentacene, possessing small $S_0 \rightarrow S_1$ transition dipoles exhibits significant mixing of the Frenkel and charge transfer states. [7],[15],[19],[50],[51]

i. Long-range Coulombic coupling

The Coulombic contribution between two molecules is mostly effective when the molecules are not in close-proximity. It is often evaluated using the Forster excitation energy transfer mechanism by employing the point-dipole approximation (Figure 1.6). The electronic excitation energy transfer occurring in this phenomenon originates from an inductive resonance interaction between the molecular transition dipole moments. In another sense, this can also be considered as the synchronous induction of electronic oscillations in an acceptor molecule by the semi-classical oscillations of the electrons on the donor molecule during its de-excitation process, thereby, leading to electronic excitation of the acceptor molecule. The Coulombic dipole-dipole interaction varies with the inverse of the cube of the center-to-center intermolecular separation between the two interacting molecules and hence stands
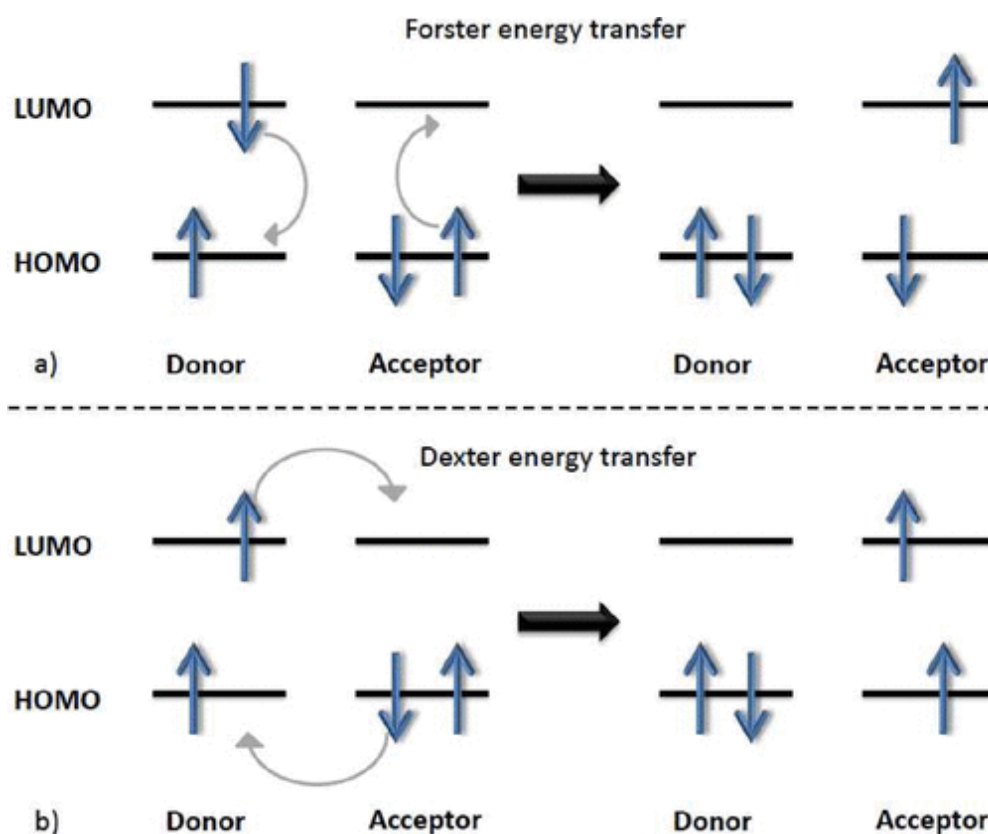
Figure 1.6: a) *Forster energy transfer (top) mechanism and b) the two-electron Dexter energy transfer (bottom) mechanism. Adapted from ref* [53]. *Copyright © 2012, American Chemical Society.*

,

valid even at distances on the nanometer scale. The coupling term facilitating the energy transfer is a quantum-mechanical entity describing the interaction between the reactant and product wavefunctions.[15],[52]

$$J_{coul} = \frac{1}{4\pi\epsilon_0} \kappa \frac{|\mu_1||\mu_2|}{R^3} \qquad\qquad \text{(EQ 1.3)}$$

μ_1 and μ_2 = transition dipole moments of the donor and acceptor molecules with SI units of coulomb-meter

R = centre-to-centre intermolecular distance between donor and acceptor

κ = orientation factor which is given by the expression:

$$\kappa^2 = (1 - 3\cos^2\theta)^2$$

θ = angle between the transition dipole moment vectors and the line connecting the molecular centres

Hence, from EQ 1.3, for the parallel side-by-side orientations, or the H aggregates, $54.7° < \theta < \pi/2$ leads to $J_{coul} > 0$. While, $\theta < 54.7°$ for the head-to-tail orientations of J-aggregates results in $J_{coul} < 0$. At $\theta = 54.7°$, also called as the magic-angle stacking, the J_{coul} attains zero value. However, at distances close to the van der Waals interactions, the short-range intermolecular orbital overlaps become comparable or even larger than the Coulombic couplings and hence evaluation of the charge transfer coupling finds importance for defining the type of aggregate structure.

ii. Short-range charge transfer coupling

Wavefunction overlap and intermolecular charge transfer (CT) processes are two important occurrences that also contributes to the fate of the photoexcited states and the transport properties of molecular aggregates having close nearest-neighbour contacts (at distances less than 5 Å).[15],[52],[54] CT mediated model for excitonic coupling appears as a double-step electron transfer process where electron and hole transfer occurs in a synchronous manner between the two interacting molecules which effectively leads to the exchange of electronic excitation from one molecule to another.

Thus, the mechanism of excitonic coupling at short-ranges is promoted by the HOMO-HOMO and LUMO-LUMO wavefunction overlaps between the adjacent chromophores (Figure 1.7). The photophysical properties as determined by the CT mediated coupling are controlled by the relative phase relationship between the hole (t_h) and electron (t_e) charge transfer integrals. The charge transfer integrals can be modulated by the changes in molecular arrangements such as the long- and short-axis displacements between the neighbouring chromophores due to the high sensitivity of t_e and t_h towards the shape and nodal patterns of the HOMO and LUMO levels.
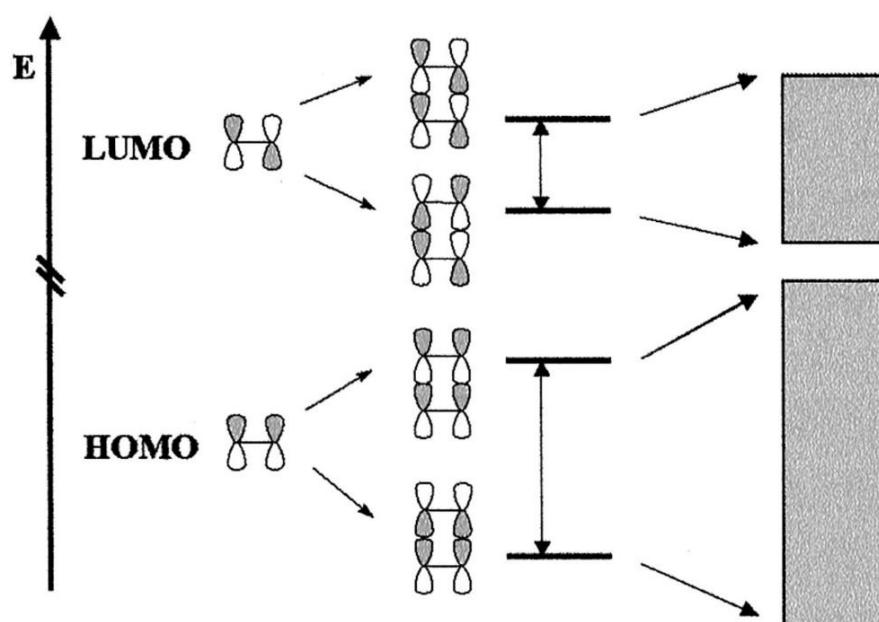
Figure 1.7: *The wavefunction overlaps between the HOMO (LUMO) levels of two representative ethylene molecules placed in cofacial configuration. Valence and conduction bands are formed when there exist strong interactions between large number of stacked molecules. Adapted from ref* [54] *Copyright (2002) National Academy of Sciences.*

The excitation energy transfer promoted by orbital overlap effects has a strong exponential dependence on the intermolecular separation between the chromophores. When the charge transfer state is well-separated from the Frenkel or local excited state, the specific form of the CT mediated excitonic coupling (J_{CT}) can be attained by the second order perturbation theory represented by:

$$J_{CT} = \frac{-2t_e t_h}{E_{CT} - E_{S_1}}, \left| E_{CT} - E_{S_1} \right| \gg |t_e|, |t_h| \qquad \text{(EQ 1.4)}$$

t_e, t_h= electron and hole transfer integrals

E_{CT}= energy of the CT state

E_{S_1}= energy of the Frenkel exciton state

Based on the charge transfer coupling, the aggregate geometries leading to $J_{CT} < 0$ are classified as J-aggregates, while the $J_{CT} > 0$ for H-aggregates.

1.3.3. Electron transport

Efficient transport of charge carriers is a vital characteristic feature of organic semiconductor materials, but for most cases achieving good carrier transport forms the bottleneck in the functioning of electronic devices. Developing strategies to increase the charge mobility in organic materials through material processing and molecular design has thus grabbed attention in the recent future.[55] The mechanisms of charge transport in organic assemblies are proposed in two regimes: (i) band regime for delocalised electrons and (ii) hopping regime for localized charges. The type of transport model followed by an organic crystal depends on the evolution of charge transport through the assembly structure as a function of temperature.[54],[56] At low temperature, charge transport through certain organic crystals followed the band-like regime. Here, the charge mobility is determined by the total width of the valence and conduction bands formed from the HOMO and LUMO levels of the interacting chromophores in the molecular assembly. The total width of the energy bands depends on the amplitude of the transfer integrals between the interacting molecular units in close-contact and the carrier transport is described by the Boltzmann transport equation. While, at higher temperatures, phonon-scattering processes reduced the effective bandwidths and the charge carriers get localized leading to thermally-activated hopping of the charge carriers over the neighbouring chromophores. At the microscopic level, this mechanism can be picturised as an electron transfer process

from a charged unit to an adjacent neutral system. In such cases, Bredas et al. first proposed the use of the semi-classical Marcus theory of electron transfer to describe the charge transport process. The charge transport through a series of organic crystals has been evaluated in the hopping regime in this dissertation. Based on the Marcus semi-classical theory, the charge carriers are assumed to be completely localised on one single molecule and the transport involved sequential hopping of the charges from one molecule to another. The rate of charge transfer or the hopping rate is expressed as:

$$k_i = \frac{V^2}{\hbar} \sqrt{\frac{\pi}{\lambda k_B T}} \, exp\left(-\frac{(\lambda+\Delta G^0)^2}{4\lambda k_B T}\right) \qquad \text{(EQ 1.5)}$$

V= electronic coupling or the intermolecular hopping integral

λ= charge reorganization energy

ΔG^0= total Gibbs free energy change

The respective electronic coupling term or the transfer integral for electron and hole transport reflects the strength of interaction between the neighboring chromophoric units and the charged states can be regarded based on the frontier molecular orbitals (FMOs). The magnitude of the coupling term as evaluated using the simple FMO approach equals to the energy level splitting of the interacting molecular orbitals wherein, HOMO-HOMO coupling corresponds to hole transport, the LUMO-LUMO coupling corresponds to electron transport.

The charge reorganization energy explains the free energy change associated with the molecular relaxations during the charge transport process. The exponential term in the EQ 1.5 describes the "inverted region". The formalism for evaluating the rate of charge transfer takes the form of the famous Arrhenius equation: $k \propto Z \, exp\left(-\frac{E_A}{k_B T}\right)$ where the E_A in the Marcus equation is equivalent to $\frac{(\lambda+\Delta G^0)^2}{4\lambda}$. Later developments led to the assumption that ΔG^0=0 for charge transport, thereby reducing

the reaction barrier to $\frac{\lambda}{4}$ for thermal activation. Thus, with the above approximations, the Marcus-Hush formalism for charge transport through an organic crystal can be evaluated using the eq:

$$k_i = \frac{V^2}{\hbar} \sqrt{\frac{\pi}{\lambda k_B T}} e^{\frac{-\lambda}{4 k_B T}} \qquad \text{(EQ 1.6)}$$

Hence, regardless of the transport mechanism, the electronic coupling and the reorganization energy terms form the two important molecular parameters that governs the charge transport phenomenon and evaluation of both these values stands essential for the development of better conducting materials for device applications. The EQ 1.6 stands valid for the cases where $V \ll \lambda$, since in this condition the charge transfer process occurs in the non-adiabatic transition regime where the charge is fully trapped by the molecular reorganization process. Also, under high temperature conditions, the environment fluctuations can be treated classically while, the thermal activation process is thought to vanish at low temperatures.

1.3.4. Characterization of excitonic and charge transfer states

Characterizing the type of excited states formed in molecular aggregates is of utmost importance to describe the photoprocesses occurring in biological systems such as DNA and in organic electronics. When two or more chromophores come in close-contact, the photoexcitation process can lead to the formation of local excitations on the interacting fragment units and charge transfer states (Figure 1.8 (I and II)).[57] The excited states in π-systems may even interact with each other when the intermolecular separation is small (<5 Å), to yield eigen functions that are arbitrary mixtures of the initial excitations (Figure 1.8 (III and IV).

In an aggregate system, the excited states resulting from transitions occurring between two molecular orbitals localized on the same fragment unit are called Frenkel

exciton states. The Frenkel excitons can remain localized on one particular fragment species, to form locally excited states or can delocalize between nearby fragments to result in excitonic resonance states. In contrast, if the initial and final orbitals are located on different fragment units for a particular transition, the resulting excited states are termed as charge separated states. Here, if there is a net transfer of charge, charge-transfer states are formed while charge-resonance states are produced when two opposing charge-transfer states come into resonance with each other without a net transfer of charge.
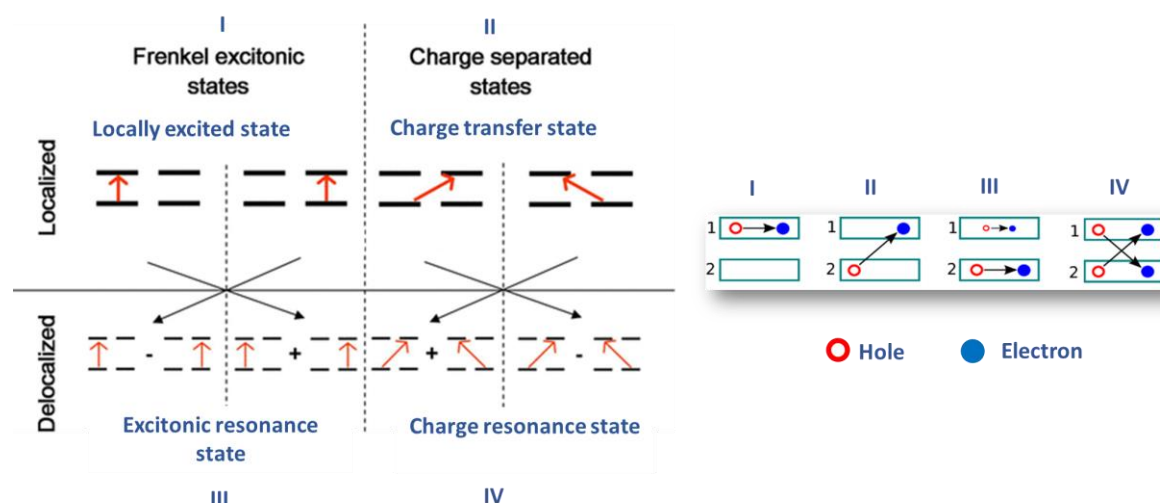
Figure 1.8: *Shows the electron-hole separation occurring between the two molecular fragments that can result in the formation of I) Locally excited states; II) Charge transfer states; III) Excitonic resonance states and IV) Charge resonance states. Adapted with permission from ref* [57]. *Copyright © 2012, American Chemical Society.*

1.4. Aggregate states in natural and artificial machineries

The light harvesting complexes (LHC) form a wonderful array of chromophoric system that facilitate efficient excitation energy transfer for photosynthesis. For eg., the bacteriochlorophyll (Bchl a) molecules in the LHCs in purple bacteria exist at high concentrations forming two rings. The B800 and B850 rings contain Bchl a molecules that result in the absorption of 800 and 850 nm light respectively. The constituting chromophores in B800 ring are weakly coupled with respect to each other resulting in

localized excitations. The transient absorption kinetics of the B800 absorption bands is associated with a biexponential decay curve constituted by a slow component of 1.2-1.9 ps corresponding to B800-B850 transfer and a fast component of 0.3-0.8 ps attributed to B800-B800 hopping. The Bchl a chromophores in the second B850 ring are arranged perpendicular to the pigments in B800 ring. The pigments in the B850 ring are closely spaced resulting in strong electronic interaction between the nearest neighbors. Due to the strong electronic coupling, Bchl a absorption band is red-shifted to 850 nm and the excitation energy is delocalized over the ring. [58]–[60]

The electronic excitation process can be harmful to DNA due to the mutagenic action of sunlight resulting in the production of various photochemical products. Understanding the onset of the ultrafast photochemical reactions in DNA from UV excitation has grabbed lot of scientific curiosity. Several experimental (steady-state absorption, emission and circular-dichroism spectroscopy) and theoretical evidences point towards the formation of excitonic states through the strong electronic coupling between the interacting nucleobases in DNA. The fate of these excited states still remains inconclusive, and one proposed model for the excited state dynamics of DNA includes generation of long-lived CT states from the initial Franck-Condon states or long-lived excimer states. Owing to the excitonic and charge transfer states, the excited state lifetimes in small oligomers of DNA have been identified to be several orders of magnitude greater than the lifetime of excited states in isolated nucleobases (identified to be in the sub-ps regime). DNA motif also acts as a pathway for efficient charge transport that has relevance for various cellular processes and development of DNA-based devices.[22]

The production of electronic excitations or excitons in dielectric solid materials can be facilitated via light absorption or through the generation of free holes and electrons after electrical or optical pumping. The excitons, which can be considered as bound electron-hole pairs with neutral charge, can delocalize through the solid
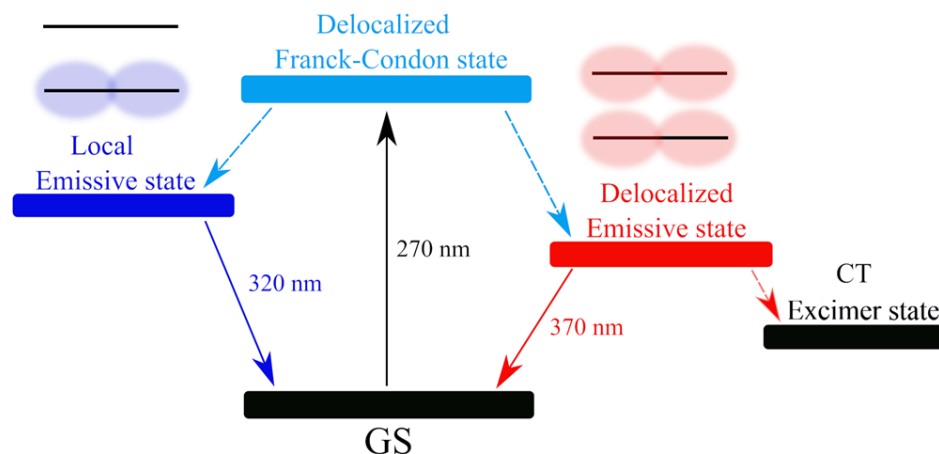
Figure 1.9: *The excited states and the corresponding photodynamics observed in i-motif form of cytosine chains (dc)$_{10}$, a representative model system to decode the photoprocesses in DNA. Adapted with permission from ref [22], Copyright © 2019, The Author(s).*

aggregates resulting in the transport of excitation energy through the system.[61] In organic solid materials, the excitons are classified into Frenkel and Wannier-Mott excitons, based on the separation between the electron and hole in the bound pair. The Frenkel excitons are associated with zero electron-hole (e-h) separation and large binding energy (~1 eV). This means, the electron and hole in the case of Frenkel excitons occur on the same molecular entity. While, for the Wannier-Mott exciton, the e-h separation is larger with small (~1 meV) binding energy values. The two types of excitons also differ in the magnitudes of e-h coupling as well as the rates of charge hopping between the adjacent molecules or atoms. Molecular orbital overlap between the neighboring molecules promotes the independent movement of electrons and holes through the nearby entities, the efficiency of which depends on the Coulombic coupling between the charged species. When the Coulombic interaction is large, the e-h binding energy is made stronger for the effective separation of both the species, thereby, hindering the facile hopping of the free charges through the system. Hence, the electrons and holes occupy the same molecule and this forms the basis for the Frenkel exciton limit, wherein, the electrons occupying the LUMO level and holes occupying the HOMO level propagates through the solid aggregates driven by electrostatic interactions between the molecules (assuming charge overlap is small).

For Wannier-Mott excitons, the presence of strong charge overlap, the e-h separation extends to several orders of angstroms leading to the generation of continuum like states characterized by large dielectric constant values. There also exist an intermediate case, termed as the charge transfer (CT) exciton which is associated with sufficient, yet not large e-h separation distances, the smallest case being that of one molecule separation length. Thus, for CT excitons, the electron resides on one molecule while the hole resides on the neighboring chromophore and propagation of such exciton states is a common occurrence in donor-acceptor complexes. The photoconductivity of organic crystals often occurs through CT excitons acting as intermediate states in the generation of free carriers from the photogenerated Frenkel excitons.

1.5. Objectives and scope of the thesis

The feasibility and efficiency of excitation energy transfer and charge transport phenomena have huge dependence on the supramolecular architecture of organic aggregates. The rates of these photoprocesses are estimated based on the electronic coupling factor between the molecular orbitals of the neighboring molecules and the density of states. Understanding the structure-property relationship wherein subtle changes in molecular packing of the organic aggregates or the nature of distribution of electronic wavefunction can lead to significant alteration of the opto-electronic properties is of paramount importance in various fields of research. Generating a perfect balance between highly conducting and lower energy molecular packing arrangements is indispensable for achieving molecular systems that encompass desired photophysical properties. This dissertation is devoted to explore the importance of achieving suitable energetically feasible interchromophoric arrangements facilitating high rates of exciton transport and charge transfer interactions through chemical or physical modifications in various organic chromophores of biophysical relevance.

Chapter 2

Exciton Interactions in Helical Crystals of a Hydrogen-Bonded Eumelanin Monomer

Abstract

Eumelanin, a naturally occurring group of heterogeneous polymers/aggregates providing photoprotection to living organisms, is understood to be made up of 5,6-dihydroxyindole (DHI) and 5,6-dihydroxyindole-2-carboxylic acid (DHICA) building blocks. Despite their prevalence in the animal world, the structure and therefore the mechanism behind the photoprotective broadband absorption and non-radiative decay of eumelanin remain largely unknown. As a small step towards solving the incessant mystery, DHI is crystallized in a non-protic solvent environment to obtain DHI crystals having a helical packing motif. The present approach reflects the solitary directional effect of hydrogen bonds between the DHI chromophores for generating the crystalline assembly and filters out any involvement of the surrounding solvent environment. The DHI single crystals having an atypical chiral packing motif ($P2_12_12_1$ Sohncke space group) incorporate enantiomeric zig-zag helical stacks arranged in a herringbone fashion with respect to each other. Each of the zig-zag helical stacks originates from a bifurcated hydrogen bonding interaction between the hydroxyl substituents in adjacent DHI chromophores which act as the backbone structure for the helical assembly. Fragment-based excited state analysis performed on the DHI crystalline assembly demonstrates exciton delocalization along the DHI units that connect each enantiomeric helical stack while, within each stack, the excitons remain localized. Fascinatingly, over the time evolution for generation of

single-crystals of the DHI-monomer, mesoscopic double-helical crystals are formed, possibly attributed to the presence of covalently connected DHI trimers in chloroform solution. The oligomeric DHI (in line with the chemical disorder model) along with the characteristic crystalline packing observed for DHI provides insights into the broadband absorption feature exhibited by the chromophore.
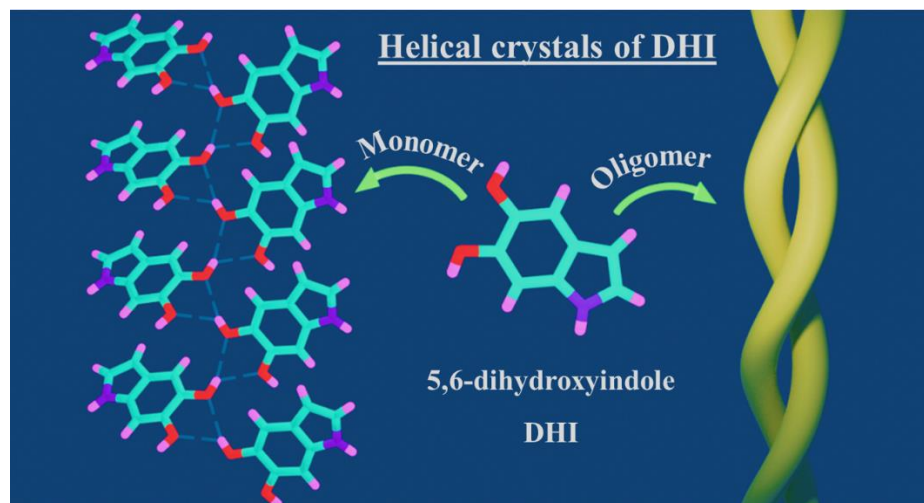
2.1. Introduction

Eumelanin, which represents a broad class of natural pigments found in the animal kingdom, acts as a biological shield for protecting the skin cells against harsh UV radiation.[62] The black colored eumelanin pigment is one of the extensively explored archetypes of the melanin family which is obtained from the oxidative polymerization of 5,6-dihydroxyindoles (DHIs) and 5,6-dihydroxyindole carboxylic acid (DHICA) units [Figure 2.1.a][63] The synergistic merits of eumelanin with respect to the broadband UV absorption and proficient dissipation of the excessive electronic energy *via* non-radiative deactivation of the excited states, provides an explanation for the photoprotective nature of the pigment.[64] Apart from the photoprotective behavior, melanin possesses exceptional antioxidant activity *via* its free radical scavenging traits.[65]–[67] However, much less has been understood about the fundamental photophysics and structural features of eumelanin due to the enormous heterogeneity in the molecular framework[68],[69] coupled with poor solubility in common solvents.[70] Recent years have witnessed a growing interest towards unravelling the excited state processes occurring in the eumelanin pigment upon interaction with light.[71],[72] A better correlation between the structure–property relationship and photoexcited state processes in eumelanin can guide the development of inspired functional materials for potential application in biomedical and dermo-cosmetic fields.[62],[73]–[75]

In the natural world, the chromophoric architecture of eumelanin can symbolize an organized and efficient organic system for photoprotection that nature developed through evolution. The outcome of the research done so far indicates the presence of continuous π-stacks of oligomers in eumelanin which induce different levels of aggregation to construct the eumelanin framework.[76] Furthermore, eumelanin has been reported to exhibit weak fluorescence which indicates the
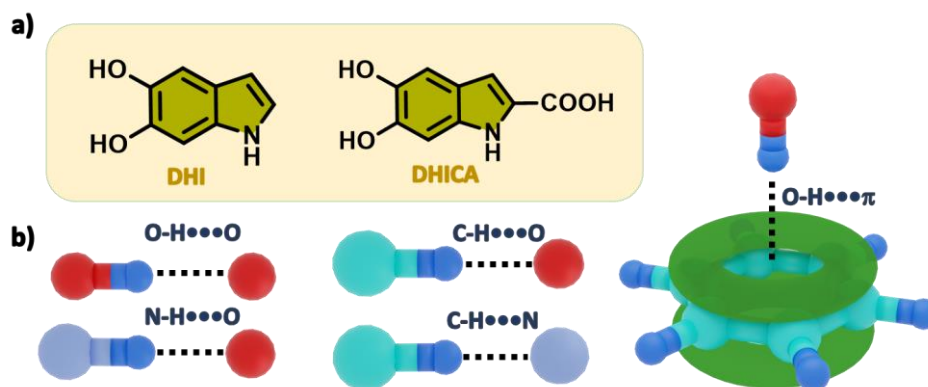
Figure 2.1: (a) *Chemical diagrams of 5,6-dihydroxyindole (DHI) and 5,6-dihydroxyindole carboxylic acid (DHICA). (b) Various unconventional hydrogen bonding interactions identified in DHI crystals.*

presence of competing non-radiative channels that provide efficient de-excitation pathways for repopulating the ground states.[77]–[80] The broadband absorption of eumelanin has theoretically and experimentally been evaluated, in part, to be a result of π-stacking interactions between the oligomers of DHI/DHICA in multiple oxidation states.[81]–[84] While dealing with biomacromolecules, non-covalent interactions such as hydrogen bonding and π–π stacking take the center stage in controlling the supramolecular architecture, especially in the 3-dimensional structures of proteins and DNA. Modulating the balance between each of these noncovalent interactions over another will produce significant changes not only in the structure but also in the functional properties.

Hydrogen bonding is simultaneously both ubiquitous and diverse and therefore its significance in biochemical systems comes as no surprise particularly due to the surrounding aqueous environment. Apart from the classical hydrogen bonding interactions, an array of hydrogen bond-like weak interactions which include a delocalized π-system acting as the acceptor group to the X–H hydrogen donor (X = O, N, C) is identified to provide additional contributions for stabilizing the biomolecular structure and controlling intrinsic functions [Figure 2.1.b.].[85],[86] Investigations aimed at identification (using X-ray crystallography) followed by energetic

quantification of the major stabilizing interactions such as those with the aromatic π-rings in biological complexes are of paramount importance for developments in diverse areas including drug design. There has been extensive research conducted on eumelanin building blocks showcasing their ability to form hydrogen bonds through the –OH and –NH functional groups.[87],[88] Most reports almost exclusively focus on the hydrogen bonding with the solvent environment surrounding the eumelanin monomer units.[89] Findings from these theoretical studies have demonstrated the role of several deactivation pathways in the presence of a protic solvent, namely –OH and –NH bond elongation and 5-/6-membered ring puckerings.[78]

Chemical and spectral evidence from the eumelanin polymeric structures identified so far points to five main levels of chemical disorder leading to the supramolecular structure, which includes (i) disorder from the simultaneous presence of different building blocks; (ii) molecular size disorder; (iii) disorder from the position of coupling; (iv) electronic/redox disorder of the constituent units and (v) supramolecular disorder.[90] Given the complex structure of melanin, a bottom-up approach using the building blocks or basic constituent molecules of eumelanin is a pertinent strategy for the mechanistic study of the photoproperties of eumelanin. This can be followed by understanding the more intricate structures of melanin formed from the constituents with less complex approaches. Due to the abundant presence of water in the natural media, the corresponding solute–solvent interactions can have profound significance in driving the fast polymerization and the consequent heterogeneity of natural melanin. The tedious task of extracting melanin from natural sources and the lack of solubility of the polymeric melanin material in organic/aqueous solvents have called for basic model systems to understand the complex eumelanin architecture. In this regard, we have adopted a facile approach to decode the perpetual puzzle by single crystal X-ray crystallographic and spectroscopic analyses of DHI crystalline aggregates derived from a non-aqueous environment (chloroform). Due to the highly autooxidative[91] nature of eumelanin precursors

even in the slight presence of protic solvents, the simple model implemented here precludes the contribution of solute–solvent hydrogen bonding interaction towards the formation and resultant structure of DHI crystalline aggregates. In chloroform, each DHI molecule experiences weak interactions solely from the neighbouring DHI chromophores thereby leading to helical aggregation.

Our efforts towards recognizing and monitoring the photogenerated excitons and charge-transfer dynamics in crystalline and contorted polyaromatic assemblies[4],[92]–[95] prompted us to explore the structure–optical property relationship in the eumelanin precursor molecule DHI. Unlike the commonly understood π-stacking in eumelanin derivatives, the single crystals of DHI arrange in a helical zig-zag fashion with a completely edge-to-face aggregate structure driven by both conventional and unconventional hydrogen bonds [Figure 2.1.b]. The structural heterogeneity imposed by the different hydrogen bonds has led to varied levels of exciton delocalization between the neighbouring chromophores in the crystalline DHI aggregates. Along with the diffracting single crystals of monomeric DHI, covalently connected trimeric units of DHI are also identified in chloroform solution, which form double-helical crystals in the mesoscopic scale. Such double-helical architectures are omnipresent in nature as exemplified by the DNA structure.

2.2. Synthesis and characterization

DHI was synthesized by following a previously reported procedure by including some minor modifications, with L-dopa as the starting material (Scheme 2.1, Appendix C1–C4 and C7).[96] A solution of 1g (5 mmol) L-dopa in water (500 ml) and a solution of $K_3[Fe(CN)_6]$ (6.6 g, 20 mmol) and $NaHCO_3$ (2.5 g, 30 mmol) in water (60 ml) were separately degassed by purging with an argon flux for 10 min. The $K_3[Fe(CN)_6]$ and $NaHCO_3$ mixture was poured at once to the solution of dopa while vigorous stirring at room temperature. L-dopa upon chemical oxidation using

L-DOPA: 3,4-dihydroxy phenyl-L-alanine
DHI: 3,4-dihydroxy indole
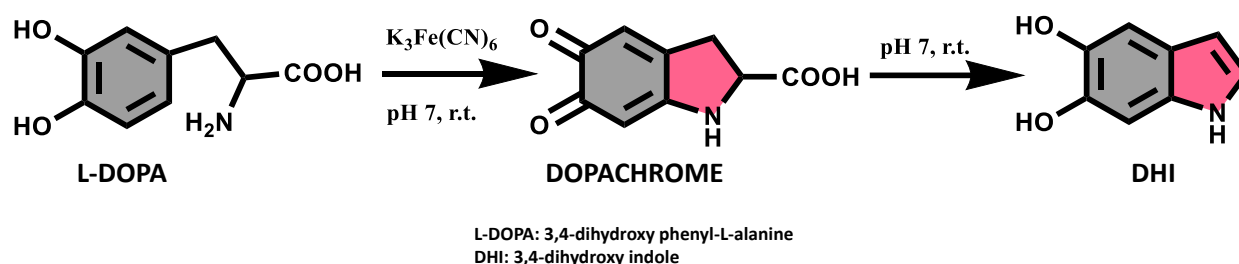
Scheme 2.1: *Shows the reaction scheme for the synthesis of DHI.*

potassium ferricyanide turns into a wine-red solution of dopachrome. Dopachrome further undergoes decarboxylation at room temperature to yield white amorphous powders of 5,6-dihydroxyindole (DHI). The reaction is maintained in a weakly basic medium that facilitates an oxidative nucleophilic reaction followed by the cyclisation of L-dopa. Solid $Na_2S_2O_5$ (5.0 g, 26 mmol) was then added to the dark brown solution, which was extracted with ethyl acetate (300 ml x 3). The ethyl acetate extracts were combined, washed once with saturated NaCl solution (100 ml), and dried over anhydrous Na_2SO_4 (50 g). Evaporation of ethyl acetate gave a brown oil to which a solution of hexane (20 ml) was added to give almost white powders of DHI. Several preparations gave yields of 61-64% (in the literature, the yield was 40%).

^{1}H NMR (500 MHz, CDCl$_3$, ppm): δ = 7.85 (s, 1H), 7.01 (t, J=3 Hz, 2H), 6.86 (s, 1H), 6.32 (s, 1H), 5.29 (s, 1H), 4.89 (s, 1H).

^{13}C NMR (125 MHz, DMSO-d6, ppm): δ = 142.91, 140.81, 130.70, 123.04, 120.70, 104.89, 100.62, 97.59.

M.P.: 170 °C

HRMS (ESI) (m/z): Calculated for $C_8H_7NO_2$: 149.0477, found: 150.0550 [M+H]$^+$

IR (cm^{-1}): 3437.15 (broad); 1631.78; 1473.62 (s); 1415.75 (s)

2.3. Results and discussions

Slow evaporation from dry chloroform solution of DHI produced colourless diamond shaped single crystals of DHI (Figure 2.2). Interestingly, the DHI molecule with no chiral center atypically crystallized in the Sohncke space group, *P*2$_1$2$_1$2$_1$ (Table 2.1).

Single-crystal X-ray structure analysis revealed the presence of conventional and unconventional hydrogen bonds directing the crystalline self-assembly of DHI chromophores about a zig-zag helical backbone. Figure 2.3 presents the four different types of non-covalent dimers (D1–4) distinguished within the DHI crystal. The zig-zag helical stacks proceed along the crystallographic *a*-axis (Figure 2.3) and are fabricated by bifurcated O–H···O hydrogen bonds ($d_{O1···H} = 2.25$ Å, $d_{O2···H} = 2.34$ Å, <O1–H–O2 = 67.89°) between the two hydroxyl substituents in the DHI chromophore (D3 in Figure 2.3). Such bifurcated hydrogen bonded assemblies are prevalent in the secondary and tertiary structures of proteins.[97] Interestingly, in the DHI crystal, enantiomeric helical stacks (Figure 2.4) that are arranged with respect to different screw axes are observed, wherein each stack aligns in a herringbone fashion to the other zig-zag helix (as represented by the dimers D1, D2 and D4). The stacks are interconnected majorly through the unconventional hydrogen bonds such as C–H···π ($d_{C-H···π} = 2.66$–2.99 Å), O–H···π ($d_{O-H···π} = 2.59$ Å), C–H···N ($d_{C-H···N} = 2.72$ Å), C–H···O ($d_{C-H···O} = 2.66$ Å) and the classical N–H···O ($d_{N-H···O} = 2.72$ Å) hydrogen bonds. The absence of π–π stacking interaction is validated by the Hirshfeld surface analysis wherein the formation of the DHI crystalline assembly is majorly stabilized by the C···H (40.5%), H···H (29.7%), N···H (4.3%) and O···H (25.4%) noncovalent interactions.

Figure 2.2: *Optical microscope images of DHI crystal.*

Table 2.1: *Crystallographic data and refinement parameters for DHI monomer*

Parameters	DHI
Formula	$C_8H_7NO_2$
Formula weight	149.15
Color	Colorless
Crystal system	Orthorhombic
Space group, Z	$P2_12_12_1$, 4
a (Å)	5.862
b (Å)	7.712
c (Å)	14.907
α, deg	90
β, deg	90
γ, deg	90
Volume, Å^3	673.9
R factor	4.71
Temp, K	296
$d_{calculated}$ (mg/m^3)	1.470
No. of reflections collected	5841
No. of unique reflections	1183
$2\theta_{max}$, deg	24.995
No. of parameters	102
R1, wR2, (l > 2s(l))	0.0689, 0.1155
R1, wR2 (all data)	0.0471, 0.1044
Goodness of fit	1.023
CCDC number	2120651

Detailed examination of the interchromophoric interactions supporting the zig-zag helical stacks in DHI crystals using Bader's quantum theory of atoms in molecules (QTAIM) analysis revealed the presence of supramolecular synthons in the crystal
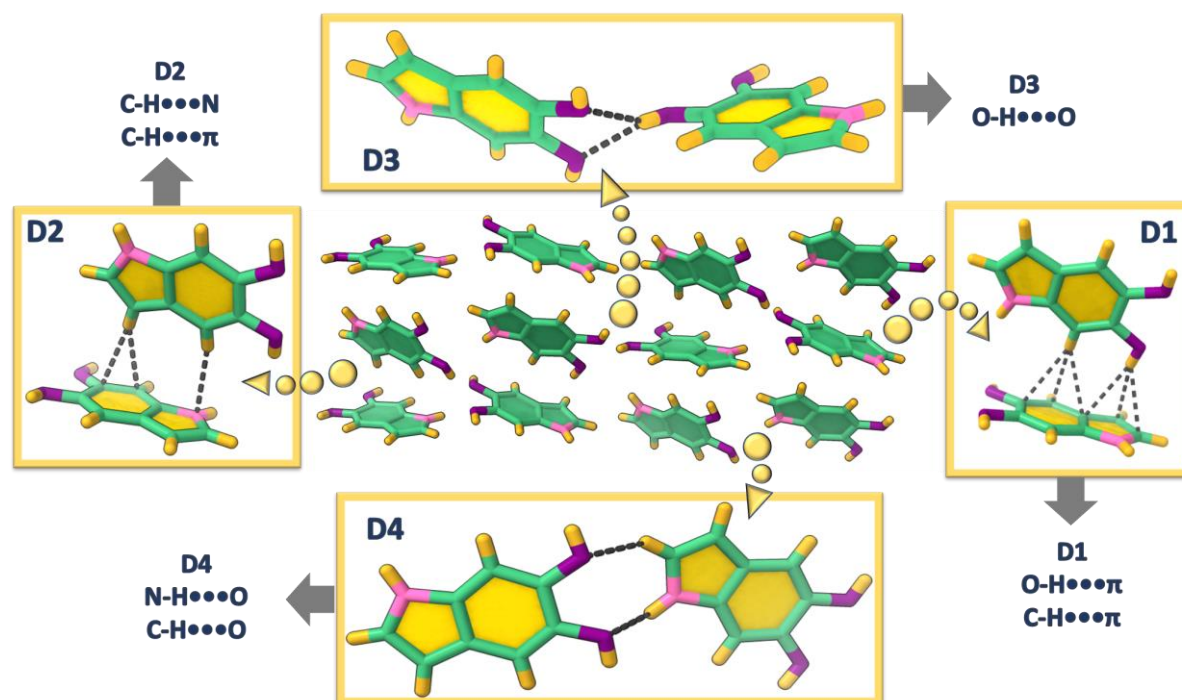
Figure 2.3: *Different orientations of DHI (D1–4) and the directing hydrogen bonds observed in the single crystal.*

system (Figure 2.5). This is evidenced by the (3,+1) ring critical points in each of the representative dimers. For a molecular self-assembly to occur efficiently, recognition between the intermolecular functionalities is important, which often culminates in the formation of smaller repetitive units or supramolecular synthons.[43] The recognition information which is then carried by these units forms the kernel of self-aggregation or crystallization processes. In the case of DHI crystals, all the dimer assemblies D1–D4 display synthon formation with the D1 and D3 synthons showing greater energetic stabilities. The dimer unit representing the helical backbone, D3, forms two supramolecular synthons orchestrated by the bifurcated O–H⋯O hydrogen bonds and a weak C–H⋯O interaction (Figure 2.5). The five- and six-membered rings so formed fabricate the helical zig-zag backbone of the DHI crystal. Similarly, the dimer D1 also forms two synthons through a classical N–H⋯O interaction along with the weak C–H⋯π and O–H⋯π interactions. D2 and D4 dimers are stabilized by one synthon each, materialized by C–H⋯π and C–H⋯N interactions in D2 and N–H⋯O and C–H⋯O interactions in D4.
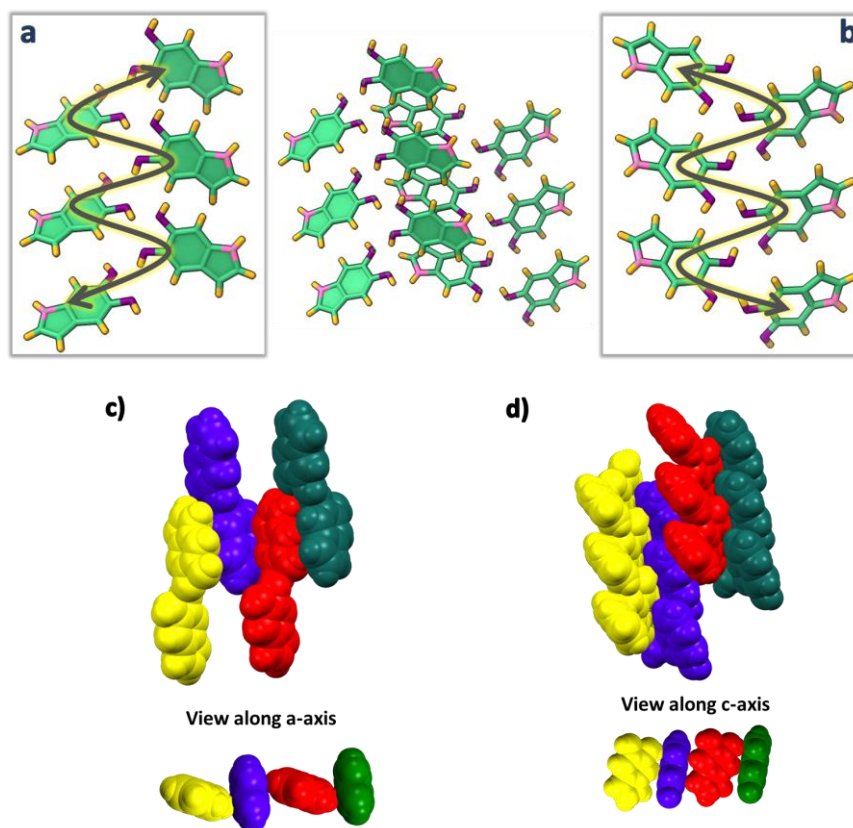
Figure 2.4: *Shows the a-b) enantiomeric zig-zag helical stacks proceeding along the crystallographic c) a-axis and d) c-axis where each colour represents the adjacent enantiomeric stacks. The enantiomeric stacks are connected in herringbone fashion as shown in (d).*
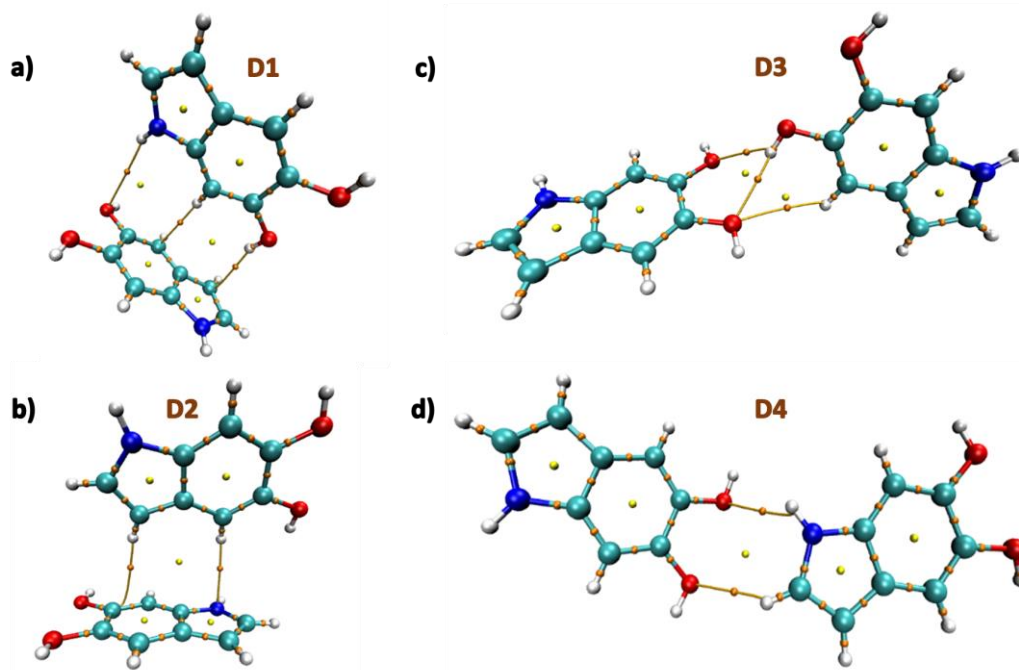
Figure 2.5: *QTAIM electron density map showing the synthon formation from hydrogen bonding interactions in a) D1, b) D2, c) D3 and d) D4.*

The synthon formation and the concomitant electron delocalization involving the π-rings in dimers D1 and D2 have resulted in the aromatic stabilization of the π-rings upon comparison with the monomer DHI. The nucleus independent chemical shift (NICS(1)) values evaluated for D1–4 and monomer DHI in the ground state indicate the aromatic stabilization of the π-surface leading to the favorable alternate stacking of the enantiomeric zig-zag helices facilitated by the unconventional hydrogen bonds. The negative NICS(1) values for the six- and five-membered (6C, 5C) rings of molecule A (Table 2.2 and Figure 2.6) increased to −27.22 ppm (6C) and −29.13 ppm (5C) when compared to the monomer DHI (6C: −26.14 ppm, 5C: −28.03 ppm). Similarly, in D2, the π-surface of molecule B that is involved in the weak interaction undergoes aromatic stabilization (6C: −29.43 ppm, 5C: −31.48 ppm). Truncated symmetry adapted perturbation theory (SAPT(0)) analysis[98] performed on the DHI dimers shows higher stabilization for D1 (E_{int}^{SAPT} = −9.70 kcal mol^{-1}) and D3 (E_{int}^{SAPT} = −6.57 kcal mol^{-1}) dimers, which could be attributed to the two supporting supramolecular synthons in both the dimers (Table 2.3). The total stabilization of D1 and D3 orientations is facilitated by the higher contributions of electrostatic energy ($E_{elc}^{(1)}$ = −6.17 to −6.14 kcal mol^{-1}) and induction energy ($E_{elc}^{(1)}$= −1.60 to −1.38 kcal mol^{-1}) towards the total SAPT energy. The dominant role of the stronger classical hydrogen bonds in the fabrication of D1 and D3 synthons when compared to the other DHI orientations (having equal contribution from the weak unconventional interactions)

Table 2.2: *NICS(1) values calculated for the various dimers in DHI crystal.*

Monomer	6C		5C	
	-26.14		-28.03	
Dimer	Molecule A [#]		Molecule B [#]	
	6C	5C	6C	5C
D1	-27.22	-29.13	-25.56	-27.63
D2	-26.41	-28.39	-29.43	-31.48
D3	-25.47	-27.57	-25.92	-27.92
D4	-25.61	-26.76	-25.42	-27.77
# The molecules represented as A and B are indicated in Figure 2.6				
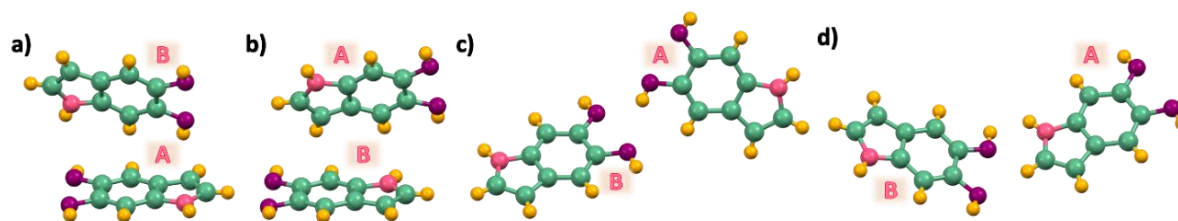
Figure 2.6: *A and B molecules for NICS(1) calculation in dimers a) D1, b) D2, c) D3 and d) D4*

Table 2.3: *Interaction energies[a] of DHI dimers evaluated using symmetry-adapted perturbation theory (SAPT(0)) aug-cc-pVDZ calculations.*

Dimer	SAPT(0) E_{int}^{SAPT}	Electrostatic energy $E_{elc}^{(1)}$	Dispersion energy $E_{dis}^{(2)}$	Induction energy $E_{ind}^{(2)}$	Exchange energy $E_{ex}^{(1)}$
D1	-9.70	-6.17	-8.49	-1.60	6.56
D2	-5.69	-1.67	-7.65	-0.70	4.34
D3	-6.57	-6.14	-3.51	-1.38	4.46
D4	-2.63	-1.52	-2.85	-0.70	2.45

[a]All energy values are provided in kcal mol^{-1}

explains the observed energy distribution in the SAPT(0) analysis.

The crystalline architecture of the DHI precursor molecule identified herein could provide a sound model for understanding the inherent nature of the excited energy states leading to the characteristic photo-function of the eumelanin pigment. Several experimental and theoretical investigations on eumelanin aggregates revealed the occurrence of excitation energy transfer within the aggregates.[82],[99] The extent of energy delocalization within the four dimer orientations in the DHI crystal structure is determined using the fragment-based excited state analysis developed by Plasser, executed in the TheoDORE package.[20],[100],[101] The expanse of excitation delocalization amongst the fragment units is described by the value of participation ratio (PR). The contribution towards the exciton delocalization from the fragments is defined by the mean position or the POS value, wherein the indicated number shows

the involvement of one or more units. The charge-transfer or Frenkel character of the excited states is defined by the CT number which assumes values closer to one for pure CT states and closer to zero for pure Frenkel states. In dimers D1 and D2, the first singlet excited state of highest oscillator strength (S2) shows Frenkel exciton character with effective delocalization of the excitons between the individual constituting units during the excitation process (Table 2.4). The low CT values of the S2 states in D1 (PR = 1.79, POS = 1.33, CT = 0.08) and D2 (PR = 1.98, POS = 1.45, CT = 0.02) along with a PR close to a value of two indicated the delocalization of the Frenkel excitons on the two monomers. Hence, there exists a possible excitation energy delocalization along the adjacent enantiomeric stacks in the DHI crystal. However, for D3 with the bifurcated hydrogen bonding interaction between the monomeric units, both S1 and S2 states have significant oscillator strength. The Frenkel excitons in S1 and S2 states remain localized on only one fragment of D3 (Table 2.4), while in D4, there exists a partial delocalization of the Frenkel excitons in the S1 state (Table 2.4). Thus, it is understood that within each enantiomeric stack the initial Frenkel excitons remain localized on one fragment. The hole–electron isosurface analysis provides a pictorial representation of the corresponding delocalized and localized nature of the initial Frenkel excitons in the four DHI orientations (Figure 2.7). The delocalization of the hole and electron density on both the fragments puts forward the possibility of effective energy transfer in dimers D1, D2 and D4.[5] In dimer D3, a very weak delocalization of the electron–hole densities was observed suggesting a localized exciton formation.

Several factors including slight exposure to air,[102] humidity and/or light have been observed to cause the autooxidative polymerization of DHI, wherein lowered temperatures decrease the kinetics of this solid-state polymerization. Although, a major fraction of the solid oligomer mixture remains as the DHI monomer (≥80%), oligomeric units up to DHI-hexamers have been identified with varying

Table 2.4: *Energy (ΔE), oscillator strength (f), mean position (POS), participation ratio (PR) of initial orbital (hole) and final orbital (electron) and charge transfer character (CT) of excited singlet states in dimers D1-4.*

Dimer	Energy State	ΔE (eV)	f	POS	PR	CT
D1	S1	4.619	0.009	1.648	1.839	0.04
	S2	4.678	0.252	1.333	1.796	0.081
	S3	4.877	0.03	1.586	1.357	0.698
	S4	4.977	0.05	1.878	1.276	0.1
	S5	5.015	0.066	1.127	1.285	0.036
D2	S1	4.625	0.001	1.54	1.987	0.024
	S2	4.689	0.282	1.453	1.982	0.021
	S3	4.935	0.007	1.423	1.929	0.14
	S4	4.946	0.055	1.049	1.102	0.036
	S5	4.983	0.064	1.584	1.944	0.047
D3	S1	4.769	0.223	1.061	1.13	0.005
	S2	4.819	0.166	1.939	1.13	0.002
	S3	5.132	0.087	1.997	1.006	0.001
	S4	5.149	0.108	1.007	1.013	0.005
	S5	5.792	0	1.5	1.002	0.998
D4	S1	4.764	0.339	1.29	1.7	0.003
	S2	4.816	0.079	1.707	1.708	0.003
	S3	5.107	0.107	1.178	1.413	0.003
	S4	5.121	0.045	1.825	1.406	0.002
	S5	5.625	0	1.496	1.009	0.991

solubilities in different solvents. MALDI-MS spectra (Appendix C5) sequentially collected for the oligomer mixture in CHCl₃ and DMSO indicated the major presence of DHI trimers (in CHCl₃; *m/z* = 442.138) and DHI-hexamers (in DMSO; *m/z* = 882.382) along with the smaller counterparts. Interestingly, over the time course for nucleation and the subsequent growth mechanism of the single crystals of monomeric DHI in
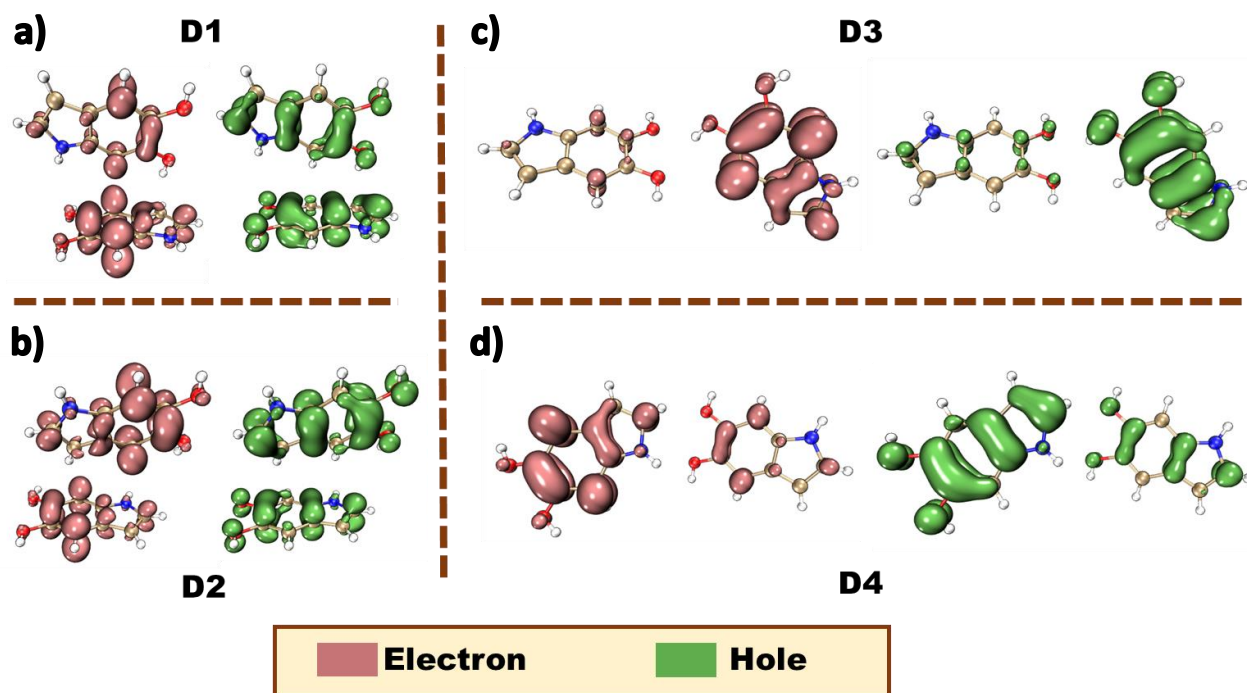
Figure 2.7: *Hole–electron isosurface plots of the DHI orientations in the crystal. (a) D1, (b) D2, (c) D3 and (d) D4.*

chloroform, oligomerization of DHI is found to occur concurrently to form the covalently connected DHI trimer (DHI-T). Along with the diffracting single crystals of DHI, small right-handed double-helical crystals (non-diffracting, Figures 2.8.a are observed for the first time, which could be attributed to the self-assembled morphology of DHI-T (Figure 2.8a). Observed only in chloroform, we speculate that the prolonged exposure of the chlorinated solvent plays a significant role in the chemical transformation of the DHI monomer to the covalent trimer, possibly through a radical initiated reaction.[103] The ^{1}H-NMR spectrum obtained for the bulk crystalline sample dissolved in CDCl$_3$ along with the observed MALDI-MS data of the DHI trimer evidenced the formation of DHI-T, although in very low yields when compared to the monomer (Appendix C5 and C6).

With the understanding that DHI readily aggregates/crystallizes in chloroform, the directionality of the hydrogen bonding interactions (to the π-ring) within the definite spatial arrangements of D1 and D2 orientations hints towards the mode/position of coupling for the associated generation of DHI-T (Appendix C9). The
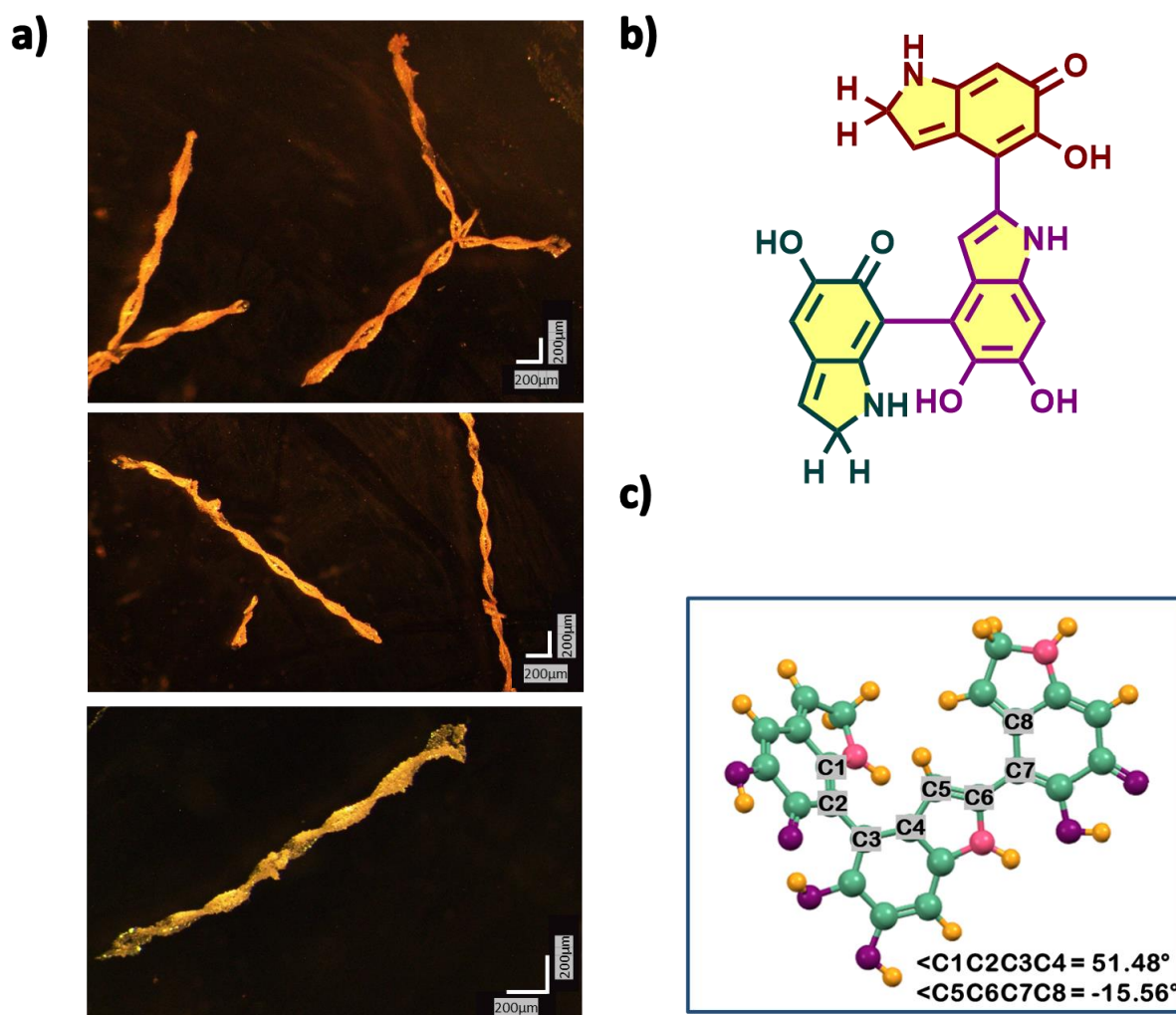
Figure 2.8: *(a) Optical microscopy images of the right-handed double-helical crystals of the DHI trimer. (b) Molecular structure predicted for DHI trimer (DHI-T). (c) Optimized structure of DHI-T at the CAM-B3LYP/6-311g+(d,p) level of theory.*

molecular structure of the DHI trimer that best fits the observed characterization data (Figure 2.8.b and Appendix C8) is in line with the chemical disorder model having semiquinone and catechol units connected covalently as an extension of the D1 and D2 noncovalent interactions. Geometry optimization of the predicted structure of the DHI-T performed using the CAM-B3LYP/6-311g+(d,p) level of theory in Gaussian 16 suite shows a twisted conformation having the possibility of forming intramolecular hydrogen bonds from the –OH and –NH functionalities (Figure 2.8). Separation of DHI-T from DHI is a real challenge since exposure of DHI to the adsorbent in column

chromatography accelerates the oxidative polymerization of DHI, resulting in a black, insoluble material difficult to characterize. Also, the presence of higher oligomer units of DHI (hexamers *etc.*) was not identified in the multiple data sets collected for the DHI sample dissolved in CHCl$_3$.

Solvent-dependent steady-state UV-vis absorption and fluorescence emission measurements of DHI were performed and the line shapes of the absorption spectra of monomeric DHI in different solvents match consistently (Figure 2.9). Two major absorption bands at $\lambda_{a1} \sim 270$ nm and $\lambda_{a2} \sim 300$ nm form the characteristic absorption spectrum of the DHI monomer. The fluorescence emission of monomeric DHI exhibits a single broad spectral feature peaking at $\lambda_{em} \sim 330$ nm in most of the solvents. The relative fluorescence quantum yields are found to be exceptionally low in chloroform, dichloromethane, THF and water (Table 2.5) indicating the presence of non-radiative decay channels for dissipating the excitation energy. In chloroform, the emergence of a red-shifted tail in the absorption spectrum of the DHI-monomer is observed over time possibly signifying the onset of DHI-T formation. The fluorescence emission in CHCl$_3$ also shows a new band peaking at $\lambda_{em} \sim 460$ nm along with the emission band at $\lambda_{em} \sim 335$ nm (Figure 2.10a). A broad red-shifted band arising at 370 nm in the
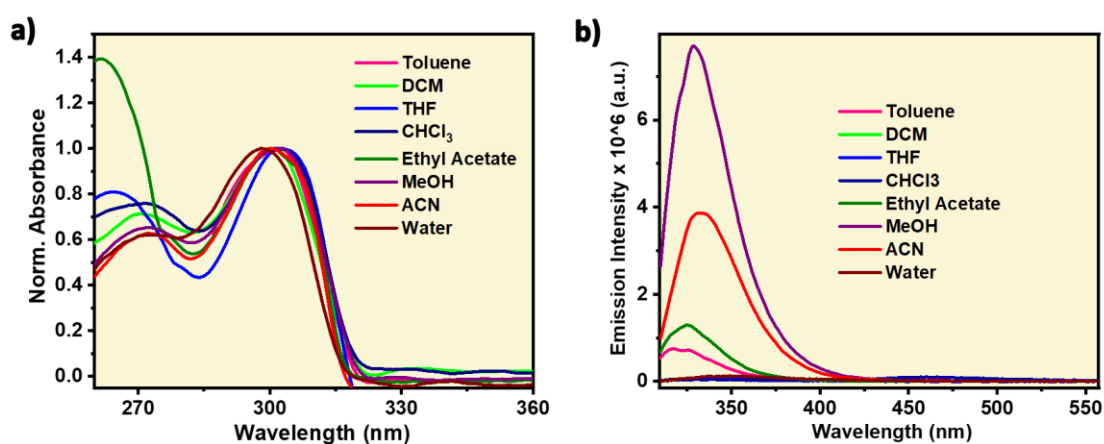
Figure 2.9: *a) Normalized absorption and b) fluorescence emission profiles of monomeric DHI in various solvents*

excitation spectrum of DHI solution collected in chloroform at $\lambda_{em} \sim 460$ nm (Figure 2.10) evidenced the presence of the DHI trimer. A similar decrease in fluorescence quantum yield in chloroform and the concomitant emergence of new bands in the fluorescence emission profiles have been noted previously in tryptophan and other indole species synthesized for eumelanin investigation.[104],[105] In such cases, the photoionization of excited indole leads to the ejection of a solvated electron which attacks the chloroform molecule, releasing a chloride ion, and further undergoes reactions to yield photoproducts.

Spectroscopic investigation of the crystalline DHI (containing both monomer single crystals and covalent trimer crystals) sample showed broad, red-shifted absorption bands spanning from 210 to 560 nm (Figure 2.10 b&c). The solid-state absorption spectrum shows two prominent bands at $\lambda_{a1} \sim 280$ nm and $\lambda_{a2} \sim 305$ nm which could be attributed to the red-shifted absorption bands of the crystalline DHI monomer (compared to the monomer absorption bands in the solution state). The observed red-shift in the absorption band of the DHI crystal arises from the nonplanar packing motif and the ensuing intermolecular interactions in the solid state. The presence of a broad shoulder band centred at $\lambda_{a3} \sim 375$ nm in the absorption spectrum could be assigned to the double-helical crystal of the covalent DHI trimer. The crystalline state fluorescence emission spectrum of DHI spans from 390 to 490 nm (Figure 2.10). The excitation energies and the allowed vertical transitions of the monomer and DHI-T have been computed at the CAM-B3LYP/6-311g+(d,p) level of theory. Unlike the precursor DHI monomer which undergoes higher energy electronic transitions (at 270 nm and 300 nm), the favorable transition in the covalent trimer is red-shifted with the $S_0 \rightarrow S_1$ electronic excitation occurring at ~434 nm. Hence, the spectroscopic and theoretical investigation of bulk crystalline DHI indicates that the broad absorption profile of the eumelanin precursor could be ascribed to the combined effects of the non-planar chromophore stacking and the presence of covalent DHI trimers that exist as double-helical aggregates.

Table 2.5: *Photophysical properties of DHI monomer in different solvents.*

Solvent	λ_{em} (nm)	Fluorescence Quantum Yield (%)	Fluorescence Emission Lifetime (ns) [Relative Amplitude in %]
Toluene	320	3.80	0.10
DCM	335	0.50	<1
THF	335	0.50	2.02
CHCl$_3$	335, 460	1.20	335 nm = <1
			460 nm = 1.17 [81%] 8.60 [19%]
Ethyl Acetate	325	4.00	0.52
MeOH	331	29.00	1.75
ACN	333	15.50	2.13
Water	350	0.90	<1 [95%] 4.38 [5%]

The photoprotective nature of eumelanin arises from the signature broadband absorption of eumelanin which spans throughout the UV and visible region tailing around 800 nm as explained by the chemical disorder model. In line with this understanding, the spectroscopic data of the DHI crystal also exhibit broadband absorption which expands up to 600 nm unlike the DHI monomer. Moreover, the low relative fluorescence quantum yields of DHI suggest the presence of non-radiative decay pathways within the DHI units. The oligomeric trimer which in itself shows structural heterogeneity aggregates as double helical structures and shows a red-shifted absorption band which is comparable to the computed TDDFT vertical excitation energies. Thus, our report on the characterization of DHI and the oligomeric trimer could possibly be beneficial in advancing melanin structure characterization and elucidating the photoprotective function of eumelanin.

The solid-state CD spectrum of crystalline DHI (in KBr, Figure 2.11) showed the signatures for the presence of helical packing[106]–[110] (possibly from the zig-zag helical motif along with the double helical arrangement). However, the basis of the CD couplet of significant intensity spanning from ~250 to 600 nm (including
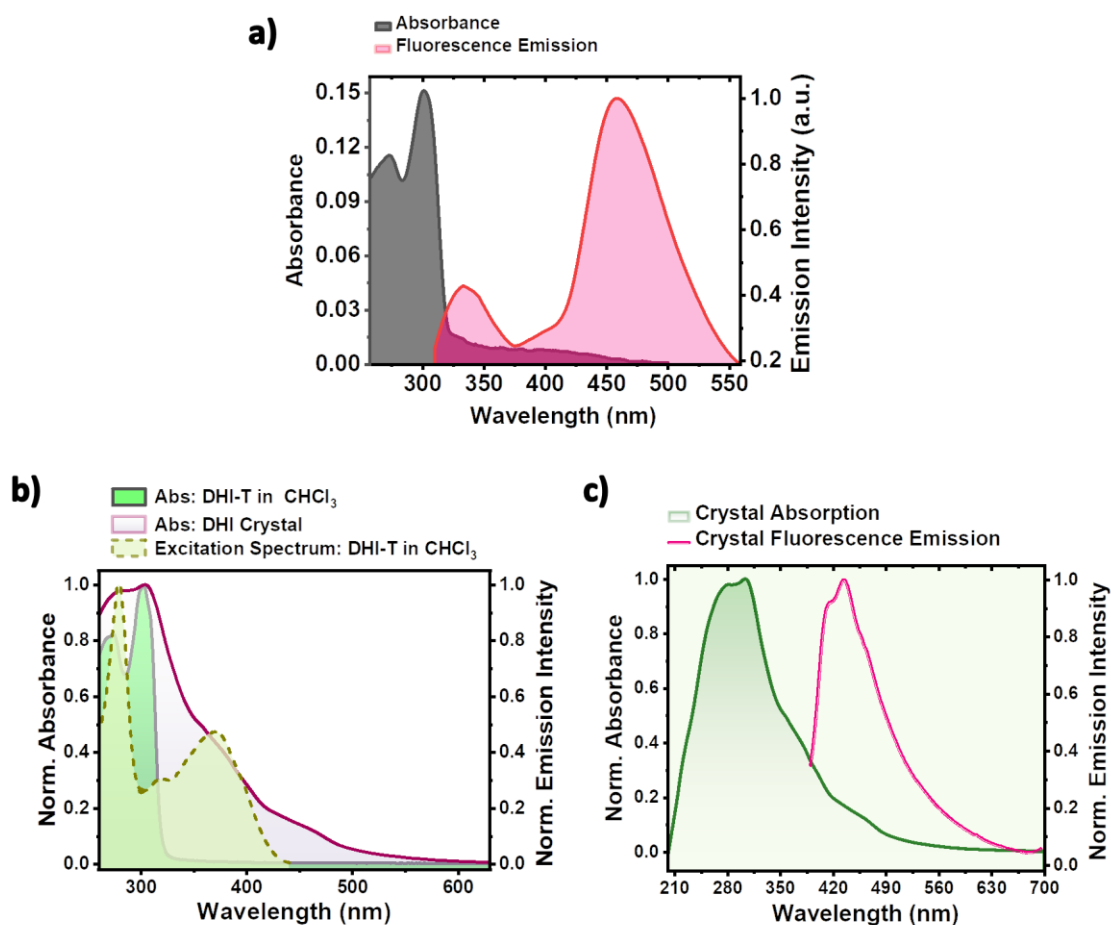
Figure 2.10: *a) UV-vis absorption (grey) and normalized fluorescence emission (red) profiles of monomeric DHI in CHCl3; b) Normalized UV-vis absorbance and fluorescence excitation spectra showing DHI-T formation in chloroform solution and the crystalline state absorption spectrum obtained from Kubelka-Munk transformed diffuse reflectance spectrum of DHI bulk crystal; c) Normalized absorption and fluorescence emission profiles for DHI crystal.*

ranges outside of the absorption maxima) could not be exclusively assigned to chiral absorption from the chromophoric packing.[111] In the case of macromolecular systems having long-range organization, differential scattering of incident left and right circularly polarized light can provide significant contributions to the observed circular dichroism.[112]–[114] The occurrence of broad CD bands outside the absorption bands of the macromolecule can signify the possible role of differential scattering in the circular dichroism.[115] Although, for the DHI sample, the characteristic CD spectrum has been found to be concurrent for the different data sets collected using freshly prepared crystalline samples on different days (Figure 2.11a),
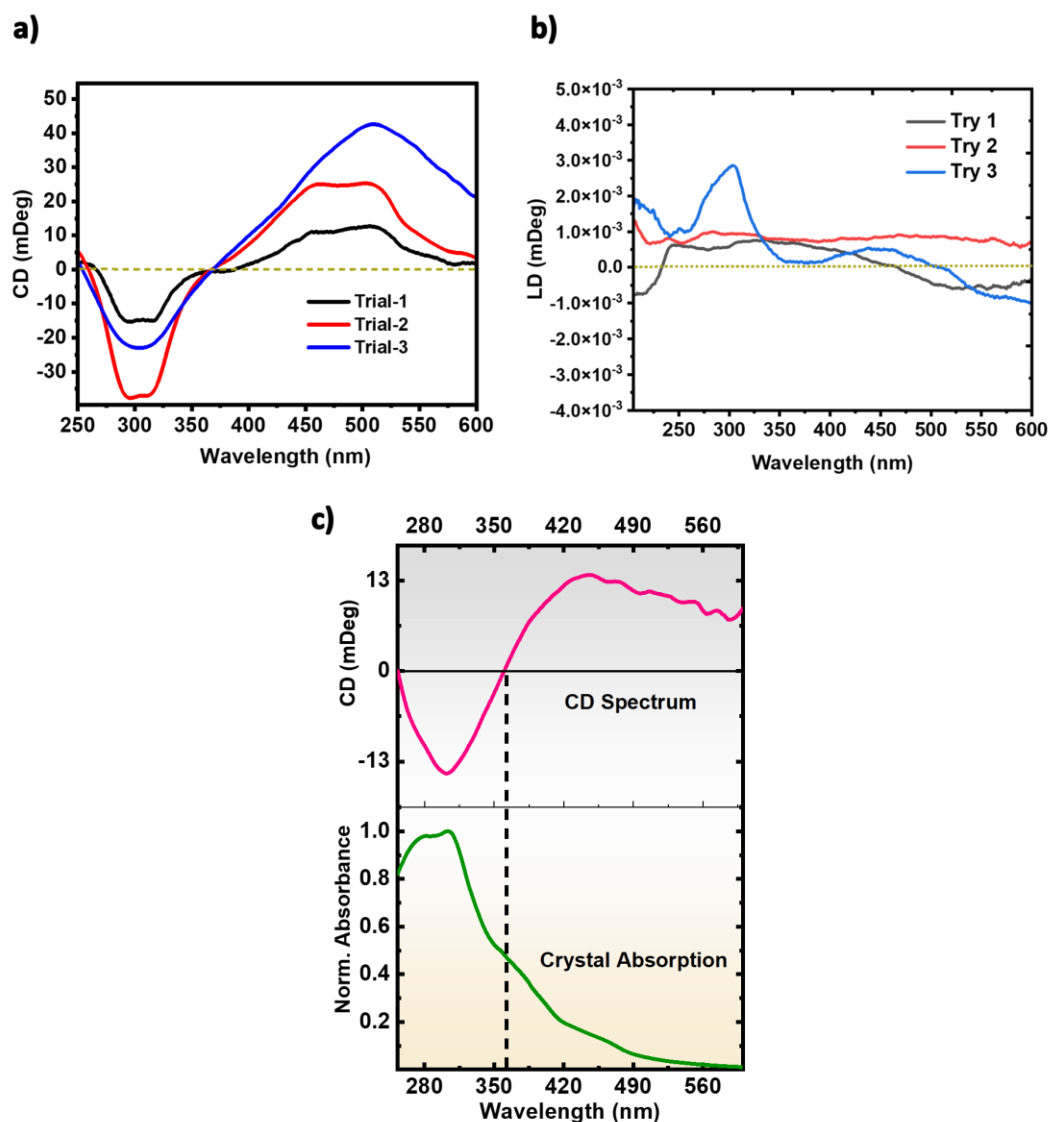
Figure 2.11: *Shows the (a) concurrent CD and (b) LD spectra obtained for the bulk DHI crystal collected on different days, each with freshly crystallized samples at varied concentration ratio of sample:KBr. c) Absorption spectrum obtained from Kubelka-Munk diffuse reflectance transformation (bottom) and CD spectrum (top) of DHI crystal with the zero crossing at ~371 nm.*

the ratios of the intensities of the positive and negative bands have been observed to vary. Such a heterogeneity in the ellipticity values of the positive and negative bands could be attributed to the possible presence of different enantiomeric assemblies that exhibit varying abilities to undergo chiral absorption and differential scattering. The possibility of having linear dichroism (LD) artifacts in the CD data was evaluated for the DHI sample (Figure 2.11b).[116] The LD artifact fell within the error bar of the

order of 10^{-3}–10^{-4} mdeg and hence, the contribution of LD to the strong CD signal of DHI could be ignored.[117],[118] Also, the idea of having a chiral nucleation centre, probably from any conformationally chiral DHI oligomer units, leading to the double-helical aggregation and the consequent mesoscopic chirality could not be ignored while assessing the origin of the observed CD spectrum. The existing uncertainties in solving the source of the double-helical aggregation of the DHI chromophores and identifying the intermolecular forces acting behind the same remain a challenge that requires detailed examination in future studies.

2.4. Conclusions

In conclusion, we introduce the helical crystalline packing arrangement of an achiral eumelanin precursor, 5,6-dihydroxyindole (DHI), derived from a non-protic environment, chloroform. The present account well describes the solitary effect of interchromophoric interactions on the crystalline self-aggregation of DHI molecules by filtering out the external hydrogen bonding association with the solvent environment. This approach resulted in a helical assembly of achiral DHI chromophores, unlike any of the previously understood structural motifs of eumelanin precursors. The diffraction quality single crystals of DHI obtained from chloroform solution encompass enantiomeric zig-zag helical stacks aligned in a herringbone fashion with respect to each stack. The origin of each of the zig-zag stacks occurs from a backbone structure constructed by bifurcated hydrogen bonding interactions between the hydroxyl substituents in adjacent DHI chromophores. The excitation energy delocalization pathways evaluated for the crystalline arrangement of DHI show effective exciton delocalization along the chromophores connecting each of the enantiomeric stacks. However, minimal exciton delocalization was observed within each enantiomeric stack.

Along with the single crystals of the DHI monomer, formation of covalently connected DHI trimer aggregates (DHI-T) is also observed in the chloroform solution.

DHI-T forms small double-helical crystals on the mesoscopic scale. The best-fit molecular structure of the DHI covalent trimer as evident from the spectroscopic characterization points to the presence of catechol and semiquinone moieties, in line with the renowned chemical disorder model proposed for eumelanin. The covalent DHI trimer shows a red-shifted absorption band (~370 nm) when compared to the DHI monomer (~270–300 nm) as demonstrated by the spectroscopic and theoretical investigations. Thus, with the unceasing ambiguity still existing for the eumelanin molecular framework and the consequent photophysics, the crystalline evidence presented here of a eumelanin precursor molecule could serve as a potential candidate for decoding the melanin mystery.

2.5. Appendix

2.5.1. Materials and methods

All chemicals were obtained from commercial suppliers and used as received without further purification. All reactions were carried out in oven-dried glassware prior to use and wherever necessary, were performed under dry nitrogen in distilled solvents using standard gastight syringes, cannula, and septa. Solvents used for characterization were dried and distilled by standard laboratory purification techniques. Yields refer to spectroscopically homogenous substances. Melting points were obtained using a capillary melting point apparatus. ^{1}H and ^{13}C NMR spectra was measured on a 500 MHz Bruker Advance DPX spectrometer. Internal standard used for ^{1}H NMR and ^{13}C NMR is 1,1,1,1-tetramethyl silane (TMS). High resolution mass spectra (HRMS) were recorded on Thermo Scientific Q Exactive Mass Spectrometer using Electrospray Ionization (ESI) technique. MALDI-TOF Mass Spectra were recorded on Bruker UltraFlextreme MALDI-TOF mass spectrometer by directly ionizing the sample without using a matrix. IR spectra were recorded on a Shimadzu IR Prestige-21 FT-IR spectrometer with KBr pellets. Photophysical measurements of the derivatives were carried out in a cuvette of 3 mm path length. Absorption and

emission spectra were recorded on Shimadzu UV-3600 UV-VIS-NIR and Horiba Jobin Yvon Fluorolog spectrometers, respectively. The Kubelka-Munk transformed reflectance spectra in the crystalline state were measured in the diffuse reflectance mode. CD spectrum of samples in solid state were recorded in circular dichroism spectrometer MOS500 supplied by BioLogic Science Instrument. For obtaining solid state CD spectrum, KBr was powdered and dried in vacuum oven at 80°C for 3 h. A transparent KBr pellet was used for recording a baseline. Transparent pellets of samples were made by pressing a mixture of 1:100 sample:KBr and the measurement was done immediately. Powder X-ray diffraction (PXRD) spectra were recorded using an X'pert PRO (PANalytics) powder diffractometer with Cu as the anode material (Kα1 = 1.54 Å). The optical microscopic images were recorded on Olympus SZX-2-ILLB Trinocular Stereomicroscope with Digital Camera. Lifetime measurements were carried out in an IBH picosecond time-correlated single-photon counting (TCSPC) system. The pulse width of the excitation (λ_{exci} = 310 nm) source is determined to be <100 ps and the fluorescence decay profiles were de-convoluted using DAS6.3 and fitted with exponential decay, minimizing the χ2 values.

2.5.2. X-ray crystallography

High quality single crystals of DHI were used for X-ray diffraction experiments. Single crystal was mounted using oil (Infineum V8512) on a glass fiber. All measurements were made on a CCD area detector with graphite monochromated Mo Kα radiation. The data was collected using Bruker APEXII detector and processed using APEX2 from Bruker. The structure was solved by direct method and expanded using Fourier technique. The non-hydrogen atoms were refined anisotropically. Hydrogen atoms were included in idealized positions, but not refined. Their positions were constrained relative to their parent atom using the appropriate HFIX command in SHELX-97.[119] All programs used during the crystal structure analysis are incorporated in the WINGX software.[120] The full validation of CIF and structure

factor of DHI was performed using the checkCIF utility and found to be free of major alert levels. Three-dimensional structure visualization and the exploration of the crystal packing of crystals under study were carried out using Mercury 3.5.1.[121]

2.5.3. Characterisation data of DHI
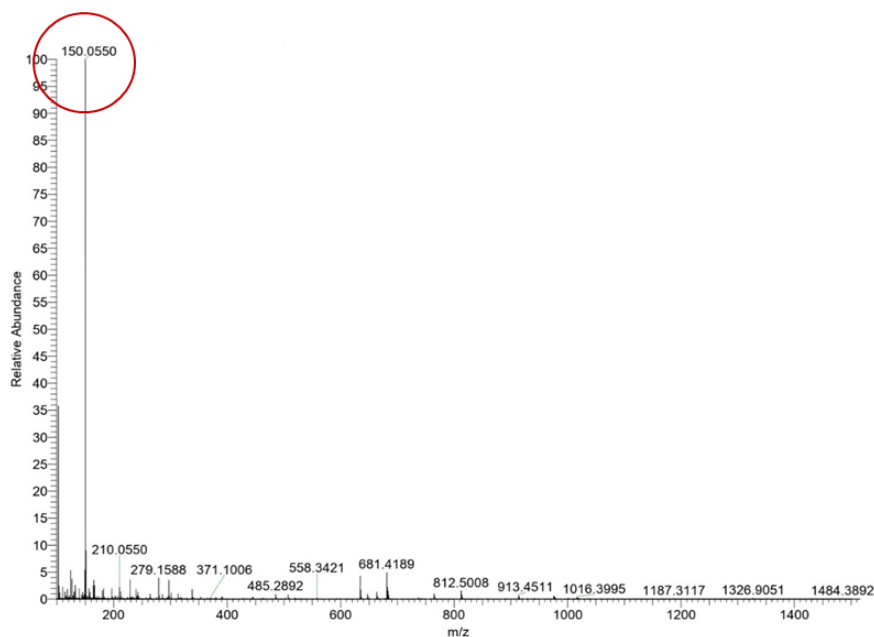
Appendix C1. *HRMS Spectrum of DHI monomer.*
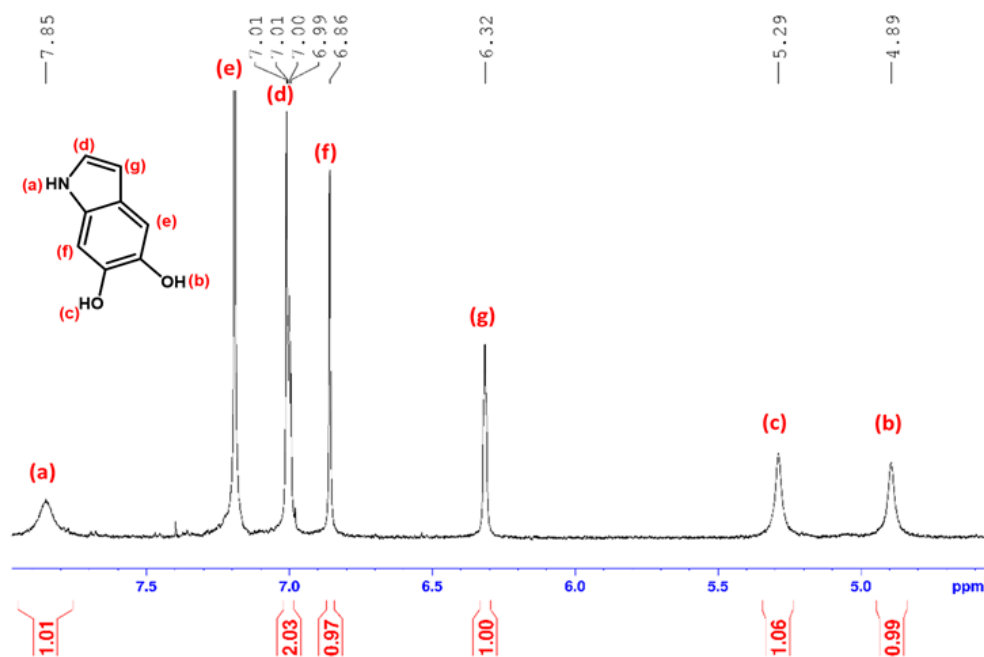
Appendix C2*: ^{1}H-NMR Spectrum of DHI-monomer in CDCl$_3$.*
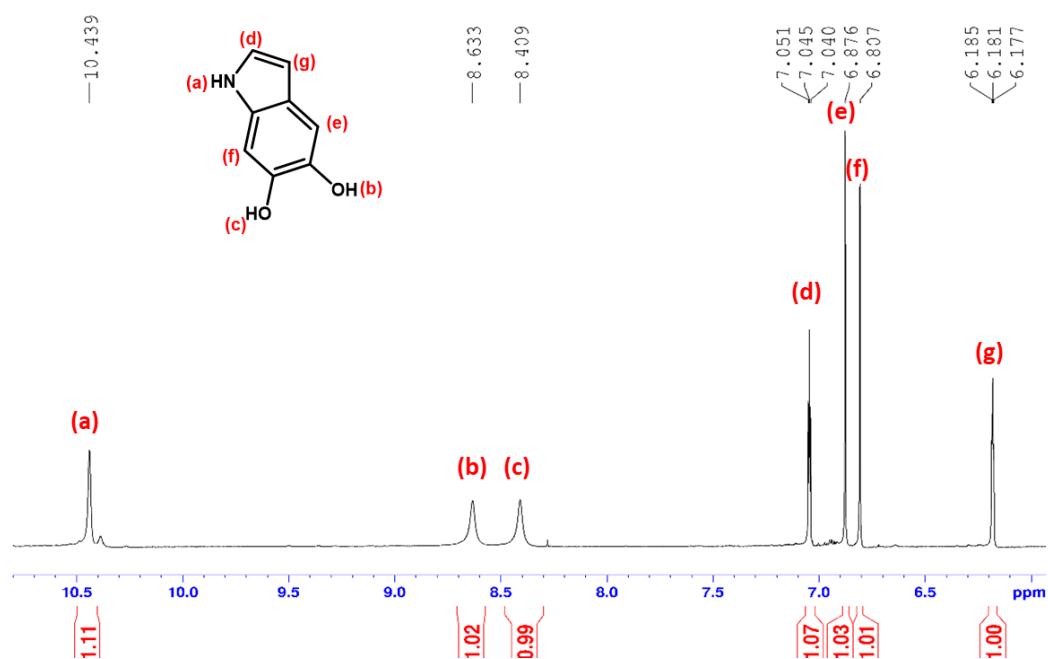
Appendix C3: *¹H-NMR Spectrum of DHI in DMSO-d₆.*
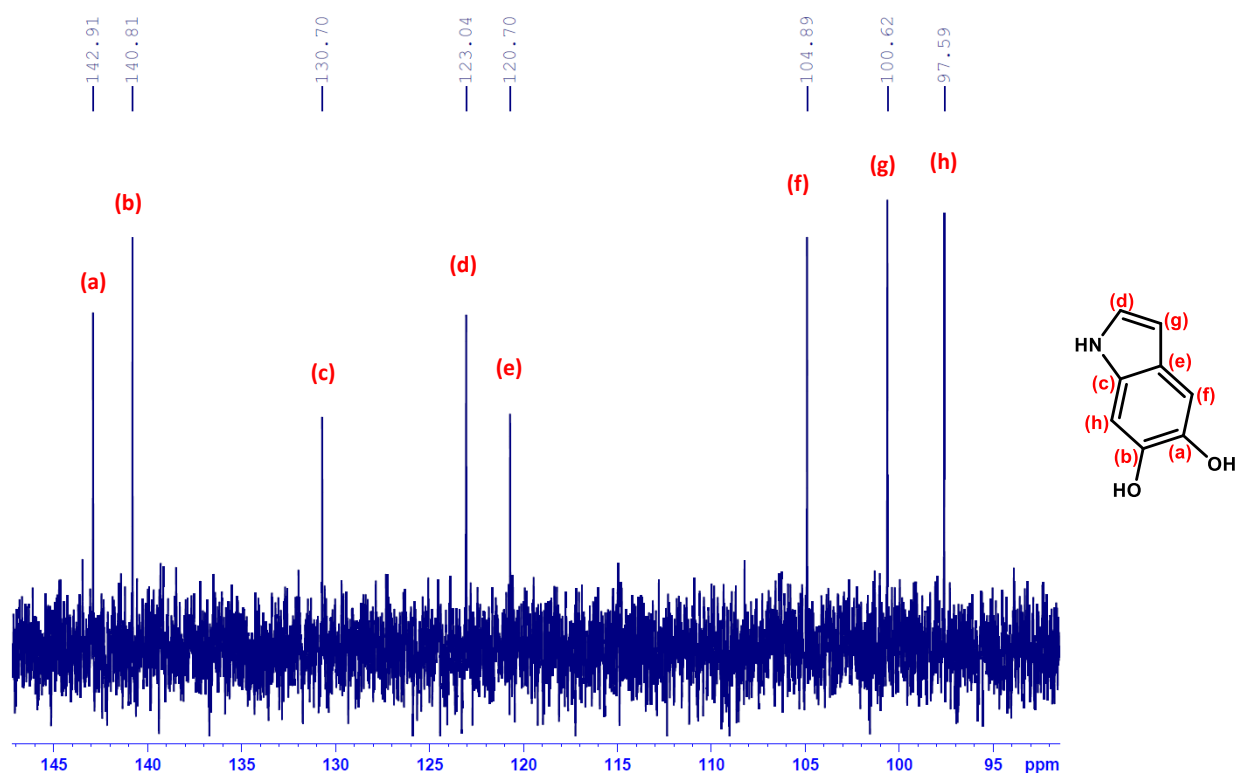
Appendix C4: *¹³C-NMR Spectrum of DHI in DMSO-d₆*
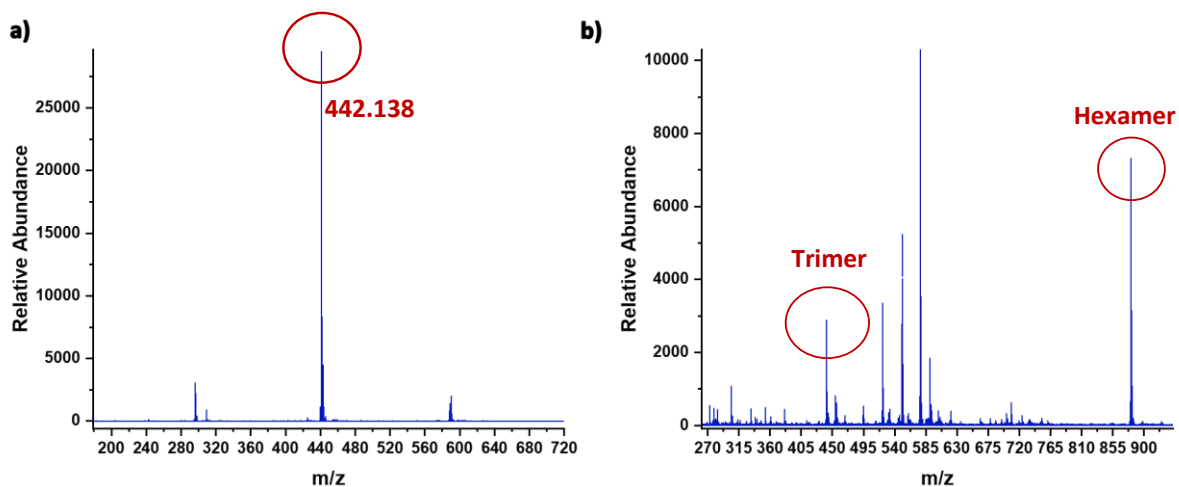
Appendix C5: *MALDI-MS Spectra of DHI-oligomer dissolved in **a)** CHCl₃ and **b)** DMSO.*
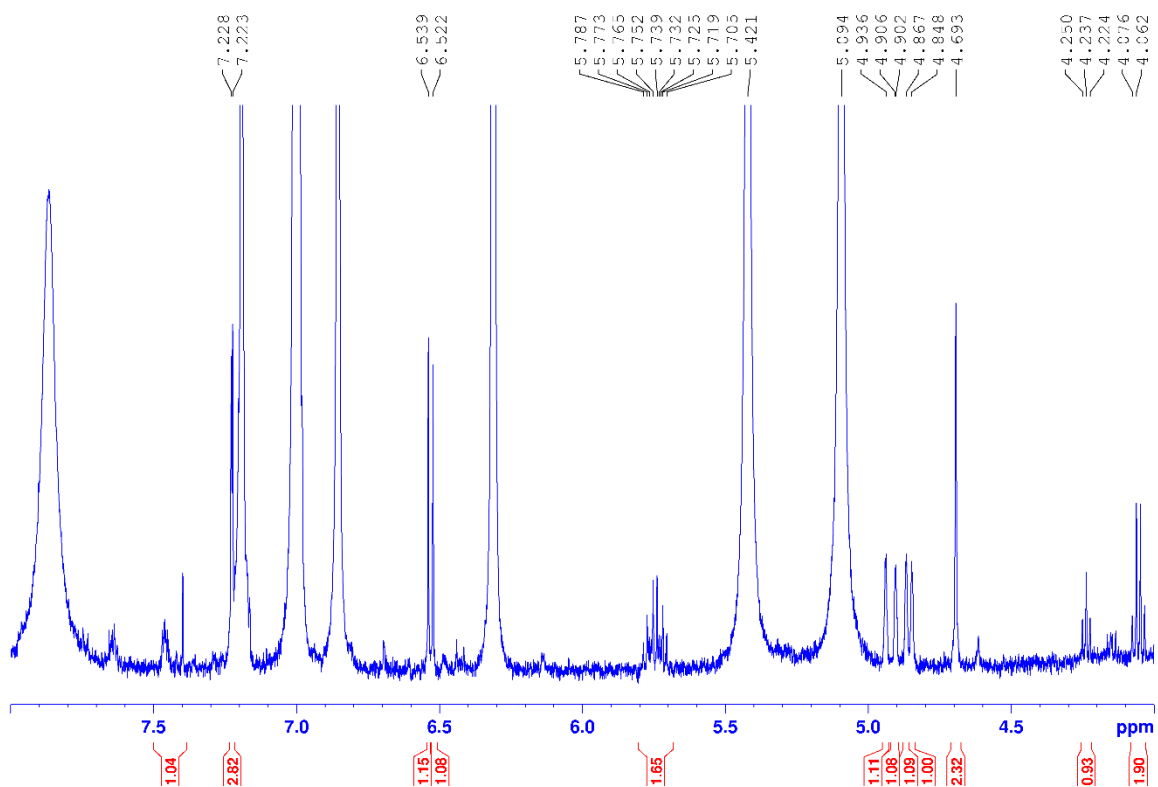
Appendix C6: *¹H-NMR spectrum showing the presence of DHI-T in aggregate concentrations of DHI in CDCl₃. The 17 protons obtained after proton integration point to a trimer structure as that of DHI-T.*
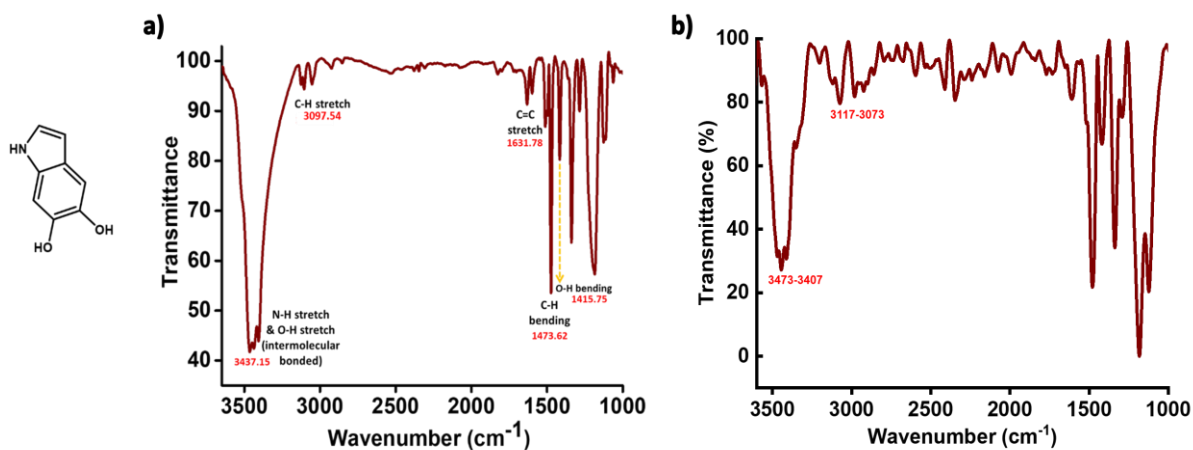
Appendix C7: *IR Spectrum of DHI in a) KBr pellet and b) Chloroform solution.*
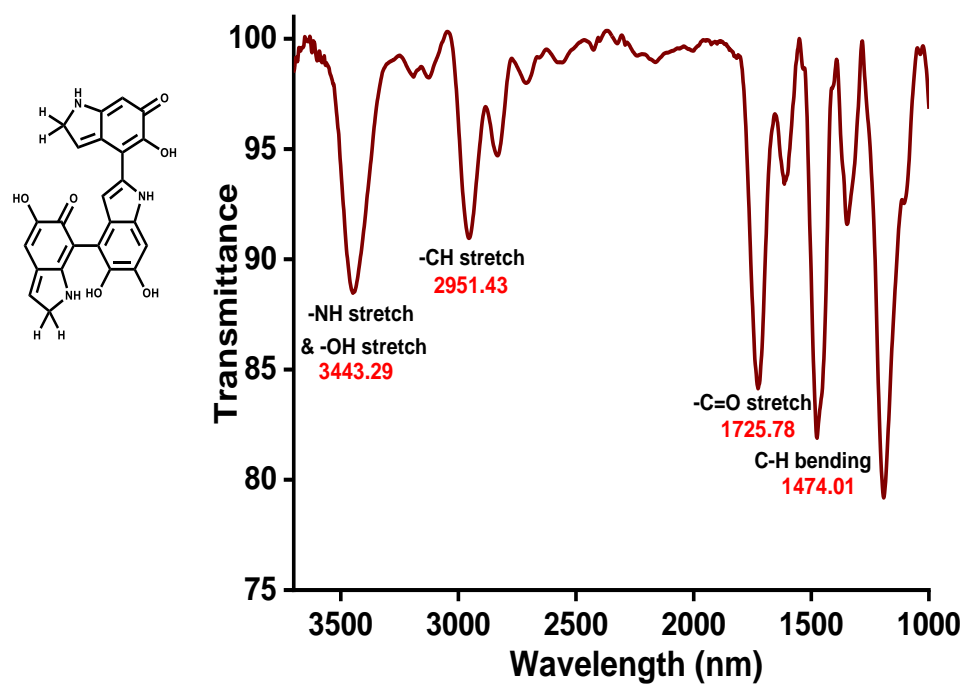
Appendix C8: *IR Spectrum of DHI-T in KBr pellet.*
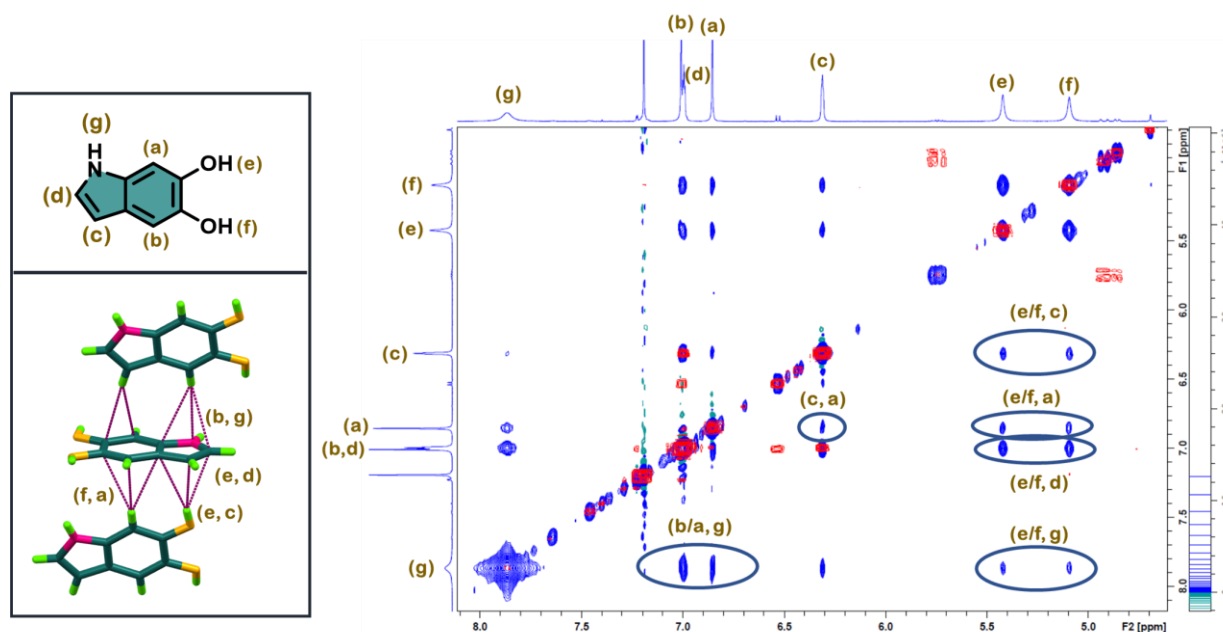
Appendix C9: *Shows the overlapped 2D 1H-COSY (red) and -NOESY (blue) NMR spectra of DHI in CDCl₃. The proximal hydrogen atoms having through space interactions are marked and are in line with the obtained crystalline packing motif of DHI crystal.*

2.6. Computational methods

2.6.1. Gaussian calculations

Single point energy and dipole moments were calculated at the CAMB3LYP/6-311g+(d,p) level of theory. All these computations were performed using the Gaussian 16 suite.[122]

2.6.2. Quantum theory of atoms in molecules (QTAIM)

The wave function generation for the DHI dimer orientations were carried out at CAM-B3LYP/6-311g+(d,p) level of theory using Gaussian16. Quantum theory of atoms in molecules (QTAIM) analyses[123] helps to understand the description of interatomic interaction in the single crystal X-ray structure. A bond is defined along the bond line between two nuclei, called a bond path, along which electron density is concentrated. The (3, -1) bond critical point (BCP) is a point along the bond path at the interatomic surface, where the shared electron density reaches a minimum. (3, +1) ring

critical point (RCP) and (3, +3) cage critical point (CCP) represents critical points in the ring and cage respectively where the electron density is minimum. The physical characteristics of the critical points [the electron density at BCP, RCP and CCP, $\rho(r)$, and its Laplacian, $(\nabla^2\rho)$ reveal the approximate measure of the amount of electron density built up in the bonding region and as such could be taken as characteristic of the bond. When $(\nabla^2\rho<0)$ there is a depletion of electronic charge in the internuclear region and it indicates a closed shell interaction. Using the AIMALL software package, the electron density was integrated over atomic basins according to the quantum theory of atoms in molecules using PROAIM, and thus the BCP, RCP, CCP data and the molecular graphs were obtained.

2.6.3. Hirshfeld analysis

Important intermolecular interactions within the structure of DHI were identified through Hirshfeld surface analysis using CrystalExplorer17. The Hirshfeld surface[124] is defined as a set of points in 3D space where the ratio of promolecule and procrystal electron densities is equal to 0.5. The exploration of intermolecular contacts is provided by mapping normalized contact distances (d_{norm}), which is a function of a closest distance from the point to the nuclei interior (d_i) and exterior (d_e) to the surface as well as on the van der Waals radii (r_{vdw}). 2D fingerprint plots derived from the Hirshfeld surface analyses, by plotting the fraction of points on the surface as the function of d_i and d_e, provides a visual summary of intermolecular contacts within the crystal.

2.6.4. TheoDORE analysis

The excitations of DHI dimers D1, D2, D3 and D4 at the DFT optimized structure were analyzed using TheoDORE.[57],[101] The parameters used to investigate the excited state characteristics are participation ratio (PR), mean position (POS) of initial orbital (hole) and final orbital (electron), and charge transfer character

(CT). The magnitude of PR relates to the number of fragments participating in the excitation; hence, in our investigation, the PR ranges from 1 to 2. POS provides the mean position of hole and electron for a particular excitation. Charge transfer states and delocalized Frenkel states show POS = 1.5. If the Frenkel state is localized on monomer A, then POS = 1, and if localized on monomer B, POS = 2, for a dimer AB. Finally, CT is related to the total weight of configurations where initial and final orbitals are situated on different fragments. A CT value of 1 denotes the presence of a charge-separated state, and CT = 0 refers to Frenkel states.

2.6.5. Symmetry adapted perturbation theory (SAPT)

SAPT(0) analysis was employed to determine the non-covalent interaction energies of dimer molecules.[125] The SAPT module of the psi4 code was employed, with jun-cc-pVDZ basis set. SAPT(0) calculations provide the contributing components of interaction energy. The results obtained from SAPT(0) analysis is a second order perturbation expansion constituting first order electrostatic and exchange energy parts and second order dispersion, induction and their exchange counterparts as the perturbation terms.

$$E_{\text{int}}^{Sapt(0)} = E_{elc}^{(1)} + E_{ex}^{(1)} + E_{ind}^{(2)} + E_{ind-ex}^{(2)} + E_{dis}^{(2)} + E_{dis-ex}^{(2)}$$

Chapter 3

Metastable Chiral Azobenzenes Stabilized in a Double Racemate

Abstract

Self-assembly of chiral organic chromophores garners huge significance owing to the abundance of supramolecular chirality found in natural systems. We report an interdigitated molecular organization involving axially chiral twisted octabrominated perylenediimide (OBPDI) transferring chiral sense to achiral aromatic moieties. The two-component crystalline architectures of OBPDI and electron rich aromatic units were facilitated through π-hole$\cdots\pi$ based donor-acceptor interactions and the charge transfer characteristics in the ground and excited states of OBPDI cocrystals were established through spectroscopic and theoretical techniques. The OBPDI cocrystals entailed a remarkable homochiral segregation of P and M enantiomers of both the molecular entities in the same crystal system to render twisted double racemic architectures. Synergistically engendered cavities with stored chiral information of twisted OBPDI stabilized higher energy P/M enantiomers of trans-azobenzene through non-covalent interactions.
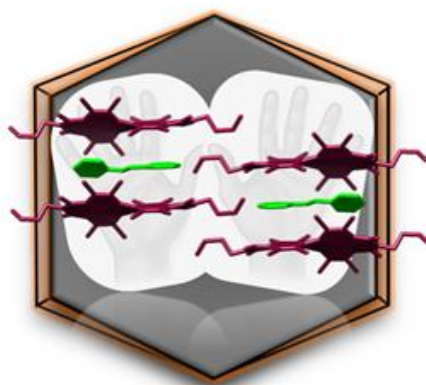
3.1. Introduction

Chirality or "handedness" in supramolecular systems have an intimate role in the organized functioning of biological, chemical and physical systems.[126]–[128] Life prefers to exist as single-handed chiral superstructures, which are believed to have originated from a racemic prebiotic world through the breakage of mirror symmetry.[129],[130] Integrating the principles of chirality and host-guest chemistry has always ignited the scientific curiosity for the development of bioinspired materials and in drug research.[131] In contrast to the long-term requirement to produce enantiopure organic materials, racemic systems have garnered immense significance in recent years owing to the ease of crystallization and onset of benign properties, when compared to the pure enantiomers.[132] Since Pasteur's first observation of enantioselective crystal formation from a racemic solution, termed conglomerates,[133],[134] multifarious crystalline packing arrangements emanating from racemic mixtures have been reported (Scheme 3.1).[135]–[137] Racemic crystallographic technique, since the first theoretical prediction in 1995,[138],[139] has been widely applied for protein structure determination and structural elucidation of nucleic acids in the past decade.[139],[140]

A crystalline supramolecular assembly having two or more diverse molecules bound together by various non-covalent interactions, namely the cocrystals, hold tremendous potential to generate novel functions that ensue from the synergistic effects of the constituent components. Racemic (A+A-) molecular units in the presence of additional chiral/achiral (B+/B) agents have a general tendency to retain the inherent chiral/achiral nature of the added co-formers while assembling either into the same crystal system (diastereomeric, Scheme 3.1a and 3.1f;i) or separate out as different crystalline units (Scheme 3.1b and 3.1e).[141]–[148] In another case, the introduction of a racemic co-former to a racemic host solution has been observed to result in double racemic cocrystal where, each entity retain their own mirror symmetry in the same crystal system (Scheme 3.1d). Yet, a twisted double racemic co-crystalline motif
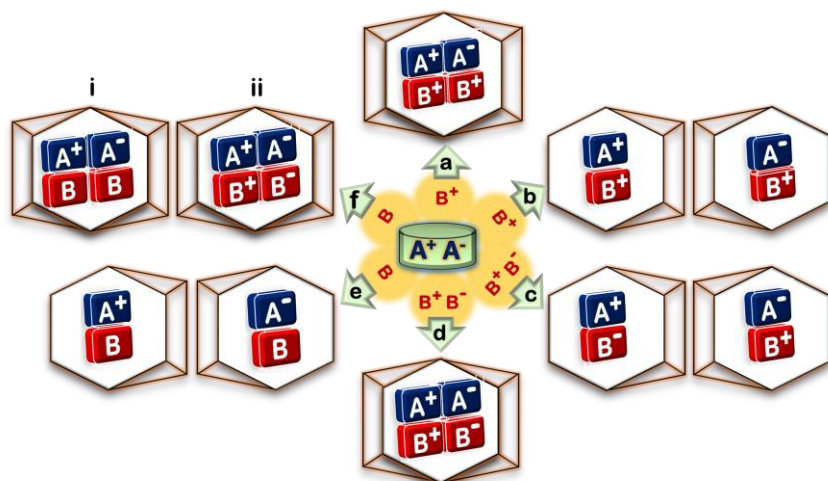
Scheme 3.1: *Representative outcome of crystallization of racemic (A+A-) mixture with: chiral (B+), racemic (B+B-) and achiral (B) guest resulting in a*,b) diastereomeric,*[141],[142] *c) kryptoracemate,*[143],[149] *d) double racemic,*[143],[144] *e) conglomerate,*[145],[146] *f;i) racemic cocrystal*[146] *and f;ii) double racemic cocrystal. *Unknown motif.*

originating from a racemic host through chiral induction in achiral guests has received less attention (Scheme 3.1f;ii). Our persistent efforts towards comprehending the origin of anomalous crystalline architectures of contorted polyaromatics and twisted bichromophores motivated us to exploit racemic octabrominated perylenediimide (OBPDI) crystal to produce mirror symmetry in achiral guests such as trans-azobenzene.[4],[35],[93],[94] Bay halogenated perylenediimides (such as OBPDI) exhibit conformational chirality generated by the steric induced twisting of the π-core and, encompass a significant activation barrier ($\Delta G^{\ddagger}_{303\ K}$~98 kJ/mol for chloro-substituted perylenediimide) for the interconversion between the P/M axially chiral enantiomers.[150]–[152] Cavities with tunable inner size in the OBPDI crystal system, effected through noncovalent interactions between the electron deficient OBPDI and electron rich benzenoids, retained the chiral character of twisted OBPDI host, thereby facilitating the trapped achiral guest molecules to imbibe the stored chiral sense (Figure 3.1). The double racemic OBPDI cocrystals thus obtained, engineered a supramolecular organization leading to the enantioselective ordering of the
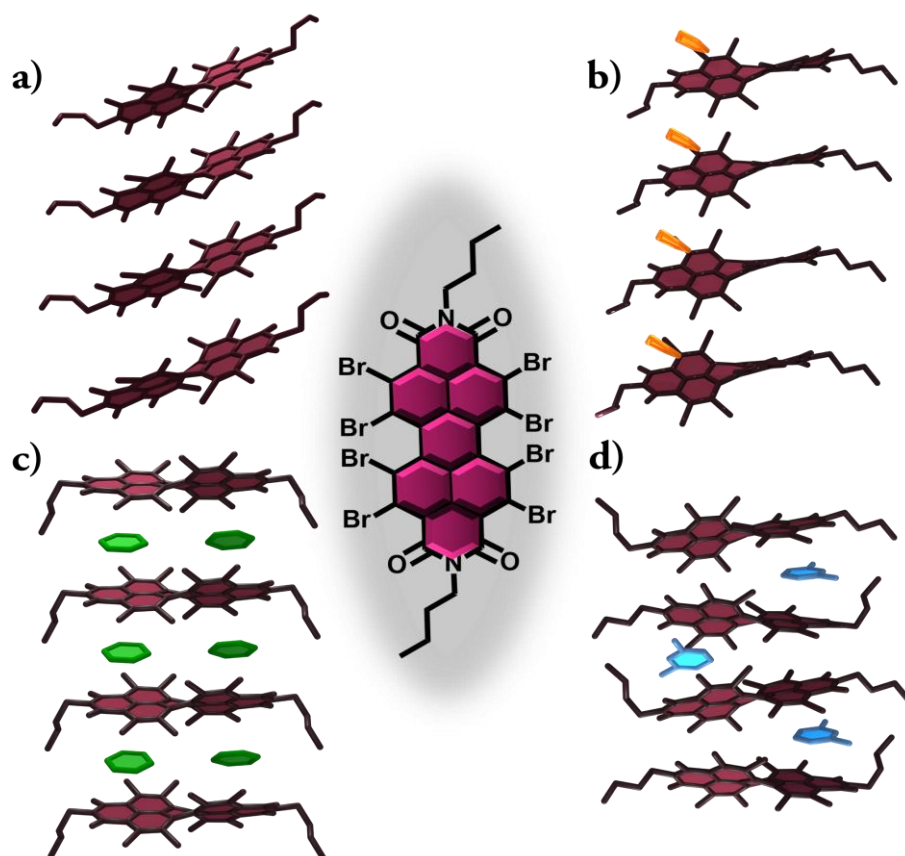
Figure 3.1: *Crystal packing of OBPDI in a) DCM-hexane, b) THF, c) benzene, toluene,** o-xylene** and d) m-xylene, p-xylene,** mesitylene.** (Representation of only one enantiomer is given for clarity in a-d. **Indicates packing structures are provided in figure 3.3.)*

interdigitated π-stacks of the two constituent chromophores in the same crystal system (Scheme 3.1f;ii). Segregating the co-enantiomers of the host-guest mixed stacks as two different crystals, representative of a stacked conglomerate assembly, embody the finest manifestation of chiral resolution, but is not realized herein. Nevertheless, continuous stacking of homochiral co-entities with transfer, amplification and memorization of racemic information materialized here can be a headway towards achieving the challenging task. The OBPDI-benzenoid double racemic cocrystals opened a possibility to generate twisted P/M configurations of azobenzene (AZO), having high energy, which are stabilized through non-covalent interactions in the crystal. The higher energy enantiomers of AZO are achieved solely from the influence of host-guest interactions, and hence contributing partially to an emergent idea of gaining the activation energy for the trans-cis isomerization of AZO by other means

such as mechanical force, electrical energy etc.[153]–[156] instead of the usual requirement of photoactivation. But, lack of enough space in the synergistically generated cavity inside the crystal system of OBPDI host, perhaps, hindered further rotation of the trapped AZO conformation to the cis form. Nevertheless, the twisted AZO conformation provided insights into the favorable pathway an AZO molecule tend to adopt, when it contracts extra energy from an external source and begins to undergo conformational change thereby emerging as an effort to shed light into the age-old debate[157]–[163] regarding the mechanism behind trans-cis cycle of azobenzene.

3.2. Synthesis and characterization

Octabromoperylenediimide (OBPDI) was synthesized and characterized as per previous literature (Scheme 3.2).[164]

1 Br$_2$, Con.H$_2$SO$_4$,I$_2$,110°C
2 DBH,Con.H$_2$SO$_4$ 110°C
3 N-Butylamine,DCM,PBr$_3$
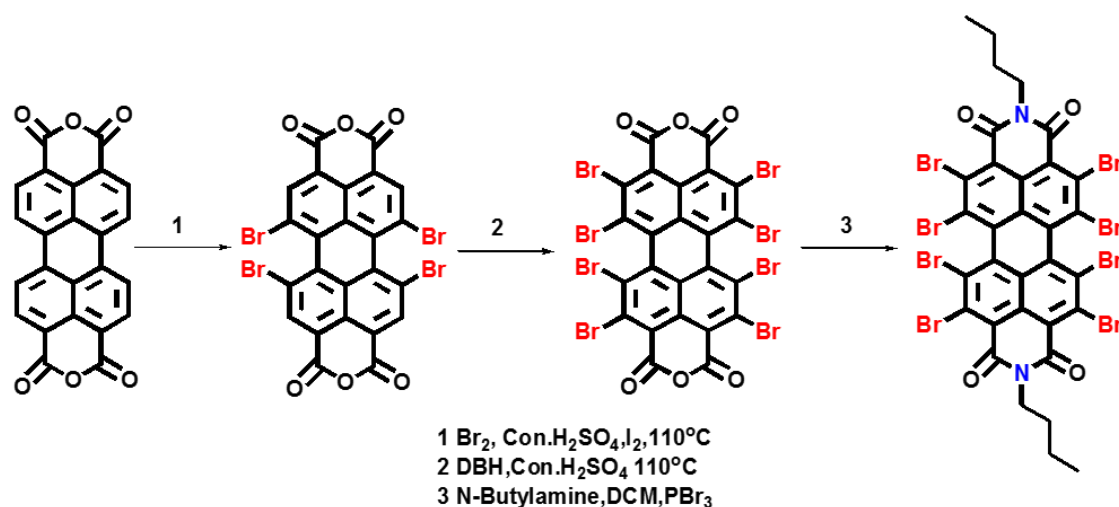
Scheme 3.2: Shows the synthesis of OBPDI.

3.2.1. Synthesis of 1,6,7,12-tetrabromoperylene-3,4,9,10-tetracarboxylic dianhydride (PTCDA-Br$_4$)

In a 250 ml round-bottom flask, 2.5 g of perylene-3,4,9,10-tetracarboxylic dianhydride (PTCDA) was stirred with 100 ml of concentrated sulphuric acid for 5 hours. Catalytic amount of elemental iodine was added and the reaction mixture was heated to 110 °C.

4.4 equivalence of elemental bromine was added dropwise into the reaction mixture, to synthesize PTCDA-Br$_4$. The reaction mixture was refluxed for 24 hours. After 24 hours, the product was precipitated by pouring the reaction mixture into crushed ice. The resultant precipitate was filtered through a Buchner funnel, washed with water and methanol. The solid was dried in hot air oven to yield PTCDA-Br$_4$ as red solid. Owing to the insolubility of the compound, it was taken for next step of synthesis without any characterization.

3.2.2 Synthesis of 1,2,5,6,7,8,11,12-octabromoperylene-3,4,9,10-tetracarboxylic dianhydride (OBPDA)

1.5 g of PTCDA-Br$_4$ was weighed into a 250 ml round-bottom flask. 50 ml of Conc. H$_2$SO$_4$ was added and stirred for 15 minutes at room temperature. The temperature was then raised to 110 °C, 1.5 g (5 mmol) of DBH (1,3-dimethyl-5,5-dibromohydantoin) was added in portions over a period of 30 minutes. The reaction mixture was refluxed for 24 hours. After 24 hours, the product was precipitated by pouring the reaction mixture into crushed ice. The resultant precipitate was filtered through a Buchner funnel, washed with water and methanol. The solid was dried in hot air oven to yield OBPDA as red solid. Yield = 70 %. Melting Point > 300 °C.

^{13}C NMR (125 MHz, CDCl$_3$, TMS): 156.55, 135.06, 133.04, 131.31, 128.27, 127.88, 120.22

HRMS (ESI): m/z calculated for C$_{24}$Br$_8$O$_6$ [M + Na]$^+$: 1046.4852, found: 1046.4858

3.2.3. Synthesis of 1, 2, 5, 6, 7, 8, 11, 12-octabromo perylene-3, 4, 9, 10-tetracarboxylic diimide (OBPDI)

OBPDA (250 mg) was taken in a 100 ml round-bottom flask, 30 ml of DCM was added. It was stirred for 10 minutes at room temperature. N-Butylamine (2.5 eq) was added dropwise, refluxed for 2 hours. After 2 hours PBr$_3$ (1eq) was added and further refluxed for 1 h. The reaction was cooled to room temperature and 100 ml of water was added. Aqueous layer was separated using DCM. The organic layer was collected

and solvent evaporated under reduced pressure. The crude mixture was purified by column chromatography with DCM:hexane (1:1) Yield=70%. Melting point >300 °C.

¹H NMR (500 MHz, CDCl₃, ppm): δ = 4.27-4.21 (m, 2H), 4.17- 4.12 (m, 2H), 1.72- 1.66 (m, 4H), 1.44-1.39 (m, 4H), 0.94 (t, J =7.5, 6H).

¹³C NMR: (125 MHz, CDCl₃, TMS): δ = 160.10, 133.42, 132.78, 132.12, 127.60, 125.83, 121.72, 42.29, 31.06, 20.64, 13.56.

HRMS (ESI): m/z calculated for $C_{32}H_{18}Br_8N_2O_4$ [M + Na]⁺: 1156.7283, found: 1156.7397.

3.3. Results and discussions

The crystallization of OBPDI from aliphatic (DCM: hexane, THF) and aromatic (benzene, toluene, o-xylene, p-xylene, m-xylene, and mesitylene) solvents yielded deep red colored needle shaped crystals (Figure 3.2, Table C-3.1 in Appendix). Detailed analysis of the single crystals of OBPDI showed a slip-stacked chromophoric organization for the crystals derived from aliphatic solvents, denoted as OBPDI-Al (Figure 3.1a). The slip-stacked chromophoric arrangement was also observed in the previously reported OBPDI crystal[164] which was obtained from a mixture of chloroform and acetone, thereby corroborating the self-assembly pattern adopted by OBPDI-Al crystals (Figure 3.3). Contrastingly, crystals of OBPDI acquired from aromatic solvents (OBPDI-Ar) preferred face-to-face stacking arrangement with the intercalation of solvent molecules between the twisted π-core of OBPDI moieties. Among the OBPDI-Ar crystals (Figure 3.1), two molecules of benzene, toluene and o-xylene respectively were trapped between the OBPDI cores whereas only one solvent molecule was incorporated during the crystallization of OBPDI from p-xylene, m-xylene and mesitylene. The observed variation in the number of encapsulated aromatic units could be attributed to an increase in the surface volume (V_w) from benzene (V_w=70.6 Å³) to mesitylene (V_w=109.0 Å³). A major attribute of the OBPDI-Ar cocrystals integrated with two aromatic units involved the induction of racemic sense

from OBPDI host to the nature of orientation of the guest molecules, driven by the interplay of several non-covalent interactions.
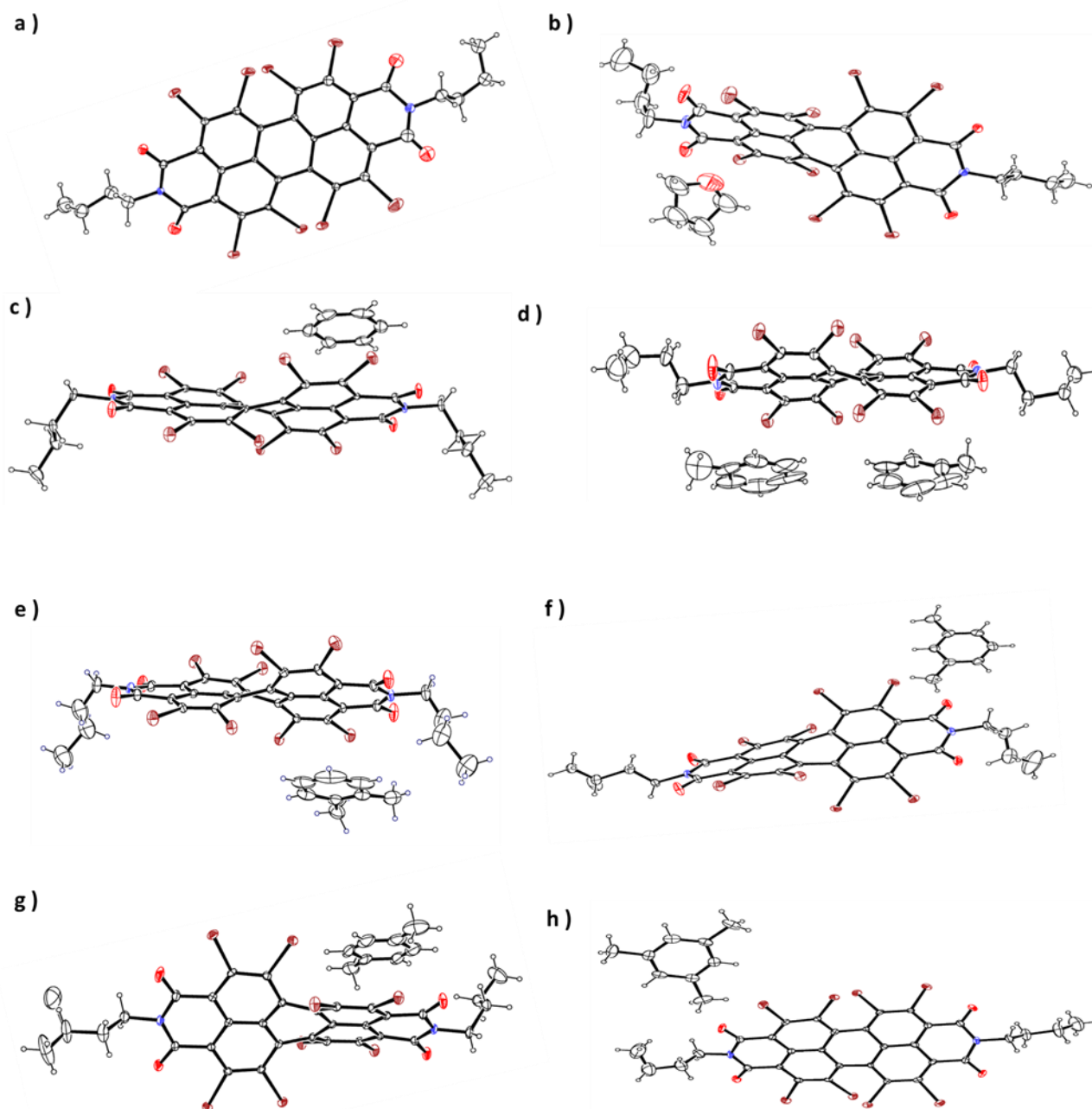
Figure 3.2: *ORTEP diagrams representing the molecular structure of OBPDI crystallized from a) DCM-hexane b) THF c) benzene d) toluene e) o-xylene f) m-xylene g) p-xylene and h) mesitylene with thermal ellipsoids drawn at the 50% probability level.*
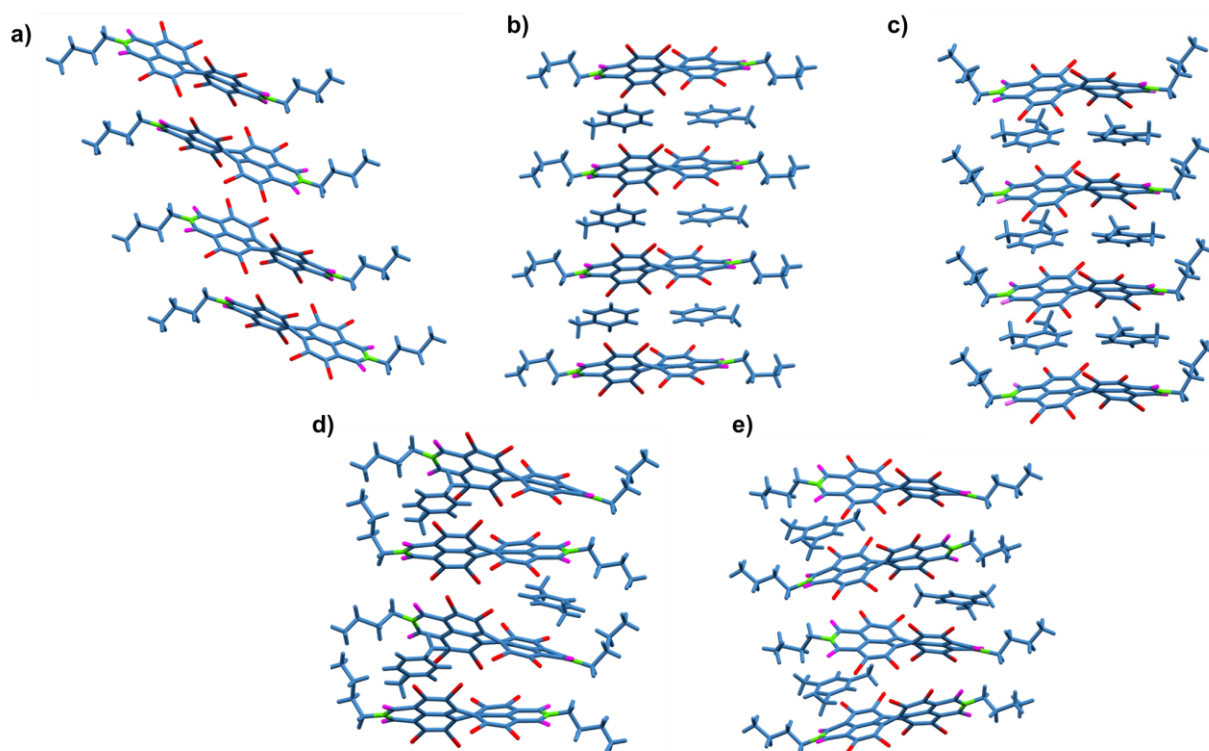
Figure 3.3: *a) Slip-stacked packing arrangement observed in the reported OBPDI crystal obtained from chloroform:acetone mixture and co-facial packing arrangement observed in OBPDI-Ar crystals obtained from b) toluene, c) o-xylene, d) p-xylene and e) mesitylene.*

Comprehensive analysis of the intermolecular interactions promoting the crystalline packing of OBPDI-Al crystals revealed a major role of type II Br···Br interactions[165] (θ_1=167.01°-170.40° & θ_2=86.62°-88.00°) in facilitating the 1-dimensional (1D) slip-stacked arrangement along the b-axis (Figure 3.4). The angles θ_1 and θ_2 in type II Br···Br interactions correspond to the angles in which the two interacting halogen atoms approach each other which, by definition, falls in the range of $\theta_1 \simeq 180°$ and $\theta_2 \simeq 90°$. In the OBPDI crystals derived from THF solvent, additional C-Br···O halogen bonding interaction between THF and OBPDI moieties ($d_{Br···O}$=3.27 Å) steered the hooking of THF molecule along the edge of the 1D crystal stack (Figure 3.3). Among the diverse non-covalent interactions in OBPDI-Ar cocrystals, π-hole···π donor-acceptor type interactions[34] ($d_{\pi-hole···\pi}$=3.39-3.58 Å, b-axis) between the OBPDI core and aromatic scaffold of respective guest molecules, and type I Br···Br interactions orchestrated an interdigitated columnar packing arrangement
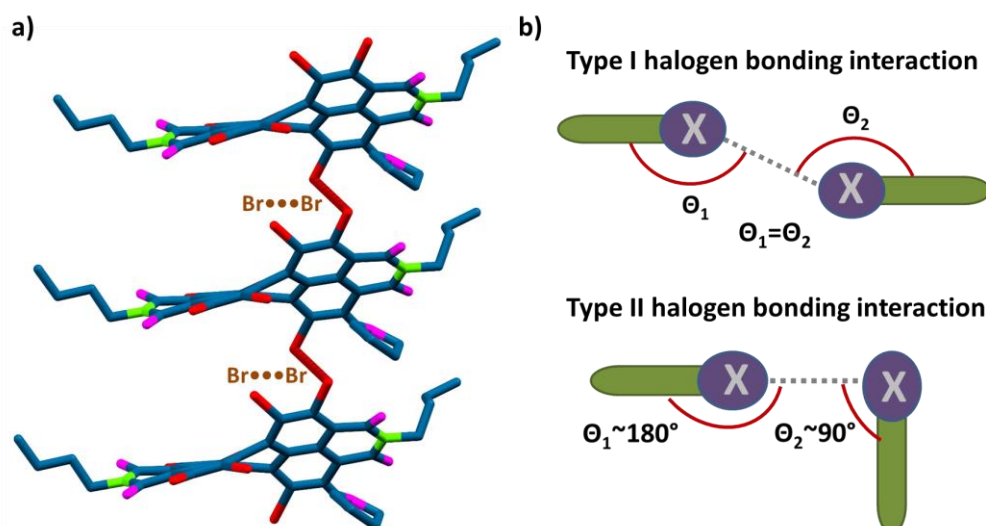
Figure 3.4: *a) Representative image of type II Br⋯Br interactions along 1D in the OBPDI-Al crystals and b) Schematic representation of type I and type II dihalogen interactions.*

(Figure 3.5). While, C-Br⋯O halogen bonding interaction between laterally displaced OBPDI molecules fabricated a 2D corrugated sheet type arrangement (Figure 3.5) in both OBPDI-Al and OBPDI-Ar crystals. Bader's quantum theory of atoms-in-molecules (QTAIM) analysis offered further insights into the notable intermolecular interactions that defined the disparate crystalline assembly of OBPDI-Al and OBPDI-Ar cocrystals (Figure 3.6).[123] QTAIM analysis provided atomic level perceptions about the crystalline assembly of OBPDI-Al derivatives and revealed the major roles played by Br⋯Br halogen bonding, π⋯π and C-H⋯H-C interactions in facilitating the slip-stacked organization in OBPDI-Al crystals. While, π-hole⋯π interactions in conjunction with Br⋯Br and C-H⋯H-C interactions directed the cofacial packing of OBPDI-Ar cocrystals. Furthermore, the synchronized arrangement of π-hole⋯π interactions, Br⋯Br and C-H⋯H-C interactions concocted well-defined cavities in the crystal (Figure 3.7).

Further, Hirshfeld surface (HS) analysis[39],[124] provided insights into the driving forces that transformed the slip-stacked assembly in OBPDI-Al crystals to cofacial packing motifs in OBPDI-Ar cocrystals. The lamellar, yet, slightly displaced packing mode in OBPDI-Al crystals could be attributed to a greater contribution from

C···H (%C···H=6.4-12.2) interactions (Table 3.1) while prominent C···C (%C···C=4.1-7.3) interactions, evolved as π-hole···π interactions in OBPDI-Ar, steered the cofacial packing assembly of OBPDI-Ar crystals. The π-hole···π interactions in OBPDI-Ar cocrystals ensued due to a donor-acceptor relation between electron deficient OBPDI host and electron rich guest molecules. Electrostatic surface potential (ESP) map of OBPDI core was generated at the B3LYP/6-311G+(d,p) level of theory to gain a deeper understanding about the electron density distribution in the host OBPDI moiety and thereby decoding the origin of the charge transfer characteristics of the π-hole···π interactions. ESP analysis carried out on monomer
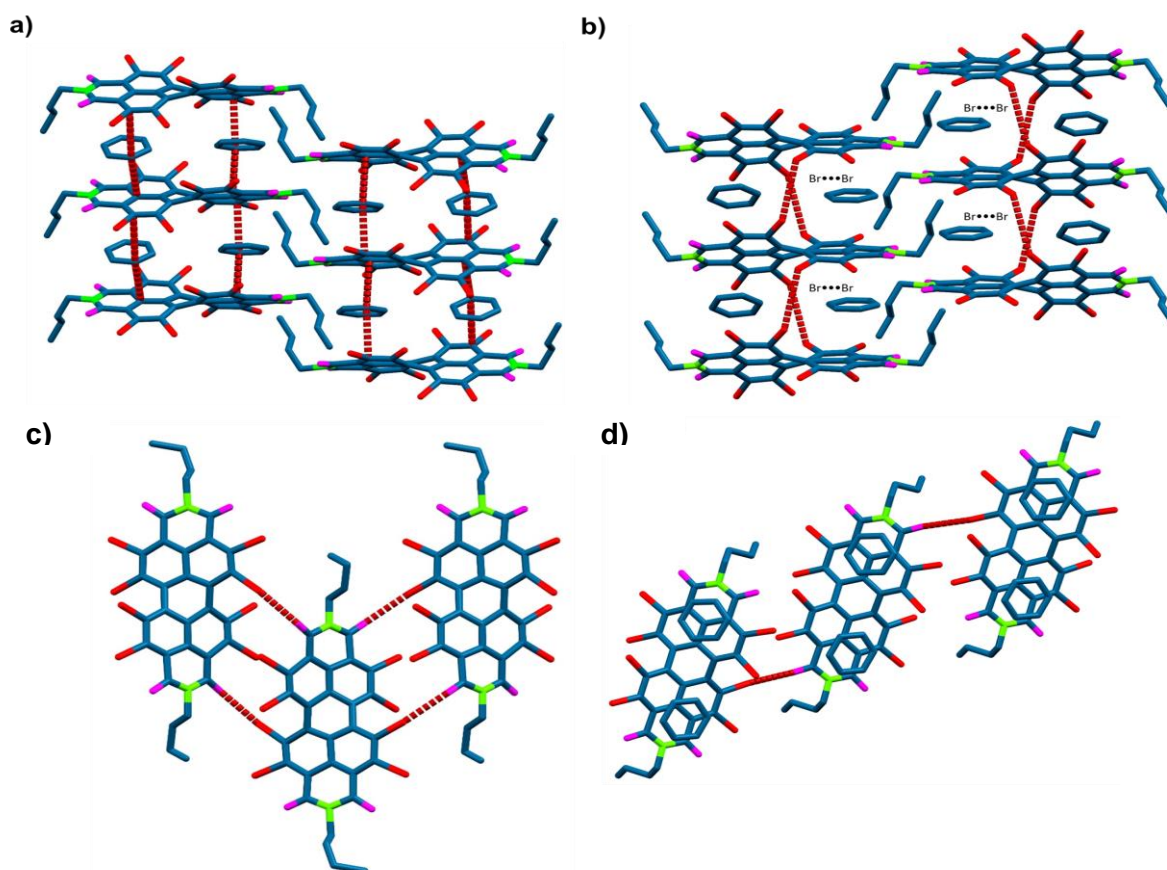
Figure 3.5: *Representative image of the observed a) π-hole···π interactions and b) Type I Br···Br interactions along 1-dimension (1D) in OBPDI-Ar crystals derived from benzene. Observed C-Br···O halogen bonding interactions along 2-dimension (2D) in c) OBPDI-Al and d) OBPDI-Ar crystals.*
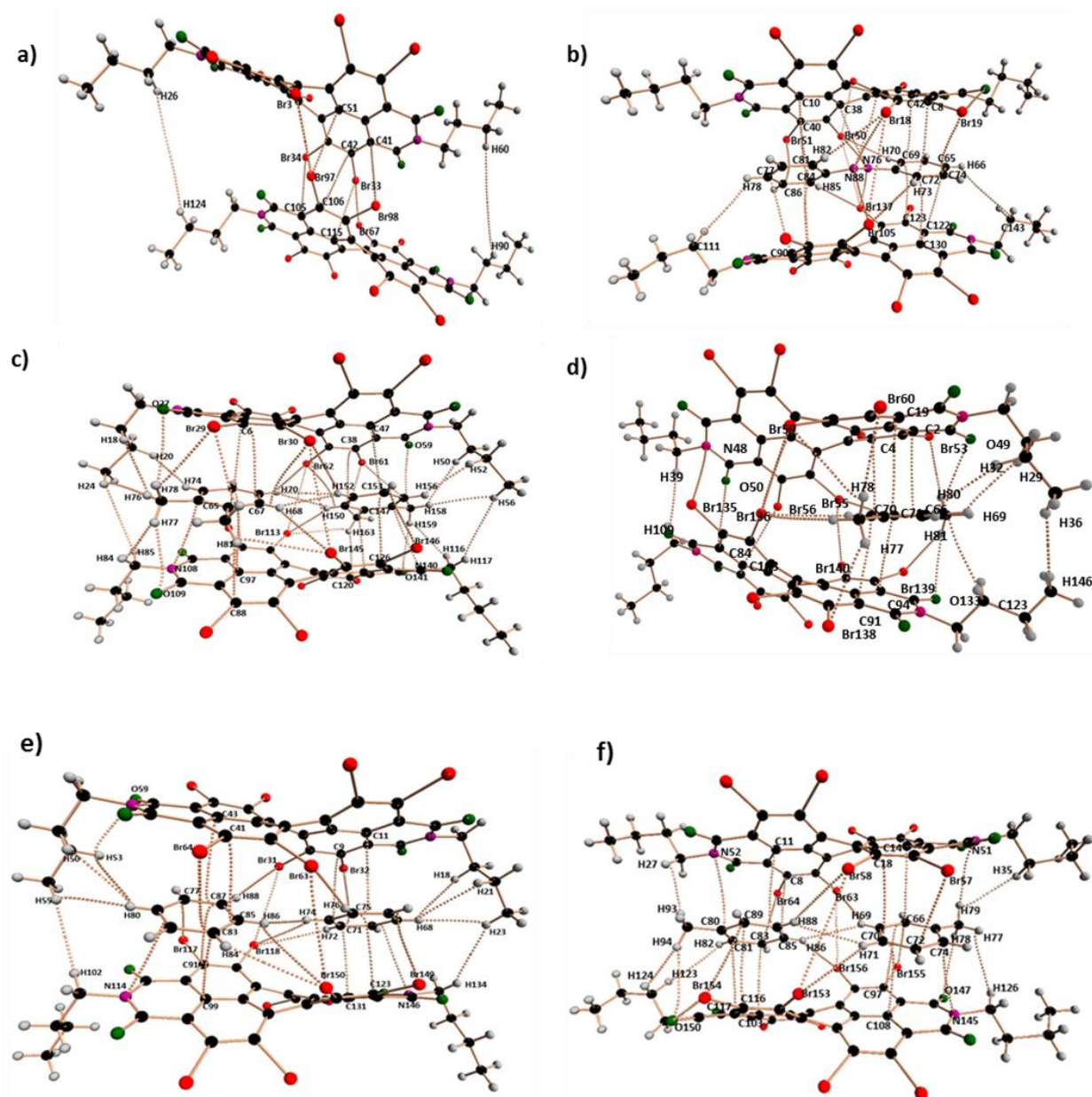
Figure 3.6: *QTAIM electron density maps of crystalline OBPDI dimers obtained from a) chloroform: acetone b) OBPDI-AZO1 c) o-xylene d) p-xylene e) benzene and f) toluene.*

OBPDI unit validated the highly electron deficient central π-hole/π-cavity in the OBPDI scaffold wherein more positive electrostatic potential region (blue region) was detected in OBPDI when compared to the non-brominated perylenediimide (PDI) analog and tetrabrominated PDI (PDIBr$_4$)[93] (Figure 3.8). The higher number of electron-withdrawing bromine atoms in OBPDI when compared to PDI and PDIBr$_4$
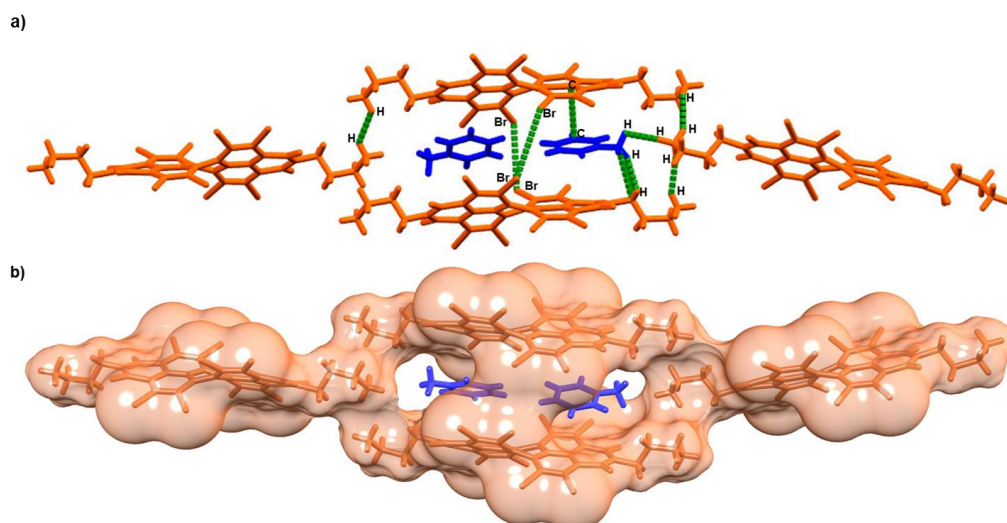
Figure 3.7: *Representative image of a) crystalline arrangement of the synergistically induced cavity in OBPDI-Ar cocrystals b) molecular surface model of the cavity.*

Table 3.1: *Values of %C···H and %C···C interactions obtained from Hirshfeld surface analysis.*

Entry	%C···H	%C···C
Chloroform:acetone	12.2	1.6
DCM:hexane	10.6	1.7
THF	6.4	1.3
benzene	9.2	7.3
toluene	11.0	6.6
o-xylene	9.2	6.7
p-xylene	10.8	7.2
m-xylene	11.6	5.4
mesitylene	11.4	4.1
OBPDI-AZO1	8.4	7.6
OBPDI-AZO2	10.3	11

materialized a highly electron deficient core, signified by the more positive electrostatic potential region in the ESP map of OBPDI. Hence, the highly electron deficient OBPDI scaffold, mediated the donor-acceptor type π-hole···π interactions with the incoming guest units, to effect the unprecedented double racemic crystalline motif. The small benzenoid molecules which acted as electron rich reservoirs assisted in the inception of π-hole···π interactions resulting in a concomitant induction of
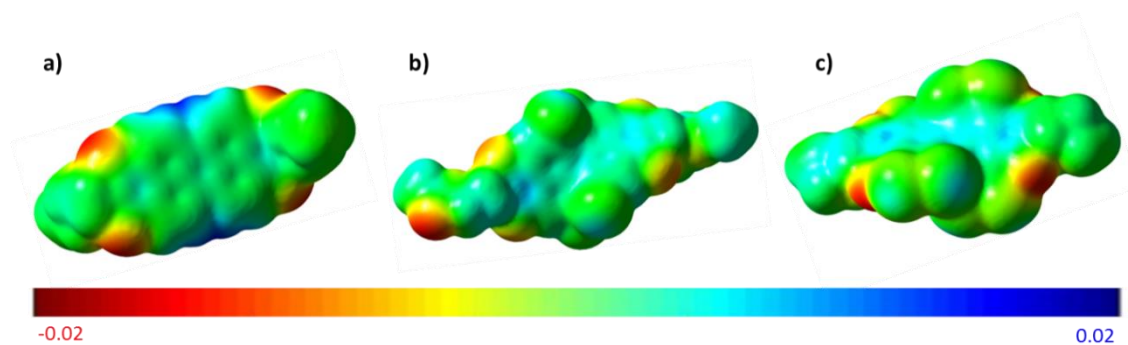
Figure 3.8: *Electrostatic surface potential (ESP) maps of a) PDI b) PDIBr$_4$ and c) OBPDI.*

twisted configuration of OBPDI and associated conformational chirality into the organizational mode of the incarcerated guests.

Rationale behind the slip-stacked and cofacial crystalline assembly in OBPDI-Al and OBPDI-Ar crystals respectively were explored on OBPDI dimers through potential energy surfaces (PES) engendered using density functional theory performed at B3LYP/6-311G++(d, p) level. The energetics of OBPDI dimer (generated from optimized monomer geometry) were evaluated at different stacking positions with respect to molecular displacements along the X, Y and Z axes (Figure 3.9a). Calculated PES of OBPDI dimer at X=4 Å to X=6 Å showed the favorable formation of
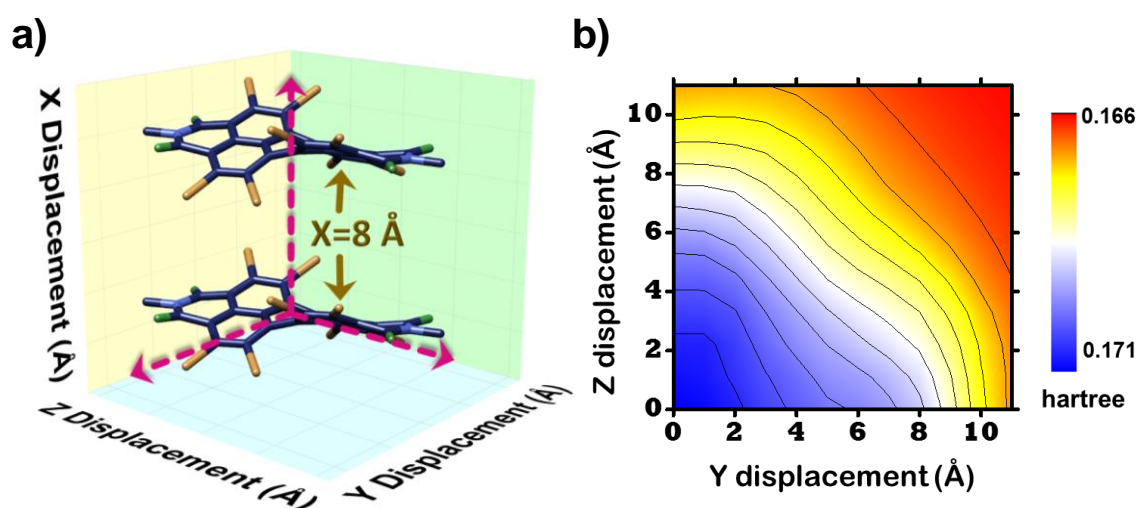
Figure 3.9: *a) Direction of molecular displacements along X,Y and Z axes performed on OBPDI-Ar model b) PES diagram of OBPDI showing interaction energy at X-axis displacement=8 Å.*
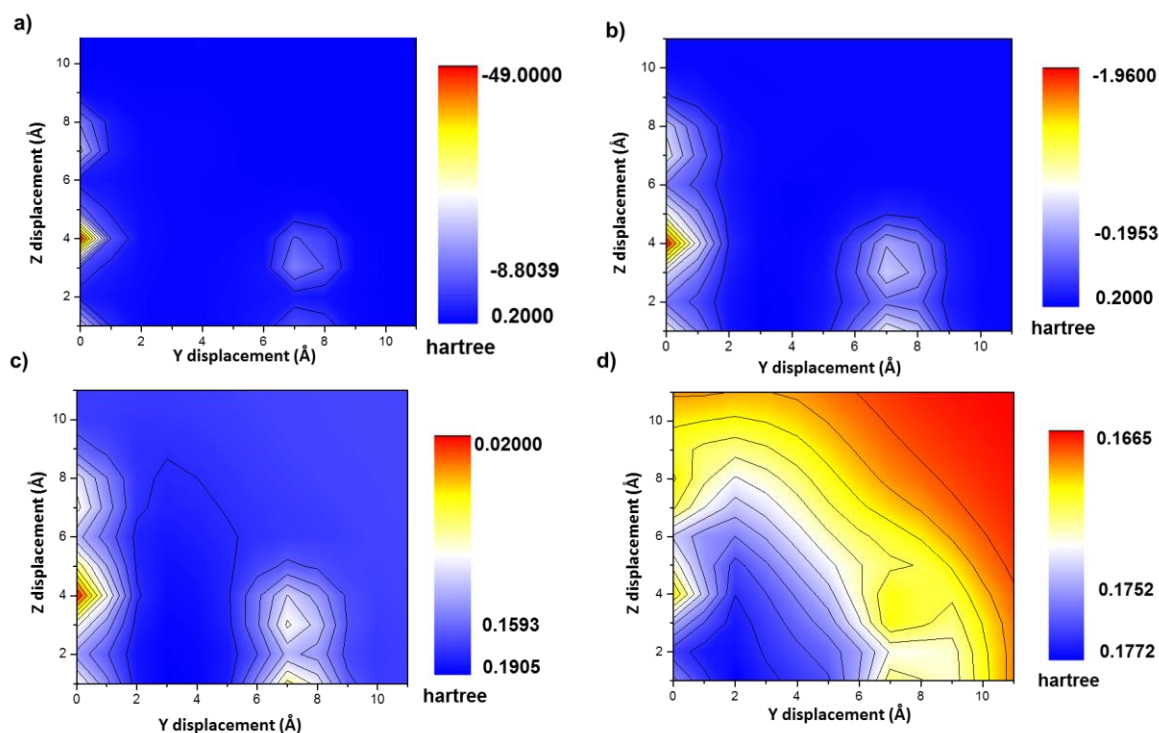
Figure 3.10*: Potential energy surface diagrams of OBPDI showing interaction energy along X-axis displacement at **a)** X= 4 Å **b)** X= 5 Å **c)** X= 6 Å **d)** X= 7 Å.*

slip-stacked packing arrangement as is seen in the OBPDI-Al crystals (Figure 3.10). At X=7 Å and X=8 Å, the PES scan indicated the energetic feasibility for cofacial stacking mode, thereby corroborating the packing in OBPDI-Ar crystal structures (Figure 3.9b & 3.10d).

Symmetry-adapted perturbation theory (SAPT0) analysis was employed to establish the stability of the observed crystalline assembly of OBPDI-Ar and OBPDI-Al crystals. SAPT(0) analysis (Table 3.2) provided a quantitative picture of the total interaction energy and the contributing non-covalent components (electrostatic, dispersion, induction and exchange repulsion).[98] A more negative value in the total SAPT(0) energy evaluated for the OBPDI-Ar dimer structures (E_{int}^{SAPT}~-62.35 kcal/mol) when compared to the OBPDI-Al dimer structures (E_{int}^{SAPT}~-24.45 kcal/mol) ascertained superior stability of the OBPDI-Ar dimer orientation. The observed greater stability of OBPDI-Ar dimer structures could be attributed to the compensative role of stabilizing electrostatic ($E_{elc}^{(1)}$~-28.20 kcal/mol) and dispersion energy ($E_{dis}^{(2)}$~-79.09 kcal/mol)

components over the destabilizing exchange repulsion ($E_{ex}^{(1)} \sim 50.66$ kcal/mol) towards the total interaction energy. The higher value of electrostatic energy in OBPDI-Ar dimer further verified the existence of π-hole$\cdots\pi$ charge transfer interaction between the host OBPDI and the entrapped aromatic guest molecules. While the higher contribution of dispersion energy in stabilizing the dimer systems of OBPDI-Ar cocrystals accounted for the close proximity between the aromatic solvents and the OBPDI molecule. In this regard, OBPDI evolved as a potential medium to selectively trap small aromatic molecules in the inherently generated voids.

Upon ascertaining the energetically favored facile generation of OBPDI-Ar double racemic cocrystals, we proceeded to exploit the chiral induction effect of OBPDI to generate P/M enantiomers of trans-azobenzene through conformational modulation. Cocrystallization of OBPDI and trans-azobenzene in 1:1 ratio from tetrahydrofuran in the presence of light yielded needle shaped crystals having C2/c space group, denoted herein as OBPDI-AZO1 cocrystal (Figure 3.11). As envisioned, π-hole$\cdots\pi$ donor-acceptor (D-A) interaction (Figure 3.11) drove the intercalation of trans-azobenzene in π-hole cages of OBPDI followed by transfer of chiral information to result in OBPDI-AZO1 double racemic cocrystal having D-A stacked assembly (Figure 3.12a and 3.12b). The P and M atropisomers of OBPDI and twisted azobenzene segregated as homochiral bichromophoric stacks in the same crystal system (Figure

Table 3.2. *Interaction energies[a] of representative OBPDI dimers from SAPT(0) jun-cc-pvdz calculations.*

Dimer	E_{int}^{SAPT}	$E_{elc}^{(1)}$	$E_{dis}^{(2)}$	$E_{ind}^{(2)}$	$E_{ex}^{(1)}$
OBPDI-Al	-24.45	-9.89	-31.44	-2.34	19.23
OBPDI-Ar	-62.35	-28.20	-79.09	-5.77	50.66
OBPDI-AZO1	-58.16	-21.22	-71.36	-3.96	38.39

[a]All energy values are provided in kcal/mol. E_{int}^{SAPT}=Total interaction energy; $E_{elc}^{(1)}$= Electrostatic; $E_{dis}^{(2)}$=Dispersion; $E_{ind}^{(2)}$=Induction and $E_{ex}^{(1)}$=Exchange repulsion energy.
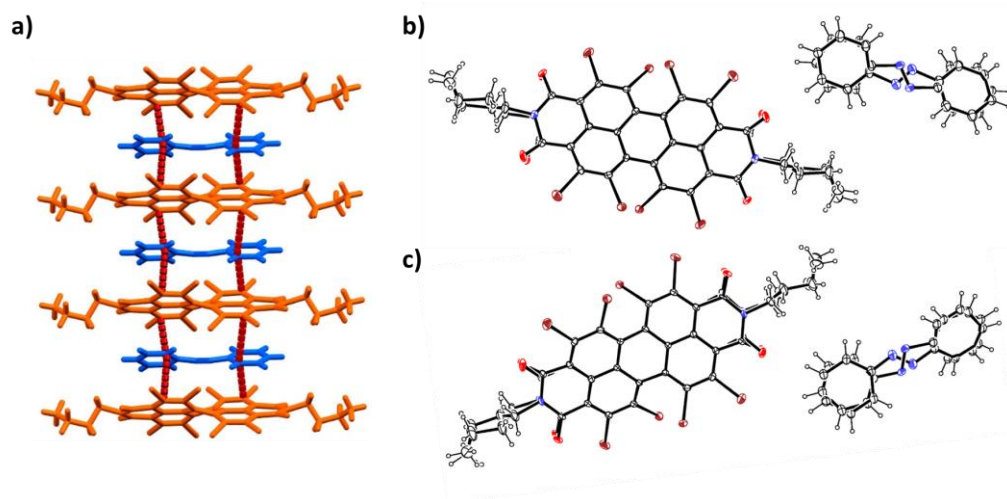
Figure 3.11. *a) Crystal assembly of OBPDI-AZO1 showing π-hole···π interactions; ORTEP images of b) OBPDI-AZO1 crystallized in the presence of light and c) OBPDI-AZO2 crystallized in dark conditions.*
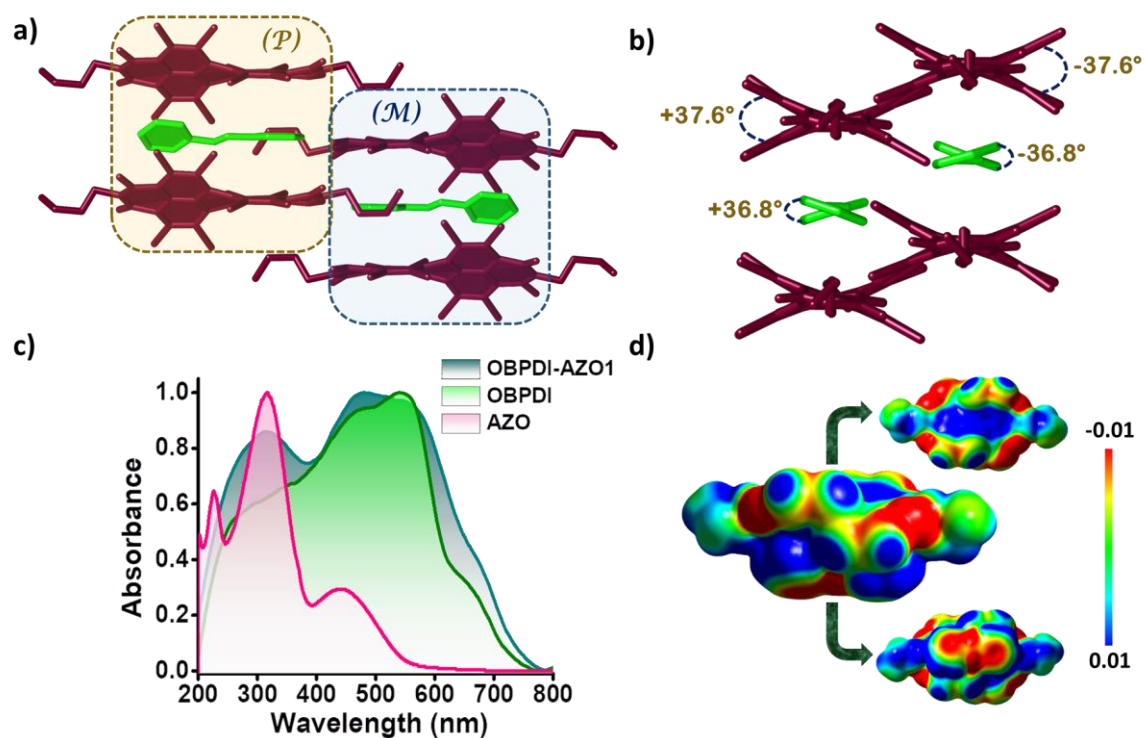
Figure 3.12: *a) Double racemic crystalline packing arrangement in OBPDI-AZO1 cocrystal highlighting (P) and (M) chiral orientations, b) view of crystal packing along (101) plane representing the dihedral angle of twisted azobenzene in OBPDI-AZO1 cocrystal, c) Kubelka-Munk diffuse reflectance spectra of OBPDI, AZO and OBPDI-AZO1 in the crystalline state and d) ESP map of OBPDI-AZO1: Arrows indicate views from the top (blue shaded OBPDI side) and bottom (red shaded AZO side) surfaces of the ESP map of OBPDI-AZO1 cocrystal.*

3.13). Evidences for the presence of charge transfer character in the ground and excited states of OBPDI-AZO1 cocrystal were verified through Kubelka-Munk diffuse reflectance and steady-state emission spectroscopic techniques, along with in-silico electrostatic surface potential (ESP) analysis. OBPDI-AZO1 cocrystal showcased broad absorption bands having characteristics of constituent OBPDI (λ_{abs}~470-545 nm) and AZO (λ_{abs}~315 nm) moieties and a ~3`0 nm red-shifted tail which could be ascribed to the charge transfer interaction between the host OBPDI and AZO guest constituents (Figure 3.12c). Similarly, the broad fluorescence emission spectral characteristics of OBPDI-AZO1 signified the presence of excited state charge transfer species with the most red-shifted band having ~28-30 nm Stokes shift when compared to OBPDI emission in the crystalline state upon photoexcitation at 450 nm (Figure 3.14). Comparison of the UV-Vis absorption spectrum and excitation spectrum of OBPDI-AZO1 collected at 643 nm indicated OBPDI emission (Figure 3.14) in the cocrystal. The ESP analysis performed on a D-A stack of OBPDI-AZO1 cocrystal revealed electron
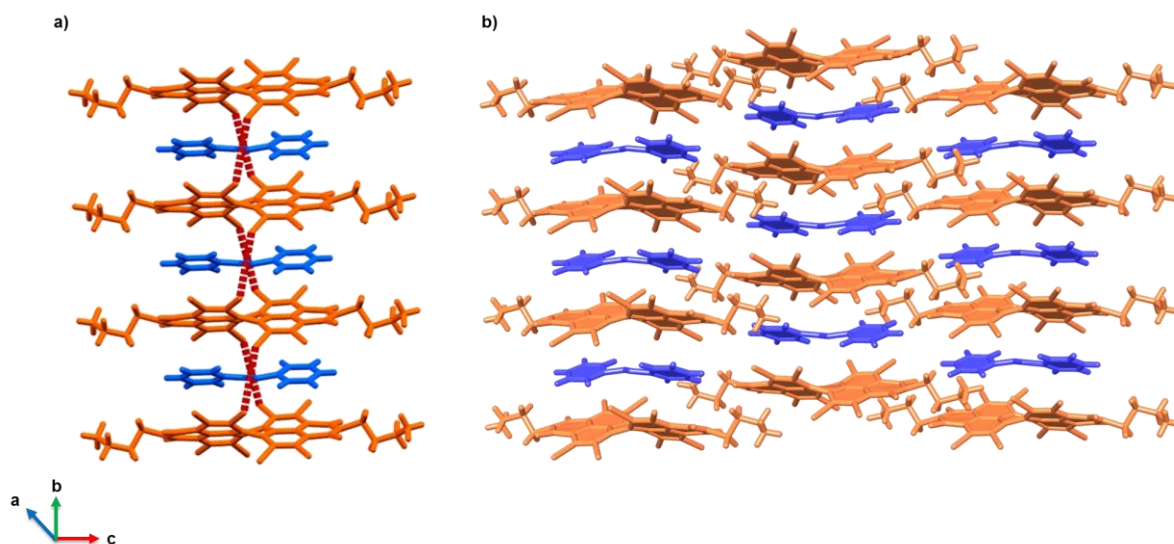
Figure 3.13: *Crystal assembly of OBPDI-AZO1 showing **a)** Type I Br···Br halogen bonding interactions and **b)** Molecular packing arrangement.*
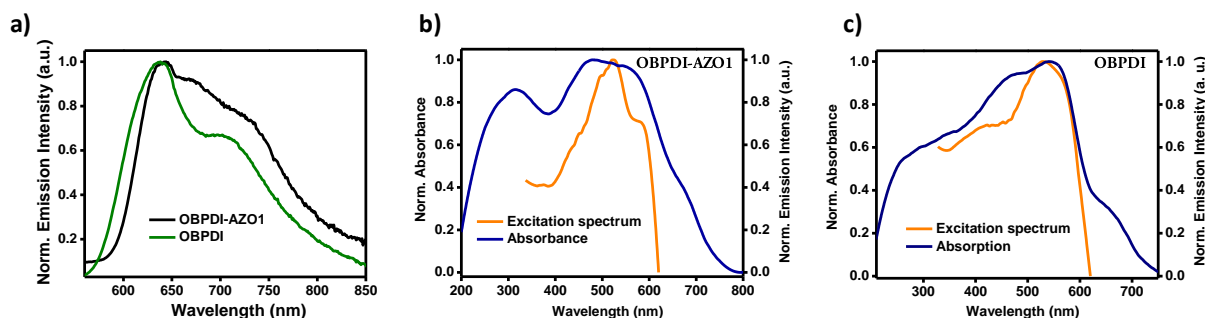
Figure 3.14: *a) Fluorescence emission spectra of representative OBPDI-AZO1 cocrystal and parent OBPDI crystal collected upon photoexcitation at 450 nm; Comparison of excitation spectrum and absorption spectrum of b) OBPDI-AZO1 at 640 nm fluorescence emission and c) OBPDI crystal at 636 nm fluorescence emission.*

deficient (blue) and electron rich (red) regions respectively on OBPDI and AZO units providing a well-painted picture of the nature of charge distribution in the cocrystal system (Figure 3.12d).

Interestingly, the formation of cocrystals with azobenzene was found to be characteristic of OBPDI derivative while PDI and PDIBr4 failed to serve as suitable acceptors (hosts) for AZO under similar conditions, despite, the inclination of PDIBr4 to attract benzene molecules as reported by Würthner and coworkers.[166] The stability of OBPDI-AZO1 cocrystal was validated through SAPT(0) analysis (Table 3.2) wherein major contributions from electrostatic ($E_{elc}^{(1)}$~-21.22 kcal/mol) and dispersion interactions ($E_{dis}^{(2)}$~-71.36 kcal/mol) facilitated the unique double racemic assembly as observed in OBPDI-Ar cocrystals. OBPDI-AZO1 cocrystal encompassed orientational disorder of the entrapped AZO units which could be attributed to "pedal motion" of AZO.[167],[168] The orientational disorder in OBPDI-AZO1 resulted from each trapped AZO unit adopting either of two conformations (Ab1 & Ab2) related by 2-fold rotation about the long axis of AZO molecules.[169] The near equivalent occupancy of Ab1 (φ=0.57)[170] and Ab2 (φ=0.43) conformations in OBPDI-AZO1 cocrystal at room temperature could arise due to N···π interaction of each AZO group to encapsulating OBPDI units (Figures 3.15 & 3.16). The twisted geometries of trapped azobenzene molecules revealed a dihedral angle of Φ_d~36.8° revealing a high energy

conformation when compared to trans (ΔE_1~140 kcal/mol)[171] and cis-azobenzene (ΔE_3~125 kcal/mol) as validated by single point energy calculations (Figure 3.17).
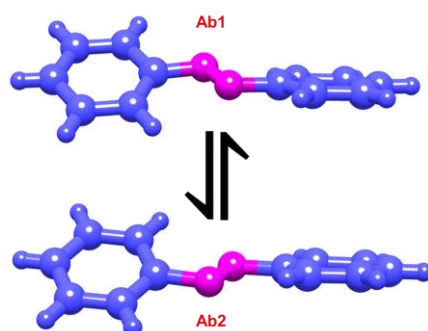
Figure 3.15: *The two conformations of AZO (Ab1 and Ab2) resulting from pedal motion.*
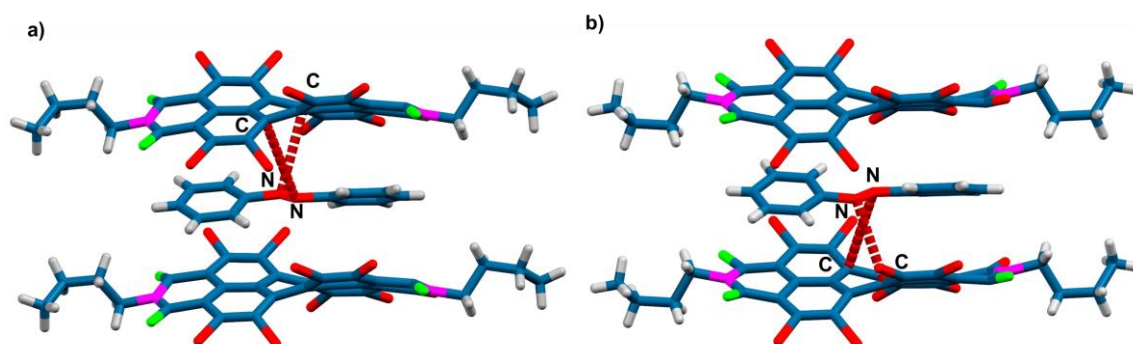
Figure 3.16: *Crystal packing of OBPDI-AZO1 showing N⋯π interactions observed in a) Ab1 and b) Ab2 conformations.*
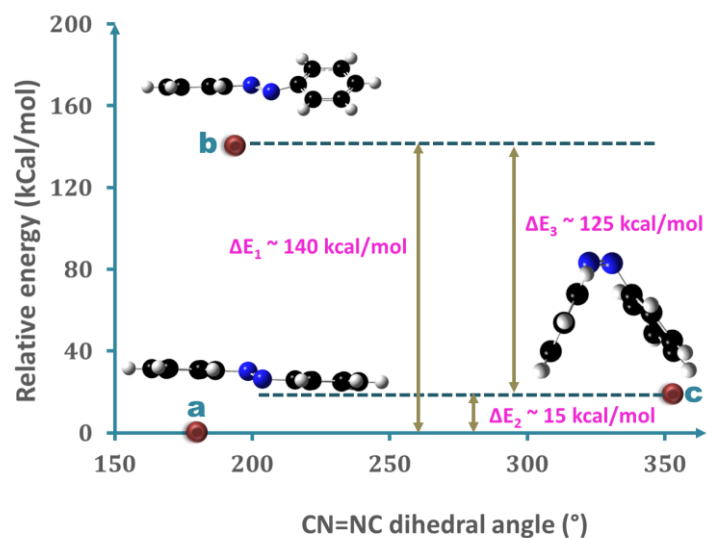
Figure 3.17: *Potential energy distribution of the different conformations of azobenzene; a) trans-azobenzene b) transition state orientation of azobenzene trapped in OBPDI-AZO1 crystal and c) cis-azobenzene.*

Azobenzene has been reported to follow two major paths during photoisomerization (rotation and inversion pathways) of which inversion mechanism is associated with one of the nitrogen atoms transitioning through sp hybridized state.[161] The N=N bond distance of skewed azobenzene in the OBPDI-AZO1 cocrystal was significantly lower ($d_{N=N}$~1.12 Å)[172] than trans-azo ($d_{N=N}$~1.24-1.26 Å) indicating a transition to sp state. Since trans-cis isomerization of azobenzene is a light driven process, OBPDI-AZO crystallization was also performed in the dark to annul all possible effects of light energy in twisting the structure of azobenzene. The cocrystals so obtained in dark conditions have been named as OBPDI-AZO2, in line with the OBPDI-AZO1 nomenclature for the cocrystals yielded in the presence of light (Figure 3.11). OBPDI-AZO2 cocrystals were also associated with decreased N=N bond length ($d_{N=N}$~1.19 Å) in the twisted azobenzene conformation,[172],[173] establishing the sole effect of OBPDI moiety in generating the higher energy AZO state without the requirement of external light energy sources to overcome the activation barrier. Thus, general tendency of AZO to decrease N=N bond distance upon conformational twisting could be an indication of more preference for the inversion pathway over the other isomerization modes. To the best of our knowledge, OBPDI-AZO epitomize a crystallographic evidence for the enumerable theoretical[159] and spectroscopic predictions regarding the most preferred pathway adopted for the conformational interconversions of azobenzene.

Evidence for the decrease in N=N bond distance in OBPDI-AZO1 cocrystal was examined using Raman spectroscopic analysis. Raman lines are considered to be the spectral fingerprint of a molecule by delivering vital evidences about bond distances from the vibrational features of the molecule. Raman spectroscopic analysis was carried out on the crystalline powder samples of OBPDI, AZO and OBPDI-AZO1 by photoexciting at 632.8 nm with an acquisition time of 5 s using a 50x objective. Raman spectrum (Figure 3.18) of OBPDI-AZO1 revealed the presence of vibrational band corresponding to N=N stretch centered at ~1453 cm^{-1} which is found to be upshifted

by 11 cm^{-1} when compared to the characteristic N=N stretch[174] of trans-azobenzene (~1442 cm^{-1}). Absence of a vibrational band corresponding to ~1453 cm^{-1} in the Raman spectrum of OBPDI corroborated the observed vibrational band centered at ~1453 cm^{-1} in OBPDI-AZO1 to be the upshifted vibrational peak of a typical N=N stretching mode of the azobenzene component. The increase in the N=N vibrational stretching frequency in OBPDI-AZO1 could be attributed to an upsurge in the N=N bond energy because of the decrease in N to N bond distance originating from the induced conformational twist of the azobenzene moiety in OBPDI-AZO1 cocrystal.

The increase in the N=N bond energy of AZO in OBPDI-AZO1 cocrystal is further substantiated through X-ray photoelectron spectroscopic (XPS) analysis wherein, change in the binding energy value of N1s peak provided significant evidences to the shift in hybridization of the nitrogen atoms. The XPS N1s core level spectrum of crystalline powder samples of OBPDI, AZO and OBPDI-AZO1 were recorded using Mg Kα X-ray source of 100 W power. Deconvolution of XPS N1s spectrum of OBPDI-AZO1 (Figure 3.18b) cocrystal revealed the presence of two N1s XPS peaks having binding energy values, E_b=403.99 eV and E_b=402.76 eV which pointed out to the presence of two nitrogen atoms in different chemical states. The N1s peak at a binding energy of 402.76 eV observed in the OBPDI-AZO1 XPS data closely overlapped with that of parent OBPDI crystal (E_b=402.76 eV). While, the binding energy value of AZO unit in OBPDI-AZO1 cocrystal shifted to higher magnitudes when compared to the trans-azobenzene (E_b=401.61 eV) molecule. The broad higher energy band observed for AZO N1s in the OBPDI-AZO1 cocrystal could be attributed to a combined effect of charge transfer interaction[175] and a possible transition of the nitrogen atom to sp state.[176]

Inquisitively, we proceeded to inspect any possibilities of photoinduced changes in the higher energy conformation of azobenzene trapped inside the OBPDI cavity by irradiating the OBPDI-AZO1 cocrystal with 318, 355 and 532 nm lasers of variable fluences. Exposure to laser pulses of powers ranging from 5 to 30 mW
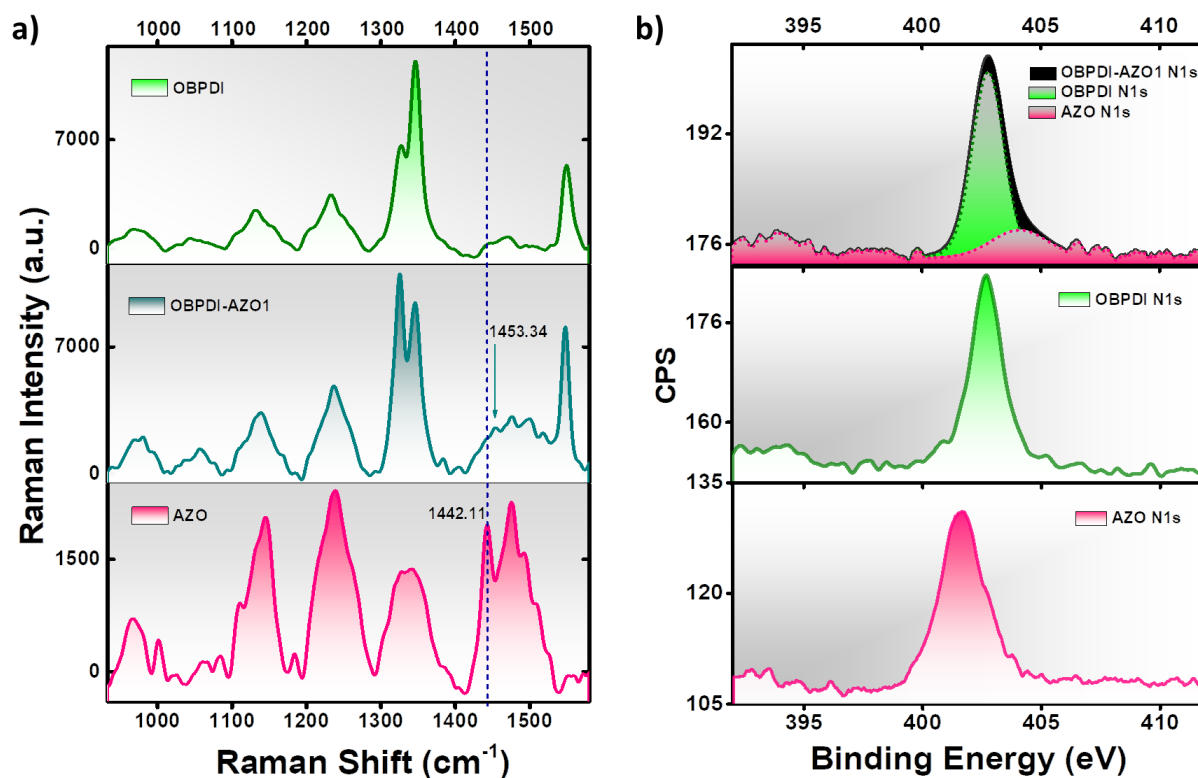
Figure 3.18: *a) Raman spectra of OBPDI, OBPDI-AZO1 and AZO measured in the crystalline powder state after photoexcitation at 632.8 nm; b) Core level N 1s XPS spectra of OBPDI-AZO1, OBPDI and AZO in the crystalline powder state.*

exhibited insignificant changes to OBPDI-AZO1 cocrystal as evinced from single crystal X-ray structure and vibrational analysis with Raman spectroscopy (Refer materials and methods for details, Figures 3.19-3.21).
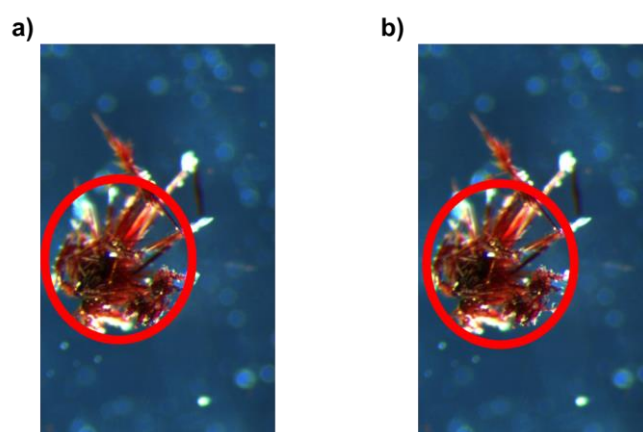
Figure 3.19: *Optical microscopy images of OBPDI-AZO1 a) before irradiation and b) after irradiation using laser with fluence of 30 mw and 318 nm wavelength for 90 minutes (red circle indicates the portion of laser irradiation).*
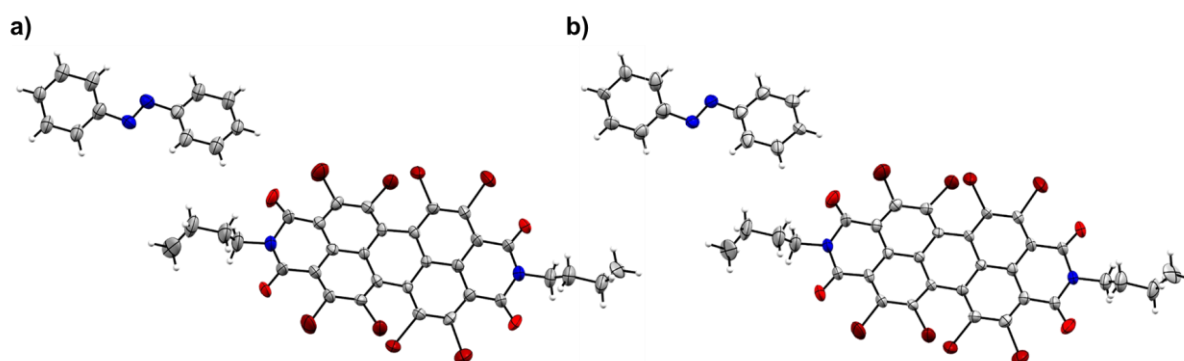
Figure 3.20: *ORTEP images of OBPDI-AZO1 a) before irradiation and b) after irradiation using 318 nm laser of 30 mW fluence for 90 minutes.*

Photostability of the OBPDI-AZO1 cocrystal could be attributed to the strong influence of π-hole···π interactions in retaining the cofacial crystalline order through inhibiting any conformational modifications to occur in the crystal lattice.
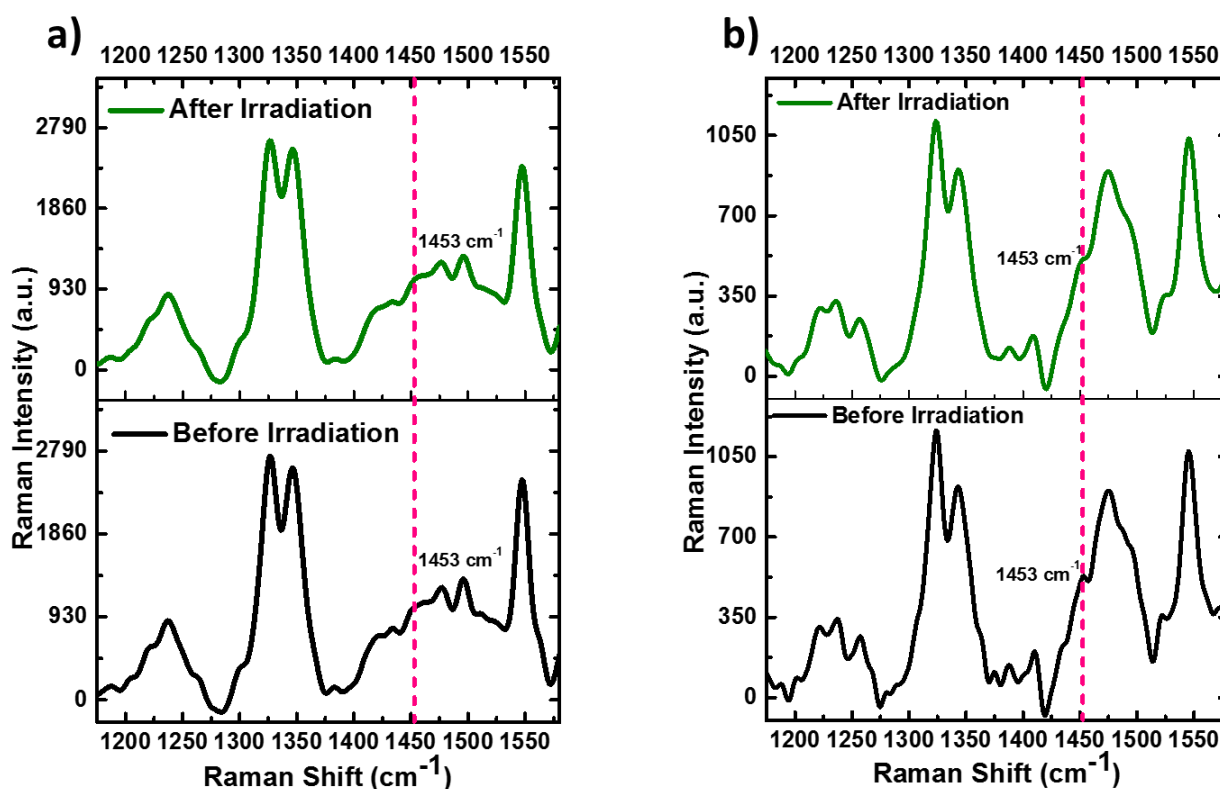
Figure 3.21: *Raman spectra of OBPDI-AZO1 collected before and after irradiation using a) 355 nm laser at a power of 30 mW for 5 minutes and b) 532 nm laser at a power of 30 mW for 5 minutes.*

3.4. Conclusions

In conclusion, twisted racemic OBPDI crystals delivered a series of novel double-racemic cocrystals, OBPDI-Ar, involving induction of twist based racemicity from OBPDI to achiral guests by virtue of various noncovalent interactions. Electron deficient cavities synergistically generated in the crystal system trapped small electron rich guest molecules and the host-guest chemistry reported herein did not necessitate complex synthetic schemes. The P and M enantiomers of OBPDI and the guest molecules segregated as homochiral mixed stacks in the same crystal system of the twisted double-racemic cocrystals, not realized hitherto. SAPT(0) analysis and DFT technique validated the energetic feasibility of OBPDI-Ar cocrystal formation. Further, trapping and transmission of chirality from OBPDI to aromatic guest was employed to achieve higher energy twisted conformations of azobenzene adopting both P and M mirror symmetries. Detailed analysis of the modulated azobenzene enantiomers in the OBPDI-AZO cocrystal using X-ray diffraction, Raman and X-ray photoelectron spectroscopic techniques indicated shortening of N=N bond, an associated phenomenon in the inversion pathway of trans-cis isomerization of azobenzene. Thus, the crystallization induced twisting of azobenzene provided a structural understanding about the favorable pathway an azobenzene molecule tend to adopt, when it extracts energy from an external source to cross the activation barrier and begins to undergo conformational change. Hence, OBPDI evolved as a promising host system involving a novel self-assembly strategy to promote chiral information transfer to achiral moieties leading to amplification of stored racemic information apt for engineering better optoelectronic devices.

3.5. Appendix

Table C-3.1: *Crystal data and structure refinement parameters of OBPDI crystals obtained from various solvents.*

Unit cell parameters	CHLOROFORM: ACETONE (REPORTED)	DCM: HEXANE	THF	BENZENE	TOLUENE	O-XYLENE
Empirical formula	$C_{32}H_{18}Br_8N_2O_4$	$C_{32}H_{20}Br_8N_2O_4$	$C_{32}H_{18}Br_8N_2O_4$ C_4H_8O	$C_{32}H_{18}Br_8N_2O_4$, $2(C_6H_6)$	$C_{32}H_{18}Br_8N_2O_4$, $2(C_7H_8)$	$C_{32}H_{18}Br_8N_2O_4$, C_8H_{10}
Formula weight	1135.78	1135.78	1205.87	1289.98	1318.73	1346.08
Colour, shape		Red, needle	Red, needle	Red, needle	Red, needle	Red, needle
Crystal system	Monoclinic	Triclinic	Triclinic	Monoclinic	Monoclinic	Monoclinic
Space group	C2/c	P-1	P-1,2	C2/c,4	P21/c,4	C2/c,4
A (Å)	15.464 (6)	7.917(2)	7.8261 (7)	21.043 (4)	22.6319(14)	20.8151(14)
B (Å)	15.462 (5)	11.602(4)	11.5229 (9)	7.3051(16)	7.5717(6)	7.5115 (6)
C (Å)	14.114 (4)	19.802(6)	22.106 (2)	28.007(6)	27.4136(16)	30.745 (2)
α, deg	90	74.178(14)	98.830 (3)	90	90	90
β, deg	104.799	79.736(16)	97.166 (3)	105.827 (8)	111.908 (4)	108.968 (3)
γ, deg	90	75.548(14)	104.610 (3)	90	90	90
Volume ($Å^3$)	3262.77	1682.5(9)	1878.12	4142.06	4358.4	4553.35
Temperature (K)	-	296	296	296	296	296
Calculated density (mg/m^3)	-	2.242	2.132	2.069	2.009	1.964
Reflections collected	-	24178	26725	16791	37627	16932
Unique reflections	-	6598	6589	4052	9505	3994
Number of parameters	-	415	460	251	512	268
R_1, wr_2 (i>2σ(i))	-	0.2334, 0.4614	0.0572,0.1443	0.0533,0.1501	0.0527,0.1040	0.0706,0.1973
R1, wr_2 (f^2) (all data)	-	0.3274, 0.5106	0.1111,01755	0.0872,0.1733	0.1740,0.1431	0.0982,0.2227
R (f %)	3.57	22.48	5.72	5.33	5.27	7.06
Goodness of fit on f^2	-	1.101	1.047	1.004	0.967	1.069
CCDC number	1412900	1913336	1913341	1913335	1913342	1913339

3.5.1. Materials and methods

All chemicals were obtained from commercial suppliers and used as received without further purification. All reactions were carried out in oven-dried glassware before use and wherever necessary, were performed under dry nitrogen in dried, anhydrous solvents using standard gastight syringes, cannula, and septa. Solvents were dried and distilled by standard laboratory purification techniques. TLC analysis were performed on recoated aluminium plates of silica gel 60 F254 plates (0.25 mm, Merck) and developed TLC plates were visualized under short and long wavelength UV lamps. Flash column chromatography was performed using silica gel of 200-400 mesh employing a solvent polarity correlated with the TLC mobility observed for the substance of interest. Yields refer to chromatographically and spectroscopically homogenous substances. Melting points were obtained using a capillary melting point apparatus. ^{1}H and ^{13}C NMR spectra were measured on a 500 MHz Bruker advanced DPX spectrometer. Internal standard used for ^{1}H and ^{13}C NMR is tetramethyl silane (TMS). High resolution mass spectra (HRMS) were recorded on Thermo Scientific Q Exactive mass spectrometer using electrospray ionization (ESI, positive mode) technique.

3.5.2. X-ray crystallography

High quality crystals of OBPDI-Al, OBPDI-Ar, OBPDI-AZO1 and OBPDI-AZO2 with appropriate dimensions were selected for the X-ray diffraction experiments. Single crystal was mounted using oil (Infineum V8512) on a glass fibre. All measurements were made on a CCD area detector with graphite monochromated Mo Kα radiation. The data was collected using Bruker APEXII detector and processed using APEX2 from Bruker. The structure was solved by direct method and expanded using Fourier technique. The non-hydrogen atoms were refined anisotropically. Hydrogen atoms were included in idealized positions, but not refined. Their positions were constrained relative to their parent atom using the appropriate HFIX command in SHELX-97. All

programs used during the crystal structure analysis are incorporated in the WINGX software. The full validation of CIF and structure factor of OBPDI crystals was performed using the checkCIF utility and found to be free of major alert levels. 3D structure visualization and the exploration of the crystal packing of OBPDI-Al, OBPDI-Ar, OBPDI-AZO1 and OBPDI-AZO2 crystals was carried out using Mercury 4.1.0.

3.5.3. Solid state UV-Vis absorption and fluorescence emission measurements

Absorption and emission spectra were recorded on Shimadzu UV-3600 UV-VIS-NIR and Horiba Jobin Yvon Fluorolog spectrometers respectively. Kubelka-Munk transformed reflectance spectra in the crystalline powder state using integrating sphere coated with $BaSO_4$ were measured in the diffuse reflectance mode. The Kubelka-Munk model is quite accurate when the particle size is smaller or similar to the wavelength of the excitation. The diffuse reflectance spectra allow no separation of the reflection, refraction and diffraction occurring from the crystalline samples. As a result, the diffuse reflectance spectrum is not as sensitive compared to the UV-vis absorption spectra and can possibly be broader as compared to the typical absorbance and fluorescence excitation spectra.

3.5.4. Raman spectroscopic analysis

Raman spectroscopic analysis of OBPDI-AZO1, OBPDI and trans-azobenzene in the crystalline powder state were recorded using a HR800 LabRAM confocal Raman spectrometer, operating at 20 mW laser power using a Peltier cooled (-74^0C) CCD detector. Raman spectra were recorded using a He-Ne laser source having an excitation wavelength of 632.8 nm with an acquisition time of 5 s using a 50x objective. Raman spectra analysis of the OBPDI-AZO1 cocrystal before and after irradiation of UV and visible light source was also done using the same experimental parameters.

3.5.5. X-ray photoelectron spectroscopic (XPS) analysis

X-ray Photoelectron Spectroscopic (XPS) measurements were performed using an ESCA Plus spectrometer (Omricon Nanotechnology Ltd, Germany). Mg K$_\alpha$ (1253.6 eV) was used as the X-ray source operating at 100 watts. General scans and core-level spectra were acquired with 1 eV and 50 eV pass energy respectively. Spectral Background (Shirely) de-convolution was done by using CasaXPS software.

3.5.6. Photoirradiation experiments

The photoirradiation experiments were performed on good quality crystals of OBPDI-AZO1 using 318 nm, 355 nm and 532 nm laser lights of power ranging from 15-30 mW. The photoirradiation experiment with 318 nm laser was monitored using optical microscopic images of the crystals collected before and after photoirradiation (for a time period of 90 minutes) using Leica m80 microscope. The images before and after irradiation displayed insignificant changes to the crystalline morphology. Single crystal x-ray diffraction analysis of the irradiated crystal (318 nm, 20 mW OBPDI-AZO1-UV) also verified the negligible changes to the OBPDI-AZO1 cocrystal. Photoirradiation of OBPDI-AZO1 cocrystal using 355 nm and 532 nm laser source (30 mW fluence for 5 minutes) were performed and the crystals were analyzed for any changes to the vibrational modes in their respective Raman spectra.

3.6. Computational methods

3.6.1. Quantum theory of atoms in molecules (QTAIM)

The wave function generation for OBPDI molecule was performed by employing the geometries taken from the crystal structure using Gaussian set of codes at B3LYP/6-311++G** level of theory using Gaussian 09.

3.6.2. Electrostatic surface potential (ESP)

Electrostatic surface potential (ESP) map illustrates the charge distribution of molecules in three dimensions. These maps allow us to visualize variably charged regions of a molecule. Knowledge of the charge distribution can be used to determine how molecules interact with one another. Gaussian supports the cube keyword to generate the cubes separately from the formatted checkpoint file (generated from energy calculation with) using the cubegen utility program. This allows for the electrostatic surface potential mapping of the molecule. The calculations were performed in Gaussian 09 suite by employing the B3LYP functional and 6-311G+** basis set at DFT level of theory.

3.6.3. Materials Science suite

The Potential energy surface (PES) scan based on density functional theory calculations were performed using the Jaguar[177] DFT module from Schrodinger Material Science Suite 2016-4. The geometry optimization and the single-point energy calculations were carried out at B3LYP/6-311G**+ level of theory. The dimers for the potential energy surface generation were created in VMD from the geometry optimized monomer in steps of 1 Å separation. The interaction energy was obtained by subtracting the energy of the dimer from twice that of the monomer.

3.6.4. Gaussian Energy Calculations

Energy calculations of different conformations of azobenzene monomers were performed by employing the B3LYP functional and 6-31G** basis set at DFT level of theory using Gaussian 09 suite.[178]

Chapter 4

Modulating Charge Transport through Chromophoric Modifications

PART A: In Silico Exploration for Maximal Charge Transport in Organized Tetrabenzoacenes through Pitch and Roll Displacements

Abstract

A series of π-conjugated tetrabenzoacenes (TBA), including nitrogen-(un)doped derivatives, are computationally evaluated to comprehend the correlation between intrinsic structural arrangements and charge-transport characteristics. The central charge-transport parameters such as reorganization energy and electronic coupling are individually tuned through peri substitutions, core substitutions, and/or π extension in TBA derivatives. Owing to significant structural changes associated with the reduction process, nitrogen doping impeded the electron transport in TBA analogs which is reflected by the reorganization energy values. Here, we have adopted an approach wherein, modulated dimeric arrangements of TBA via displacements along the molecular long (pitch) and short (roll) axes are mapped with respect to the charge transfer coupling. The results so obtained disclosed potential charge-transport regions exhibited by slip-stacked geometries in addition to the ideal cofacial modes. Charge transport characteristics of TBA dimers mimicking the different orientations of graphene bilayers were analyzed, providing insights into the possible material applicability of TBA derivatives. The transition from completely aligned graphitic AA packing sequence to slip-stacked AB and AA' stacking domains revealed a dent in the charge-transport map owing to node–antinode interaction of the frontier molecular orbitals. TBA analogs encompassing the

expanded π-system materialized highly displaced dimeric orientation from AB-type packing to occupy a hierarchy favoring higher charge transfer coupling than the AB type. Thus, realizing stable interchromophoric arrangements of small organic molecules through chemical or physical techniques to control their charge-transporting efficiencies is an indispensable step toward the generation of better organic electronic devices.
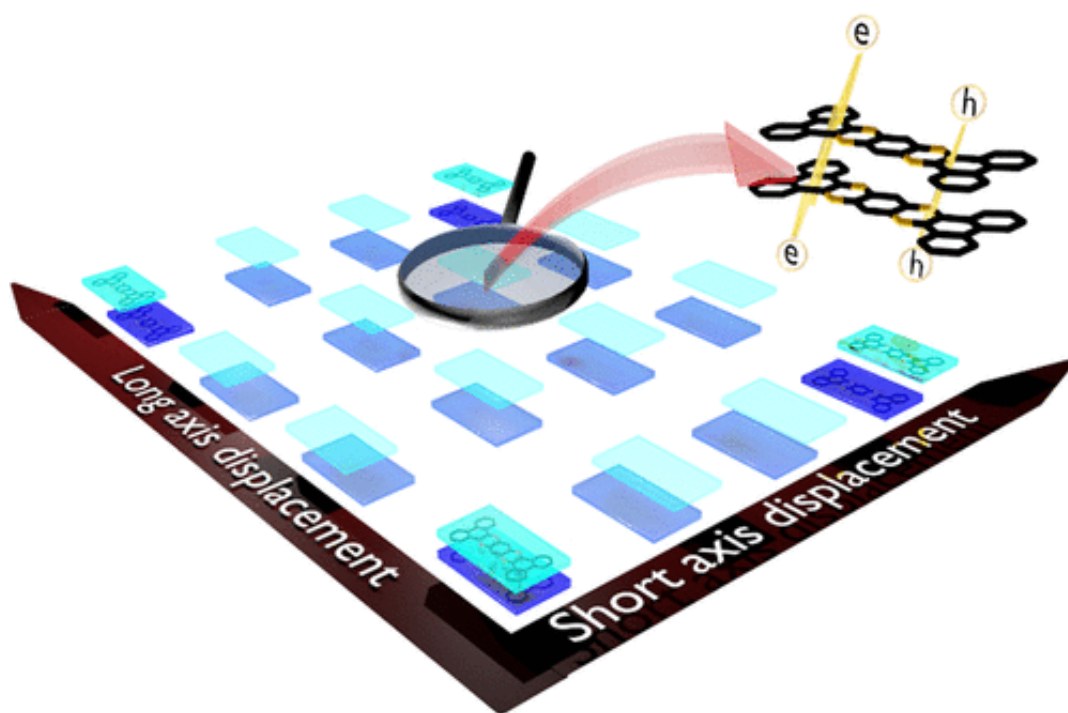
4.A.1. Introduction

Molecular systems having a π-conjugated backbone have attracted significant attention in recent decades as organic semiconductors [179],[180] for the development of numerous optoelectronic devices such as light-emitting diodes,[181] field effect transistors,[182] and solar cells.[3],[183] The easily processable organic crystals form ideal test beds to evaluate the basic parameters affecting charge transport such as the electronic coupling which varies with respect to the relative orientation and multidimensional close-packing arrangements of the chromophores.[1],[184]–[188] The different packing arrangements of organic chromophores in the condensed phase are achieved as an outcome of various noncovalent interactions such as C–H···π [45],[46] and π–π[40] interactions.[189] Understanding the dependence of charge mobility with possible polymorphic arrangements of the organic chromophores stands essential[190] since subtle changes in molecular architectures can affect the charge-conducting nature of the π-conjugated materials. [191]

Efficient charge mobility in organic crystals entails minimizing the impeding pathways such as trapping and scattering of charged particles in the crystalline lattices.[37] Highly ordered cofacial packing modes predominated by π–π stacking interactions are considered ideal for maximizing the charge transport exhibited by the organic crystals due to the efficient orbital wave function overlap. Nonetheless, most of the bare π-conjugated organic assemblies tend to align in edge-to-face fashion upon crystallization which, a priori, is not the favorable orientation for charge transport due to the weakened interorbital overlap.[192] Generating a perfect balance between highly conducting and lower energy crystalline packing arrangement is indispensable in the development of good charge-transporting materials.[193] Derivatizing the all-carbon containing backbone of the polyaromatic systems with heteroatoms is one way of modulating the packing orientation to make the crystals more conducive for charge transport.[194],[195] This approach of modifying the backbone to achieve better

charge-transport materials has been well explored and proved effective over the years as exemplified in the works of Anthony and co-workers.[196]–[198]

In this regard, in our continuing efforts toward understanding the charge mobility of small crystalline organic molecules,[4],[190],[199],[200] the charge-transporting abilities of a series of crystalline tetrabenzoacene (TBA) derivatives having varying substituent moieties[201],[202] are analyzed herein. The dependency of the charge mobility on electronic and structural parameters of the TBA derivatives is explored right from the molecular level using the DFT technique to comprehend the applicability of the TBA derivatives as better and promising materials for organic electronics.

4.A.2. Results and discussion

The crystallographic information files (.cif) of the four tetrabenzoacene (TBA) derivatives were extracted from CSD version 5.38 via the ConQuest 1.19 search engine. The series of wing-shaped TBA derivatives analyzed herein contains different substituent moieties attached on to the same linear acene core to yield a good comparative report on the relationship between charge transport and (supra)molecular structure. Among the TBA analogs, NTP derivative with four pyridinyl nitrogen atoms in the core constitutes the archetypical geometry wherein halide substitutions at the periphery positions and extension of the π-conjugated core, respectively, yielded BNTP and NTH derivatives (Figure 4.A.1). The non-nitrogenated analog of NTH, which is TH, is chosen as a representative example for an all-carbon-containing winged polyacene. The extended flat π-surface along with the chemical composition of TBA derivatives facilitated a face-to-face crystalline packing arrangement as revealed from the investigation of respective crystal structures.

Since the charge-transport property of an organic crystal is determined by the molecular alignment in the crystal,[203] it is imperative to comprehend the correlation between mode of dimeric orientation and the efficiency of charge mobility through all

the major neighboring face-to-face dimers present in the crystal structure. The dimer orientations can vary depending upon the relative shifts of the monomer units through the long (Δ_L) or short axis (Δ_S) of the molecule along with any possible changes in the intermolecular spacing (d_s).

TBA crystals belong to $P2_1/n$ space group. The TBA derivatives adopted a columnar packing arrangement (Figure 4.A.2) promoted by various intermolecular contacts such as C–H$\cdots\pi$, H$\cdots$H, and $\pi\cdots\pi$ interactions. The stabilizing interactions in the TBA crystals along with their percentage contributions are probed in detail using Hirshfeld surface (HS) analysis (Table 4.A.1). The TBA derivatives are found to align in β-packing motif that is associated with columnar $\pi\cdots\pi$-stacked construction (the ρ value ranged from 0.5 to 0.8).[204] The HS analysis revealed a dominating presence of H$\cdots$H interaction in the packing of NTP, NTH, and TH, while the H$\cdots$Br hydrogen-bonding interaction predominantly affected the packing of BNTP.
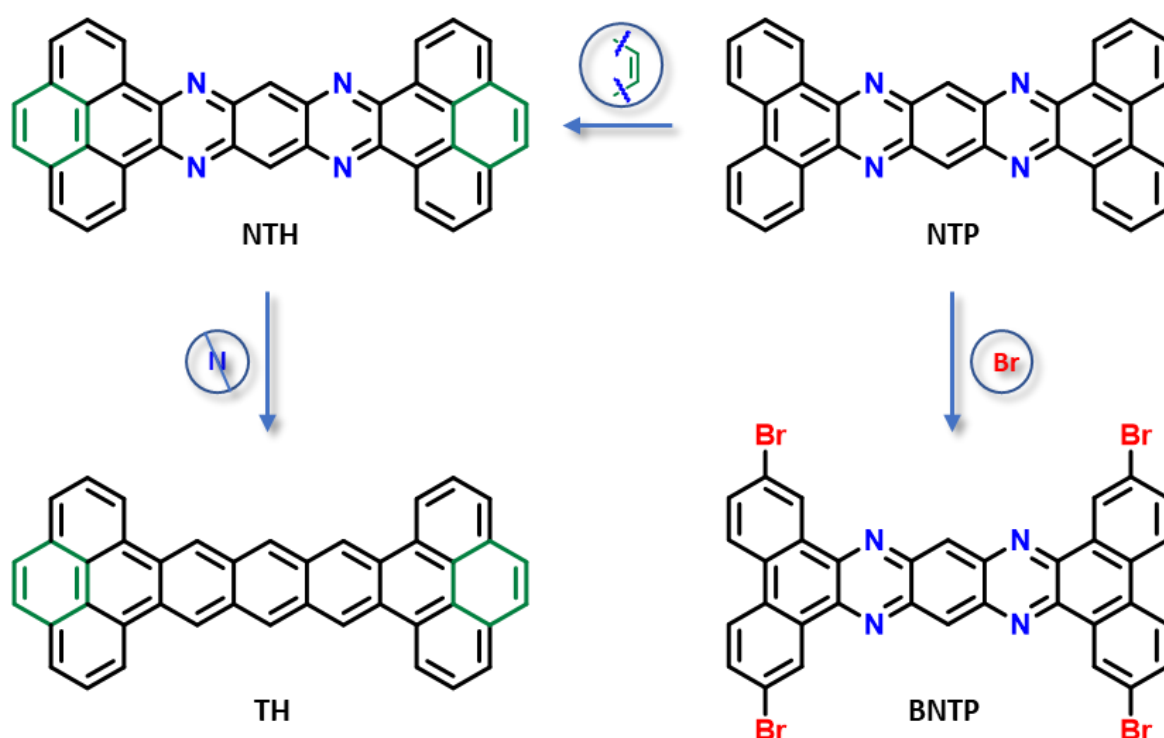
Figure. 4.A.1: *Molecular structures of the winged TBA derivatives under study.*
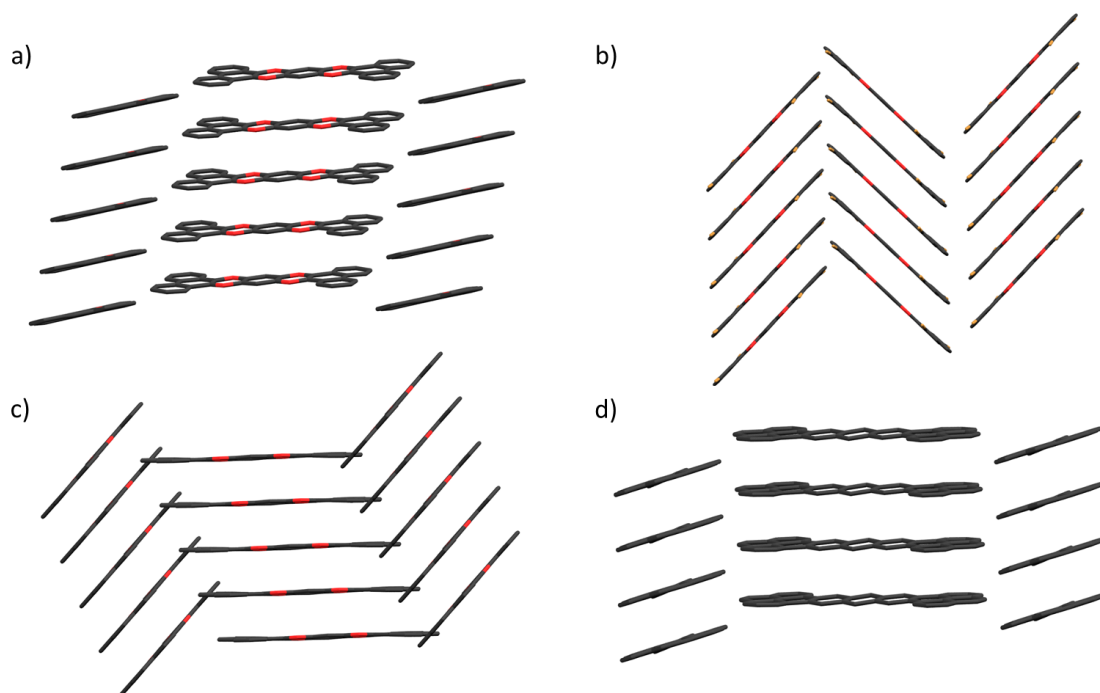
Figure 4.A.2: *Columnar crystal packing of a) NTP, b) BNTP, c) NTH and d) TH.*

Table 4.A.1: *Hirshfeld surface analysis of NTP, BNTP, NTH and TH.*

	% C···C	% C···H	% H···H	% N···H	% N···N	% N···C	% N···Br	% C···Br	% H···Br	% Br···Br	ρ^a
NTP	22.9	14.5	49.4	7.4	0.6	5.1	--	--	--	--	0.633
BNTP	11.2	25.5	14.0	1.3	0.1	8.0	2.4	1.2	32.3	4.1	0.709
NTH	23.2	18.1	47.7	6.0	1.3	3.7	--	--	--	--	0.780
TH	28.9	16.9	54.2	--	--	--	--	--	--	--	0.584

[a]total percentage of intermolecular contacts is 100% in NTP, BNTP, NTH and TH.
$\rho = [(\%C \bullet\bullet\bullet H)/(\%C \bullet\bullet\bullet C)]$. All fall under β packing motif [β (0.46< ρ<1.0)]

The crystal packing of the NTP derivative that formed the model geometry and the nonbrominated analog, BNTP, contained a single uniquely oriented dimer, while in the cases of NTH and TH derivatives, two different face-to-face-oriented dimers existed (NTH-D$_1$ and NTH-D$_2$ and TH-D$_1$ and TH-D$_2$, respectively) (Figure 4.A.3). Close inspection of the stacking configuration of dimers in the TBA crystals showed that, among the winged polyacenes, BNTP dimer possessed the highest shift along the long axis (Δ_L = 3.16 Å) of the molecule. The sizable Δ_L value could be reasoned with the requirement of BNTP dimer to minimize the destabilization that can ensue due to
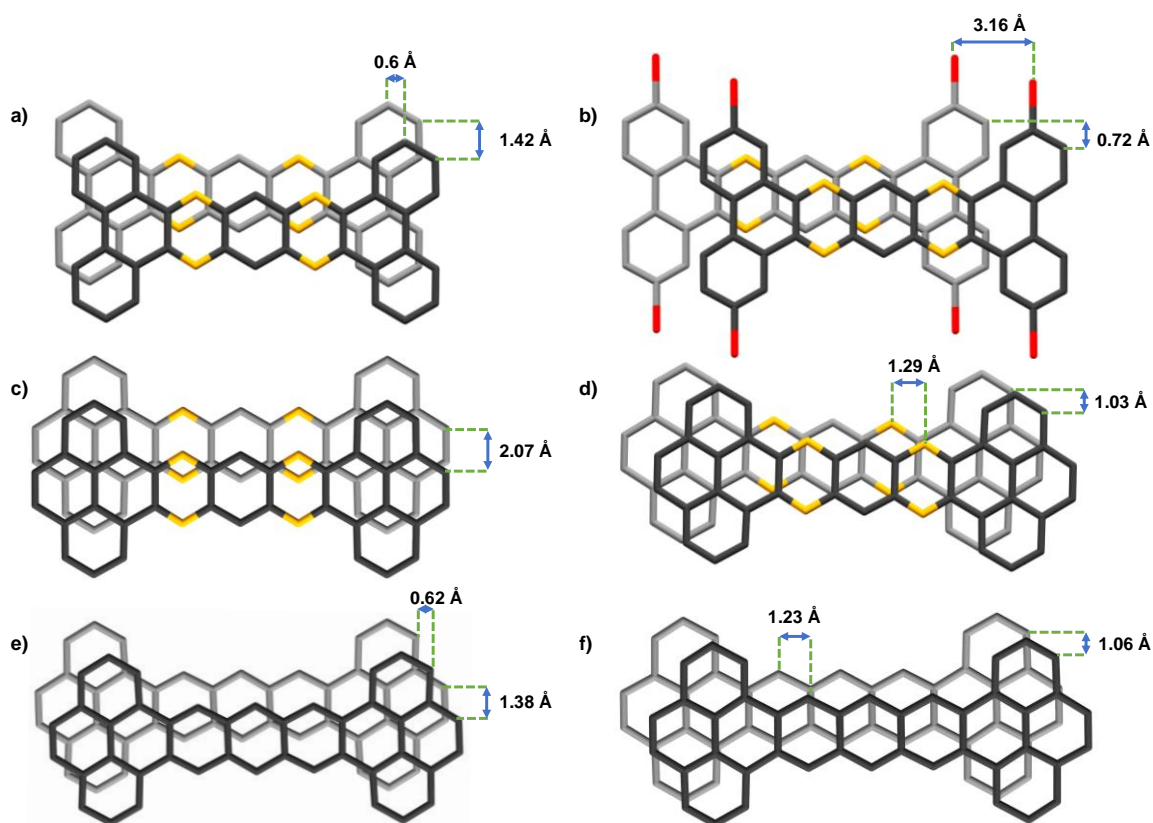
Figure 4.A.3: *Dimers present in the crystal structures of (a) NTP, (b) BNTP, (c) NTH-D$_1$, (d) NTH-D$_2$, (e) TH-D$_1$, and (f) TH-D$_2$.*

the steric repulsion between the four-electron denser bromine atoms at the periphery. The long axis displacement in BNTP dimer also facilitated an inherent reduction in the electronic repulsion between the four core-substituted nitrogen atoms of each monomer unit to cause minimal shift along the short axis. Thus, the BNTP dimer possessed the shortest lateral displacement (Δ_S) of 0.7 Å among the TBA derivatives (Δ_S ranging from 1.03 to 2.07 Å) as the nitrogen atoms are not in proximity and steric crowding is minimized. The nonbrominated analog, NTP, did not showcase large long axis displacement (Δ_L in NTP = 0.6 Å). However, the observed displacement of about 1.4 Å of the NTP dimer along the short axis assisted in reducing possible repulsion between the core-substituted nitrogen atoms in each molecule. NTH-D$_1$ exhibited the highest short axis displacement of 2.07 Å with zero shift along the long axis among the TBA derivatives, while the other energetically favorable dimer orientation in NTH

crystal, NTH-D$_2$, contained displacements along both the long and the short axes of the molecule (Δ_L = 1.29 Å and Δ_S = 1.04 Å, Figure 4.A.3). The dimer orientations in the TH crystal, TH-D$_1$ and TH-D$_2$, contained shifts along both the transverse and the longitudinal directions as depicted in Figure 4.A.3. The different dimer orientations show significant implications in the charge-transporting abilities of the TBA crystals which have been closely explored herein.

The interplanar spacing between the crystalline dimers of TBA derivatives displayed prominent variations with respect to the type of substituent groups present in the aromatic core. Nitrogen atoms in the core system facilitated a decrease in the interchromophoric distance in NTP, BNTP, and NTH crystals with values of d_s = 3.30–3.51 Å when compared to nitrogen-deficient TH (d_s = 3.54–3.55 Å). The observed difference in the interplanar spacing between nitrogen-doped and undoped derivatives emanated because of constriction in electron density toward the nitrogen centers.[205] Electrostatic surface potential (ESP) plots qualitatively substantiated the difference in the electron density distribution in the TBA derivatives (Figure 4.A.4). The ESP plots revealed high electron density regions, indicated in red, on the nitrogen centers of NTP, BNTP, and NTH. The shift in electron density to specific points
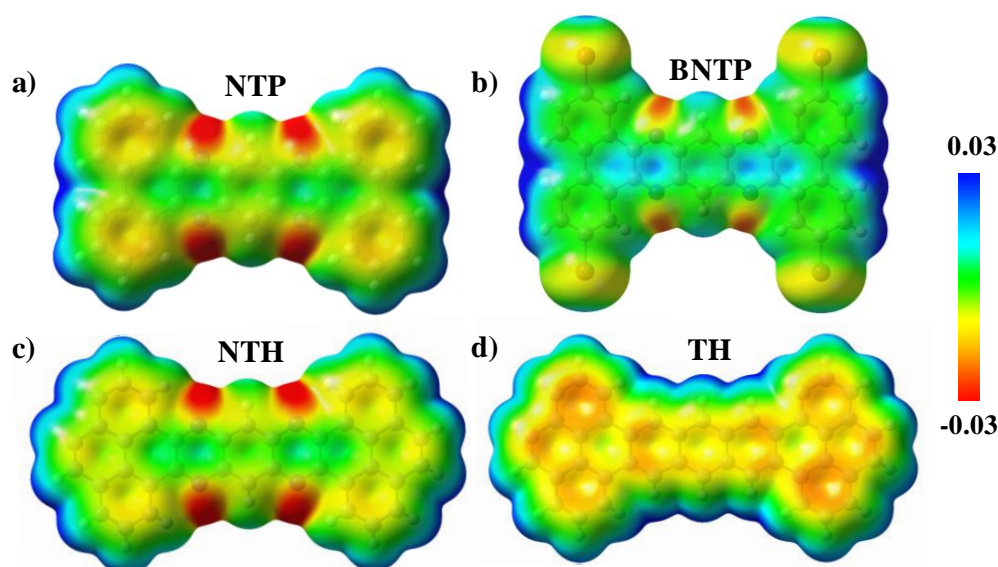
Figure 4.A.4: *Electrostatic surface potential plots of a) NTP, b) BNTP, c) NTH and d) TH.*

(toward nitrogen centers) resulted in an uneven electron distribution with the aromatic π-surface becoming electron deficient (blue/green-colored regions) in the nitrogenated TBA analogs, while the all-carbon-containing TH derivative was associated with a uniform distribution of electron density over the aromatic core. The differential dispersal of electron density facilitated the columnar packing in NTP, BNTP, and NTH wherein N···C interaction reminiscent of a donor–acceptor-type bonding, stabilized the stacking orientations. The higher percentage of N···C interactions (NTP, BNTP, and NTH has 5.1%, 8.0%, and 3.7% of N···C interactions, respectively) aided the shortening of the interchromophoric distance in the TBA dimers as corroborated by the HS analysis, indicating the role of nitrogen doping in tuning the molecular packing arrangement.

Symmetry-adapted perturbation theory (SAPT), one of the mainstream energy decomposition analysis (EDA) approaches in theoretical chemistry, provided a quantitative depiction of the counterbalancing intermolecular forces that favored closer dimer orientation in nitrogen-doped TBA derivatives when compared to the undoped TH dimers (Figure 4.A.5, Table 4.A.2). The electrostatic interaction energy factor in π–π stacked molecular systems originated because of the interaction between
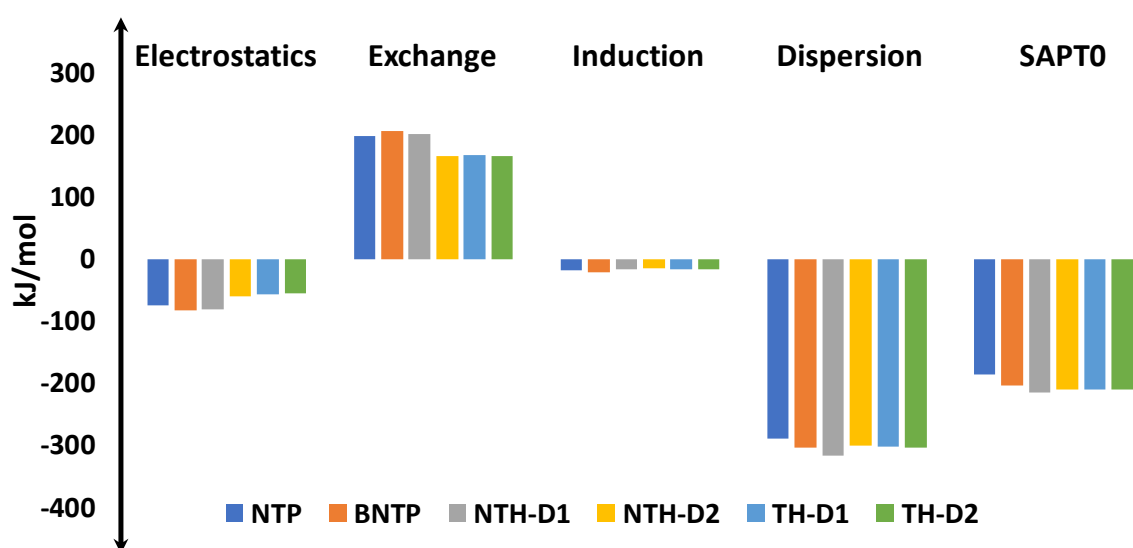
Figure 4.A.5: *SAPT analysis of neighboring dimers in TBA crystals.*

Table 4.A.2: *Interaction energies in selected dimers of NTP, BNTP, NTH and TH determined by SAPT(0) analysis.*

Dimer	Electrostatics (kJ/mol)	Exchange (kJ/mol)	Induction (kJ/mol)	Dispersion (kJ/mol)	SAPT0 (kJ/mol)
NTP	-75.79	198.22	-17.85	-290.64	-186.06
BNTP	-83.99	206	-21.57	-304.93	-204.48
NTH-D$_1$	-81.32	200.60	-17.65	-317.87	-216.24
NTH-D$_2$	-60.04	165.88	-15.36	-301.50	-211.02
TH-D$_1$	-57.57	166.84	-16.30	-303.29	-210.32
TH-D$_2$	-54.98	165.68	-16.32	-305.59	-211.22

the multipoles on each molecule. At short intermolecular distances the electrostatic interactions are largely associated with charge penetration effects[206],[207] (electron–nuclear attraction between two different units) due to which better orbital overlap of the monomers could be achieved in a dimer. When the interplanar spacing between the individual moieties in a dimer becomes minimal, the improved orbital overlaps between the component units that facilitated efficient charge penetration consequently counteracted the destabilizing exchange repulsion between the nearby electron densities. Thus, the negative value of the electrostatic interaction obtained in the TBA dimers followed the order TH-D$_2$ < TH-D$_1$ < NTH-D$_2$ < NTP < NTH-D$_1$ < BNTP and were consistent with the trend observed with respect to the intermolecular spacing associated with the respective dimers (Figure 4.A.5, Table 4.A.3). For instance, BNTP dimer had the shortest intermolecular spacing and hence encompassed the highest exchange repulsion interaction with a value of around 206 kJ/mol. However, a stronger stabilizing contribution from the electrostatic interaction (−83.99 kJ/mol) counteracted the destabilizing effect of the exchange repulsion term, stabilizing the BNTP dimer. Hence, when compared to the nonbrominated NTP derivative (total interaction energy = −186.06 kJ/mol), the dimer arrangement of BNTP with a total energy of −204.48 kJ/mol was found to be more stable in the crystalline state. The high electrostatic interaction in BNTP dimer was also corroborated from the ESP plot

Table 4.A.3: *Values showing relation of interplanar distance to the electrostatic and exchange interactions of the crystalline dimers.*

Dimer	Interplanar spacing (d_s) (Å)	Electrostatics (kJ/mol)	Exchange (kJ/mol)
NTP	3.39	-75.79	198.22
BNTP	3.30	-83.99	206
NTH(D_1)	3.40	-81.32	200.60
NTH(D_2)	3.51	-60.04	165.88
TH(D_1)	3.54	-57.57	166.84
TH(D_2)	3.55	-54.98	165.68

wherein both nitrogen and bromine centers constricted the electron density toward nitrogen and bromine, resulting in an overall decrease in the π-electron cloud at the aromatic core (represented by the blue/green-colored region in BNTP, Figure 4.A.4). The most prevailing attractive interaction that stabilized the π–π-stacked TBA crystals was the dispersion interaction that occurred due to instantaneous charge fluctuations. Among the TBA crystals, BNTP, NTH-D_2, and the two TH dimers exhibited similar dispersion interaction with values ranging from −301.50 to −305.59 kJ/mol. NTH-D_1 dimer with zero long axis displacement had the highest contribution from dispersion interaction to the total energy with a value of −317.87 kJ/mol, and NTP showed the least dispersion energy contribution with a value of −290.64 kJ/mol. The significance of interplanar spacing with regards to the charge-transporting abilities of self-assembled organic chromophores has been well established in the literature to have an exponential relation between interplanar spacing and charge transfer coupling.[187]

Within the hopping transport regime, proficiency of charge mobility in organic crystals is dependent on reorganization energy and charge transfer coupling.[208]–[211] In this regard, both the electronic and the geometrical parameters of a molecule should have equivalent roles in defining the charge-transport abilities of the organic material. The nature of substituent moieties has a significant impact on the

reorganization energies of the molecule apart from modulating the crystalline packing through intermolecular interactions.[199] A small value for reorganization energy improves the feasibility of charge transport, reflecting the ease of a monomer to undergo oxidation (λ_h) or reduction (λ_e) during hole and electron transport, respectively.[212] The total reorganization energy during the migration of charges through an organic material is associated with an inner component owing to the chemical composition of the chromophore and an outer component resulting from the changes in the surrounding environment.[213] The outer reorganization energy of the TBA derivatives was not evaluated due to the meager contribution toward the total reorganization energy in the crystalline state in addition to the large computational cost involved.[214],[215] The calculation of reorganization energy of TBA derivatives (Table 4.A.4) for the transport of respective charge carriers (hole and electron) was performed in the Schrodinger material science suite by following an adiabatic potential energy surface (Figure 4.A.6). Comparable hole reorganization energies (λ_h) were observed for all TBA derivatives with values ranging from 0.082 to 0.099 eV, indicating similar geometry relaxation of the TBA derivatives upon oxidation. However, unlike the hole reorganization energy, electron reorganization energy of the all-carbon-containing TH derivative (λ_e = 0.105 eV) was observed to be even lower than the λ_e of NTP, BNTP and NTH derivatives (ranging from 0.163 to 0.184 eV). The lowest electron reorganization energy exhibited by TH among the TBA derivatives indicated the effect of core-substituted nitrogen atoms in implementing significant variations to the monomer geometries of NTP, BNTP, and NTH during the reduction process. The observed low reorganization energy values for both hole and electron transport in TH derivative makes it a prospective molecule to exhibit ambipolar charge-transporting characteristics. However, generalizing the charge-transport abilities solely based on the reorganization energy values is fallacious, considering the equally strong influence of the crystal-packing arrangement of the molecules.[216] Hence, a thorough understanding of both the electronic and the structural parameters

Table 4.A.4: *Charge Transport Parameters of Different Dimers Present in the Crystal Structure and Reference Geometry of the TBA Derivatives.[a]*

Molecule	d_C (Å)	d_S (Å)	Δ_S (Å)	Δ_L (Å)	λ_h (eV)	λ_e (eV)	V_h (eV)	V_e (eV)
NTP	3.770	3.396	1.424	0.600	0.099	0.167	0.040	0.144
NTP(D_0)	3.780	3.780	0	0			0.293	0.315
BNTP	4.650	3.303	0.720	3.160	0.093	0.184	0.071	0.011
BNTP(D_0)	3.780	3.780	0	0			0.409	0.317
NTH(D_1)	3.850	3.402	2.070	0			0.185	0.172
NTH(D_2)	3.850	3.512	1.041	1.290	0.082	0.163	0.015	0.065
NTH(D_0)	3.780	3.780	0	0			0.331	0.338
TH(D_1)	3.860	3.548	1.386	0.620			0.010	0.213
TH(D_2)	3.860	3.552	1.057	1.230	0.092	0.105	0.156	0.014
TH(D_0)	3.780	3.780	0	0			0.325	0.406

[a]*d_C = centroid distance; d_S = interplanar spacing; Δ_S = short axis displacement; Δ_L = long axis displacement; λ_h = hole reorganization energy; λ_e = electron reorganization energy; V_h = HOMO charge transfer coupling; V_e = LUMO charge transfer coupling; D_0 = cofacial dimers that have been computationally modified.*
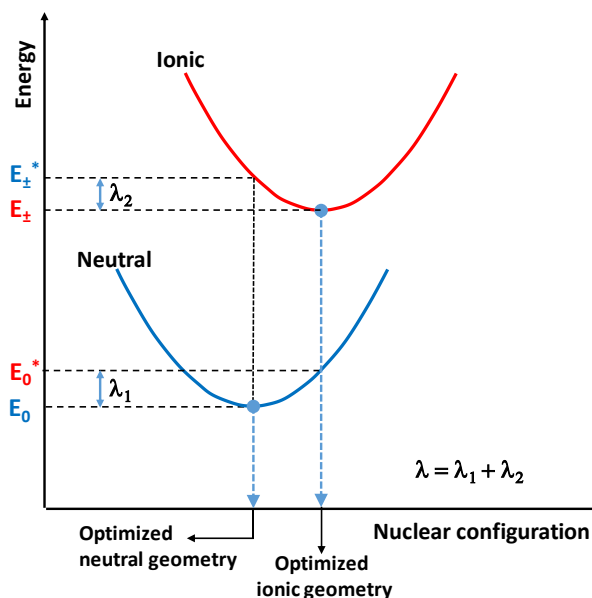
Figure 4.A.6: *Representative figure for the calculation of reorganization energy.*

of organic materials is essential as the interplay between both of these factors will determine the efficiency of charge carrier mobility in an organic molecule. The

interchromophoric electronic coupling has a close connection with the spatial orientation of interacting molecules aligned about the molecular long (Δ_L) and short (Δ_S) axes or with respect to the interplanar spacing (d_s) in the involved dimers. The variation of electronic coupling along the interplanar axis of various organic crystals has a well-established exponential relationship,[54] and the same analysis in the case of TBA derivatives is out of the scope of this work. For a constant d_s between the monomers in a dimer, the upper limit of the magnitude of charge transfer coupling as a consequence of molecular displacements along Δ_L and Δ_S is attained at the cofacial (D_0,(Δ_L,Δ_S)=(0,0)) dimer orientation wherein the monomer π-conjugated backbones are perfectly aligned on top of each other. The maximal electronic coupling in the D_0 arrangement could be attributed to the constructive overlap (node-to-node) of the perfectly aligned molecular orbitals of each monomer units. The distribution of wave function in the HOMO and LUMO levels are dependent on the constituent substituent moieties in the molecule. The wave function distribution in the frontier molecular orbitals of the winged TBA polyacene monomers influenced by the substituent groups attached to the π-conjugated core is depicted in Figure 4.A.7. The electronic coupling of the HOMO levels (V_h) facilitates the transport of holes through the crystalline lattice while electron transport originates from the effective overlap of vacant LUMO levels (V_e).[217] Among TBA derivatives, bromine-substituted analog BNTP showed the highest coupling between the HOMO levels in the D_0 arrangement (Table 4.A.4), analyzed at an interplanar spacing of 3.78 Å. The nonbrominated derivative NTP having the same π-conjugated core is associated with the least HOMO–HOMO coupling, thereby leading to the lowest hole-transporting characteristics amidst the TBA derivatives in the ideal D_0 arrangement. The higher HOMO–HOMO coupling of BNTP (V_h = 0.409 eV), when compared to the NTP core (V_h = 0.293 eV), could be attributed to the presence of additional wave functions distributed over the four bromine atoms. Accordingly, the different behavior of the HOMO–HOMO overlap in BNTP (high V_h) and NTP (low V_h) signified the effect of peripheral bromine
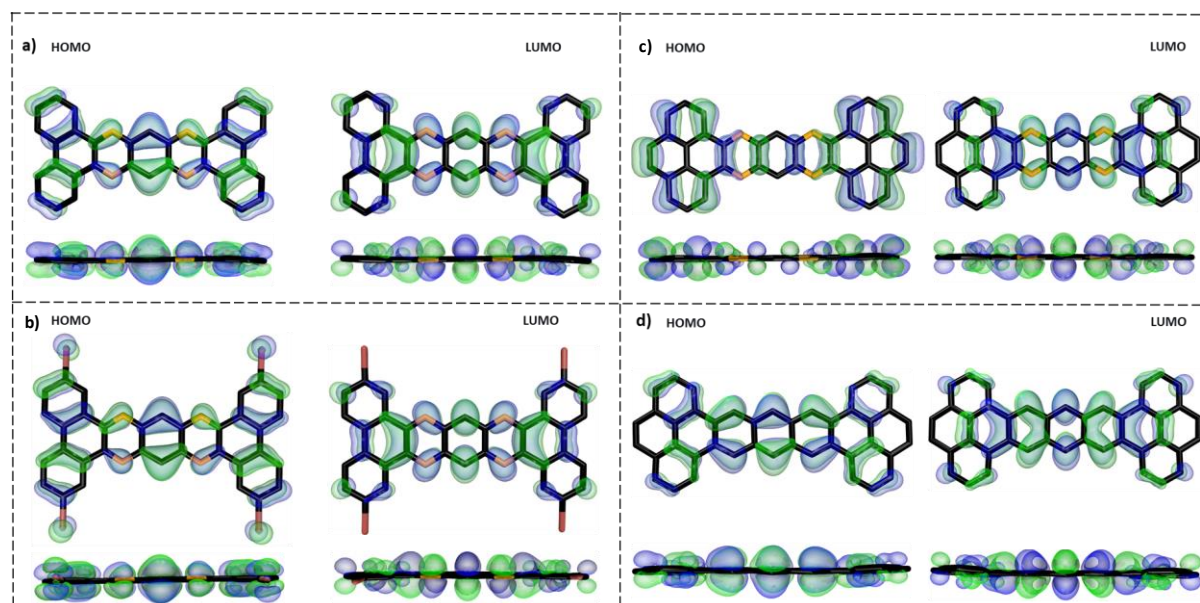
Figure 4.A.7: *Monomer FMOs of (a) NTP, (b) BNTP, (c) NTH, and (d) TH.*

substitutions in the extent of electronic coupling, unlike as was observed with respect to the reorganization energies of NTP and BNTP (similar values) previously. Nevertheless, the LUMO–LUMO coupling (V_e) that governs the electron mobility of the crystal was found to be analogous for NTP and BNTP wherein the V_e value was obtained as 0.315 eV in NTP and 0.317 eV in BNTP. The hole and electron transfer couplings of the cofacially stacked dimers of NTH and TH, having an extended π-conjugated core, however, were observed to be contrasting with respect to each other. NTH showed a higher V_h of 0.331 eV (V_h = 0.325 eV in TH), while TH exhibited a higher V_e of 0.406 eV (V_e = 0.338 eV in NTH). NTP with no π-extension had the lowest V_h and V_e in comparison with NTH and TH. The complementary hole and electron transport characteristics in NTH and TH, respectively, implied the role of substituted nitrogen atoms at the core in altering the nature of the charge transfer coupling between the chromophores, while the extended π-conjugated aromatic core facilitated efficient charge transfer coupling compared to NTP.

Spatial perturbation from the D_0 arrangement directed along Δ_L and Δ_S of the closely associated chromophoric moieties significantly impacted the efficiency of charge transport with no definitive pattern for the electronic coupling variation unlike

the predicted exponential dependence relative to interplanar spacing. Bredas and co-workers highlighted the irregularly periodic nature of the deviation in charge transfer coupling with respect to molecular displacements along either Δ_L/Δ_S axes.[54],[216] The evolution of charge transfer properties with changes in dimer orientation for a fixed interplanar spacing of the winged polyacenes are mapped out as a 2D contour color plot between the charge transfer coupling (V_h/V_e) and the slip-stacking displacement along the short (Δ_S) and long axis (Δ_L) of the respective molecules (Figures 4.A.8 and 4.A.9) The contour diagram (Figure 4.A.9) indicated a periodic dependence of electronic coupling with stacking displacements along Δ_L/Δ_S axes which highlighted the influence of nodal characteristic in the FMO structures of organic molecules as previously reported.[54] Due to the different extent of wave function overlap between the monomer units in a molecular stack at varying distances, the transport coupling fluctuated at each stacking positions.[218] In addition, the 2D contour plot featured stacking sequences reminiscent of the layered packing modes associated with graphite and graphite-like hydrocarbons such as AA, AA', and AB (Figure 4.A.10).[219],[220]
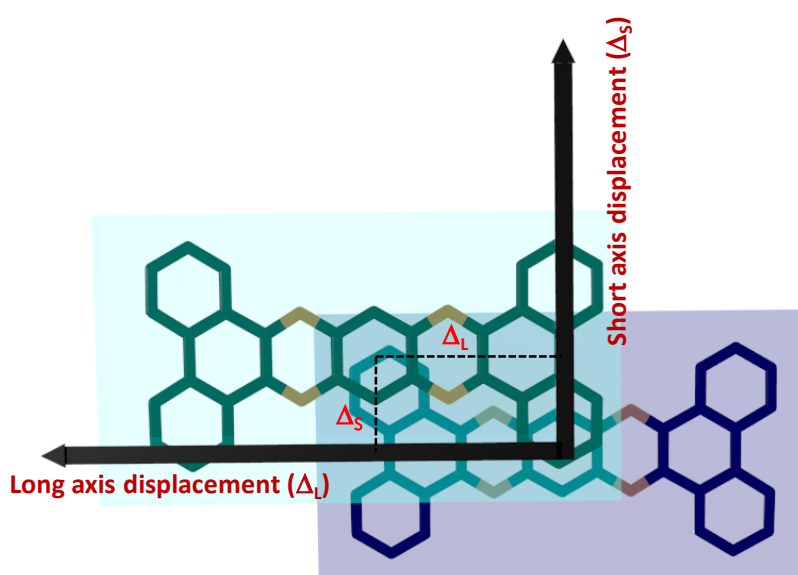
Figure 4.A.8: *Representative figure showing the long (Δ_L) and short axis (Δ_S) displacements in NTP dimer.*
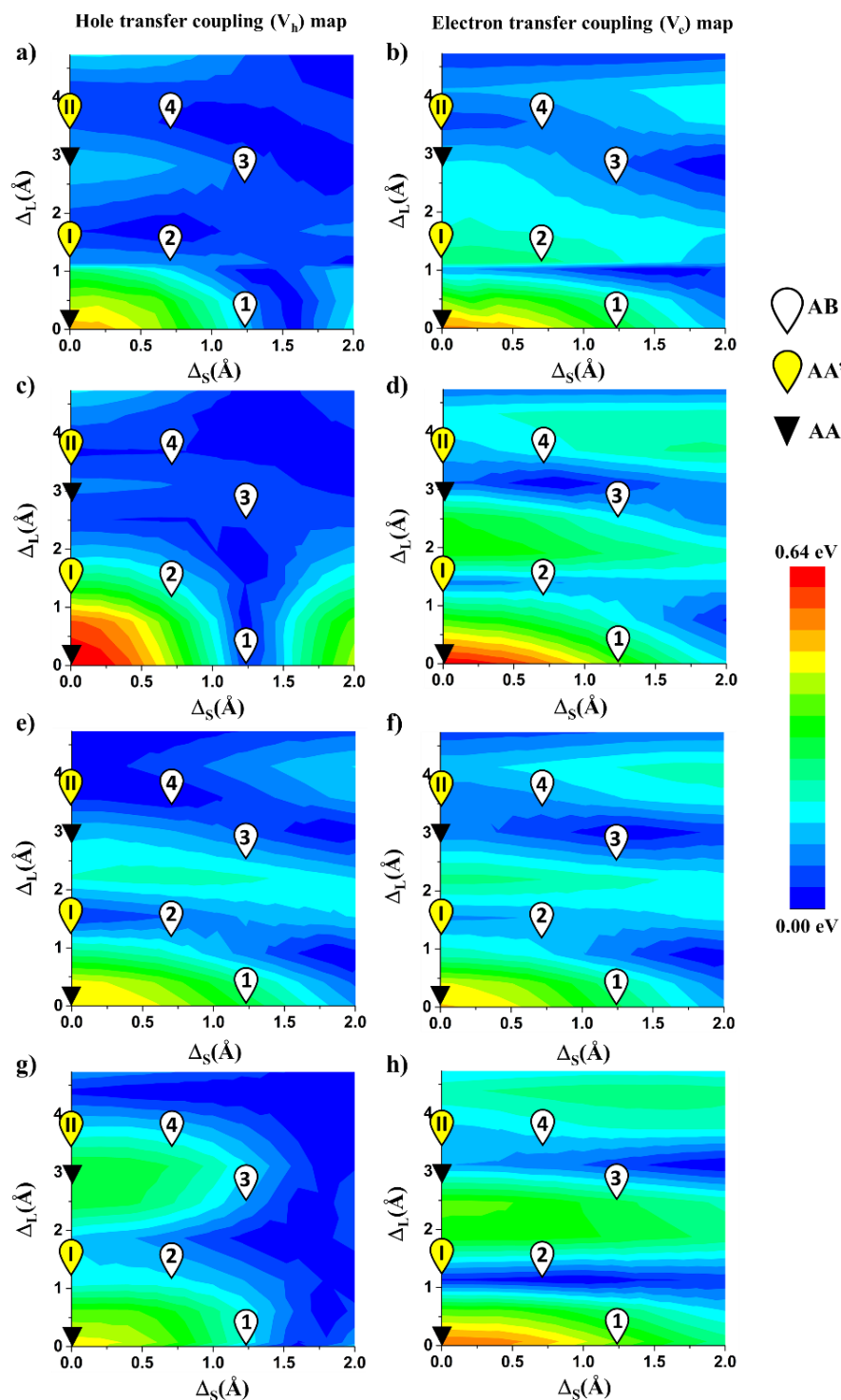
Figure 4.A.9: *Contour plots showing charge transfer coupling variation about long and short axis displacements of (a, b) NTP, (c, d) BNTP, (e, f) NTH, and (g, h) TH dimers with the hole transfer coupling maps represented in the left column (a, c, e, g) and electron transfer coupling maps in the right column (b, d, f, h). White flags with Arabic numerals designate graphitic-like AB orientation, yellow flags with Roman numerals indicate AA' orientation, while black triangles indicates graphitic AA packing sequence.*

102
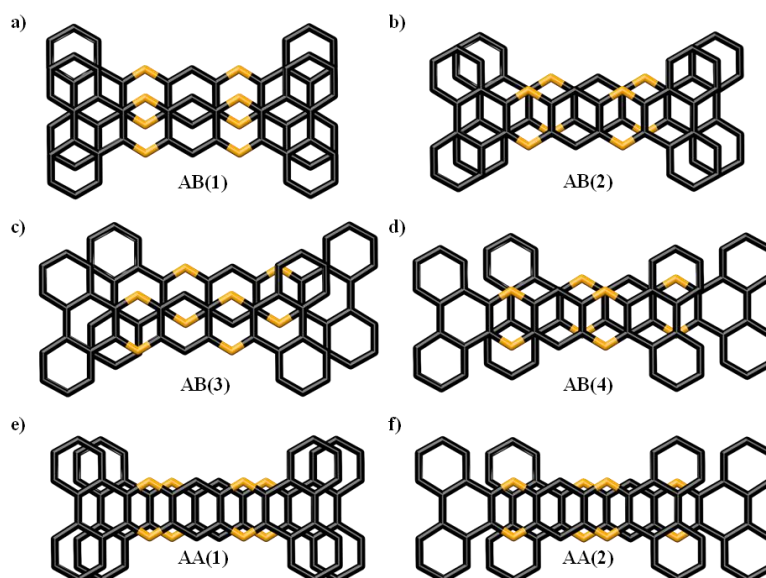
Figure 4.A.10: *Graphitic AA' and AB orientations of representative NTP dimer.*

Graphitic AA-stacking arrangement represents atom-on-atom orientations covering the ideal cofacial (D_0) mode discussed previously. Associated with node-to-node molecular orbital overlap, the AA packing sequence favors charge transport. However, attaining a face-to-face crystalline arrangement realistically has been proven to be an arduous task owing to an upsurge in the electronic repulsion factor between the cofacial chromophores.[221] Thermodynamically more favored slip-stacked layered arrangements include AA' (defined by a long axis slip of half benzene hexagon from AA mode) and AB (with a short axis slip covering quarter benzene hexagon from AA') type packing sequences.

The 2D plot of hole transfer coupling in Figure 4.A.9a, c, e, and g shows a periodic trend with the crest (high HOMO–HOMO coupling) flanked by AB packing motifs denoting the onset of low hole transport regions (trough) along Δ_L and Δ_S displacements. From the molecular orbital distribution represented in Figure 4.A.8, it could be understood that the HOMO of NTP, BNTP, and TH is associated with a continuous nodal region longitudinally extending along the center of the π-conjugated core. Due to the presence of this nodal region, a transversal (roll) displacement of the monomeric units of NTP, BNTP, and TH dimers could result in a

similar degree of orbital overlap which corroborated the analogous features (declining charge transfer coupling regions up to Δ_s = 1.4 Å, i.e., AB-1 orientation) observed in the variation of hole transfer integral along the short axis as indicated in Figure 4.A.9a, b and d. Most of the AB-type dimers (1–4) in the 2D contour map of NTP, BNTP, and TH referred to lower hole transfer coupling orientations (V_h ≈ 0.04–0.2 eV). The AB packing motifs formulated by positions 1 and 3 in the hole transfer map of NTH (Figure 4.A.9e) showcased comparatively higher HOMO–HOMO coupling (V_h ≈ 0.4 eV) than NTP, BNTP, and TH owing to the absence of central nodal regions in the HOMO energy level. Dimeric shifts along the long axis of TBA molecules also showed periodic variation in the HOMO–HOMO electronic coupling. AA' motifs (I and II) attained by long axis displacement of the monomeric units of TBA occupied regions of low hole transfer integral (V_h ≈ 0.04–0.2 eV) compared to the corresponding AA arrangement (V_h ≈ 0.5–0.6 eV). BNTP dimer having an extension of electron density toward the peripheral positions effected better HOMO–HOMO coupling (V_h ≈ 0.30 eV) at the AA'-I position than the accompanying TBA analogs. Hence, radial displacements from the two AA arrangements toward AA' and AB packing sequences resulted in the decrease of hole transfer coupling because of the pattern of wave function distributed in the HOMO of the monomer TBA units, while the absence of longitudinal nodal region in the LUMO levels of TBA molecules extended the periodicity of LUMO–LUMO coupling to higher short axis displacements (Δ_s ≈ 2 Å). The AB packing motifs marked by points 1 and 3 in Figure 4.A.9b, d, f, and h however showcased greater electronic coupling in the TBA derivatives, promoting better electron transport (V_e ≈ 0.20–0.45 eV) compared to hole transport. Hence, AB packing positions at 1 and 3 could be convoluted as better electron conduits, whereas packing positions 2 and 4 with similar but lower electronic coupling for both hole and electron transport mirrored ambipolar charge-transport characteristics.

Acquiring a more realistic picture, charge transfer coupling of the thermodynamically favorable dimer orientation (present in the crystal structure) of

NTP and BNTP could be well corroborated from the contour plot indicating submaximal efficiency for the orbital overlap at the orientations found in the crystalline lattice when compared to the cofacial packing mode. NTP crystalline dimers occupying position coordinates close to the AB arrangement (point 1) exhibited higher LUMO–LUMO coupling (V_e = 0.144 eV), facilitating better electron transport than hole transport (V_h = 0.040 eV). In bromine-substituted BNTP crystal the dimers existed in an orientation close to the AB-4 packing arrangement, facilitating lower extent of orbital coupling for both HOMO (V_h = 0.071 eV) and LUMO (V_e = 0.011 eV) levels and thereby low hole and electron transport characteristics as a function of electronic coupling. Among the twin dimers in NTH crystal, NTH-D$_1$ exhibited better overlap of the HOMO and LUMO orbitals (V_h = 0.185 eV, iV_e = 0.172 eV) than NTH-D$_2$ dimer (V_h = 0.015 eV, V_e = 0.065 eV), wherein both dimers bordered the crest of the electronic coupling wave pattern. The difference in interplanar spacing of NTH-D$_1$ (3.40 Å) and NTH-D$_2$ (3.51 Å) could have promoted the observed difference in the extent of orbital overlap, while the TH-D$_1$ and TH-D$_2$ dimers in TH crystal showcased opposing charge-transporting capabilities with TH-D$_1$, supporting electron transport (V_e = 0.213 eV) compared to TH-D$_2$ encompassing hole transport (V_h = 0.156 eV). The position of the NTH and TH dimers in the charge transfer coupling map indicated the greater efficiency of aromatic core expansion over peri-substitution in adopting a packing arrangement that enhanced the molecular orbital overlap nearing that of the AA motif.

The columnar packing arrangement of TBA crystals accentuated the anisotropic charge-transporting phenomenon[222]–[224] in the crystals wherein the charge hopping acquired a directional dependency due to the differential electronic coupling between the neighboring stacks in different directions. The anisotropic nature of charge transport through the crystalline lattices also symbolized the close relationship between the efficiency of charge transfer and the relative positions of the interacting chromophores in the crystal. The anisotropic nature of the charge carrier

mobility of TBA crystals was calculated by taking the crystallographic *a* axis as the principal axis and *ab* plane as the reference plane. The principal axis chosen for the anisotropic mobility calculation was aligned parallel to the respective π–π stacking direction of each TBA molecular clusters. The transfer mobility of both hole and electron was detected at its peak along the π–π stacking direction (φ = 0°) (Figure 4.A.11) of the TBA crystals since the face-to-face arrangement with short interplanar spacing induced large electronic coupling between the interacting chromophores. The minimal hole and electron mobility values observed at directions perpendicular to the π–π stacking in TBA crystals (φ = 90° and 270°) (Figure 4.A.11) indicated the less
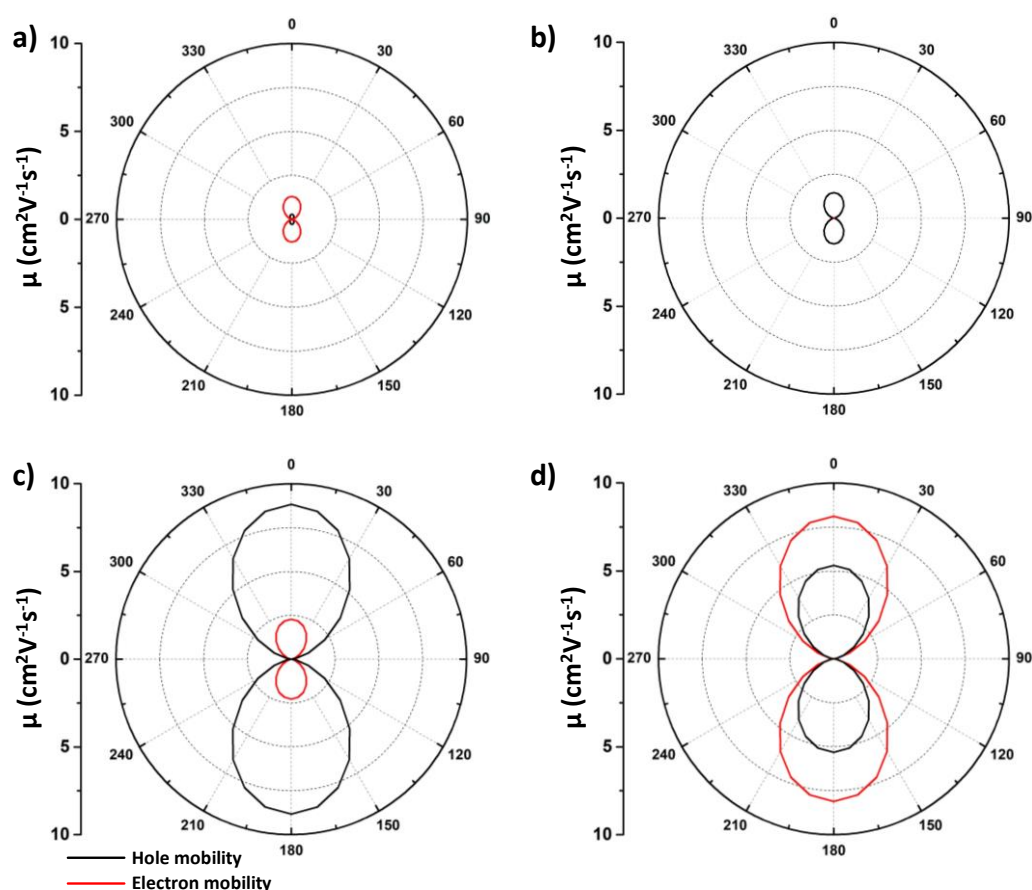
Figure 4.A.11: *Anisotropic electron and hole mobility calculated for (a) NTP, (b) BNTP, (c) NTH, and (d) TH. Crystallographic a axis was taken as the principle axis, and ab plane is considered as the plane of interest, and projection of all hopping pathways to this plane was taken for calculation.*

efficient electronic coupling between the neighboring columnar stacks. The charge transfer along the directions perpendicular to the $\pi-\pi$ stacks of TBA crystals contained dimers which are not aligned in a face-to-face manner, thereby resulting in negligible charge transfer coupling. Since the overall charge mobility was small in NTP and BNTP (0.02–1.55 cm^2 V^{-1} s^{-1}, Table 4.A.5) when compared to NTH and TH crystals (2.28–8.82 cm^2 V^{-1} s^{-1}), plotting the angular dependency of the charge transport gave more conspicuous results in NTH and TH crystals when compared to that of NTP and BNTP crystals (Figure 4.A.11). The anisotropic plots of NTH and TH also emphasized the contrasting hole- and electron-transporting behaviors, respectively, showcased by the two crystals. NTH displayed the highest hole mobility (black trace in Figure 4.A.11 along the $\pi-\pi$ stacking direction, while TH showed reversed transport behavior with the highest electron mobility (red trace in Figure 4.A.11d) in the same direction. Significant mobility values for the electrons in NTH and holes in TH crystals in the respective anisotropy plots further emphasized the pronounced ambipolar charge-transporting abilities in NTH and TH when compared to NTP and BNTP crystals.

Table 4.A.5: *Charge mobility of TBA derivatives.*

Crystal	μ_h (cm^{2}V^{-1}s^{-1})	μ_e (cm^{2}V^{-1}s^{-1})
NTP	0.29	1.55
BNTP	1.48	0.02
NTH	8.82	2.28
TH	5.32	8.11

4.A.3. Conclusions

Herein, quantum chemical calculations were exploited to determine the charge-transport characteristics of four tetrabenzoacene derivatives in their crystalline state by evaluating their reorganization energies and extent of electronic coupling between the neighboring molecular orbitals. The hole reorganization energy values of

the TBA derivatives were observed to be similar, while the electron reorganization energy was comparatively low in TH when compared to the nitrogen-doped TBA derivatives, NTP, BNTP, and NTH, implying the detrimental effect of nitrogen doping to facilitate feasible electron transport. Nonetheless, the equally strong influence of charge transfer coupling (dependent on the crystal packing arrangement of the molecules) ensured vibrant charge mobility characteristics in the TBA crystals. Nitrogen doping showcased yet another influential role in the TBA derivatives in reducing the interplanar spacing between the chromophoric units through a donor–acceptor-type N⋯C interaction between each moiety. Electrostatic surface potential plots revealed the constriction of electron density toward the nitrogen centers to effect in electron-rich points and electron-deficient aromatic core, while the stability of the hence formed molecular stacks was corroborated using symmetry-adapted perturbation theory. Mapping the charge transfer coupling at different pitch and roll displacements of TBA dimers revealed the unconventional capability of highly slip-stacked dimeric arrangements to exhibit efficient charge transport owing to the nature of the distribution of wave functions in the HOMO and LUMO orbitals of the TBA derivatives. The charge transfer coupling evaluated for the crystalline dimers of TBA analogs showed submaximal efficiencies than the ideal cofacial or graphitic AA packing arrangement. As demonstrated by the charge transfer coupling map, the decreased electronic coupling of NTP and BNTP crystals could be attributed to the packing orientation of the constituent dimers resembling the AB-type packing sequence in graphitic materials, while π-extended NTH and TH analogs having widely deviated packing from AB mode showed greater charge-transport efficiency due to an increased percentage of node–node overlap of the molecular orbitals.

4.A.4. Materials and methods

The computational approach adopted to calculate the charge-transport properties of TBA derivatives was based on the Jaguar[177] density functional theory

(DFT) model in the B3LYP/LAC3VP** level of theory from Schrodinger Materials Science Suite 2016-4.[225] The frontier molecular orbitals (FMOs) such as the highest occupied molecular orbitals (HOMOs) and lowest unoccupied molecular orbitals (LUMOs) of the TBA derivatives were evaluated at the DFT B3LYP/6-311G** level of theory using Gaussian-09.[178] Symmetry-adapted perturbation theory (SAPT(0)) calculations which allocated the total dimer interaction energies of TBA derivatives into the contributions of different noncovalent interaction energy parameters such as electrostatics, exchange, induction, and dispersion terms were performed using the Psi4 code[226] with the jun-cc-pvdz basis set.

PART B: Deciphering the Multifarious Charge-Transport Behaviour of Crystalline Propeller-Shaped Triphenylamine Analogues

Abstract

A collection of *para*-substituted propeller-shaped triphenylamine (TPA) derivatives have been computationally investigated for charge-transport characteristics exhibited by the derivatives by using the Marcus–Hush formalism. The various substituents chosen herein, with features that range from electron withdrawing to electron donating in nature, play a key role in defining the reorganisation energy and electronic coupling properties of the TPA derivatives. The TPA moiety is expected to possess weak electronic coupling based on the poor orbital overlap upon aggregation, owing to the restriction imposed by the propeller shape of the TPA core. However, the substituent groups attached to the TPA core can significantly dictate the crystal-packing motif of the TPA derivatives, wherein the variety of noncovalent intermolecular interactions subsequently generated drive the packing arrangement and influence electronic coupling between the neighbouring orbitals. Intermolecular interactions in the crystalline architecture of TPA derivatives were probed by using Hirshfeld and quantum theory of atoms-in-molecules techniques. Furthermore, symmetry-adapted perturbation theory analysis of the TPA analogues has revealed

that a periodic arrangement of energetically stable dimers with significant electronic

coupling is essential to contribute high charge-carrier mobility to the overall crystal.
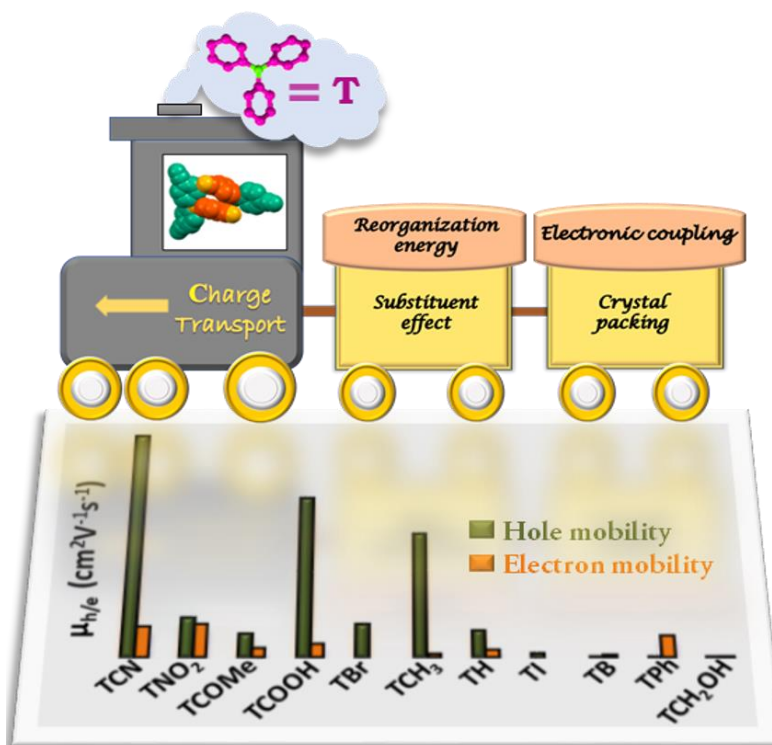
4.B.1. Introduction

Interest in the field of organic semiconductors has burgeoned over the past few decades, with regard to their potential applications as organic displays, organic light-emitting diodes (OLEDs),[227],[228] organic field-effect transistors (OFETs)[229],[230] and photodetectors.[3],[231] The electrical and optical performances of the optoelectronic devices rely on the efficient charge-transporting capabilities of the carrier organic materials contained in the devices. The process of crystallisation is one method for regulating the charge-carrier characteristics of organic materials because molecular ordering and the packing arrangement of the molecules in crystals play a huge role in modulating the charge-transport abilities.[232] The crystalline architectures that encompass higher degrees of intermolecular orbital overlap enhance the mobility of charges throughout the organic charge transporters.[31],[197],[203],[233]–[235] The propeller-shaped triphenylamine (TPA) core has gained immense interest in OLEDs, owing to good thermal stability, a high glass transition temperature, and efficient hole-transporting ability coupled with low ionisation potential.[236]–[241] Functionalisation of the TPA molecule would result in diverse crystalline packing arrangements,[242] which, in turn, could fine-tune the optoelectronic properties of the core TPA moiety by enhancing the π–π interorbital interaction between phenyl rings.[232] Thus, a thorough understanding of the interconnection between the molecular structure, packing arrangement and transport properties is indispensable in designing efficient and economical organic materials that are pertinent for optoelectronic devices.[187],[190]

Herein, we have attempted to perform a comprehensive computational evaluation of the charge-transport characteristics of a collection of crystalline *para*-substituted TPA analogues. Different substituents that vary from electron withdrawing to electron donating in character, upon attachment to the TPA moiety at the -para positions, result in multifarious packing motifs and charge-transport abilities

among the derivatives. In general, the carrier-transport properties of organic molecules are mostly evaluated by using band theory (coherent mechanism), which is suitable for low-temperature conditions, and the hopping mechanism (incoherent mechanism), which is suitable for high-temperature conditions.[241],[243] Herein, we have computed non-adiabatic charge transfer between two neighbouring molecules in the TPA analogues in the hopping regime. The rate of charge transfer evaluated in the hopping regime predominantly depends upon the reorganisation energy, λ, and charge-transfer integral, V.[205],[244],[245] Although there have been reports in the past on the correlation of reorganisation energy with the overall charge-transport abilities of various TPA derivatives by using computationally generated geometries,[236] a complete assessment by utilising the existing crystalline TPA motifs to correlate the reorganisation energy, electronic coupling and transport properties is still in demand. Figure 4.B.1 shows the TPA derivatives evaluated herein. The TPA analogue containing $BO_2C_6H_{12}$ as the substituent moiety was synthesised and crystallised in our laboratory, whereas the crystal structures of the remaining TPA derivatives were accessed from the Cambridge Structural Database (CSD).
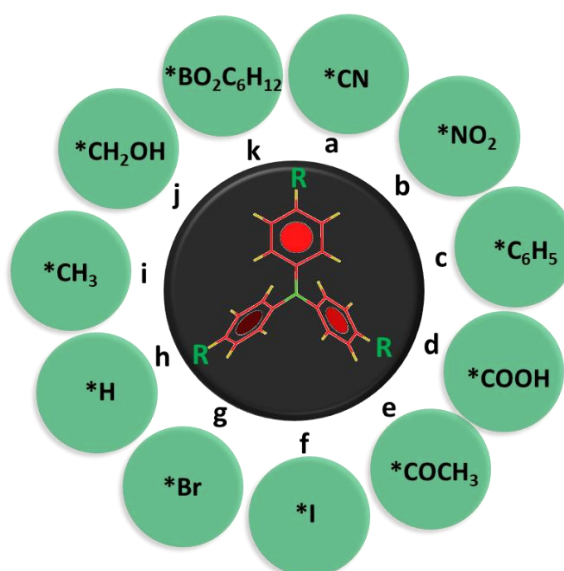
Figure 4.B.1: *Derivatives of TPA: a) TCN, b) TNO2, c) TPh, d) TCOOH, e) TCOMe, f) TI, g) TBr, h) TH, i) TCH3, j) TCH2OH and k) TB.*

4.B.2. Results and Discussion

A single molecule of TPA is C_3 symmetrical and propeller-shaped, owing to the sp^3-nitrogen core, which is predicted to have a low carrier mobility due to the lower extent of orbital overlap expected between the non-planar phenyl rings of TPA upon aggregation. However, despite the non-planar shape, the substituent groups present in the TPA moiety can contribute to a wide range of interactions in the crystals, eventually leading to different packing motifs. This facilitates tuning of the charge-carrier mobility of a crystal, along with the reorganisation energy of the molecule. Gescheidt and co-workers paved the way to understanding the effect of the substitution on the reorganisation energy of TPA analogues by undertaking a theoretical analysis with computationally generated structures of various TPA derivatives.[236] However, according to Marcus theory, the mobility of charge carriers in organic crystals relies on both intramolecular reorganisation energy (λ) and the charge-transfer integral (electronic coupling, *V*) between the molecules. Therefore, herein we attempt to expound on the effect of the substituent on the charge-carrier ability of crystalline TPA derivatives by probing both the reorganisation energy and electronic coupling of molecules in their crystalline geometry.

The crystallographic information files (.cif) of propeller-shaped TPA derivatives, except TB, were extracted from CSD version 5.38 by using ConQuest 1.19 as the search engine. Qualitative single-crystal analysis of TB, which was synthesised and crystallised in our laboratory, revealed an orthorhombic crystal system in the *Pbca* space group (Tables B.C.1 and B.C.2 in Appendix). Subtle non-covalent interactions, such as C–H···π, π–π, H···H, dihalogen and hydrogen-bonding interactions, predominantly directed the crystalline packing of TPA derivatives, thereby leading to the eclectic range of properties exhibited by the crystals. In addition, TPA derivatives possessed many other remarkable interactions, which resulted in the crystal-packing arrangement of the series of TPA derivatives analysed herein.

In detail, the crystal packing of TCN and TNO$_2$ crystals comprised of a wave-like arrangement of molecules extending along the *a* axis (Figure 4.B.2). Whereas the C−H···π interaction ($d_{\text{C-H}\cdots\pi}$=2.79 Å) alone contributed to the wave-like packing in TNO$_2$, an interplay of both C−H···π and N−C···π ($d_{\text{C-H}\cdots\pi}$=2.85 Å and $d_{\text{N-C}\cdots\pi}$=3.27 Å) interactions directed the crystal packing of TCN. In addition, weak C−H···O hydrogen-bonding interactions ($d_{\text{C-H}\cdots\text{O}}$=2.50, 2.56 and 2.60 Å) also influenced the crystalline packing of TNO$_2$. In the TCOMe crystal, C−H···π ($d_{\text{C-H}\cdots\pi}$=2.71, 2.82 and 2.85 Å) and C−H···O ($d_{\text{C-H}\cdots\text{O}}$=2.67 Å) interactions resulted in a wave-like packing arrangement, which was directed along the *c* axis (Figure 4.B.2).[246] The crystal structure of halogen-substituted TPA derivatives, TBr and TI, were marked by a wave extending along the *b* and *c* axes, respectively (Figures 4.B.2 and 4.B.3). C−H···π interactions ($d_{\text{C-H}\cdots\pi}$=2.87 and 2.82 Å) contributed to the crystal packing in TI, whereas diverse interactions, such as C−H···π ($d_{\text{C-H}\cdots\pi}$=2.80, 2.68 and 2.80 Å), C−Br···π ($d_{\text{C-Br}\cdots\pi}$=3.46 Å), Br···H ($d_{\text{Br}\cdots\text{H}}$=2.96 Å) and a Br···Br dihalogen interaction ($d_{\text{Br}\cdots\text{Br}}$=3.52 Å) aided in the crystal packing of TBr. The intermolecular interactions that governed the crystalline packing of TCH$_3$ and TH
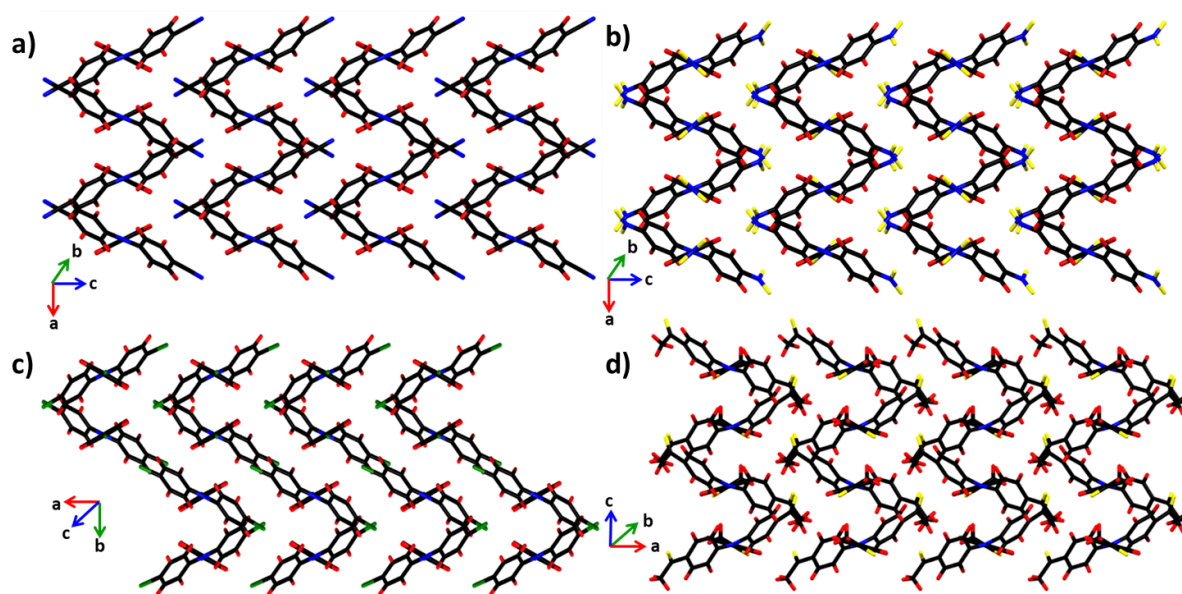
Figure 4.B.2: *Wave-like crystalline-packing arrangements of a) TCN, b) TNO2, c) TBr and d) TCOMe.*
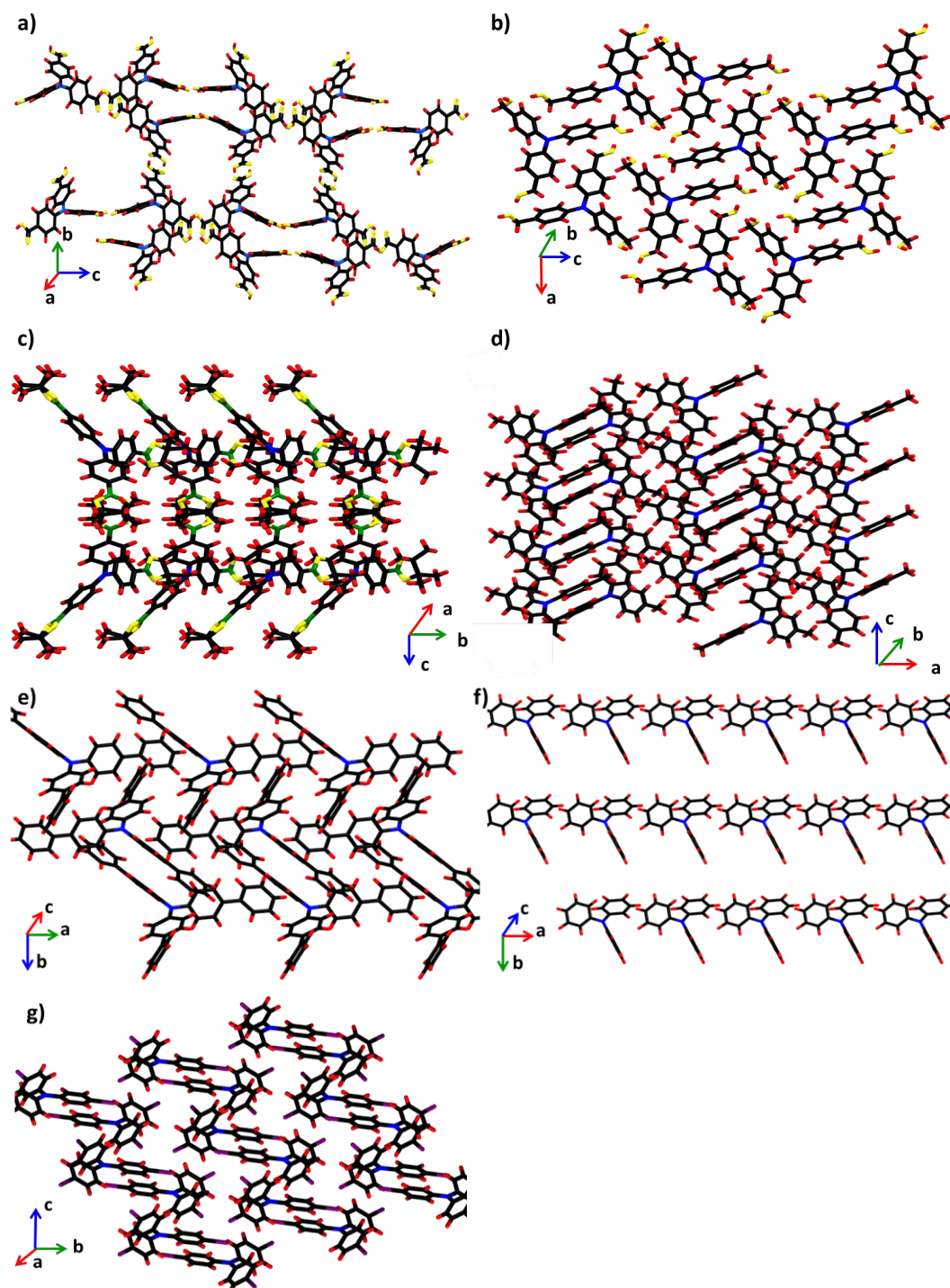
Figure 4.B.3: *Crystal packing diagrams of a) TCOOH, b) TCH2OH, c) TB, d) TCH3, e) TPh, f) TH and g) TI.*

included C−H···π ($d_{\text{C−H···π}}$=2.88 and 2.87 Å) and H···H interactions (ranging from 2.34 to 2.60 Å), whereas C−H···π noncovalent interactions at distances of 2.79 and 2.87 Å facilitated the crystal-packing arrangement in TPh (Figure 4.B.3).[247] The presence of

boron atoms introduced intermolecular B···H interactions into the TB crystal ($d_{B···H}$=2.95 Å), which influenced the crystal packing of TB. C−H···π and H···H interactions, along with hydrogen-bonding interactions, operating at distances of 1.87, 2.72 and 2.34 Å, respectively, directed the crystal packing of TCH$_2$OH (Figure 4.B.4).[248] Interestingly, crystal structure analysis of TCOOH revealed the presence of voids (approximate volume 600 Å^3) in the crystal (Figure 4.B.4); an effect of strong cyclic hydrogen-bonding interactions ($d_{O···H}$=1.77 Å), which resulted in a network arrangement.[249] The cyclic hydrogen-bonding interaction was found to be a characteristic property of the TCOOH crystal, and it is possible that the absence of such cyclic hydrogen-bonding interactions in the TCH$_2$OH derivative might have resulted in the lack of voids of large volume in the TCH$_2$OH crystal. C−H···O non-classical hydrogen bonding ($d_{C-H···O}$=2.54 Å), C−H···π ($d_{C-H···π}$=2.74 Å) and O−H···C ($d_{O-H···C}$=2.67 Å) are the other major interactions that contribute to the overall packing of the TCOOH crystal. No discernible wave-like pattern could be observed in crystals of hydrogen-bonded (TCOOH and TCH$_2$OH) and hydrocarbon-substituted (TCH$_3$ and TPh) TPA derivatives, in addition to TB and TH crystals. The prominent wave-like pattern of molecules in TPA crystals implicate a well-ordered and patterned arrangement of nonplanar TPA derivatives.
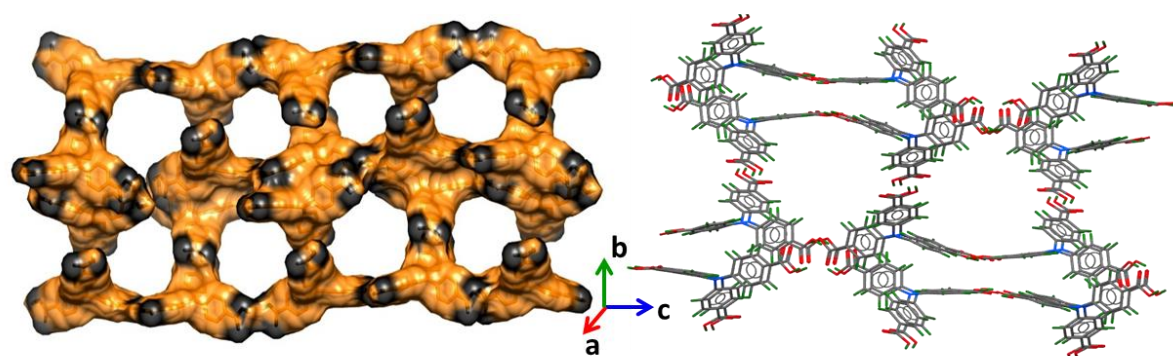
Figure 4.B.4: *Shows the voids present in TCOOH crystal formed due to the cyclic hydrogen bonds.*

Hirshfeld surface (HS) analysis, which is a remarkable method to explore the packing modes and intermolecular interactions in molecular crystals by using partitioning of crystal space, was carried out to quantify the weak intermolecular interactions present in the TPA derivatives (Figure 4.B.5).[124],[250],[251] Different packing modes of a molecular crystal, as defined by the ρ (ratio of %C···H to %C···C interactions) values in HS analysis, include herringbone ($\rho>4.5$), sandwich herringbone ($3.2<\rho<4.0$), gamma (γ) ($1.2<\rho<2.7$), and β ($0.46<\rho<1.0$) type packing arrangements.[252] The studied TPA derivatives, with the exception of TCN, TNO$_2$ and TCOMe, have ρ values in the range of about 8–73, which is indicative of a herringbone packing motif (face-to-edge-type packing arrangement). TCN (ρ=1.80) and TNO$_2$ (ρ=2.03) derivatives have ρ values indicating the gamma packing arrangement (face-to-face packing arrangement), whereas the ρ value of TCOMe (ρ=4.42) falls in the range expected for a sandwich herringbone type packing motif. An increase in the percentage of C···C contacts, resulting in the concomitant transformation from herringbone- to gamma-type packing, was observed with a corresponding increase in the electron-withdrawing nature of the substituent group attached to the TPA moiety. The observed increment in C···C contacts could be attributed to decreased electron density on the phenyl rings of TPA derivatives
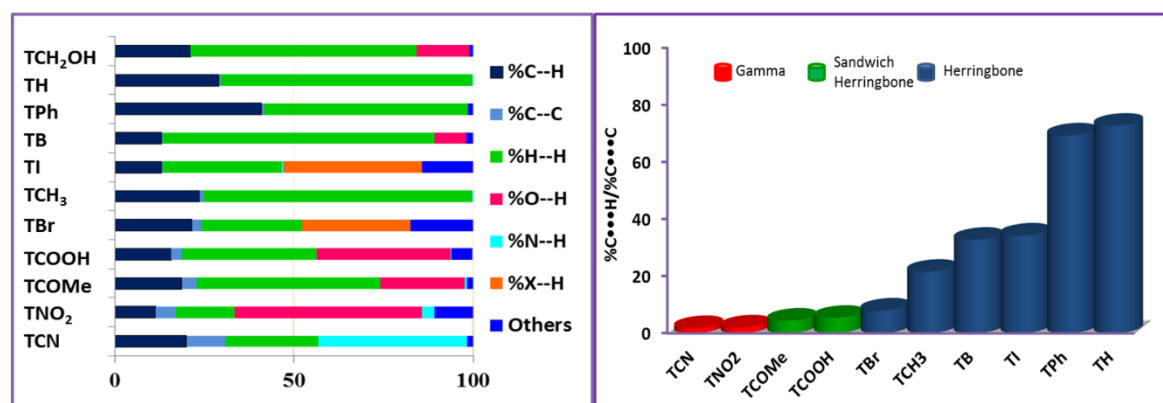
Figure 4.B.5: *Stacked bar plot of HS analyses (left) and ρ values of derivatives of TPA calculated from analysis of 2D fingerprint plots (right).*

substituted with electron-withdrawing groups, which, in turn, would enhance the scope of face-to-face arrangement (π–π stacking) in the crystals. Improved π stacking with an increase in %C$\cdots$C contacts is evident in TCN and TNO$_2$ derivatives, wherein one out of the three phenyl rings of each TPA moiety are aligned face to face with another phenyl ring of the adjacent molecule. Separations between phenyl rings aligned in this way are 4.70 and 4.89 Å in TCN and TNO$_2$ derivatives, respectively. N$\cdots$H interactions (41.2 %), along with C$\cdots$H (19.9 %), C$\cdots$C (11.1 %) and H$\cdots$H (25.9 %) interactions, dictated the packing of TCN, whereas TNO$_2$ crystal packing was determined by C$\cdots$C (5.6 %), C$\cdots$H (11.4 %), H$\cdots$H (16.3 %), C$\cdots$N (2.7 %), N$\cdots$H (3.5 %), C$\cdots$O (3.6 %) and N$\cdots$O (1.9 %) interactions. The acetyl group is less electron withdrawing in nature, relative to cyano and nitro groups, so the ρ value of TCOMe crystal increases to 4.42, with a decrease in %C$\cdots$C interactions compared with those of TCN and TNO$_2$ crystals. Additionally, H$\cdots$H (51 %) and C–O$\cdots$H (23.6 %) interactions also contributed to the total HS of TCOMe. Fingerprint plots of TH, TPh, TB and TCH$_3$ revealed the presence of C$\cdots$C, C–H$\cdots$$\pi$ and H$\cdots$H interactions in the range of 0.6–1.1 %, 13.1–41.6 %, and 57.8–75.8 %, respectively. Moreover, B$\cdots$H (1.9 %) and O$\cdots$H (8.7 %) interactions also contributed to the HS of TB. HS analysis indicated the presence of Br$\cdots$Br and I$\cdots$I dihalogen interactions in TBr and TI crystals, respectively. Furthermore, C$\cdots$C (2.7 and 0.4 %), C$\cdots$H (21.6 and 13.7 %), H$\cdots$H (28 and 33.6 %) and X$\cdots$H (X=Br and I, 38.9 and 34.6 %) interactions also influenced the crystalline packing of TBr and TI derivatives. TCOOH with 2.9 % C$\cdots$C contacts and 15.7 % C$\cdots$H contacts resulted in a ρ value of 5.41. Hydrogen-bonding interactions contributed to 37.3 % of the total HS in TCOOH and 14.8 % in TCH$_2$OH. Interestingly, analysis of the TCH$_2$OH crystal revealed no C$\cdots$C contacts; hence the ρ value converged to infinity.

The charge-transport characteristics of the TPA crystals were investigated by employing first-principles quantum mechanical calculations through the method established by Goddard and Deng.[253] Marcus theory expresses the rate of charge

transfer between molecules in terms of the coupling matrix element and reorganisation energy of the molecule. Electronic coupling between the molecular orbitals and reorganisation energy of individual molecules are the major factors that affect the charge-transport properties. The functional groups on the TPA molecule alter molecular vibrations, so that the reorganisation energy will be affected.[55] The electrostatic surface potential (ESP) was generated at the B3LYP/6-311G+(d,p) level of theory to gain further insight into the effect of substituent groups by qualitatively providing a picture of the electron density distribution in the TPA derivatives (Figure 4.B.6). Electropositive and electronegative regions of the ESP surfaces are represented in blue and red, respectively, in the ESP plots. The transformation of phenyl rings from electron rich to electron deficient in nature was observed with increasing electron-withdrawing ability of substituent groups attached to the TPA moiety. For instance, the phenyl rings of TCN are blue, whereas the TPh phenyl rings are red in Figure 4.B.6.
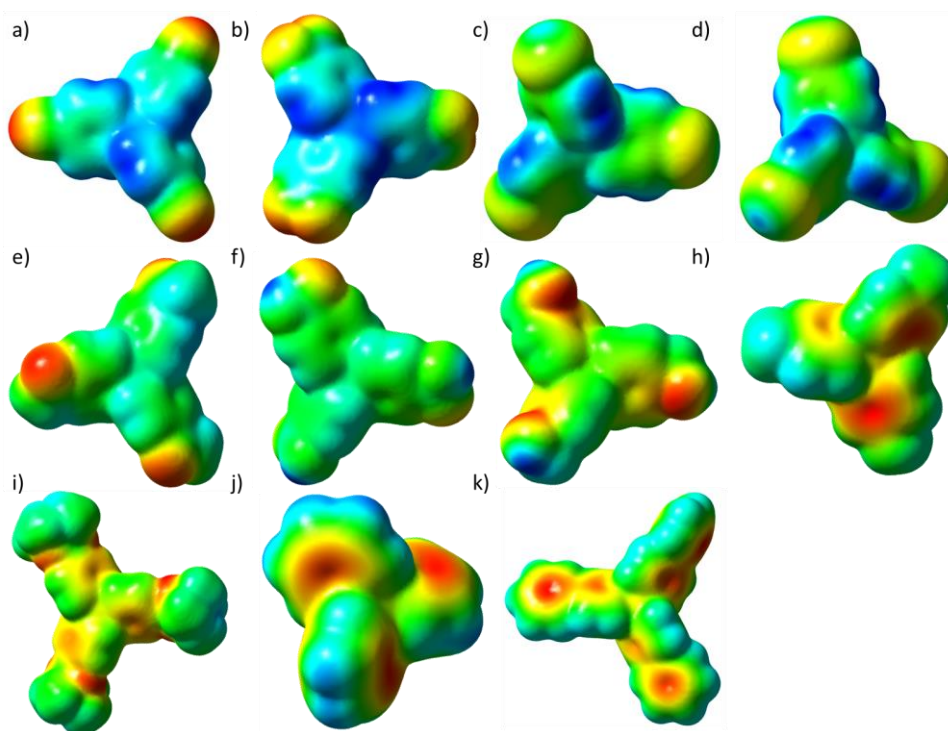
Figure 4.B.6*: ESP surfaces of a) TCN, b) TNO2, c) TBr, d) TI, e) TCOMe, f) TCOOH, g) TCH2OH, h) TCH3, i) TB, j) TH and k) TPh.*

QTAIM analysis offered further insights into noteworthy intermolecular interactions that defined the packing arrangement of molecules in the TPA crystals (Figures 4.B.7 and 4.B.8). TPA derivatives that displayed distinct intermolecular interactions in the crystal-packing arrangement (obtained from HS analysis) were chosen for QTAIM analysis. Bond critical points (BCP) and bond paths (BP) were determined while performing QTAIM calculations and the positive electron density at BCP confirmed the existence of short contacts between interacting atoms in the TPA molecules. TCOMe displayed several intermolecular C−H···O short contacts in the range of 2.67–6.56 Å, with varying electron densities. QTAIM analysis of TCOOH demonstrated the existence of an O···C interaction at a distance of 3.11 Å and an O···O interaction at a distance of 3.24 Å. To probe the nature of the O···O interaction in TCOOH, the Pendas interacting quantum atoms (IQA) analysis[254]–[256] was performed on the derivative. The net interaction energy, E_{IQA}, obtained from the IQA analysis determines whether the interaction is repulsive or attractive. The E_{IQA} value obtained from the IQA analysis of TCOOH revealed the destabilising nature of the O···O interaction (Table 4.B.1).[257] Strong hydrogen bonding between oxygen and hydrogen atoms at a distance of 1.77 Å, with a high electron density value of 0.25 a.u. at the BCP, was identified in TCOOH, whereas weaker acyclic hydrogen bonding was found to exist in the TCH_2OH crystal, at a distance of 1.87 Å with a relatively reduced electron density of 0.18 a.u. at the BCP.
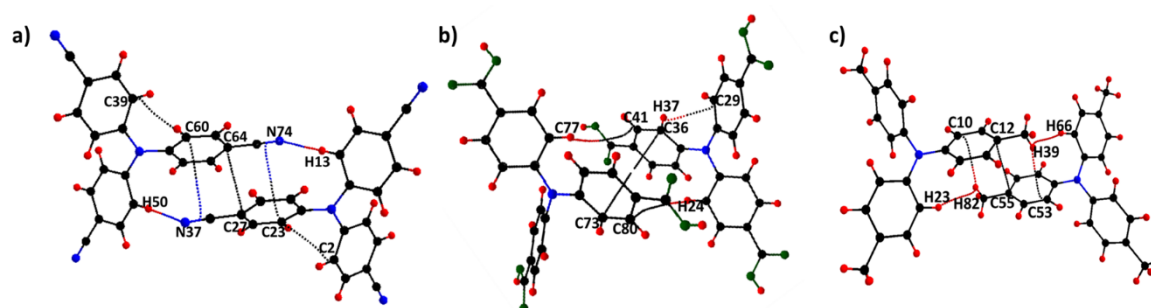
Figure 4.B.7: *Quantum theory of atoms-in-molecules (QTAIM) images of a) D1 of TCN, b) D of TCOOH and c) TCH3.*
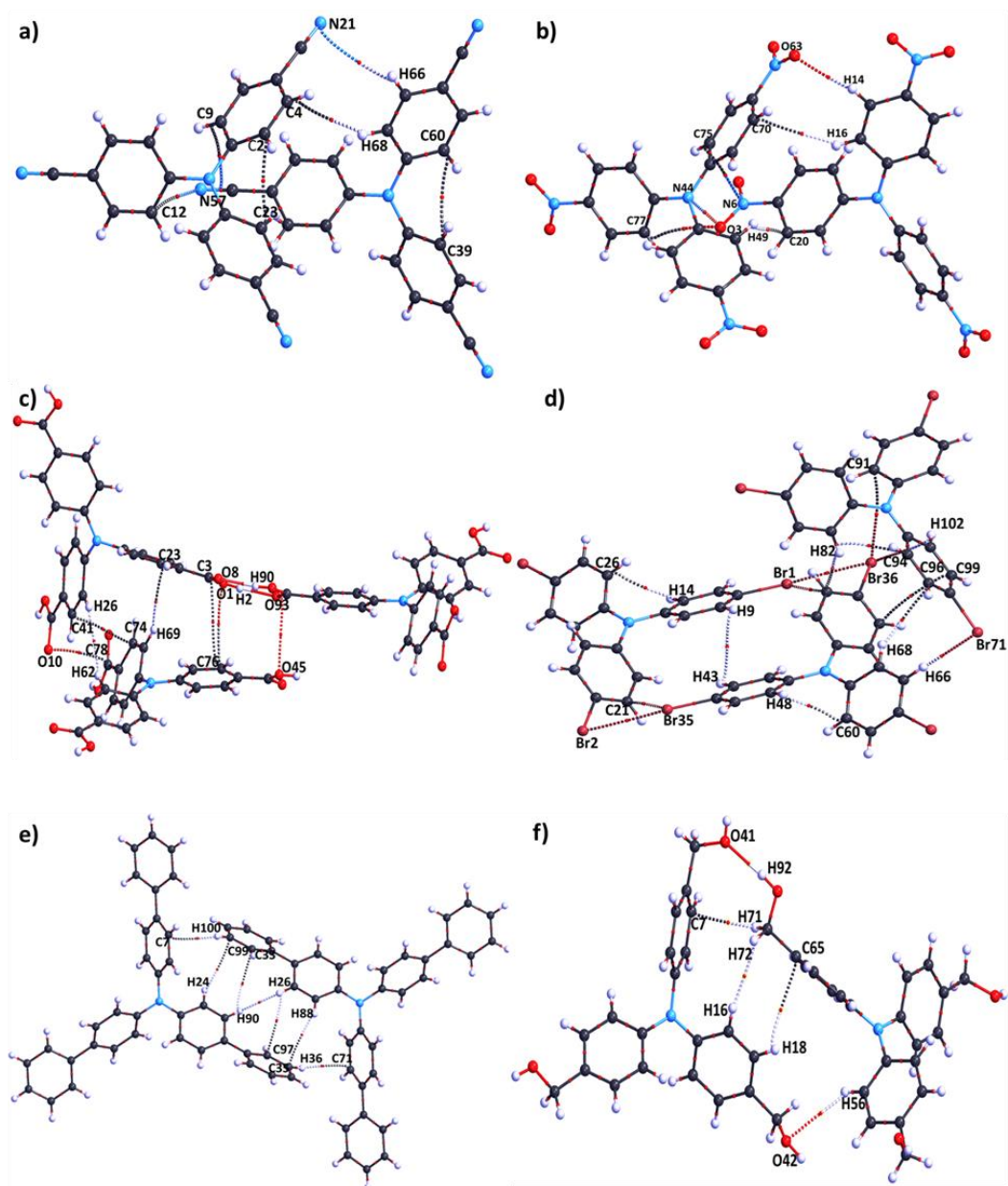
Figure 4.B.8: *QTAIM images of a) D2 of TCN, b) TNO2, c) TCOOH, d) TBr, e) TPh and f) TCH2OH.*

QTAIM analysis of the TBr crystal revealed a Br⋯Br dihalogen interaction at 3.52 Å. The Br⋯Br interaction was found to be attractive in terms of E_{IQA} energy (Table 4.B.1), and was observed to constitute type II dihalogen bonding. Dihalogen interactions are classified into type I (if $\theta_1=\theta_2$) and type II (if $\theta_1=90°$ and $\theta_2=180°$) classes based upon the interacting angles, θ_1 and θ_2, and generally the dihalogen interactions falling into

Table 4.B.1: *Results of IQA analyses*

Interaction	$E_{IQA}(A,B)$	$V_{ne}(A,B)$	$V_{en}(A,B)$	$V_{ee}(A,B)$	$V_{nn}(A,B)$	$V_{ee}C(A,B)$	$V_{ee}X(A,B)$
Br•••Br (TBr)	-1.91×10^{-2}	-1.842×10^{1}	-1.842×10^{1}	1.844×10^{1}	1.821×10^{1}	1.844×10^{1}	-1.474×10^{-2}
O•••O (TCOOH)	4.76×10^{-2}	-2.945	-2.951	3.345	2.598	3.345	-2.376×10^{-1}
C•••H (TCH$_3$)	$-9,51\times10^{-3}$	-1.548	-1.908	1.893	1.554	1.903	-9.753×10^{-3}
C•••C (TCH$_3$)	3.06×10^{-4}	-1.187	-9.413×10^{-1}	1.190	9.385×10^{-1}	1.190	-5.240×10^{-4}

$E_{IQA}(A,B) = V_{ne}(A,B) + V_{en}(A,B) + V_{ee}(A,B) + V_{nn}(A,B)$ in kJ/mol. $V_{ne}(A,B)$ = attraction energy between nucleus of atom A and electron density distribution of atom B in kJ/mol. $V_{en}(A,B)$ = attraction energy between electron density distribution of atom A and nucleus of atom B in kJ/mol. $V_{ee}(A,B)$ = two electron interaction energy between atom A and atom B in kJ/mol. $V_{nn}(A,B)$ = repulsion energy between nucleus of atom A and nucleus of atom B in kJ/mol. $V_{ee}C(A,B)$ = coulomb part of $V_{ee}(A,B)$ in kJ/mol. $V_{ee}X(A,B)$ = exchange correlation part of $V_{ee}(A,B)$ in kJ/mol.

the type II category are rarely observed among halogen-containing crystals.[28],[258] The ESP surface generated for TBr unveiled a sigma hole on bromine, which further substantiated the presence of type II halogen-bonding interactions in the TBr crystal. C−H⋯Br weak hydrogen bonding at 3.07 Å and a π⋯Br halogen-bonding interaction at 3.66 Å are the other interactions observed in the TBr crystal. In contrast, the TI crystal did not exhibit any halogen-bonding interactions, in spite of a prominent sigma hole being observed on iodine in the ESP surface.

QTAIM analysis of TCN revealed the existence of intramolecular C⋯C interactions between two phenyl rings of the TCN molecule at a short distance of 2.98 Å, with a substantial positive electron density of 0.077 a.u. at BCP. The gamma-type packing arrangement established two different kinds of dimers, which characterises the crystal packing in both TCN (Figure 4.B.9) and TNO$_2$. The presence of O⋯N short contacts ($d_{N⋯O}$=3.47 Å) with an electron density of 0.024 a.u. and N⋯C interactions at a distance of 3.26 Å (ρ=0.034 a.u.) were identified in the TNO$_2$ crystal. Moreover, C−H⋯N weak hydrogen bonding was also observed in the TNO$_2$ crystal, operating at a distance of 2.60 Å and with an electron density of 0.043 a.u. QTAIM analysis was performed separately on the two different kind of dimers of TCN, with an

intermolecular distance of 9.35 (D1) and 7.11 Å (D2) between the centroids of monomers (Figure 4.B.9).[259] D1 and D2 of TCN derivatives both contained C−N···π and C−H···N interactions at distances of 3.43–3.90 and 2.77–3.88 Å,
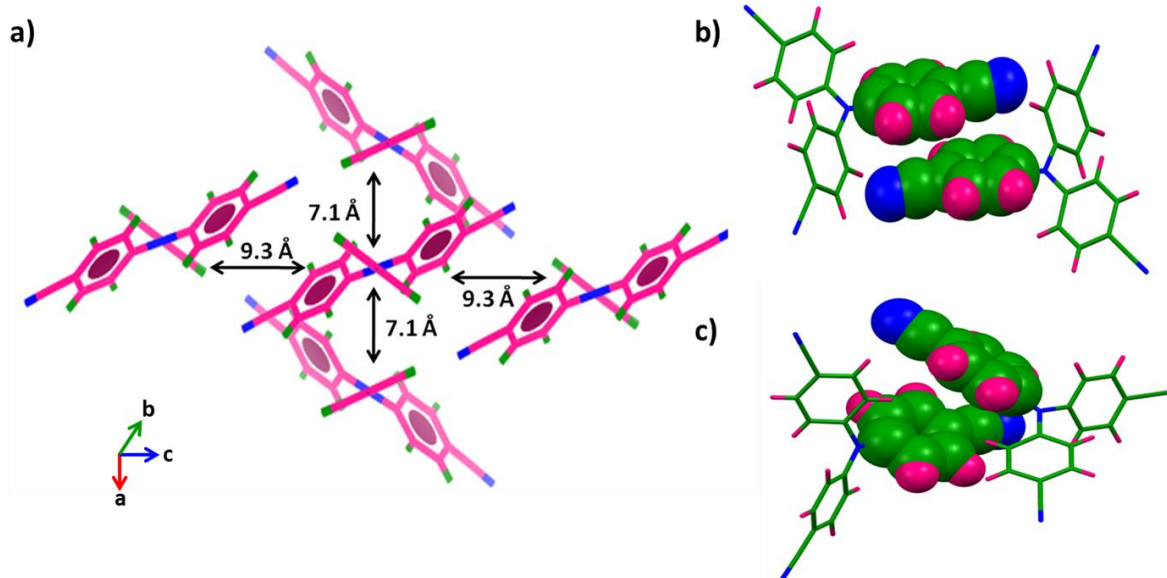
Figure 4.B.9*: a) Structures of dimers 1 (D1) and 2 (D2) that constitute the crystalline-packing motif of TCN. Overlap between the phenyl rings of b) D1 and c) D2.*

respectively. QTAIM analysis revealed a π−π intermolecular interaction at a distance of 3.76 Å in D1 (Figure 4.B.7), whereas the intermolecular π−π interaction was absent in D2. The presence of intermolecular π−π interactions in D1 substantiated the considerable contribution of D1 to the establishment of gamma packing in the TCN crystal. Crystal-structure analyses revealed that, out of all of the diverse intermolecular interactions that governed the packing arrangement of TPA crystals, π−π non-covalent interactions predominantly facilitated the characteristic gamma packing motif of TCN and TNO$_2$ crystals among the TPA derivatives. The key role played by the π−π interactions in TCN and TNO$_2$ can be attributed to the high electron-withdrawing nature of the CN and NO$_2$ moieties in comparison with the remaining units contained in the TPA derivatives. The gamma packing arrangement thus preferred in TCN and TNO$_2$ has profusely affected the charge-transport

characteristics of TCN and TNO$_2$, among all TPA derivatives, owing to the improved overlap of molecular orbitals contained in the phenyl rings.

The overall charge-transport characteristics of the TPA crystals were evaluated by employing the Marcus–Hush formalism, and the results are presented in Figure 4.B.10 and Table 4.B.2. Generally, TPA crystals are classified as hole transporters and, among the series of TPA derivatives considered, TCN, TCOOH and TCH$_3$ exhibited significant hole-transport characteristics. The electron mobility values of the TPA derivatives studied were found to be low relative to the hole mobility. The halogenated TPA derivatives, TBr and TI, have a high hole reorganisation energy that, if coupled with a herringbone packing arrangement, proved to be detrimental for efficient hole-transport properties. Furthermore, TB, TPh and TCH$_2$OH showcase comparatively low hole mobility due to the high hole reorganisation energy, along with a low intermolecular coupling ability. Hence, regardless of having a wide variety of intermolecular interactions, suitable crystal packing for an efficient hole-transporting nature could not be achieved by the above-mentioned TPA derivatives (TBr, TI, TB, TPh and TCH$_2$OH), and hence, showed insignificant hole mobility compared with that of TCN, TCOOH and TCH$_3$. Despite having a favourable

Figure 4.B.10: *Graphical representation of hole and electron mobility of TPA derivatives*

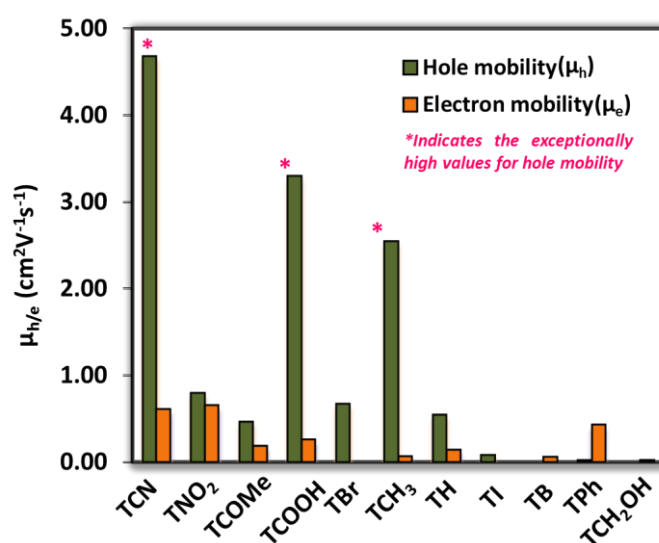**Table 4.B.2:** *Results obtained from mobility calculations performed on the TPA derivatives based on Marcus theory of charge-transfer rates.[a]*

Molecule	λ_h (eV)	λ_e (eV)	V_h (eV)	V_e (eV)	k_h (s^{-1}, ×10^{13})	k_e (s^{-1}, ×10^{13})	μ_h (cm^2 V^{-1} s^{-1})	μ_e (cm^2 V^{-1} s^{-1})
TCN	0.073	0.174	0.054	0.042	9.081	2.291	4.67	$6.02×10^{-1}$
TNO$_2$	0.125	0.290	0.037	0.045	2.176	0.503	$7.93×10^{-1}$	$6.47×10^{-1}$
TCOMe	0.138	0.323	0.031	0.041	1.154	0.198	$4.65×10^{-1}$	$1.84×10^{-1}$
TCOOH	0.150	0.315	0.084	0.083	4.844	1.015	3.29	$2.53×10^{-1}$
TBr	0.129	2.74	0.066	0.150	5.842	0.001	$6.66×10^{-1}$	$1.09×10^{-11}$
TCH$_3$	0.123	0.338	0.057	0.067	3.852	0.385	2.54	$6.85×10^{-2}$
TI	0.114	1.18	0.014	0.095	0.378	0.002	$7.70×10^{-2}$	$2.05×10^{-5}$
TB	0.179	0.368	0.001	0.052	0.002	0.316	$1.77×10^{-3}$	$5.49×10^{-2}$
TPh	0.125	0.262	0.007	0.059	0.078	0.922	$2.04×10^{-2}$	$4.23×10^{-1}$
TH	0.099	0.109	0.009	0.028	1.398	0.040	$5.43×10^{-1}$	$1.38×10^{-1}$
TCH$_2$OH	0.383	0.164	0.016	0.026	0.019	0.629	$6.01×10^{-3}$	$2.01×10^{-1}$

λ_h = hole reorganization energy; λ_e = electron reorganization energy, V_h = highest HOMO charge transfer coupling; V_e = highest LUMO charge transfer coupling, k_h = highest hole hopping rate; k_e = highest electron hopping rate, μ_h = hole mobility; μ_e = electron mobility.

sandwich herringbone and gamma-type packing arrangement, TCOMe and TNO$_2$ crystals, respectively, showcased a low hole transporting capability, as a result of a significantly higher hole reorganisation energy. TCN possessed the highest hole mobility among the TPA derivatives, which could be a consequence of both the gamma-type packing arrangement and very low value for the hole reorganisation energy (0.073 eV). Generally, functional groups attached to the parent molecule increase the reorganisation energy by providing a greater number of molecular vibrational modes.[212],[260] However, earlier theoretical works demonstrated that the substitution of a cyano group was an exception, and considerably reduced the internal reorganisation energy of a molecule.[55],[261] In addition, cyanation

increased electronic coupling between neighbouring molecules by promoting π-stacking between them. Major contributing dimers of TCN for charge transport are shown in Figure 4.B.9. Interestingly, a 1D hole-transporting pathway with an exceptional hole mobility of 15.3 cm^2 V^{-1} s^{-1} was observed for TCN by extending the dimer, D1 (explained in the section on QTAIM analysis), along the *c* axis (Figure 4.B.11). Attaining a highly conducting 1D charge-transport pathway is favourable in the development of efficient optoelectronic devices. The fabrication of an extended system constituted by monomer D1 has resulted in the development of a 1D hole-transporting pathway, thereby bestowing significant transport properties on the TCN crystal.[262] In organic semiconductors, the charge-transport characteristics are affected by the extent of overlap between the corresponding molecular orbitals of neighbouring molecules. The hole mobility across an organic crystal is determined by the degree of overlap between the HOMOs of adjacent molecules, whereas the overlap of corresponding LUMOs profoundly affect the electron mobility of the crystal.[217],[263]

Hence, to better explain the charge-carrier abilities of the TCN molecule, frontier molecular orbital (FMO) analysis of the TPA derivative was performed by using the B3LYP/6-311G+(d,p) basis set. FMO analysis revealed a uniform distribution
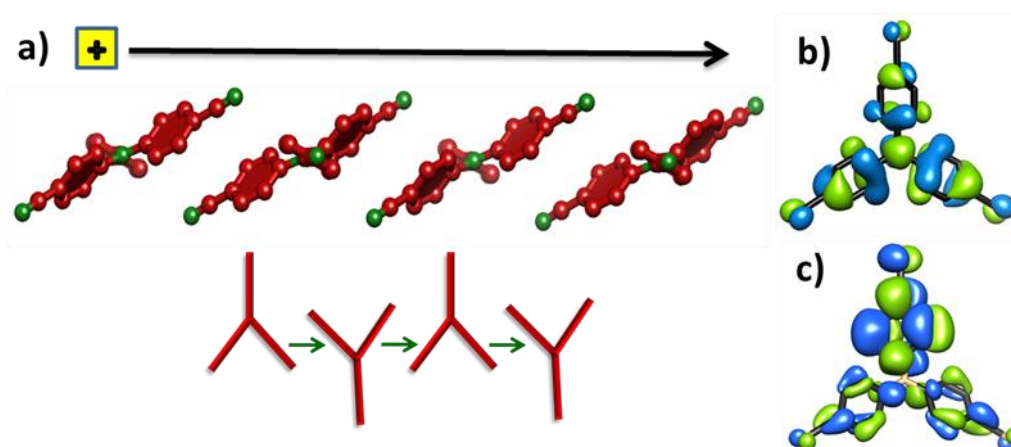

Figure 4.B.11: *a) 1-D hole transporting pathway of TCN crystal; b) HOMO and c) LUMO orbitals of TCN (Surfaces are at isovalue of 0.02 e/Å^3).*

of electron density over the three phenyl rings of the TPA moiety in the HOMO of TCN derivative (Figure 4.B.11). Consequently, upon extending the TCN molecule along the c axis, efficient overlap of the HOMOs between the phenyl rings of adjacent molecules was observed; this possibly played a key role in generating a 1D hole-transport pathway of high hole mobility. However, the LUMOs are constituted by an asymmetric distribution of electrons, and the electron density is concentrated on only one of the three phenyl rings of the TPA moiety in TCN. Thus, in contrast to the hole-transporting ability of TCN, the electron-transport characteristics are comparatively inefficient because the asymmetric distribution of electron density over the phenyl rings in the LUMO would ensure quality overlap with only one of the immediate neighbours. Hence, the extension of D1 or D2 cannot generate a 1D electron-transporting pathway in the TCN derivative. Dimers D1 and D2 of TCN, which resulted from the gamma packing motif, are different in terms of the contribution towards charge-transfer coupling. To understand the relationship between the stability of the dimers and the observed mobility of the constituent dimers of TCN, symmetry-adapted perturbation theory (SAPT) analysis[98],[125] was employed (Table 4.B.3). SAPT analysis offered a quantitative picture by determining the total interaction energy of dimers, along with the physical contributions in stabilising the dimers, such as electrostatics, induction, dispersion and exchange energies (unlike the qualitative data obtained from ESP). A more negative SAPT(0) energy obtained for D1 indicated greater stability of D1 over that of D2 in TCN. The electrostatic contribution to stability was much more pronounced in D1 than that in D2, which was consistent with the presence of $\pi-\pi$ intermolecular interactions in D1 obtained from QTAIM analysis.[264] Because of the small separation between the monomers of D2, the contribution of dispersion energy dominated in stabilising D2. Thus, the dimer contributing more to gamma packing and with greater charge-transfer coupling, D1, was found to be more stable.

Table 4.B.3: *Results obtained from SAPT(0) analyses.*[a]

	d(Å)	E_e	E_i	E_d	E_{ex}	E_t
D1	9.3	-22.1	-7.4	-34.5	19.1	-43.8
D2	7.1	-9.9	-5.8	-49.5	30.6	-34.5

[a]d = Dimer separation; E_e = Electrostatic energy in kJ/mol; E_i = Induction energy in kJ/mol; E_d = Dispersion energy in kJ/mol; E_{ex} = Exchange energy in kJ/mol; E_t = Total SAPT(0) energy in kJ/mol.

Because the TCN derivative possesses high hole mobility among all TPA derivatives with a gamma-type packing arrangement, anisotropic mobility calculations[222],[265],[266] were performed on TCN to understand the angular variation of mobility for both holes and electrons along the a^*c^* plane of TCN. The calculated anisotropic hole mobility reaches a maximum of 6.284 cm² V⁻¹ s⁻¹ along the directions Φ=160 and 340°, whereas a minimum hole mobility value of 0.818 cm² V⁻¹ s⁻¹ was obtained along the directions of Φ=50 and 250° (Figure 4.B.12). Hence, the TCN crystal has an anisotropy (ratio of highest to lowest hole mobility) of 7.68 along the *ac* plane, which implies that the effective mobility displayed by the crystal upon use in OFETs would vary significantly with the orientation of the crystal with the transistor channel. The maximum hole mobility is observed along the crystallographic *c* axis, which corresponds to the direction of extension of dimer D1. Due to the additional hole mobility contributions from neighbouring molecules oriented in other directions to the D1 extension channel, the maximum anisotropic mobility value is not comparable with the obtained 1D hole mobility value. The minimum value has been observed along the *a* axis, which is orthogonal to the axis of reference (*c* axis). The highest mobility value along the *c* axis is a result of better orbital overlap and larger charge-transfer integral of D1. The maximum hole mobility directed along the *c* axis further substantiated the presence of an efficient 1D hole transport pathway, which could be exploited for use in electronic applications necessitating high mobility. Electronic mobility is not significant in comparison with the hole-transport ability of TCN, and is represented by the red plot in (Figure 4.B.12). Surprisingly, TCOOH and
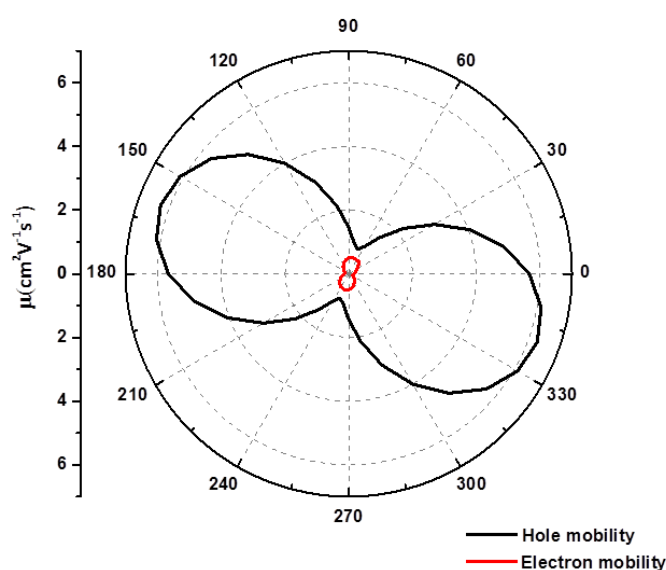
Figure 4.B.12*: The predicted anisotropic hole and electron mobilities for the TCN crystal.*

TCH$_3$ crystals exhibited significant charge-transport characteristics, even though they lacked an efficiently organised arrangement of molecules in the crystal state. The presence of voids in TCOOH, as established by cyclic hydrogen-bonding interactions, is attributed to the high hole-carrier mobility in the TCOOH crystal, although individual TCOOH molecules have a high hole reorganisation energy of 0.15 eV. The periodic organisation of voids in the TCOOH crystal, as highlighted by Vaidhyanathan and co-workers,[249] resulted in a 1D hole-transporting channel constituted by the extension of dimer D along the *a* axis.

Dimer D (Figure 4.B.7) greatly contributed to the high hole-transporting ability of the TCOOH crystal. Individual dimer (D) units are separated by a large distance of 8.89 Å, yet the dimer possesses high electronic coupling (0.08 eV) between the constituent monomers, which, in turn, result in the high charge-carrier transport ability of dimer D. In spite of having a ρ value of 21.54, the TCH$_3$ crystal exhibited appreciable hole mobility, with a drift mobility value of 2.54 cm^2 V^{-1} s^{-1}. The values of ρ have been calculated for all TPA crystals, and the high ρ values (ρ>4.5) are indicative of the herringbone packing motif. In the TCH$_3$ molecule (with a methyl substituent on

the phenyl ring), part of the C−H···π contacts were contributed by the interactions between methyl hydrogen atoms and the carbon on the phenyl ring of TCH$_3$. In detail, TCH$_3$ showed high hole mobility for the following reasons: 1) Contrary to C−H···π contacts, wherein both participating atoms are from the phenyl rings, C−H···π interactions between methyl hydrogen atoms and phenyl carbon atoms in TCH$_3$ promote face-to-face packing through π–π interactions rather than edge-to-face packing (Figure 4.B.7). Because calculations of the ρ value might overestimate the herringbone character of crystal packing in TCH$_3$, correlation of the ρ value with charge-transport properties cannot validate the high mobility value of TCH$_3$. 2) The TCH$_3$ crystal is the most densely packed crystal among all TPA derivatives analysed herein. The densely packed structure increased the number of dimers contributing to the overall crystal mobility and improved the orbital coupling between the neighbouring molecules.[267] Together, both factors could explain the increase in the overall mobility of the TCH$_3$ crystal. IQA analysis performed on the TCH$_3$ crystal confirmed that the C···H interaction was attractive in nature, whereas the π–π interaction was found to be repulsive in nature (Table 4.B.1). Thus, the stabilising nature of the C···H interaction promoted the face-to-face packing arrangement of the phenyl rings in TCH$_3$, rather than the π–π interaction, thereby generating a comparatively higher hole-transport value in TCH$_3$.

In contrast to TCN, the higher hole reorganisation energy and lower charge-transfer coupling values resulted in a considerable reduction in the efficiency of hole transport in TNO$_2$, although crystals of TCN and TNO$_2$ share a common gamma-type packing arrangement. As we can observe, the charge-transport properties of TCN are unique, owing to the low hole reorganisation energy of the molecule in comparison with the other TPA derivatives studied. Overall, the general trend in mobility of TPA crystals decreased with respect to the electron-withdrawing effect of the substituents attached to the *para* position of the phenyl ring of TPA, if no other traits, such as the

void in TCOOH and dense packing of the TCH$_3$ crystal, bestowed exceptional abilities on the crystals.

4.B.3. Conclusions

We have calculated the carrier mobility values of designated TPA crystals through quantum chemical calculations. In addition, we have inspected the structure–property correlation of TPA derivatives by exploring the intermolecular interactions in the crystalline-packing arrangements of the studied TPA derivatives. HS analysis and QTAIM calculations were employed to quantify the intermolecular interactions characteristic of the TPA crystals analysed. The electron-withdrawing nature of the substituent group governed the face-to-face packing arrangement of molecules in the TPA crystals with a methodical transition to herringbone packing motif in the presence of electron-donating substituents. From detailed analyses of the charge-transporting abilities, it can be inferred that the TPA derivatives generally act as hole transporters, rather than as electron-transporting species. The substituent groups attached to the TPA core can alter the vibrational modes of individual molecules of the TPA derivatives, thereby varying the hole reorganisation energy of the parent TPA molecule with respect to the substituent group present. The general hole-transporting characteristics of the TPA crystals were found to be exceptionally high in TCN, owing to the fact that TCN had a lower reorganisation energy and highly ordered gamma packing arrangement. The stability of dimers D1 and D2 obtained from the gamma packing arrangement, which contributed efficiently to the hole mobility of TCN, were examined by using SAPT(0) calculations. Thus, we have traversed the mobility–stability correlation through TCN dimers, wherein D1 has higher stability because of the high electrostatic contribution obtained from the efficient π stacking of monomer units of dimer D1. The organisation of molecules (D1 dimer) in the TCN crystal contributed to an efficient 1D hole-conducting pathway with a high hole mobility. In addition, TCH$_3$ and TCOOH also had comparably high hole transport values, with

respect to the selected TPA derivatives. The presence of voids resulting in 1D hole-transporting channels and the extra stability driven by dense packing of molecules accounted for the large mobility values of TCOOH and TCH$_3$ crystals, respectively. Comprehensive investigations performed, to date, in the present work implies the possibility of tuning the hole-transporting properties of a series of TPA derivatives by virtue of the attached substituent groups, although the propeller shape of the TPA core can appear to be a hindrance for efficient molecular packing. This study of the trilateral relationship (structure–property–stability) of TPA crystals by tuning the substituents provides a strategy to improve the charge-transport characteristics of a widely employed material, TPA, for OLED applications.

4.B.4. Synthesis and characterization

4.B.4.1. Synthesis and crystallization of TB

Tris(4-bromophenyl)amine (TBA) (1.93 g, 4 mmol), bis(pinacolato)diborane (BPD) (3.75 g, 15 mmol) and 1,4-dioxane (60 ml) were mixed together in a 100 ml round bottom flask. [Pd(dppf)Cl$_2$] (0.5 g) was added under N$_2$ atmosphere. The reaction mixture was kept at 85○C for overnight. The organic solvent was removed under reduced pressure. Then the reaction mixture was dissolved in DCM and washed with water for several times. The crude product was purified using silica column chromatography (hexane:DCM = 2:1). A white solid was obtained as the product in 59% yield. ^{1}H NMR (500 MHz, CDCl$_3$): ppm= 7.60-7.61 (d, 6H), 6.99-7.01 (d, 6H), 1.26 (s, 36H).
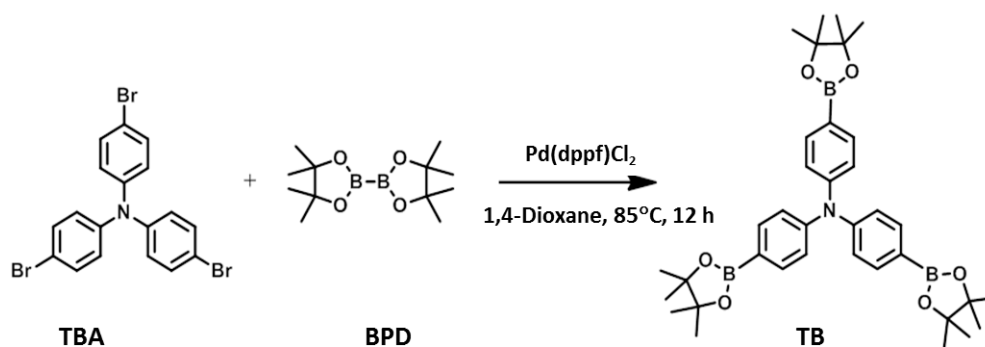
Scheme 4.B.1: *Synthesis scheme of TB.*

4.B.5. Appendix

Table C-4.B.1: *Crystal data and structure refinement parameters of TPA derivatives accessed from CSD version 5.38 using ConQuest 1.19 as the search engine*

Parameters	TCN	TNO$_2$	TCOMe	TCOOH	TBr	TCH$_3$
Crystal system	Orthorhombic	Orthorhombic	Orthorhombic	Monoclinic	Monoclinic	Triclinic
Space group, Z	*Pbcn*	*Pbcn*	*Pna*2$_1$	*P*2$_1$/*n*	*P*2$_1$/*c*	*P*-1
a, Å	8.165	8.042	18.697	7.235	9.397	12.403
b, Å	11.636	11.345	11.899	27.116	16.035	10.872
c, Å	17.565	18.344	8.722	50.042	11.368	12.944
α, deg	90	90	90	90	90	88.48
β, deg	90	90	90	92.752	107.534	103.34
γ, deg	90	90	90	90	90	88.93
V, Å^3	1668.81	1673.72	1940.43	9806.13	1633.49	1697.19

Table C4.B.2: *Crystal data and structure refinement parameters of TPA derivatives accessed from CSD version 5.38 using ConQuest 1.19 as the search engine, except TB.*

Parameters	TI	TB	TPh	TH	TCH$_2$OH
Crystal system	Monoclinic	Orthorhombic	Triclinic	Monoclinic	Monoclinic
Space group, Z	*P*2$_1$/*n*	*Pbca*	*P*-1	*B*11*b*	*P*2$_1$/*n*
a, Å	10.603	12.557	9.975	15.655	13.076
b, Å	11.422	12.399	10.632	22.257	6.162
c, Å	16.078	47.324	13.337	15.807	23.616
α, deg	90	90	98.627	90	90
β, deg	106.987	90	107.578	90	102.183
γ, deg	90	90	101.338	91.04	90
V, Å^3	1862.38	7368.96	1288.74	5506.78	1859.9.9

4.B.5.1. X-ray crystallography

High-quality single crystals were used for X-ray diffraction experiments. Crystals were mounted on a glass fibre by using oil (infineum V8512). The X-ray source used was monochromatic Mo K$_\alpha$ radiation (λ=0.710 Å at 298 K) and the diffraction spots were collected. A Bruker APEXII diffractometer was used for processing the data. Structures were solved by direct methods and expanded by using Fourier techniques. Hydrogen atoms were included in idealised positions, but not

refined, whereas non-hydrogen atoms were refined anisotropically. The HFIX command in SHELXL-97 was used to constrain hydrogen atom positions relative to their parent positions. The CIF files were validated by using Check CIF. The 3D structure visualisation and crystal packing were explored by using the Mercury 3.8 program.

4.B.6. Computational details

4.B.6.1 Hirshfeld analysis:

HS analysis was performed by using Crystal explorer 3.1 to study various intermolecular interactions present in the volume, in which the contribution to total electron density at any point exceeded that of all neighbouring molecules. The HS was mapped by normalising the contact distance, d_{norm}, which was a function of both d_i and d_e, as evaluated by EQ 4.B.1:

$$d_{norm} = \frac{d_i - r_i}{r_i} + \frac{d_e - r_e}{r_e} \qquad \text{(EQ 4.B.1)}$$

in which d_i is the distance from a point on the surface to the nearest nucleus inside the surface; d_e is the distance from a point on the surface to the nearest nucleus outside the surface; and r_e and r_i are the van der Waals radii of atoms involved in the exterior and interior to the surface at a point, respectively. The 2D fingerprint plots obtained from the HS analysis presents the fraction of surface points corresponding to each (d_i, d_e) pair. It helps to find the various intermolecular interactions present in the crystal and their percentage contribution to HS area.

4.B.6.2. QTAIM

The wave functions of TPA crystal structures were generated by employing the B3LYP functional and 6-311++G** basis set at the DFT level of theory by using the Gaussian 09 suite of programs. The generated wave functions were used for QTAIM analysis by using PROAIM in the AIM 2000 software package.[268] QTAIM analysis

helps to determine and characterise the interatomic interactions in a crystal, and are presented in the form of molecular graphs. QTAIM is a generalisation of quantum mechanics to open the quantum system. The molecular space was partitioned to atomic basins, and the expectation value of any molecular property was expressed as sum of averages over the atomic basins. QTAIM defined BCP of a bond as a point along the bond at which the electron density was minimum. It also corresponded to the point at which the BP interacted with the zero flux surface separating the atoms. The electron density and energy density at BCP was indicative of the strength and nature of the bond. The Laplacian of electron density at BCP ($\nabla^2\rho$), if lower in magnitude ($\nabla^2\rho<0$), defined a covalent bond, whereas closed interactions, such as van der Waals interactions, electrostatic interactions and hydrogen bonds had $\nabla^2\rho>0$.

4.B.6.3. IQA:

The IQA method[255],[256] was used to determine the energy of a molecular system and to analyse the electron density of stabilising interactions obtained from the QTAIM formalism. This was performed by using AIMALL software. The energy of the molecular system is defined by EQ 4.B.2:

$$E = \sum_A E^A_{intra} + \frac{1}{2}\sum_A \sum_{B \neq A} E^{AB}_{inter} \qquad \text{(EQ 4.B.2)}$$

in which the summation ran over all atoms. Intra-atomic energy, E^A_{intra}, is defined by EQ 4.B.3:

$$E^A_{intra} = T^A + V^A_{ne} + V^A_{ee} \qquad \text{(EQ 4.B.3)}$$

in which T^A is the kinetic energy of electrons in an atom, V^A_{ne} is the energy corresponding to the attraction between electrons and nucleus of an atom and V^A_{ee} is the energy corresponding to the repulsion between electrons in an atom. Interatomic energy between atoms A and B is calculated by EQ 4.B.4:

$$E^{AB}_{inter} = V^{AB}_{nn} + V^{AB}_{ne} + V^{AB}_{en} + V^{AB}_{ee} \qquad \text{(EQ 4.B.4)}$$

in which V_{nn}^{AB} is the repulsion between nuclei of A and B, V_{ee}^{AB} is the repulsion between electrons of A and B and V_{ne}^{AB} and V_{en}^{AB} corresponds to the attraction between the nucleus of one atom and the electrons of the other atom. IQA helps to understand the nature of intermolecular interactions from the interatomic energy contribution values.

4.B.6.4. Material science suite

Charge-carrier mobility was calculated by using the Jaguar[177] DFT model from Schrodinger Materials Science Suite 2016-2.[225] Calculations were performed at the B3LYP/6-311G** level of theory by using the geometry obtained from the crystal structure. The functional and basis set used for the charge-transport calculations in this work were selected by following previously reported theoretical studies on various TPA derivatives and other organic chromophores, wherein the charge-transport characteristics were analysed separately from the calculated reorganisation energy values. Marcus theory for charge-transfer rates considers electron/hole hopping as a non-adiabatic process at high temperatures. The rate of electron or hole transfer (k) is calculated by using the Marcus–Hush formalism (EQ 4.B.5)[209]

$$k = \frac{V^2}{\hbar} \left(\frac{\pi}{\lambda k_B T} \right)^{\frac{1}{2}} e^{-\lambda/4 k_B T} \qquad \text{(EQ 4.B.5)}$$

in which k_B is the Boltzmann constant, T is the temperature in Kelvin, λ is the reorganisation energy and V is the coupling matrix constant. Reorganisation energy is given by EQ 4.B.6:

$$\lambda_{\pm} = \lambda_1 + \lambda_2 = (E_0^* - E_0) + (E_{\pm}^* - E_{\pm}) \qquad \text{(EQ 4.B.6)}$$

in which E_0 and $E_{\pm}$ correspond to the energies of neutral and cationic/anionic species, respectively, in the optimised geometry. E_0^* is the energy of a neutral molecule in cationic/anionic geometry; $E_{\pm}^*$ is the energy of cation/anion in the neutral geometry for vertical transitions during electron transfer. Coupling matrix element V, which quantifies the extent of HOMO–HOMO overlap in hole transfer and LUMO–LUMO

overlap in the case of electron transfer, is obtained from the Marcus–Hush two-state model. The diffusion coefficient evaluated from the hopping value is given by EQ 4.B.7:

$$D = \frac{1}{2N}\sum_i r_i^2 \, k_i P_i \qquad \text{(EQ 4.B.7)}$$

in which N is the dimensionality of distance, P_i is the probability of electron/hole transfer to the ith neighbour and k_i is the rate of hole/electron hopping to the ith neighbour. P_i is given by EQ (4.B.8):

$$P_i = \frac{k_i}{\sum k_i} \qquad \text{(EQ 4.B.8)}$$

Charge-carrier mobility, μ, is evaluated from the Einstein relationship given by EQ 4.B.9:

$$\mu = \frac{e}{k_B T} \qquad \text{(EQ 4.B.9)}$$

in which e is the electronic charge.

The orientation-dependent charge-carrier mobility of molecules in crystals, with respect to the conducting channel, was determined by using EQ 4.B.10:

$$\mu_\varphi = \frac{e}{2k_B T} \sum_i r^2 k_i P_i \, COS^2 \gamma_i \, COS^2 (\theta_i - \varphi) \qquad \text{(EQ 4.B.10)}$$

in which γ_i is the angle between the charge-hopping pathway and the plane of interest, and $(\theta_i - \varphi)$ is the angle between the hopping pathway and the conducting channel.

Bibliography

[1]   Varghese, S.; Das, S. Role of Molecular Packing in Determining Solid-State Optical Properties of π-Conjugated Materials. *J. Phys. Chem. Lett.* **2011**, *2*, 863–873.

[2]   Hoeben, F. J. M.; Jonkheijm, P.; Meijer, E. W.; Schenning, A. P. H. J. About Supramolecular Assemblies of π-Conjugated Systems. *Chem. Rev.* **2005**, *105*, 1491–1546.

[3]   Ostroverkhova, O. Organic Optoelectronic Materials: Mechanisms and Applications. *Chem. Rev.* **2016**, *116*, 13279–13412.

[4]   Sebastian, E.; Philip, A. M.; Benny, A.; Hariharan, M. Null Exciton Splitting in Chromophoric Greek Cross (+) Aggregate. *Angew. Chemie Int. Ed.* **2018**, *57*, 15696–15701.

[5]   Brixner, T.; Hildner, R.; Köhler, J.; Lambert, C.; Würthner, F. Exciton Transport in Molecular Aggregates - From Natural Antennas to Synthetic Chromophore Systems. *Adv. Energy Mater.* **2017**, *7*, 1700236.

[6]   Ma, S.; Du, S.; Pan, G.; Dai, S.; Xu, B.; Tian, W. Organic Molecular Aggregates: From Aggregation Structure to Emission Property. *Aggregate* **2021**, *2*, 1–15.

[7]   Hestand, N. J.; Spano, F. C. Expanded Theory of H- and J-Molecular Aggregates: The Effects of Vibronic Coupling and Intermolecular Charge Transfer. *Chem. Rev.* **2018**, *118*, 7069–7163.

[8]   Chen, C.-T.; Chuang, C.; Cao, J.; Ball, V.; Ruch, D.; Buehler, M. J. Excitonic Effects from Geometric Order and Disorder Explain Broadband Optical Absorption in Eumelanin. *Nat. Commun.* **2014**, *5*, 3859.

[9]   Benny, A.; Ramakrishnan, R.; Hariharan, M. Mutually Exclusive Hole and Electron Transfer Coupling in Cross Stacked Acenes. *Chem. Sci.* **2021**, *12*, 5064–5072.

[10]   Chen, Z.; Lohr, A.; Saha-Möller, C. R.; Würthner, F. Self-Assembled π-Stacks of Functional Dyes in Solution: Structural and Thermodynamic Features. *Chemical Society Reviews*. 2009, pp 564–584.

[11]   Thalacker, C.; Würthner, F. Chiral Perylene Bisimide-Melamine Assemblies: Hydrogen Bond-Directed Growth of Helically Stacked Dyes with Chiroptical Properties. *Adv. Funct. Mater.* **2002**, *12*, 209–218.

[12]   Johnson, J. C.; Nozik, A. J.; Michl, J. The Role of Chromophore Coupling in Singlet Fission. *Acc. Chem. Res.* **2013**, *46*, 1290–1299.

[13] Yu, P.; Zhen, Y.; Dong, H.; Hu, W. Crystal Engineering of Organic Optoelectronic Materials. *Chem* **2019**, *5*, 2814–2853.

[14] Li, Y.; Jia, Z.; Xiao, S.; Liu, H.; Li, Y. A Method for Controlling the Synthesis of Stable Twisted Two-Dimensional Conjugated Molecules. *Nat. Commun.* **2016**, *7*, 11637.

[15] Mirkovic, T.; Ostroumov, E. E.; Anna, J. M.; Van Grondelle, R.; Govindjee; Scholes, G. D. Light Absorption and Energy Transfer in the Antenna Complexes of Photosynthetic Organisms. *Chem. Rev.* **2017**, *117*, 249–293.

[16] Krüger, T. P. J.; Malý, P.; Alexandre, M. T. A.; Mančal, T.; Büchel, C.; van Grondelle, R. How Reduced Excitonic Coupling Enhances Light Harvesting in the Main Photosynthetic Antennae of Diatoms. *Proc. Natl. Acad. Sci.* **2017**, *114*, E11063–E11071.

[17] Ramakrishnan, R.; Niyas, M. A.; Lijina, M. P.; Hariharan, M. Distinct Crystalline Aromatic Structural Motifs: Identification, Classification, and Implications. *Acc. Chem. Res.* **2019**, *52*, 3075–3086.

[18] Li, W.; Pan, Y.; Yao, L.; Liu, H.; Zhang, S.; Wang, C.; Shen, F.; Lu, P.; Yang, B.; Ma, Y. A Hybridized Local and Charge-Transfer Excited State for Highly Efficient Fluorescent OLEDs: Molecular Design, Spectral Character, and Full Exciton Utilization. *Adv. Opt. Mater.* **2014**, *2*, 892–901.

[19] Scholes, G. D. Limits of Exciton Delocalization in Molecular Aggregates. *Faraday Discuss.* **2019**, *221*, 265–280.

[20] Plasser, F.; Lischka, H. Analysis of Excitonic and Charge Transfer Interactions from Quantum Chemical Calculations. *J. Chem. Theory Comput.* **2012**, *8*, 2777–2789.

[21] Lijina, M. P.; Benny, A.; Ramakrishnan, R.; Nair, N. G.; Hariharan, M. Exciton Isolation in Cross-Pentacene Architecture. *J. Am. Chem. Soc.* **2020**, *142*, 17393–17402.

[22] Reveguk, Z. V.; Khoroshilov, E. V.; Sharkov, A. V.; Pomogaev, V. A.; Buglak, A. A.; Tarnovsky, A. N.; Kononov, A. I. Exciton Absorption and Luminescence in I-Motif DNA. *Sci. Rep.* **2019**, *9*, 1–9.

[23] Tretiak, S.; Zhang, W. M.; Chernyak, V.; Mukamel, S. Excitonic Couplings and Electronic Coherence in Bridged Naphthalene Dimers. *Proc. Natl. Acad. Sci.* **1999**, *96*, 13003–13008.

[24] Telfer, S. G.; McLean, T. M.; Waterland, M. R. Exciton Coupling in Coordination Compounds. *Dalt. Trans.* **2011**, *40*, 3097.

[25] Crespo-Hernández, C. E.; Cohen, B.; Kohler, B. Base Stacking Controls Excited-

State Dynamics in A·T DNA. *Nature* **2005**, *436*, 1141–1144.

[26]   Desiraju, G. R. Crystal Engineering: A Holistic View. *Angew. Chemie Int. Ed.* **2007**, *46*, 8342–8356.

[27]   Desiraju, G. R. Hydrogen Bridges in Crystal Engineering: Interactions without Borders. *Acc. Chem. Res.* **2002**, *35*, 565–573.

[28]   Cavallo, G.; Metrangolo, P.; Milani, R.; Pilati, T.; Priimagi, A.; Resnati, G.; Terraneo, G. The Halogen Bond. *Chem. Rev.* **2016**, *116*, 2478–2601.

[29]   Yao, Z. F.; Wang, J. Y.; Pei, J. Control of π-π Stacking via Crystal Engineering in Organic Conjugated Small Molecule Crystals. *Cryst. Growth Des.* **2018**, *18*, 7–15.

[30]   Meyer, E. A.; Castellano, R. K.; Diederich, F. Interactions with Aromatic Rings in Chemical and Biological Recognition. *Angew. Chemie Int. Ed.* **2003**, *42*, 1210–1250.

[31]   Choi, J. H.; Honda, T.; Seki, S.; Fukuzumi, S. Relationship between Crystal Packing and High Electron Mobility in the Single Crystal of Thienyl-Substituted Methanofullerene. *Chem. Commun.* **2011**, *47*, 11213.

[32]   Schubert, A.; Beenken, W. J. D.; Stiel, H.; Voigt, B.; Leupold, D.; Lokstein, H. Excitonic Coupling of Chlorophylls in the Plant Light-Harvesting Complex LHC-II. *Biophys. J.* **2002**, *82*, 1030–1039.

[33]   Phillips, R.; Kondev, J.; Theriot, J.; Garcia, H. G.; Orme, N. *Physical Biology of the Cell*; 2012.

[34]   Wang, H.; Wang, W.; Jin, W. J. σ-Hole Bond vs π-Hole Bond: A Comparison Based on Halogen Bond. *Chem. Rev.* **2016**, *116*, 5072–5104.

[35]   Niyas, M. A.; Ramakrishnan, R.; Vijay, V.; Sebastian, E.; Hariharan, M. Anomalous Halogen–Halogen Interaction Assists Radial Chromophoric Assembly. *J. Am. Chem. Soc.* **2019**, *141*, 4536–4540.

[36]   Salini, P. S.; Rajagopal, S. K.; Hariharan, M. Haloacetylation-Driven Transformation of Sandwich Herringbone to Lamellar/Columnar Packing in Pyrene. *Cryst. Growth Des.* **2016**, *16*, 5822–5830.

[37]   Yao, Z.-F.; Wang, J.-Y.; Pei, J. Control of π–π Stacking via Crystal Engineering in Organic Conjugated Small Molecule Crystals. *Cryst. Growth Des.* **2018**, *18*, 7–15.

[38]   Margulies, E. A.; Miller, C. E.; Wu, Y.; Ma, L.; Schatz, G. C.; Young, R. M.; Wasielewski, M. R. Enabling Singlet Fission by Controlling Intramolecular Charge Transfer in π-Stacked Covalent Terrylenediimide Dimers. *Nat. Chem.* **2016**, *8*, 1120–1125.

[39] Loots, L.; Barbour, L. J. A Simple and Robust Method for the Identification of $\pi - \pi$ Packing Motifs of Aromatic Compounds. *CrystEngComm* **2012**, *14*, 300–304.

[40] Hunter, C. A.; Sanders, J. K. M. The Nature of π-π Interactions. *J. Am. Chem. Soc.* **1990**, *112*, 5525–5534.

[41] Benny, A.; Sasikumar, D.; Hariharan, M. In Silico Exploration for Maximal Charge Transport in Organized Tetrabenzoacenes through Pitch and Roll Displacements. *J. Phys. Chem. C* **2019**, *123*, 26758–26768.

[42] Emamian, S.; Lu, T.; Kruse, H.; Emamian, H. Exploring Nature and Predicting Strength of Hydrogen Bonds: A Correlation Analysis Between Atoms-in-Molecules Descriptors, Binding Energies, and Energy Components of Symmetry-Adapted Perturbation Theory. *J. Comput. Chem.* **2019**, *40*, 2868–2881.

[43] Desiraju, G. R. Supramolecular Synthons in Crystal Engineering—A New Organic Synthesis. *Angew. Chemie Int. Ed. English* **1995**, *34*, 2311–2327.

[44] Steiner, T. The Hydrogen Bond in the Solid State. *Angew. Chemie Int. Ed.* **2002**, *41*, 48–76.

[45] Nishio, M. CH/π Hydrogen Bonds in Crystals. *CrystEngComm*. Royal Society of Chemistry May 2004, pp 130–158.

[46] Karle, I. L.; Butcher, R. J.; Wolak, M. A.; da Silva Filho, D. A.; Uchida, M.; Brédas, J.-L.; Kafafi, Z. H. Cooperative CH⋯π Interactions in the Crystal Structure of 2,5-Di(3-Biphenyl)-1,1-Dimethyl-3,4-Diphenyl-Silole and Its Effect on Its Electronic Properties. *J. Phys. Chem. C* **2007**, *111*, 9543–9547.

[47] Politzer, P.; Murray, J. S.; Clark, T. Halogen Bonding and Other σ-Hole Interactions: A Perspective. *Phys. Chem. Chem. Phys.* **2013**, *15*, 11178.

[48] Zhang, J.; Xu, W.; Sheng, P.; Zhao, G.; Zhu, D. Organic Donor-Acceptor Complexes as Novel Organic Semiconductors. *Acc. Chem. Res.* **2017**, *50*, 1654–1662.

[49] Hsu, C. P. The Electronic Couplings in Electron Transfer and Excitation Energy Transfer. *Acc. Chem. Res.* **2009**, *42*, 509–518.

[50] Clayton, A. H. A.; Scholes, G. D.; Ghiggino, K. P.; Paddon-Row, M. N. Through-Bond and Through-Space Coupling in Photoinduced Electron and Energy Transfer: An Ab Initio and Semiempirical Study. *J. Phys. Chem.* **1996**, *100*, 10912–10918.

[51] Scholes, G. D.; Ghiggino, K. P. Electronic Interactions and Interchromophore Excitation Transfer. *J. Phys. Chem.* **1994**, *98*, 4580–4590.

[52] Hestand, N. J.; Spano, F. C. Interference between Coulombic and CT-Mediated Couplings in Molecular Aggregates: H- to J-Aggregate Transformation in

Perylene-Based π-Stacks. *Journal of Chemical Physics*. 2015.

[53] Yost, S. R.; Hontz, E.; Yeganeh, S.; Van Voorhis, T. Triplet vs Singlet Energy Transfer in Organic Semiconductors: The Tortoise and the Hare. *J. Phys. Chem. C* **2012**, *116*, 17369–17377.

[54] Brédas, J. L.; Calbert, J. P.; Da Silva Filho, D. A.; Cornil, J. Organic Semiconductors: A Theoretical Characterization of the Basic Parameters Governing Charge Transport. *Proc. Natl. Acad. Sci. U. S. A.* **2002**, *99*, 5804–5809.

[55] Geng, H.; Niu, Y.; Peng, Q.; Shuai, Z.; Coropceanu, V.; Brédas, J. L. Theoretical Study of Substitution Effects on Molecular Reorganization Energy in Organic Semiconductors. *J. Chem. Phys.* **2011**, *135*.

[56] Shuai, Z.; Li, W.; Ren, J.; Jiang, Y.; Geng, H. Applying Marcus Theory to Describe the Carrier Transports in Organic Semiconductors: Limitations and Beyond. *J. Chem. Phys.* **2020**, *153*.

[57] Plasser, F.; Lischka, H. Analysis of Excitonic and Charge Transfer Interactions from Quantum Chemical Calculations. *J. Chem. Theory Comput.* **2012**, *8*, 2777–2789.

[58] Kennis, J. T. M.; Streltsov, A. M.; Vulto, S. I. E.; Aartsma, T. J.; Nozawa, T.; Amesz, J. Femtosecond Dynamics in Isolated LH2 Complexes of Various Species of Purple Bacteria. *J. Phys. Chem. B* **1997**, *101*, 7827–7834.

[59] Sauer, K.; Cogdell, R. J.; Prince, S. M.; Freer, A.; Isaacs, N. W.; Scheer, H. Structure-Based Calculations of the Optical Spectra of the LH2 Bacteriochlorophyll-Protein Complex from Rhodopseudomonas Acidophila. *Photochem. Photobiol.* **1996**, *64*, 564–576.

[60] Hu, X.; Ritz, T.; Damjanović, A.; Autenrieth, F.; Schulten, K. Photosynthetic Apparatus of Purple Bacteria. *Quarterly Reviews of Biophysics*. Cambridge University Press 2002, pp 1–62.

[61] Knoester, J.; Agranovich, V. M. Frenkel and Charge-Transfer Excitons in Organic Solids; Academic Press, 2003; Vol. 31, pp 1–96.

[62] d'Ischia, M.; Napolitano, A.; Ball, V.; Chen, C.; Buehler, M. J. Polydopamine and Eumelanin: From Structure–Property Relationships to a Unified Tailoring Strategy. *Acc. Chem. Res.* **2014**, *47*, 3541–3550.

[63] Cao, W.; Zhou, X.; McCallum, N. C.; Hu, Z.; Ni, Q. Z.; Kapoor, U.; Heil, C. M.; Cay, K. S.; Zand, T.; Mantanona, A. J.; Jayaraman, A.; Dhinojwala, A.; Deheyn, D. D.; Shawkey, M. D.; Burkart, M. D.; Rinehart, J. D.; Gianneschi, N. C. Unraveling the Structure and Function of Melanin through Synthesis. *J. Am. Chem. Soc.* **2021**, *143*, 2622–2637.

[64] Pezzella, A.; Iadonisi, A.; Valerio, S.; Panzella, L.; Napolitano, A.; Adinolfi, M.; D'Ischia, M. Disentangling Eumelanin "Black Chromophore": Visible Absorption Changes As Signatures of Oxidation State- and Aggregation-Dependent Dynamic Interactions in a Model Water-Soluble 5,6-Dihydroxyindole Polymer. *J. Am. Chem. Soc.* **2009**, *131*, 15270–15275.

[65] Panzella, L.; Gentile, G.; D'Errico, G.; Della Vecchia, N. F.; Errico, M. E.; Napolitano, A.; Carfagna, C.; D'Ischia, M. Atypical Structural and π-Electron Features of a Melanin Polymer That Lead to Superior Free-Radical-Scavenging Properties. *Angew. Chemie Int. Ed.* **2013**, *52*, 12684–12687.

[66] Ni, Q. Z.; Sierra, B. N.; La Clair, J. J.; Burkart, M. D. Chemoenzymatic Elaboration of the Raper–Mason Pathway Unravels the Structural Diversity within Eumelanin Pigments. *Chem. Sci.* **2020**, *11*, 7836–7841.

[67] Chen, C.-T.; Martin-Martinez, F. J.; Jung, G. S.; Buehler, M. J. Polydopamine and Eumelanin Molecular Structures Investigated with Ab Initio Calculations. *Chem. Sci.* **2017**, *8*, 1631–1641.

[68] Hong, S.; Na, Y. S.; Choi, S.; Song, I. T.; Kim, W. Y.; Lee, H. Non-Covalent Self-Assembly and Covalent Polymerization Co-Contribute to Polydopamine Formation. *Adv. Funct. Mater.* **2012**, *22*, 4711–4717.

[69] Della Vecchia, N. F.; Avolio, R.; Alfè, M.; Errico, M. E.; Napolitano, A.; D'Ischia, M. Building-Block Diversity in Polydopamine Underpins a Multifunctional Eumelanin-Type Platform Tunable Through a Quinone Control Point. *Adv. Funct. Mater.* **2013**, *23*, 1331–1340.

[70] Meredith, P.; Sarna, T. The Physical and Chemical Properties of Eumelanin. *Pigment Cell Res.* **2006**, *19*, 572–594.

[71] Kohl, F. R.; Grieco, C.; Kohler, B. Ultrafast Spectral Hole Burning Reveals the Distinct Chromophores in Eumelanin and Their Common Photoresponse. *Chem. Sci.* **2020**, *11*, 1248–1259.

[72] Grieco, C.; Kohl, F. R.; Hanes, A. T.; Kohler, B. Probing the Heterogeneous Structure of Eumelanin Using Ultrafast Vibrational Fingerprinting. *Nat. Commun.* **2020**, *11*, 4569.

[73] Baker, L. A.; Marchetti, B.; Karsili, T. N. V; Stavros, V. G.; Ashfold, M. N. R. Photoprotection: Extending Lessons Learned from Studying Natural Sunscreens to the Design of Artificial Sunscreen Constituents. *Chem. Soc. Rev.* **2017**, *46*, 3770–3791.

[74] d'Ischia, M.; Napolitano, A.; Pezzella, A.; Meredith, P.; Sarna, T. Chemical and Structural Diversity in Eumelanins: Unexplored Bio-Optoelectronic Materials. *Angew. Chemie Int. Ed.* **2009**, *48*, 3914–3921.

[75] Dreyer, D. R.; Miller, D. J.; Freeman, B. D.; Paul, D. R.; Bielawski, C. W. Perspectives on Poly(Dopamine). *Chem. Sci.* **2013**, *4*, 3796.

[76] Ju, K.-Y.; Fischer, M. C.; Warren, W. S. Understanding the Role of Aggregation in the Broad Absorption Bands of Eumelanin. *ACS Nano* **2018**, *12*, 12050–12061.

[77] Corani, A.; Huijser, A.; Gustavsson, T.; Markovitsi, D.; Malmqvist, P.-Å.; Pezzella, A.; D'Ischia, M.; Sundström, V. Superior Photoprotective Motifs and Mechanisms in Eumelanins Uncovered. *J. Am. Chem. Soc.* **2014**, *136*, 11626–11635.

[78] Ghosh, P.; Ghosh, D. Effect of Microsolvation on the Non-Radiative Decay of the Eumelanin Monomer. *Phys. Chem. Chem. Phys.* **2019**, *21*, 26123–26132.

[79] Datar, A.; Hazra, A. Pathways for Excited-State Nonradiative Decay of 5,6-Dihydroxyindole, a Building Block of Eumelanin. *J. Phys. Chem. A* **2017**, *121*, 2790–2797.

[80] Roberts, G. M.; Stavros, V. G. The Role of $\Pi\sigma^*$ States in the Photochemistry of Heteroaromatic Biomolecules and Their Subunits: Insights from Gas-Phase Femtosecond Spectroscopy. *Chem. Sci.* **2014**, *5*, 1698.

[81] Micillo, R.; Panzella, L.; Iacomino, M.; Prampolini, G.; Cacelli, I.; Ferretti, A.; Crescenzi, O.; Koike, K.; Napolitano, A.; D'Ischia, M. Eumelanin Broadband Absorption Develops from Aggregation-Modulated Chromophore Interactions under Structural and Redox Control. *Sci. Rep.* **2017**, *7*, 41532.

[82] Chen, C.-T.; Chuang, C.; Cao, J.; Ball, V.; Ruch, D.; Buehler, M. J. Excitonic Effects from Geometric Order and Disorder Explain Broadband Optical Absorption in Eumelanin. *Nat. Commun.* **2014**, *5*, 3859.

[83] Dreyer, D. R.; Miller, D. J.; Freeman, B. D.; Paul, D. R.; Bielawski, C. W. Elucidating the Structure of Poly(Dopamine). *Langmuir* **2012**, *28*, 6428–6435.

[84] Watt, A. A. R.; Bothma, J. P.; Meredith, P. The Supramolecular Structure of Melanin. *Soft Matter* **2009**, *5*, 3754.

[85] Plevin, M. J.; Bryce, D. L.; Boisbouvier, J. Direct Detection of CH/π Interactions in Proteins. *Nat. Chem.* **2010**, *2*, 466–471.

[86] Tsuzuki, S.; Honda, K.; Uchimaru, T.; Mikami, M.; Tanabe, K. Origin of the Attraction and Directionality of the NH/π Interaction: Comparison with OH/π and CH/π Interactions. *J. Am. Chem. Soc.* **2000**, *122*, 11450–11458.

[87] Voityuk, A. A. Effects of Dynamic Disorder on Exciton Delocalization and Photoinduced Charge Separation in DNA. *Photochem. Photobiol. Sci.* **2013**, *12*, 1303–1309.

[88] Choudhury, A.; Ghosh, D. Charge Transfer in DHICA Eumelanin-like

Oligomers: Role of Hydrogen Bonds. *Chem. Commun.* **2020**, *56*, 10481–10484.

[89] Gauden, M.; Pezzella, A.; Panzella, L.; Neves-Petersen, M. T.; Skovsen, E.; Petersen, S. B.; Mullen, K. M.; Napolitano, A.; D'Ischia, M.; Sundström, V. Role of Solvent, PH, and Molecular Size in Excited-State Deactivation of Key Eumelanin Building Blocks: Implications for Melanin Pigment Photostability. *J. Am. Chem. Soc.* **2008**, *130*, 17038–17043.

[90] d'Ischia, M.; Napolitano, A.; Pezzella, A.; Meredith, P.; Buehler, M. Melanin Biopolymers: Tailoring Chemical Complexity for Materials Design. *Angew. Chemie Int. Ed.* **2020**, *59*, 11196–11205.

[91] Sugumaran, M.; Evans, J.; Ito, S.; Wakamatsu, K. Nonenzymatic Spontaneous Oxidative Transformation of 5,6-Dihydroxyindole. *Int. J. Mol. Sci.* **2020**, *21*, 7321.

[92] Mohan, A.; Sasikumar, D.; Bhat, V.; Hariharan, M. Metastable Chiral Azobenzenes Stabilized in a Double Racemate. *Angew. Chemie* **2020**, *132*, 3227–3234.

[93] Nagarajan, K.; Mallia, A. R.; Muraleedharan, K.; Hariharan, M. Enhanced Intersystem Crossing in Core-Twisted Aromatics. *Chem. Sci.* **2017**, *8*, 1776–1782.

[94] Mallia, A. R.; Salini, P. S.; Hariharan, M. Nonparallel Stacks of Donor and Acceptor Chromophores Evade Geminate Charge Recombination. *J. Am. Chem. Soc.* **2015**, *137*, 15604–15607.

[95] Benny, A.; Ramakrishnan, R.; Hariharan, M. Mutually Exclusive Hole and Electron Transfer Coupling in Cross Stacked Acenes. *Chem. Sci.* **2021**, *12*, 5064–5072.

[96] Wakamatsu, K.; Ito, S. Preparation of Eumelanin-Related Metabolites 5,6-Dihydroxyindole, 5,6-Dihydroxyindole-2-Carboxylic Acid, and Their O-Methyl Derivatives. *Anal. Biochem.* **1988**, *170*, 335–340.

[97] Feldblum, E. S.; Arkin, I. T. Strength of a Bifurcated H Bond. *Proc. Natl. Acad. Sci.* **2014**, *111*, 4085–4090.

[98] Jeziorski, B.; Moszynski, R.; Szalewicz, K. Perturbation Theory Approach to Intermolecular Potential Energy Surfaces of van Der Waals Complexes. *Chem. Rev.* **1994**, *94*, 1887–1930.

[99] Wang, J.; Blancafort, L. Stability and Optical Absorption of a Comprehensive Virtual Library of Minimal Eumelanin Oligomer Models**. *Angew. Chemie Int. Ed.* **2021**, *60*, 18800–18809.

[100] Wirsing, S.; Hänsel, M.; Belova, V.; Schreiber, F.; Broch, K.; Engels, B.; Tegeder, P. Excited-State Dynamics in Perylene-Based Organic Semiconductor Thin Films: Theory Meets Experiment. *J. Phys. Chem. C* **2019**, *123*, 27561–27572.

[101] Plasser, F. TheoDORE: A Toolbox for a Detailed and Automated Analysis of Electronic Excited State Computations. *J. Chem. Phys.* **2020**, *152*, 084108.

[102] Seagle, B.-L. L.; Rezai, K. A.; Gasyna, E. M.; Kobori, Y.; Rezaei, K. A.; Norris, J. R. Time-Resolved Detection of Melanin Free Radicals Quenching Reactive Oxygen Species. *J. Am. Chem. Soc.* **2005**, *127*, 11220–11221.

[103] Pezzella, A.; Crescenzi, O.; Panzella, L.; Napolitano, A.; Land, E. J.; Barone, V.; D'Ischia, M. Free Radical Coupling of o -Semiquinones Uncovered. *J. Am. Chem. Soc.* **2013**, *135*, 12142–12149.

[104] Edwards, R. A.; Jickling, G.; Turner, R. J. The Light-Induced Reactions of Tryptophan with Halocompounds. *Photochem. Photobiol.* **2002**, *75*, 362.

[105] Nighswander-Rempel, S. P.; Mahadevan, I. B.; Bernhardt, P. V.; Butcher, J.; Meredith, P. Solvochromic Effects in Model Eumelanin Compounds. *Photochem. Photobiol.* **2008**, *84*, 620–626.

[106] Nizar, N. S. S.; Sujith, M.; Swathi, K.; Sissa, C.; Painelli, A.; Thomas, K. G. Emergent Chiroptical Properties in Supramolecular and Plasmonic Assemblies. *Chem. Soc. Rev.* **2021**, *50*, 11208–11226.

[107] George, S. J.; De Bruijn, R.; Tomović, Željko; Van Averbeke, B.; Beljonne, D.; Lazzaroni, R.; Schenning, A. P. H. J.; Meijer, E. W. Asymmetric Noncovalent Synthesis of Self-Assembled One-Dimensional Stacks by a Chiral Supramolecular Auxiliary Approach. *J. Am. Chem. Soc.* **2012**, *134*, 17789–17796.

[108] Kulkarni, C.; Bejagam, K. K.; Senanayak, S. P.; Narayan, K. S.; Balasubramanian, S.; George, S. J. Dipole-Moment-Driven Cooperative Supramolecular Polymerization. *J. Am. Chem. Soc.* **2015**, *137*, 3924–3932.

[109] Ajayaghosh, A.; Vijayakumar, C.; Varghese, R.; George, S. J. Cholesterol-Aided Supramolecular Control over Chromophore Packing: Twisted and Coiled Helices with Distinct Optical, Chiroptical, and Morphological Features. *Angew. Chemie Int. Ed.* **2006**, *45*, 456–460.

[110] Rao, K. V.; Miyajima, D.; Nihonyanagi, A.; Aida, T. Thermally Bisignate Supramolecular Polymerization. *Nat. Chem.* **2017**, *9*, 1133–1139.

[111] Crassous, J.; Amon, A.; Crassous, J. Circular Differential Scattering of Polarized Light by a Chiral Random Medium. *Phys. Rev. A* **2012**, *85*, 023806.

[112] Rubires, R.; Farrera, J.-A.; Ribó, J. M. Stirring Effects on the Spontaneous Formation of Chirality in the Homoassociation of Diprotonatedmeso-Tetraphenylsulfonato Porphyrins. *Chem. - A Eur. J.* **2001**, *7*, 436–446.

[113] Auguié, B.; Alonso-Gómez, J. L.; Guerrero-Martínez, A.; Liz-Marzán, L. M. Fingers Crossed: Optical Activity of a Chiral Dimer of Plasmonic Nanorods. *J.*

Phys. Chem. Lett. **2011**, *2*, 846–851.

[114] Wang, L. Y.; Smith, K. W.; Dominguez-Medina, S.; Moody, N.; Olson, J. M.; Zhang, H.; Chang, W. S.; Kotov, N.; Link, S. Circular Differential Scattering of Single Chiral Self-Assembled Gold Nanorod Dimers. *ACS Photonics* **2015**, *2*, 1602–1610.

[115] Bustamante, C.; Tinoco, I.; Maestre, M. F. Circular Differential Scattering Can Be an Important Part of the Circular Dichroism of Macromolecules. *Proc. Natl. Acad. Sci.* **1983**, *80*, 3568–3572.

[116] Sang, Y.; Yang, D.; Duan, P.; Liu, M. Towards Homochiral Supramolecular Entities from Achiral Molecules by Vortex Mixing-Accompanied Self-Assembly. *Chem. Sci.* **2019**, *10*, 2718–2724.

[117] Hendrikse, S. I. S.; Su, L.; Hogervorst, T. P.; Lafleur, R. P. M.; Lou, X.; Van Der Marel, G. A.; Codee, J. D. C.; Meijer, E. W. Elucidating the Ordering in Self-Assembled Glycocalyx Mimicking Supramolecular Copolymers in Water. *J. Am. Chem. Soc.* **2019**, *141*, 13877–13886.

[118] Narushima, T.; Okamoto, H. Circular Dichroism Microscopy Free from Commingling Linear Dichroism via Discretely Modulated Circular Polarization. *Sci. Rep.* **2016**, *6*, 35731.

[119] Sheldrick, G. M. A Short History of SHELX. *Acta Crystallographica Section A: Foundations of Crystallography*. International Union of Crystallography January 1, 2008, pp 112–122.

[120] Farrugia, L. J. WinGX Suite for Small-Molecule Single-Crystal Crystallography. *J. Appl. Crystallogr.* **1999**, *32*, 837–838.

[121] Bruno, I. J.; Cole, J. C.; Edgington, P. R.; Kessler, M.; Macrae, C. F.; McCabe, P.; Pearson, J.; Taylor, R. New Software for Searching the Cambridge Structural Database and Visualizing Crystal Structures. *Acta Crystallogr. Sect. B Struct. Sci.* **2002**, *58*, 389–397.

[122] Frisch, M. J.; Trucks, G. W.; Schlegel, H. B.; Scuseria, G. E.; Robb, M. A.; Cheeseman, J. R.; Scalmani, G.; Barone, V.; Petersson, G. A.; Nakatsuji, H.; Li, X.; Caricato, M.; Marenich, A. V.; Bloino, J.; Janesko, B. G.; Gomperts, R.; Mennucci, B.; Hratch, D. J. Gaussian 16, Revision C.01. Gaussian, Inc., Wallingford CT 2016.

[123] Bader, R. F. W. *Atoms in Molecules : A Quantum Theory*; Clarendon Press, 1990.

[124] Spackman, M. A.; Jayatilaka, D. Hirshfeld Surface Analysis. *CrystEngComm* **2009**, *11*, 19–32.

[125] Szalewicz, K. Symmetry-Adapted Perturbation Theory of Intermolecular

Forces. *Wiley Interdiscip. Rev. Comput. Mol. Sci.* **2012**, *2*, 254–272.

[126] Yashima, E. Breaking Free of Chiral Symmetry. *Nat. Chem.* **2011**, *3*, 12–14.

[127] García, F.; Sánchez, L. Structural Rules for the Chiral Supramolecular Organization of OPE-Based Discotics: Induction of Helicity and Amplification of Chirality. *J. Am. Chem. Soc.* **2012**, *134*, 734–742.

[128] Ajayaghosh, A.; Varghese, R.; George, S. J.; Vijayakumar, C. Transcription and Amplification of Molecular Chirality to Oppositely Biased Supramolecular π Helices. *Angew. Chem Int. Ed.* **2006**, *45*, 1141–1144.

[129] Foroughi, L. M.; Matzger, A. J. Intelligent Design. *Nat. Chem.* **2011**, *3*, 663–665.

[130] Miller, S. L. A Production of Amino Acids Under Possible Primitive Earth Conditions. *Science (80-.).* **1953**, *117*, 528–529.

[131] Morrow, S. M.; Bissette, A. J.; Fletcher, S. P. Transmission of Chirality through Space and across Length Scales. *Nat. Nanotechnol.* **2017**, *12*, 410–419.

[132] Cheng, X.-F.; Xia, S.-G.; Hou, X.; Xiao, X.; He, J.-H.; Ren, Z.-G.; Xu, Q.-F.; Li, H.; Li, N.-J.; Chen, D.-Y.; Lu, J.-M. Racemic Effect on the Performance of Organic Multilevel Memory: Beyond Molecular Design. *Adv. Mater. Technol.* **2017**, *2*, 1700202.

[133] Pasteur; L. Sur Les Relations Qui Peuvent Exister Entre La Forme Crystalline, La Composition Chimique et Le Sens de La Polarization Rotatoire. *Ann. Chim. Phys.* **1848**, *24*, 442–459.

[134] Gal, J. Pasteur and the Art of Chirality. *Nat. Chem.* **2017**, *9*, 604–605.

[135] Haq, S.; Liu, N.; Humblot, V.; Jansen, A. P. J.; Raval, R. Drastic Symmetry Breaking in Supramolecular Organization of Enantiomerically Unbalanced Monolayers at Surfaces. *Nat. Chem.* **2009**, *1*, 409–414.

[136] Thomas, S. P.; Grosjean, A.; Flematti, G. R.; Karton, A.; Sobolev, A. N.; Edwards, A. J.; Piltz, R. O.; Iversen, B. B.; Koutsantonis, G. A.; Spackman, M. A. Investigation of an Unusual Crystal Habit of Hydrochlorothiazide Reveals Large Polar Enantiopure Domains and a Possible Crystal Nucleation Mechanism. *Angew. Chem. Int. Ed.* **2019**, *58*, 10255–10259.

[137] Gan, Q.; Wang, X.; Kauffmann, B.; Rosu, F.; Ferrand, Y.; Huc, I. Translation of Rod-like Template Sequences into Homochiral Assemblies of Stacked Helical Oligomers. *Nat. Nanotechnol.* **2017**, *12*, 447–452.

[138] Wukovitz, S. W.; Yeates, T. O. Why Protein Crystals Favour Some Space-Groups over Others. *Nat. Struct. Mol. Biol.* **1995**, *2*, 1062–1067.

[139] Yeates, T. O.; Kent, S. B. H. Racemic Protein Crystallography. *Annu. Rev. Biophys.*

2012, *41*, 41–61.

[140] Mandal, P. K.; Collie, G. W.; Kauffmann, B.; Huc, I. Racemic DNA Crystallography. *Angew. Chem. Int. Ed.* **2014**, *53*, 14424–14427.

[141] Chen, D.; Tuchband, M. R.; Horanyi, B.; Korblova, E.; Walba, D. M.; Glaser, M. A.; Maclennan, J. E.; Clark, N. A. Diastereomeric Liquid Crystal Domains at the Mesoscale. *Nat. Commun.* **2015**, *6*, 1–10.

[142] Bock, D. A.; Lehmann, C. W. Chirality Determination from X-Ray Powder Data - Diastereomeric Co-Crystals of Mandelic Acid and Proline Amide. *CrystEngComm* **2012**, *14*, 1534–1537.

[143] Rao Khandavilli, U. B.; Lusi, M.; Bhogala, B. R.; Maguire, A. R.; Stein, M.; Lawrence, S. E. Diversity in a Simple Co-Crystal: Racemic and Kryptoracemic Behaviour. *Chem. Commun.* **2016**, *52*, 8309–8312.

[144] Imai, Y.; Kawaguchi, K.; Tajima, N.; Sato, T.; Kuroda, R.; Matsubara, Y. A Coincident Spontaneous Resolution System for Racemic 1,1′-Binaphthyl-2,2′-Dicarboxylic Acid and 1,2-Diphenylethylenediamine Induced by Water. *Chem. Commun.* **2008**, *0*, 362–364.

[145] Dutta, S.; Gellman, A. J. Enantiomer Surface Chemistry: Conglomerate: Versus Racemate Formation on Surfaces. *Chem. Soc. Rev.* **2017**, *46*, 7787–7839.

[146] Neurohr, C.; Marchivie, M.; Lecomte, S.; Cartigny, Y.; Couvrat, N.; Sanselme, M.; Subra-Paternault, P. Naproxen–Nicotinamide Cocrystals: Racemic and Conglomerate Structures Generated by CO_2 Antisolvent Crystallization. *Cryst. Growth Des.* **2015**, *15*, 4616–4626.

[147] Zhang, Y. Q.; Lin, T.; Cirera, B.; Hellwig, R.; Palma, C. A.; Chen, Z.; Ruben, M.; Barth, J. V.; Klappenberger, F. One-Dimensionally Disordered Chiral Sorting by Racemic Tiling in a Surface-Confined Supramolecular Assembly of Achiral Tectons. *Angew. Chem. Int. Ed.* **2017**, *56*, 7797–7802.

[148] Kulkarni, C.; Berrocal, J. A.; Lutz, M.; Palmans, A. R. A.; Meijer, E. W. Directing the Solid-State Organization of Racemates via Structural Mutation and Solution-State Assembly Processes. *J. Am. Chem. Soc.* **2019**, *141*, 6302–6309.

[149] Steed, K. M.; Steed, J. W. Packing Problems : High Z ′ Crystal Structures and Their Relationship to Cocrystals , Inclusion Compounds , and Polymorphism. *Chem. Rev.* **2015**, *115*, 2895–2933.

[150] Safont-Sempere, M. M.; Stepanenko, V.; Lehmann, M.; Würthner, F. Impact of Core Chirality on Mesophase Properties of Perylene Bisimides. *J. Mater. Chem.* **2011**, *21*, 7201.

[151] Osswald, P.; Würthner, F. Effects of Bay Substituents on the Racemization

Barriers of Perylene Bisimides: Resolution of Atropo-Enantiomers. *J. Am. Chem. Soc.* **2007**, *129*, 14319–14326.

[152] Sapotta, M.; Spenst, P.; Saha-Möller, C. R.; Würthner, F. Guest-Mediated Chirality Transfer in the Host–Guest Complexes of an Atropisomeric Perylene Bisimide Cyclophane Host. *Org. Chem. Front.* **2019**, *6*, 892–899.

[153] Wu, Z.; Xue, R.; Xie, M.; Wang, X.; Liu, Z.; Drechsler, M.; Huang, J.; Yan, Y. Self-Assembly-Triggered Cis-to-Trans Conversion of Azobenzene Compounds. *J. Phys. Chem. Lett.* **2018**, *9*, 163–169.

[154] Tong, X.; Pelletier, M.; Lasia, A.; Zhao, Y. FastCis–Trans Isomerization of an Azobenzene Derivative in Liquids and Liquid Crystals under a Low Electric Field. *Angew. Chemie Int. Ed.* **2008**, *47*, 3596–3599.

[155] Henzl, J.; Mehlhorn, M.; Gawronski, H.; Rieder, K. H.; Morgenstern, K. Reversible Cis-Trans Isomerization of a Single Azobenzene Molecule. *Angew. Chemie - Int. Ed.* **2006**, *45*, 603–606.

[156] Alemani, M.; Peters, M. V.; Hecht, S.; Rieder, K.-H.; Moresco, F.; Grill, L. Electric Field-Induced Isomerization of Azobenzene by STM. *J. Am. Chem. Soc.* **2006**, *128*, 14446–14447.

[157] Otolski, C. J.; Mohan Raj, A.; Ramamurthy, V.; Elles, C. G. Ultrafast Dynamics of Encapsulated Molecules Reveals New Insight on the Photoisomerization Mechanism for Azobenzenes. *J. Phys. Chem. Lett.* **2019**, *10*, 121–127.

[158] Crecca, C. R.; Roitberg, A. E. Theoretical Study of the Isomerization Mechanism of Azobenzene and Disubstituted Azobenzene Derivatives. *J. Phys. Chem. A* **2006**, *110*, 8188–8203.

[159] Wei-Guang Diau, E. A New Trans-to-Cis Photoisomerization Mechanism of Azobenzene on the S 1 (n,Π*) Surface. *J. Phys. Chem. A* **2004**, *108*, 950–956.

[160] Cembran, A.; Bernardi, F.; Garavelli, M.; Gagliardi, L.; Orlandi, G. On the Mechanism of the Cis−trans Isomerization in the Lowest Electronic States of Azobenzene: S 0 , S 1 , and T 1. *J. Am. Chem. Soc.* **2004**, *126*, 3234–3243.

[161] Bandara, H. M. D.; Burdette, S. C. Photoisomerization in Different Classes of Azobenzene. *Chem. Soc. Rev.* **2012**, *41*, 1809–1825.

[162] Adam, A.; Haberhauer, G. Switching Process Consisting of Three Isomeric States of an Azobenzene Unit. *J. Am. Chem. Soc.* **2017**, *139*, 9708–9713.

[163] Beharry, A. A.; Sadovski, O.; Woolley, G. A. Azobenzene Photoswitching without Ultraviolet Light. *J. Am. Chem. Soc.* **2011**, *133*, 19684–19687.

[164] Kumar, Y.; Kumar, S.; Kumar Keshri, S.; Shukla, J.; Singh, S. S.; Thakur, T. S.; Denti, M.; Facchetti, A.; Mukhopadhyay, P. Synthesis of Octabromoperylene

Dianhydride and Diimides: Evidence of Halogen Bonding and Semiconducting Properties. *Org. Lett.* **2016**, *18*, 472–475.

[165] Capdevila-Cortada, M.; Novoa, J. J. The Nature of the C–Br···Br–C Intermolecular Interactions Found in Molecular Crystals: A General Theoretical-Database Study. *CrystEngComm* **2015**, *17*, 3354–3365.

[166] Oh, J. H.; Sun, Y. S.; Deppisch, M.; Erk, P.; Bao, Z. A.; Wu, F.; Schmidt, R.; Oh, J. H.; Sun, Y. S.; Deppisch, M.; Krause, A. M.; Radacki, K.; Braunschweig, H.; Konemann, M.; Erk, P.; Bao, Z. A.; Wurthner, F. High-Performance Air-Stable n-Channel Organic Thin Film Transistors Based on Halogenated Perylene Bisimide Semiconductors. *J. Am. Chem. Soc.* **2009**, *131*, 6215–6228.

[167] Harada, J.; Ogawa, K. Invisible but Common Motion in Organic Crystals: A Pedal Motion in Stilbenes and Azobenzenes. *J. Am. Chem. Soc.* **2001**, *123*, 10884–10888.

[168] Harada, J.; Ogawa, K. Pedal Motion in Crystals. *Chem. Soc. Rev.* **2009**, *38*, 2244.

[169] *Multiple Acquisitions of OBPDI-Azo1 Cocrystal at Variable Temperatures (296 K & 77 K) Showcased Different Populations for Ab1 and Ab2 Azo Conformations Indicating Origin of the Disorders to Be from Pedal Motion.*

[170] *φ Represents Atom Site Occupancy in a Crystal.*

[171] *The Single Point Energies of Twisted Azo Conformation in OBPDI-Azo Cocrystal Are Reported Herein with Respect to Ab1 Geometry.*

[172] *The Values Correspond to Representative Ab1 Conformation.*

[173] Harada, J.; Ogawa, K. X-Ray Diffraction Analysis of Nonequilibrium States in Crystals: Observation of an Unstable Conformer in Flash-Cooled Crystals. *J. Am. Chem. Soc.* **2004**, *126*, 3539–3544.

[174] Stuart, C. M.; Frontiera, R. R.; Mathies, R. A. Excited-State Structure and Dynamics of Cis - and Trans -Azobenzene from Resonance Raman Intensity Analysis. *J. Phys. Chem. A* **2007**, *111*, 12072–12080.

[175] Zhu, W.; Zheng, R.; Fu, X.; Fu, H.; Shi, Q.; Zhen, Y.; Dong, H.; Hu, W. Revealing the Charge-Transfer Interactions in Self-Assembled Organic Cocrystals: Two-Dimensional Photonic Applications. *Angew. Chemie Int. Ed.* **2015**, *54*, 6785–6789.

[176] Neukirch, A. J.; Shamberger, L. C.; Abad, E.; Haycock, B. J.; Wang, H.; Ortega, J.; Prezhdo, O. V.; Lewis, J. P. Nonadiabatic Ensemble Simulations of Cis-Stilbene and Cis-Azobenzene Photoisomerization. *J. Chem. Theory Comput.* **2014**, *10*, 14–23.

[177] Bochevarov, A. D.; Harder, E.; Hughes, T. F.; Greenwood, J. R.; Braden, D. A.; Philipp, D. M.; Rinaldo, D.; Halls, M. D.; Zhang, J.; Friesner, R. A. Jaguar: A

High-Performance Quantum Chemistry Software Program with Strengths in Life and Materials Sciences. *Int. J. Quantum Chem.* **2013**, *113*, 2110–2142.

[178] Frisch, M. J.; Trucks, G. W.; Schlegel, H. B.; Scuseria, G. E.; Robb, M. A.; Cheeseman, J. R.; Scalmani, G.; Barone, V.; Mennucci, B.; Petersson, G. A.; Nakatsuji, H.; Caricato, M.; Li, X.; Hratchian, H. P.; Izmaylov, A. F.; Bloino, J.; Zheng, G.; Sonnenberg, J. L.; Hada, M.; Ehara, M. D. J. Gaussian 09, Revision A.02. *Gaussian 09, Revision A.02*. 2009.

[179] Swick, S. M.; Zhu, W.; Matta, M.; Aldrich, T. J.; Harbuzaru, A.; Lopez Navarrete, J. T.; Ponce Ortiz, R.; Kohlstedt, K. L.; Schatz, G. C.; Facchetti, A.; Melkonyan, F. S.; Marks, T. J. Closely Packed, Low Reorganization Energy π-Extended Postfullerene Acceptors for Efficient Polymer Solar Cells. *Proc. Natl. Acad. Sci.* **2018**, *115*, E8341–E8348.

[180] Gsänger, M.; Bialas, D.; Huang, L.; Stolte, M.; Würthner, F. Organic Semiconductors Based on Dyes and Color Pigments. *Adv. Mater.* **2016**, *28*, 3615–3645.

[181] Chen, H.-W.; Lee, J.-H.; Lin, B.-Y.; Chen, S.; Wu, S.-T. Liquid Crystal Display and Organic Light-Emitting Diode Display: Present Status and Future Perspectives. *Light Sci. Appl.* **2018**, *7*, 17168.

[182] Wang, C.; Dong, H.; Hu, W.; Liu, Y.; Zhu, D. Semiconducting π-Conjugated Systems in Field-Effect Transistors: A Material Odyssey of Organic Electronics. *Chem. Rev.* **2012**, *112*, 2208–2267.

[183] Sirringhaus, H. 25th Anniversary Article: Organic Field-Effect Transistors: The Path Beyond Amorphous Silicon. *Adv. Mater.* **2014**, *26*, 1319–1335.

[184] Yang, X.; Wang, L.; Wang, C.; Long, W.; Shuai, Z. Influences of Crystal Structures and Molecular Sizes on the Charge Mobility of Organic Semiconductors: Oligothiophenes. *Chem. Mater.* **2008**.

[185] Saeki, A.; Koizumi, Y.; Aida, T.; Seki, S. Comprehensive Approach to Intrinsic Charge Carrier Mobility in Conjugated Organic Molecules, Macromolecules, and Supramolecular Architectures. *Acc. Chem. Res.* **2012**, *45*, 1193–1202.

[186] Sirringhaus, H.; Brown, P. J.; Friend, R. H.; Nielsen, M. M.; Bechgaard, K.; Langeveld-Voss, B. M. W.; Spiering, A. J. H.; Janssen, R. A. J.; Meijer, E. W.; Herwig, P.; de Leeuw, D. M. Two-Dimensional Charge Transport in Self-Organized, High-Mobility Conjugated Polymers. *Nature* **1999**, *401*, 685–688.

[187] Coropceanu, V.; Cornil, J.; da Silva Filho, D. A.; Olivier, Y.; Silbey, R.; Brédas, J.-L. Charge Transport in Organic Semiconductors. *Chem. Rev.* **2007**, *107*, 926–952.

[188] Beaujuge, P. M.; Fréchet, J. M. J. Molecular Design and Ordering Effects in π-Functional Materials for Transistor and Solar Cell Applications. *J. Am. Chem. Soc.*

2011, *133*, 20009–20029.

[189] Alcívar León, C. D.; Echeverría, G. A.; Piro, O. E.; Ulic, S. E.; Jios, J. L.; Pereañez, J. A.; Henao Castañeda, I. C.; Pérez, H. The Role of Non-Covalent Interactions in Some 2-Trifluoromethylchromones in the Solid State. *New J. Chem.* **2017**, *41*, 14659–14674.

[190] Bhat, V.; Gopan, G.; Nair, N. G.; Hariharan, M. γ-Herringbone Polymorph of 6,13-Bis(Trimethylsilylethynyl)Pentacene: A Potential Material for Enhanced Hole Mobility. *Chem. Eur. J.* **2018**, *24*, 8679–8685.

[191] Awais, M. A.; Cai, Z.; Zhang, N.; Yu, L. Molecular Design towards Controlling Charge Transport. *Chem. Eur. J.* **2018**, *24*, 17180–17187.

[192] Gómez, P.; Georgakopoulos, S.; Cerón, J. P.; da Silva, I.; Más-Montoya, M.; Pérez, J.; Tárraga, A.; Curiel, D. Hydrogen-Bonded Azaphenacene: A Strategy for the Organization of π-Conjugated Materials. *J. Mater. Chem. C* **2018**, *6*, 3968–3975.

[193] Kawano, K.; Hayashi, H.; Yoshimoto, S.; Aratani, N.; Suzuki, M.; Yoshinobu, J.; Yamada, H. An Ethynylene-Bridged Pentacene Dimer: Two-Step Synthesis and Charge-Transport Properties. *Chem. - A Eur. J.* **2018**.

[194] Zhou, F.; Liu, S.; Santarsiero, B. D.; Wink, D. J.; Boudinet, D.; Facchetti, A.; Driver, T. Synthesis and Properties of New N-Heteroheptacenes for Solution-Based Organic Field Effect Transistors. *Chem. Eur. J.* **2017**, *23*, 12542–12549.

[195] Liang, Z.; Tang, Q.; Mao, R.; Liu, D.; Xu, J.; Miao, Q. The Position of Nitrogen in N-Heteropentacenes Matters. *Adv. Mater.* **2011**, *23*, 5514–5518.

[196] Anthony, J. E.; Eaton, D. L.; Parkin, S. R. A Road Map to Stable, Soluble, Easily Crystallized Pentacene Derivatives. *Org. Lett.* **2002**, *4*, 15–18.

[197] Anthony, J. E. Functionalized Acenes and Heteroacenes for Organic Electronics. *Chem. Rev.* **2006**, *106*, 5028–5048.

[198] Anthony, J. E. The Larger Acenes: Versatile Organic Semiconductors. *Angew. Chemie Int. Ed.* **2008**, *47*, 452–483.

[199] Ambili, R. V.; Sasikumar, D.; Hridya, P.; Hariharan, M. Deciphering the Multifarious Charge-Transport Behaviour of Crystalline Propeller-Shaped Triphenylamine Analogues. *Chem. – A Eur. J.* **2019**, *25*, 1992–2002.

[200] Philip, A. M.; Mallia, A. R.; Hariharan, M. Prolonged Charge Separated States in Twisted Stacks of All-Carbon Donor and Acceptor Chromophores. *J. Phys. Chem. Lett.* **2016**.

[201] Wu, Y.; Yin, Z.; Xiao, J.; Liu, Y.; Wei, F.; Tan, K. J.; Kloc, C.; Huang, L.; Yan, Q.; Hu, F.; Zhang, H.; Zhang, Q. Crystal Structure and Phototransistor Behavior of

N-Substituted Heptacence. *ACS Appl. Mater. Interfaces* **2012**, *4*, 1883–1886.

[202] Liu, W.; Luo, X.; Bao, Y.; Liu, Y. P.; Ning, G.-H.; Abdelwahab, I.; Li, L.; Nai, C. T.; Hu, Z. G.; Zhao, D.; Liu, B.; Quek, S. Y.; Loh, K. P. A Two-Dimensional Conjugated Aromatic Polymer via C–C Coupling Reaction. *Nat. Chem.* **2017**, *9*, 563–570.

[203] Wang, C.; Dong, H.; Jiang, L.; Hu, W. Organic Semiconductor Crystals. *Chem. Soc. Rev.* **2018**, *47*, 422–500.

[204] Schatschneider, B.; Phelps, J.; Jezowski, S. A New Parameter for Classification of Polycyclic Aromatic Hydrocarbon Crystalline Motifs: A Hirshfeld Surface Investigation. *CrystEngComm* **2011**, *13*, 7216–7223.

[205] Sutton, C.; Risko, C.; Brédas, J. L. Noncovalent Intermolecular Interactions in Organic Electronic Materials: Implications for the Molecular Packing vs Electronic Properties of Acenes. *Chem. Mater.* **2016**, *28*, 3–16.

[206] Hohenstein, E. G.; Duan, J.; Sherrill, C. D. Origin of the Surprising Enhancement of Electrostatic Energies by Electron-Donating Substituents in Substituted Sandwich Benzene Dimers. *J. Am. Chem. Soc.* **2011**, *133*, 13244–13247.

[207] Parker, T. M.; Sherrill, C. D. Assessment of Empirical Models versus High-Accuracy Ab Initio Methods for Nucleobase Stacking: Evaluating the Importance of Charge Penetration. *J. Chem. Theory Comput.* **2015**, *11*, 4197–4204.

[208] Turro, N. J.; Ramamurthy, V.; Scaiano, J. C. *Principles of Molecular Photochemistry: An Introduction*; 2009.

[209] Turro, N. J.; Ramamurthy, V.; Scaiano, J. C. Modern Molecular Photochemistry of Organic Molecules. *Photochem. Photobiol.* **2012**, *88*, 1033–1033.

[210] Brédas, J.-L.; Beljonne, D.; Coropceanu, V.; Cornil, J. Charge-Transfer and Energy-Transfer Processes in π-Conjugated Oligomers and Polymers: A Molecular Picture. *Chem. Rev.* **2004**, *104*, 4971–5004.

[211] Oberhofer, H.; Reuter, K.; Blumberger, J. Charge Transport in Molecular Materials: An Assessment of Computational Methods. *Chem. Rev.* **2017**, *117*, 10319–10357.

[212] Hutchison, G. R.; Ratner, M. A.; Marks, T. J. Hopping Transport in Conductive Heterocyclic Oligomers: Reorganization Energies and Substituent Effects. *J. Am. Chem. Soc.* **2005**.

[213] Deng, W. Q.; Sun, L.; Huang, J. D.; Chai, S.; Wen, S. H.; Han, K. L. Quantitative Prediction of Charge Mobilities of π-Stacked Systems by First-Principles Simulation. *Nat. Protoc.* **2015**, *10*, 632–642.

[214] Sokolov, A. N.; Atahan-Evrenk, S.; Mondal, R.; Akkerman, H. B.; Sánchez-

Carrera, R. S.; Granados-Focil, S.; Schrier, J.; Mannsfeld, S. C. B.; Zoombelt, A. P.; Bao, Z.; Aspuru-Guzik, A. From Computational Discovery to Experimental Characterization of a High Hole Mobility Organic Crystal. *Nat. Commun.* **2011**, *2*, 437.

[215] Norton, J. E.; Brédas, J.-L. Polarization Energies in Oligoacene Semiconductor Crystals. *J. Am. Chem. Soc.* **2008**, *130*, 12377–12384.

[216] Da Silva Filho, D. A.; Kim, E. G.; Brédas, J. L. Transport Properties in the Rubrene Crystal: Electronic Coupling and Vibrational Reorganization Energy. *Adv. Mater.* **2005**, *17*, 1072–1076.

[217] Cornil, J.; Beljonne, D.; Calbert, J. P.; Brédas, J. L. Interchain Interactions in Organic π-Conjugated Materials: Impact on Electronic Structure, Optical Response, and Charge Transport. *Adv. Mater.* **2001**, *13*, 1053–1067.

[218] Ivanov, M. V.; Reid, S. A.; Rathore, R. Game of Frontier Orbitals: A View on the Rational Design of Novel Charge-Transfer Materials. *J. Phys. Chem. Lett.* **2018**, *9*, 3978–3986.

[219] Ziogos, O. G.; Konstantinopoulos, S.; Tsetseris, L.; Theodorou, D. N. Computational Studies of Nanographene Systems: Extended Discotics, Covalently Linked "Supermolecules," and Functionalized Supramolecular Assemblies. *J. Phys. Chem. C* **2018**, *122*, 18715–18731.

[220] Lee, J.-K.; Kim, J.-G.; Hembram, K. P. S. S.; Kim, Y.-I.; Min, B.-K.; Park, Y.; Lee, J.-K.; Moon, D. J.; Lee, W.; Lee, S.-G.; John, P. The Nature of Metastable AA′ Graphite: Low Dimensional Nano- and Single-Crystalline Forms. *Sci. Rep.* **2016**, *6*, 39624.

[221] Rose, C.; Lebrun, A.; Clément, S.; Richeter, S. Cofacial Porphyrin Dimers Assembled from N-Heterocyclic Carbene–Metal Bonds. *Chem. Commun.* **2018**, *54*, 9603–9606.

[222] Nguyen, T. P.; Shim, J. H.; Lee, J. Y. Density Functional Theory Studies of Hole Mobility in Picene and Pentacene Crystals. *J. Phys. Chem. C* **2015**, *119*, 11301–11310.

[223] Chai, S.; Wen, S. H.; Huang, J. D.; Han, K. L. Density Functional Theory Study on Electron and Hole Transport Properties of Organic Pentacene Derivatives with Electron-Withdrawing Substituent. *J. Comput. Chem.* **2011**, *32*, 3218–3225.

[224] Zhang, Y.; Duan, Y.; Liu, J.; Zheng, D.; Zhang, M.; Zhao, G. Influence of the Halogenated Substituent on Charge Transfer Mobility of Aniline Tetramer and Derivatives: Remarkable Anisotropic Mobilities. *J. Phys. Chem. C* **2017**, *121*, 17633–17640.

[225] Materials Science Suite 2016–2014. Schrodinger, LLC, New York, NY (USA).

2016.

[226] Parrish, R. M.; Burns, L. A.; Smith, D. G. A.; Simmonett, A. C.; DePrince, A. E.; Hohenstein, E. G.; Bozkaya, U.; Sokolov, A. Y.; Di Remigio, R.; Richard, R. M.; Gonthier, J. F.; James, A. M.; McAlexander, H. R.; Kumar, A.; Saitow, M.; Wang, X.; Pritchard, B. P.; Verma, P.; Schaefer, H. F.; Patkowski, K.; King, R. A.; Valeev, E. F.; Evangelista, F. A.; Turney, J. M.; Crawford, T. D.; Sherrill, C. D. <scp>Psi4</Scp> 1.1: An Open-Source Electronic Structure Program Emphasizing Automation, Advanced Libraries, and Interoperability. *J. Chem. Theory Comput.* **2017**, *13*, 3185–3197.

[227] Su, S.-J.; Chiba, T.; Takeda, T.; Kido, J. Pyridine-Containing Triphenylbenzene Derivatives with High Electron Mobility for Highly Efficient Phosphorescent OLEDs. *Adv. Mater.* **2008**, *20*, 2125–2130.

[228] Thomas, K. R. J.; Velusamy, M.; Lin, J. T.; Chuen, C. H.; Tao, Y.-T. Hexaphenylphenylene Dendronised Pyrenylamines for Efficient Organic Light-Emitting Diodes. *J. Mater. Chem.* **2005**, *15*, 4453.

[229] Allard, S.; Forster, M.; Souharce, B.; Thiem, H.; Scherf, U. Organic Semiconductors for Solution-Processable Field-Effect Transistors (OFETs). *Angew. Chem. Int. Ed.* **2008**, *47*, 4070–4098.

[230] Song, Y.; Di, C.; Yang, X.; Li, S.; Xu, W.; Liu, Y.; Yang, L.; Shuai, Z.; Zhang, D.; Zhu, D. A Cyclic Triphenylamine Dimer for Organic Field-Effect Transistors with High Performance. *J. Am. Chem. Soc.* **2006**, *128*, 15940–15941.

[231] Shirota, Y. Organic Materials for Electronic and Optoelectronic Devices. *J. Mater. Chem.* **2000**, *10*, 1–25.

[232] Kunihiro, M.; Nakasone, Y.; Matsuda, S.; Shironita, S.; Nagayama, N.; Umeda, M. Crystal Structure Oriented Carrier Transport Characteristic of Triphenylamine Derivative Single Crystal. *AIP Adv.* **2018**, *8*, 035324.

[233] Mas-Torrent, M.; Hadley, P.; Bromley, S. T.; Ribas, X.; Tarrés, J.; Mas, M.; Molins, E.; Veciana, J.; Rovira, C. Correlation between Crystal Structure and Mobility in Organic Field-Effect Transistors Based on Single Crystals of Tetrathiafulvalene Derivatives. *J. Am. Chem. Soc.* **2004**, *126*, 8546–8553.

[234] Pola, S.; Kuo, C.-H.; Peng, W.-T.; Islam, M. M.; Chao, I.; Tao, Y.-T. Contorted Tetrabenzocoronene Derivatives for Single Crystal Field Effect Transistors: Correlation between Packing and Mobility. *Chem. Mater.* **2012**, *24*, 2566–2571.

[235] Anthony, J. E.; Brooks, J. S.; Eaton, D. L.; Parkin, S. R. Functionalized Pentacene: Improved Electronic Properties from Control of Solid-State Order. *J. Am. Chem. Soc.* **2001**, *123*, 9482–9483.

[236] Cias, P.; Slugovc, C.; Gescheidt, G. Hole Transport in Triphenylamine Based

OLED Devices: From Theoretical Modeling to Properties Prediction. *J. Phys. Chem. A* **2011**, *115*, 14519–14525.

[237] Justin Thomas, K. R.; Lin, J. T.; Tao, Y.-T.; Ko, C.-W. New Star-Shaped Luminescent Triarylamines: Synthesis, Thermal, Photophysical, and Electroluminescent Characteristics. *Chem. Mater.* **2002**, *14*, 1354–1361.

[238] Li, Z.; Wu, Z.; Fu, W.; Liu, P.; Jiao, B.; Wang, D.; Zhou, G.; Hou, X. Versatile Fluorinated Derivatives of Triphenylamine as Hole-Transporters and Blue-Violet Emitters in Organic Light-Emitting Devices. *J. Phys. Chem. C* **2012**, *116*, 20504–20512.

[239] Kanibolotsky, A. L.; Perepichka, I. F.; Skabara, P. J. Star-Shaped π-Conjugated Oligomers and Their Applications in Organic Electronics and Photonics. *Chem. Soc. Rev.* **2010**, *39*, 2695.

[240] Shirota, Y.; Kageyama, H. Charge Carrier Transporting Molecular Materials and Their Applications in Devices. *Chem. Rev.* **2006**, *107*, 953–1010.

[241] Malagoli, M.; Brédas, J. L. Density Functional Theory Study of the Geometric Structure and Energetics of Triphenylamine-Based Hole-Transporting Molecules. *Chem. Phys. Lett.* **2000**, *327*, 13–17.

[242] Mallia, A. R.; Ramakrishnan, R.; Niyas, M. A.; Hariharan, M. Crystalline Triphenylamine Substituted Arenes: Solid State Packing and Luminescence Properties. *CrystEngComm* **2017**, *19*, 817–825.

[243] Zhang, N.-X.; Ren, A.-M.; Ji, L.-F.; Zhang, S.-F.; Guo, J.-F. Theoretical Investigations on Molecular Packing Motifs and Charge Transport Properties of a Family of Trialkylsilylethynyl-Modified Pentacenes/Anthradithiophenes. *J. Phys. Chem. C* **2018**, *122*, 18880–18894.

[244] Bromley, S. T.; Mas-Torrent, M.; Hadley, P.; Rovira, C. Importance of Intermolecular Interactions in Assessing Hopping Mobilities in Organic Field Effect Transistors: Pentacene versus Dithiophene-Tetrathiafulvalene. *J. Am. Chem. Soc.* **2004**, *126*, 6544–6545.

[245] Lin, B. C.; Cheng, C. P.; Lao, Z. P. M. Reorganization Energies in the Transports of Holes and Electrons in Organic Amines in Organic Electroluminescence Studied by Density Functional Theory. *J. Phys. Chem. A* **2003**, *107*, 5241–5251.

[246] Cui, C. M.; Zhou, H. P.; Zhu, C. H.; Wu, J. Y. Tris(4-Acetylphenyl)Amine. *Acta Crystallogr. Sect. E Struct. Reports Online* **2006**, *62*, 1762–1763.

[247] Shirota, Y. Photo- and Electroactive Amorphous Molecular Materials—Molecular Design, Syntheses, Reactions, Properties, and Applications. *J. Mater. Chem.* **2005**, *15*, 75–93.

[248] Cîrcu, M.; Paşcanu, V.; Soran, A.; Braun, B.; Terec, A.; Socaci, C.; Grosu, I. Solid State Supramolecular Assemblies of Triol Podands through H-Bonds. *CrystEngComm* **2012**, *14*, 632–639.

[249] Nandi, S.; Chakraborty, D.; Vaidhyanathan, R. A Permanently Porous Single Molecule H-Bonded Organic Framework for Selective CO 2 Capture. *Chem. Commun.* **2016**, *52*, 7249–7252.

[250] McKinnon, J. J.; Jayatilaka, D.; Spackman, M. A. Towards Quantitative Analysis of Intermolecular Interactions with Hirshfeld Surfaces. *Chem. Commun.* **2007**, No. 37, 3814.

[251] McKinnon, J. J.; Spackman, M. A.; Mitchell, A. S. Novel Tools for Visualizing and Exploring Intermolecular Interactions in Molecular Crystals. *Acta Crystallogr., Sect. B Struct. Sci.* **2004**, *60*, 627–668.

[252] Spackman, M. A.; McKinnon, J. J. Fingerprinting Intermolecular Interactions in Molecular Crystals. *CrystEngComm* **2002**, *4*, 378–392.

[253] Deng, W.-Q.; Goddard, W. A. Predictions of Hole Mobilities in Oligoacene Organic Semiconductors from Quantum Mechanical Calculations †. *J. Phys. Chem. B* **2004**, *108*, 8614–8621.

[254] Dillen, J. Congested Molecules. Where Is the Steric Repulsion? An Analysis of the Electron Density by the Method of Interacting Quantum Atoms. *Int. J. Quantum Chem.* **2013**, *113*, 2143–2153.

[255] Blanco, M. A.; Martín Pendás, A.; Francisco, E. Interacting Quantum Atoms: A Correlated Energy Decomposition Scheme Based on the Quantum Theory of Atoms in Molecules. *J. Chem. Theory Comput.* **2005**, *1*, 1096–1109.

[256] Martín Pendás, A.; Blanco, M. A.; Francisco, E. The Nature of the Hydrogen Bond: A Synthesis from the Interacting Quantum Atoms Picture. *J. Chem. Phys.* **2006**, *125*, 184112.

[257] Zhurova, E. A.; Tsirelson, V. G.; Stash, A. I.; Pinkerton, A. A. Characterizing the Oxygen−Oxygen Interaction in the Dinitramide Anion. *J. Am. Chem. Soc.* **2002**, *124*, 4574–4575.

[258] Saha, B. K.; Rather, S. A.; Saha, A. Interhalogen Interactions in the Light of Geometrical Correction. *Cryst. Growth Des.* **2016**, *16*, 3059–3062.

[259] Patra, A.; Anthony, S. P.; Radhakrishnan, T. P. Tris(4-Cyanophenyl)Amine: Simple Synthesis via Self-Assembly; Strong Fluorescence in Solution, Nano/Microcrystals, and Solid. *Adv. Funct. Mater.* **2007**, *17*, 2077–2084.

[260] Wang, L.; Nan, G.; Yang, X.; Peng, Q.; Li, Q.; Shuai, Z. Computational Methods for Design of Organic Materials with High Charge Mobility. *Chem. Soc. Rev.*

2010, *39*, 423–434.

[261] Kuo, M.-Y.; Chen, H.-Y.; Chao, I. Cyanation: Providing a Three-in-One Advantage for the Design Ofn-Type Organic Field-Effect Transistors. *Chem. Eur. J.* **2007**, *13*, 4750–4758.

[262] Jérome, D. Organic Conductors: From Charge Density Wave TTF–TCNQ to Superconducting (TMTSF) 2 PF 6. *Chem. Rev.* **2004**, *104*, 5565–5592.

[263] Koh, S. E.; Risko, C.; da Silva Filho, D. A.; Kwon, O.; Facchetti, A.; Brédas, J.-L.; Marks, T. J.; Ratner, M. A. Modeling Electron and Hole Transport in Fluoroarene-Oligothiopene Semiconductors: Investigation of Geometric and Electronic Structure Properties. *Adv. Funct. Mater.* **2008**, *18*, 332–340.

[264] Fiethen, A.; Jansen, G.; Hesselmann, A.; Schütz, M. Stacking Energies for Average B-DNA Structures from the Combined Density Functional Theory and Symmetry-Adapted Perturbation Theory Approach. *J. Am. Chem. Soc.* **2008**, *130*, 1802–1803.

[265] Wen, S.; Deng, W.-Q.; Han, K.-L. Ultra-Low Resistance at TTF–TCNQ Organic Interfaces. *Chem. Commun.* **2010**, *46*, 5133.

[266] Wen, S.-H.; Li, A.; Song, J.; Deng, W.-Q.; Han, K.-L.; Goddard, W. A. First-Principles Investigation of Anistropic Hole Mobilities in Organic Semiconductors. *J. Phys. Chem. B* **2009**, *113*, 8813–8819.

[267] Mitsui, C.; Soeda, J.; Miwa, K.; Tsuji, H.; Takeya, J.; Nakamura, E. Naphtho[2,1-B :6,5- b ']Difuran: A Versatile Motif Available for Solution-Processed Single-Crystal Organic Field-Effect Transistors with High Hole Mobility. *J. Am. Chem. Soc.* **2012**, *134*, 5448–5451.

[268] Biegler-könig, F. W.; Bader, R. F. W.; Tang, T.-H. Calculation of the Average Properties of Atoms in Molecules. II. *J. Comput. Chem.* **1982**, *3*, 317–328.

List of Publications

1. Sohan D. Jadhav, **Devika Sasikumar** and Mahesh Hariharan, Modulating Singlet Fission through Interchromophoric Rotation, *Phys. Chem. Chem. Phys.* 2022, *24*, 16193-16199

2. **Devika Sasikumar**, Kavya Vinod, Jeswin Sunny and Mahesh Hariharan, Exciton Interactions in Helical Crystals of a Hydrogen-bonded Eumelanin Monomer. *Chem. Sci.* 2022, *13*, 2331-2338.

3. **Devika Sasikumar ‡**, Athira T. John ‡, Jeswin Sunny and Mahesh Hariharan, Access to Triplet Excited States of Organic Chromophores. *Chem. Soc. Rev.* 2020, *49*, 6122-6140 **(Front Inside Cover)**.

4. Amalu Mohan ‡, **Devika Sasikumar ‡**, Vinayak Bhat and Mahesh Hariharan, Metastable Chiral Azobenzenes Stabilized in a Double Racemate. *Angew. Chem. Int. Ed.* 2020, *59*, 3201–3208 **(Research Article Frontispiece).**

5. Alfy Benny ‡, **Devika Sasikumar ‡** and Mahesh Hariharan, In Silico Exploration for Maximal Charge Transport in Organized Tetrabenzoacenes through Pitch and Roll Displacements. *J. Phys. Chem. C* 2019, *123*, 26758–26768 **(Front Cover).**

6. Ambili R. V. ‡, **Devika Sasikumar ‡**, Hridya P ‡ and Mahesh Hariharan, Deciphering the Multifarious Charge-Transport Behaviour of Crystalline Propeller-Shaped Triphenylamine Analogues. *Chem. Eur. J.* 2019, *25*, 1992-2002.

7. Shinaj K. Rajagopal ‡, Nagaraj K. ‡, Somadrita Deb, Vinayak Bhat, **Devika Sasikumar**, Ebin Sebastian and Mahesh Hariharan, Extending the Scope of Carbonyl Facilitated Triplet Excited State towards Visible Light Excitation. *Phys. Chem. Chem. Phys.* 2018, *20*, 19120–19128.

‡ Equal Contribution

Workshops and Conferences

1. 11th Asian Photochemistry Conference (APC-2021, 31 October - 4 November 2021), Korea (Presented Poster).

2. Virtual Chemistry Course "Functional π-Systems–Organic Materials Design by Molecular and Supramolecular Engineering", (19-23 July 2021), Julius-Maximilians-Universität, Würzburg.

3. Femto-UP 2020: Ultrafast lasers technologies and applications-Online, (8 Mar-1 Apr 2021), France.

4. Fluorescence Correlation Spectroscopy Workshop 2020 (7–12 December 2020), Virtual Workshop, Department of Chemistry, IIT Bombay. (Presented Poster)

5. 2nd International Conference on "Crystal Engineering: From Molecule to Crystal-2020 (CE:FMC)" (19-20 June 2020), Virtual Conference. (Presented poster)

6. International Conference on Ultrafast Spectroscopy (ICUS2020) (21-22 February 2020), IISER TVM, Kerala India.

7. IISERTVM-RSC Symposium on Advances in Chemical Sciences (4 February 2020), IISER TVM, Kerala India. (Presented poster)

8. Frontier Symposium in Chemistry 2020 (17-18 January 2020), IISER TVM, Kerala India. (Presented poster)

9. 15th JNC Research Conference on Chemistry of Materials (30 September-02 October 2019), Thiruvananthapuram, Kerala, India. (Presented poster)

10. 24th CRSI National Symposium in Chemistry (CRSI-NSC-24) (8-10 February 2019), CLRI and IIT Madras, Chennai, Tamil Nadu, India. (Presented poster)

11. Sorbonne-JNCASR School on Advanced Computational Material Science (29 January-02 February 2018), JNCASR, Bengaluru, Karnataka, India.

12. Faraday Discussions: Photoinduced Processes in Nucleic acids and Proteins (11-13 January 2018), Thiruvananthapuram, Kerala, India. (Presented poster)

13. 13th JNC Research Conference on Chemistry of Materials (01-03 October 2017), Thiruvananthapuram, Kerala, India. (Presented poster)

14. 8th East Asia Symposium on Functional Dyes and Advanced Materials (20-22 September 2017), CSIR-NIIST, Thiruvananthapuram, Kerala, India.

15. Inter-IISER Chemistry Meet 2015 (IICM 2015) (11-13 December 2015), Thiruvananthapuram, Kerala, India.

Achievements in Workshops and Conferences

1. The Best Short Oral Award of APC-2021 during the 11th Asian Photochemistry Conference (APC-2021, 31 October - 4 November 2021), Korea.

2. Best Poster Presentation Prize in IISERTVM-RSC Symposium on Advances in Chemical Sciences (4 February 2020), IISER TVM, Kerala India.

3. Best Poster Presentation Prize in 13th JNC Research Conference on Chemistry of Materials (01-03 October 2017), Thiruvananthapuram, Kerala, India.

Copyrights and Permissions

Copyrights and Permissions

Copyrights and Permissions